

Marquette University

e-Publications@Marquette

Dissertations (1934 -)

Dissertations, Theses, and Professional
Projects

Photophysical and Photocatalytic Properties of Covalent Organic Frameworks

Daniel Streater H.
Marquette University

Follow this and additional works at: https://epublications.marquette.edu/dissertations_mu

 Part of the [Chemistry Commons](#)

Recommended Citation

H., Daniel Streater, "Photophysical and Photocatalytic Properties of Covalent Organic Frameworks" (2023). *Dissertations (1934 -)*. 3057.
https://epublications.marquette.edu/dissertations_mu/3057

PHOTOPHYSICAL AND PHOTOCATALYTIC PROPERTIES OF COVALENT ORGANIC
FRAMEWORKS

By

Daniel H. Streater

A Dissertation submitted to the Faculty of the Graduate School,

Marquette University,

in Partial Fulfillment of the Requirements for

the Degree of Doctor of Philosophy

Milwaukee, Wisconsin

August 2023

ABSTRACT

PHOTOPHYSICAL AND PHOTOCATALYTIC PROPERTIES OF COVALENT ORGANIC
FRAMEWORKS

Daniel H. Streater

Marquette University, August 2023

This dissertation is most interested in how a class of materials known as covalent organic frameworks (COFs) can be designed to capture photon energy to initiate chemical reactions. Different COF designs change how long the energy is held, how it migrates, and how it is dispersed – and these differences can be used to change their performance as *artificial* photosynthesis platforms. Thus, it is helpful to have an informative discussion about the processes behind *natural* photosynthesis, that is, nature's light harvesting strategies and photocatalytic schemes (Section 1.2) and will lead into an introduction of COFs and why they possess unique potential as artificial photosynthesis platforms (Section 1.3). Their beneficial physical qualities are complemented by understanding their electronic structures from theoretically predicted properties with specific focus on topological symmetry (Section 1.4). Synthesizing and characterizing COF systems then becomes an important consideration (Section 1.5) along with how their excited state behaviors are probed and interpreted at reaction timescales by ultrafast spectroscopic techniques (Section 1.6). Finally, a look is taken at how COF structure versatility adds unique potential in catalyst engineering (Section 1.7).

The main body of this dissertation will present five research projects that seek to test theoretical predictions, assess the impact of COF planarity, or fine tune electronic structures. To test theoretical predictions, Chapter 3 involves exploring nodal symmetry in topologically similar COFs by varying monomers. Chapter 4 looks at the role of dihedral angles on intersystem crossing (ISC) rates in organic chromophores with star-shaped motifs like those often found in COFs. Chapter 5 explores planar and non-planar COFs with nonpolar C=C linkers that affect the deactivation of their photoexcited states. Chapter 6 investigates changes in donor-acceptor arrangements lead to differences in excited state populations. Finally, the seminal work in Chapter 7 directly shows the effect the direction of the imine bond has on photophysical and photocatalytic properties in COFs.

ACKNOWLEDGEMENTS

Daniel H. Streater

Reaching the end of my graduate studies at Marquette University always seemed far off on the horizon. Now that the end is approaching, I have begun to reflect on all the challenges and successes encountered along the way. Throughout it all, my advisor Professor Jier Huang, kept the ship pointed in the right direction while simultaneously giving me the latitude to explore my ideas. Apart from being a wonderful scientific advisor she cared for the whole person – that is, the mental and emotional well-being of the student on top of stimulating their academic curiosity. In my opinion, that is the mark of a great PhD advisor, and I will always be grateful to her for her guidance as a scientist, and as a person. Of course, many others played a role in helping reach the end of my studies.

To my lab mates Sizhuo, Wenhui, James, Korlan, Quishi, and Humphrey you taught me so much about chemistry, mentorship, and friendship and I would not have made it through without you. Thank you to Dr. Kevin Kohlstedt, you always made yourself available to provide help when I needed it, and when problems seemed daunting, you would often help me break them into manageable pieces. To Dr. Kedem and Dr. Reid, thank you for allowing me to ask you questions, for providing advice, or for helping me to use new instruments to satisfy my curiosity. To Dave Virgillito of Spectra-Physics, a special thank you for having the patience to dedicate your time helping troubleshoot issues with the Solstice and teaching me so much about lasers. I would also like to thank the Marquette chemistry department staff - Lori, Jen, the Gregs, Paul, and Sergei – they kept everything running throughout the years and made Todd Wehr Chemistry somewhere I always enjoyed coming to work.

To my family, who never really understood what I was researching but offered support regardless, thank you. Sister Charlotte – you are always a source of joy and fun I'm so glad to have had you close throughout these years. Sister Katherine – you are an exceptional role model who showed me to be independent, and to follow my dreams. Sister Samantha – your curiosity and drive are inspiring and are things I try to embody every single day of my life. Parents Patrick and Kimberly – your unwavering belief that I could accomplish what I set out to do was everything to me, you never doubted, you always expressed pride in me, and you've always been there.

Finally, to my wife Tiffany – you were such an important force in my life during these years. You provided so much support, endless love, and unconditional faith. These years have been beautiful with you and I'm so glad to have you on this journey with me. I can't wait to see where the next leg of our life will take us, but together we can accomplish anything.

TABLE OF CONTENTS

CHAPTER 1 – INTRODUCTION.....	1
1.1 Environmentally Friendly Resource Security	1
1.2 Nature’s Photocatalyst Design	3
1.3 Overview of Covalent Organic Frameworks.....	6
1.4 Electronic Structure of Covalent Organic Frameworks	11
1.5 Synthesis, Activation, and Characterization of Covalent Organic Frameworks	17
1.6 Ultrafast Spectroscopy Studies of Covalent Organic Frameworks	24
1.7 Photocatalysis by Covalent Organic Frameworks.....	28
CHAPTER 2 – EXPERIMENTAL AND THEORETICAL METHODS & DETAILS.....	32
2.1 Experimental and Computational Methods for Chapter 3.....	32
2.2 Experimental and Computational Methods for Chapter 4.....	35
2.3 Experimental and Computational Methods for Chapter 5.....	37
2.4 Experimental and Computational Methods for Chapter 6.....	41
2.5 Experimental and Computational Methods for Chapter 7.....	43
CHAPTER 3 – TUNING PHOTOEXCITED CHARGE TRANSFER AND NODAL SYMMETRY IN IMINE-LINKED TWO-DIMENSIONAL COVALENT ORGANIC FRAMEWORKS.....	47
3.1 Introduction.....	47
3.2 Synthesis and Characterization of BTPA COFs.....	46
3.3 Ultrafast Transient Absorption Spectroscopy of BTPA COFs.....	51
3.4 Conclusions.....	60
CHAPTER 4 – IMPACT OF π -CONJUGATION LENGTH ON THE EXCITED-STATE DYNAMICS OF STAR SHAPED CARBAZOLE- π -TRIAZINE ORGANIC CHROMOPHORES.....	59
4.1 Introduction.....	59
4.2 Steady State Spectroscopic Properties of pTCT Series	63
4.3 Theoretical Relaxation Dynamics of pTCT Series.....	64

4.4 Excited State Dynamics of pTCT series.....	68
4.5 Prediction of ISC Rates for pTCT Series Molecules.....	71
4.6 Global Fitting and ISC Rate Observation.....	73
4.7 Conclusions.....	74
 CHAPTER 5 – CONJUGATION AND AGGREGATION DIRECTED DESIGN OF COVALENT ORGANIC FRAMEWORKS AS WHITE-LIGHT-EMITTING DIODES	75
5.1 Introduction.....	78
5.2 Synthesis and Structural Characterization of TAT-COF and TPB-COF.....	80
5.3 Spectroscopic Characterization of TAT-COF and TPB-COF and Their Utility as WLEDs	81
5.4 Excited State Dynamics of TAT-COF and TPB-COF	83
5.5 Theoretical Modeling of TAT-COF and TPB-COF	86
5.6 Conclusions.....	91
 CHAPTER 6 – WAVELENGTH DEPENDENT EXCITONIC PROPERTIES OF COVALENT ORGANIC FRAMEWORKS EXPLORED BY THEORY AND EXPERIMENT.....	92
6.1 Introduction.....	92
6.2 Synthesis and Characterization of Isostructural 2D COFs	94
6.3 The Nature of Intralayer CT in Isostructural N ₂ N ₃ and N ₂ C ₃ COFs.....	96
6.4 The Role of Interlayer Interactions on CT in N ₂ N ₃ COF.....	100
6.5 Tail State Analysis of Isostructural COFs.....	102
6.6 Excited State Dynamics of CT Excitons in Isostructural COFs by fs-OTA Spectroscopy	104
6.7 Conclusions.....	114
 CHAPTER 7 – IMINE REVERSAL MEDIATES CHARGE SEPARATION AND CO ₂ PHOTOREDUCTION IN COVALENT ORGANIC FRAMEWORKS	112
7.1 Introduction.....	112
7.2 Synthesis and Characterization of r-COF and Re-r-COF.....	114
7.3 Impact of Imine Direction on Ground State Transitions of f-COF and r-COF	119
7.4 Impact of Imine Direction on Excited State Dynamics of f-COF and r-COF	120

7.5 Impact of Imine Direction on Ground State Transitions of Re-f-COF and Re-r-COF	122
7.6 Impact of Imine Direction on Excited State Dynamics of Re-f-COF and Re-r-COF	124
7.7 Modeling Excited State Pathways of Re-f-COF and Re-r-COF	126
7.8 Impact of Imine Direction on Photocatalytic Performance	129
7.9 Conclusion	130
CHAPTER 8 – CONCLUSIONS & FUTURE DIRECTIONS	132
8.1 Topology, Aggregation, and Intramolecular Charge Transfer Make COFs Unique Photocatalyst Platforms	132
8.2 Future Directions for Covalent Organic Framework Research in Catalysis and Optoelectronics	133
CHAPTER 9 – APPENDICES	136
9.1 Density Functional Tight-Binding	136
9.2 Overview of Theoretical Background of DFT and TDDFT	141
9.3 Orbital Configurations and Natural Transition Orbitals	150
9.4 Transition Density Matrix Analysis	152
9.5 Brunauer-Emmett-Teller Theory	154
9.6 Fundamentals of Water Oxidation	157
Water Nucleophilic Attack vs. Two Interacting Metallo-Oxyls	158
Kinetic & Thermodynamic Challenges	159
9.7 Fundamentals of CO ₂ Reduction for Artificial Photosynthesis Using Molecular Catalysts	160
Hydride-First Pathway	162
Protonation-First Pathway	164
REFERENCES	166

LIST OF TABLES

Table 3.1 BTPA COFs Transient Absorption Global Fitting	57
Table 3.2 BTPA COFs TDM Charge Transfer Statistics	59
Table 4.1 pTCT Series TDM Charge Transfer Statistics	65
Table 4.2 pTCT Series Parameters for ISC Estimation	72
Table 4.3 pTCT Series Transient Absorption Global Fitting	73
Table 4.4 pTCT Series TCSPC Fitting.....	75
Table 5.1 TAT-COF and TPB-COF Solvent Dependent Quantum Yield	83
Table 5.2 TAT-COF and TPB-COF TCSPC Fitting	84
Table 5.3 TAT-COF and TPB-COF TDDFT Aggregation Predicted Transitions	87
Table 5.4 TAT-COF and TPB-COF TDM Charge Transfer Statistics	88
Table 6.1 Isostructural COFs DFTB Unit Cell Parameters.....	95
Table 6.2 Isostructural COFs TDDFT Predicted Transitions vs Experiment	96
Table 6.3 Isostructural COFs One Layer TDM Charge Transfer Statistics	96
Table 6.4 Isostructural COFs N2N3 Transient Absorption Fitting	109
Table 6.5 Isostructural COFs N2C3 Transient Absorption Fitting	110
Table 6.6 Isostructural COFs C2N3 Transient Absorption Fitting	111
Table 6.7 Isostructural COFs C2C3 Transient Absorption Fitting	112
Table 7.1 Imine Reversal COFs DFT C \equiv O Analytic Frequencies	120
Table 7.2 Imine Reversal COFs Transient Absorption Fitting	125
Table 7.3 Imine Reversal COFs S0 TDDFT Predicted Transitions.....	128

LIST OF FIGURES

Figure 1.1 Artificial Photosynthesis Ecosystem	1
Figure 1.2 Carbon Product Upconversion	2
Figure 1.3 Natural and Artificial Photosynthesis Comparison	4
Figure 1.4 LH2 Structure and Absorption Spectrum.....	6
Figure 1.5 COF Topologies.....	7
Figure 1.6 2D and 3D COF Topologies	8
Figure 1.7 Examples of Monomers for Imine COFs	9
Figure 1.8 COF, Polymer, and Zeolite Comparison Venn Diagram	10
Figure 1.9 Band Transport vs Hopping Transport.....	12
Figure 1.10 Hexagonal COF Band Structure with Variable Lengths	13
Figure 1.11 Hexagonal COF Band Structure with Symmetry Lowering.....	14
Figure 1.12 Orthorhombic COF Band Structure with Interlayer Contributions	15
Figure 1.13 COF Synthesis Timeline and Refinement of Crystallization Hypothesis	18
Figure 1.14 Timeline of Multicomponent COF Synthesis	19
Figure 1.15 Colloidal COF Synthesis.....	20
Figure 1.16 Fragility of COF Structures.....	22
Figure 1.17 Transient Absorption Spectroscopy Overview.....	27
Figure 1.18 Transient Absorption Spectroscopy of COFs.....	28
Figure 1.19 Simplified Artificial Photosynthesis Mechanism.....	30
Figure 1.20 COF Designed for Water Oxidation	31
Scheme 3.1 BTPA COF Synthetic Scheme.....	48
Figure 3.1 BTPA COF PXRD Patterns	50

Figure 3.2 BTPA COF FTIR, ^{13}C NMR, and Absorption Spectra and SEM Images	51
Figure 3.3 BTPA COF N_2 Adsorption Isotherms and Pore Size Distributions	52
Figure 3.4 BTPA COF Transient Absorption Spectra and Kinetic Traces	53
Figure 3.5 BTPA COF Monomer Transient Absorption Spectra	54
Figure 3.6 BTPA COF TDDFT NTOs and Conjugation Diagram	56
Figure 3.7 BTPA COF Photophysical Model	57
Figure 3.8 BTPA COF Dihedral Angles	59
Scheme 4.1 pTCT Series Molecular Diagram	62
Figure 4.1 pTCT Series Absorption and Emission Spectra	63
Scheme 4.2 pTCT Series Dihedral Angles	64
Figure 4.2 pTCT Series TDM Electron Correlation Matrices	65
Figure 4.3 pTCT Series TDDFT NTOs	66
Figure 4.4 pTCT Series TA Spectra	68
Scheme 4.3 pTCT Series Photophysical Model	70
Figure 4.5 pTCT Series Global Fitting	73
Figure 4.6 pTCT Series TCSPC Kinetics	75
Scheme 5.1 TAT-COF and TPB-COF Synthesis Diagram	79
Figure 5.1 TAT-COF and TPB-COF Structural Characterization	80
Figure 5.2 TAT-COF and TPB-COF N_2 Adsorption Isotherms	81
Figure 5.3 TAT-COF and TPB-COF Steady-State Photophysical Characterization	82
Figure 5.4 TAT-COF and TPB-COF TCSPC and TA Kinetic Traces	84
Figure 5.5 TAT-COF and TPB-COF Transient Absorption Spectra	85
Figure 5.6 TAT-COF and TPB-COF Dihedral Angles and NTOs	86

Figure 5.7 TAT-COF and TPB-COF Stacking Structure and Aggregation.....	89
Figure 5.8 TAT-COF and TPB-COF Photophysical Model	91
Scheme 6.1 Isostructural COFs Synthesis Diagram	93
Figure 6.1 Isostructural COFs Structural Characterization and ICT	93
Figure 6.2 Isostructural COFs Absorption-Strain Correlation.....	94
Figure 6.3 Isostructural COFs NTOs.....	97
Figure 6.4 Isostructural COFs Interlayer CT	100
Figure 6.5 Isostructural COFs Strain CT	102
Figure 6.6 Isostructural COFs Transient Absorption Spectra.....	104
Figure 6.7 Isostructural COFs N2 Model Absorption	105
Figure 6.8 Isostructural COFs Transient Absorption Kinetics	107
Figure 6.9 Isostructural COFs Photophysical Model	114
Scheme 7.1 Imine Reveral COFs Synthesis Diagram	117
Figure 7.1 Imine Reveral COFs Structural Characterization.....	118
Figure 7.2 Imine Reveral COFs Structural Characterization #2.....	122
Figure 7.3 Imine Reveral COFs ICT	123
Figure 7.4 Imine Reveral COFs Transient Absorption Spectra and Kinetics	124
Figure 7.5 Imine Reveral COFs NTOs and Frontier Orbitals.....	126
Figure 7.6 Imine Reveral COFs Transient Absorption Spectra and Kinetics #2	129
Figure 7.7 Imine Reveral COFs Photophysical Model.....	132
Figure 7.8 Imine Reveral COFs Photocatalysis.....	134
Figure 7.9 Imine Reveral COFs Photocatalysis #2.....	135

CHAPTER 1 – INTRODUCTION

1.1 Environmentally Friendly Resource Security

Responding to rising global temperatures brought about by excessive release of greenhouse gases requires adaptation of society's resource consumption from fossil fuels to more sustainable alternatives.^{1,2} Our current dependence on fossil fuels is expansive; ranging from energy collection by combustion of oil, coal, and natural gas to feedstocks for plastic packaging.^{3,4} To curb this dependence, new technologies like flexible solar cells⁵ and enzymatic recycling⁶ offer promising methods to harmonize our built environment with our natural one. A crucial piece of renewable resource security is the conversion of carbon dioxide (CO_2) into recycled products by carbon-neutral, or carbon-negative methods (Figure 1.1).⁷ Plants, of course, naturally serve this purpose; and while efforts like reforestation are necessary and should proceed in haste, we should also consider artificial ways to upconvert CO_2 to provide economic and environmental security. Widely known as artificial photosynthesis, it is still unknown what form it could take on an industrial scale. Future reactors could push combustion products through tanks lined with catalysts where solar electricity powers electrochemical or thermochemical reactions.⁸ Another possibility is to take inspiration from nature and bypass solar electricity generation, instead using light to directly drive photochemical reactions. Regardless of the design, pursuing artificial photosynthesis has economic and academic motivations that make it a necessary and intriguing area of research.

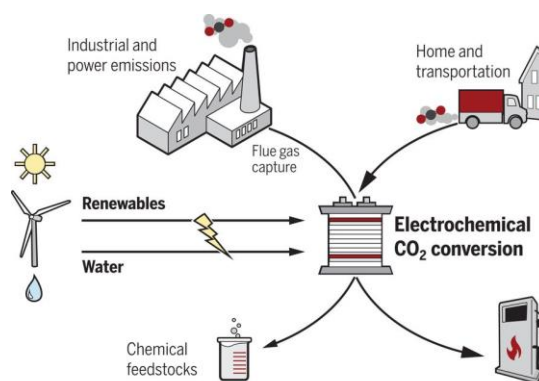


Figure 1.1 General scheme showing artificial photosynthetic ecosystem. Renewables power conversion of industrial CO_2 emissions into fuels and chemicals that are used in a cyclical manner.⁷

The near-term economic motivation to pursue artificial photosynthesis is to provide bottom-up chemical pathways to change a portion of atmosphere-bound CO_2 into market-bound fuels, raw materials, or minerals.^{7,9,10} Beyond profit, mastering artificial photosynthesis could provide the economic security that necessary carbon-based products can be sourced without dependence on oil. Longer-term value would come from CO_2 reactors that could create closed-loop systems to allow for nearly limitless value extraction from an atmospheric pollutant. Current industrial processes already exist that could help accomplish CO_2 recycling. For instance, Fischer-Tropsch processing of CO_2 derived syn gas (CO and H_2) into alkyl products represents an industrially relevant CO_2 recycling pipeline. Alternatively, CO_2 derived methanol can be converted into higher-carbon (C_2+) products in a methanol-to-olefin (MTO) or a methanol-to-aromatics (MTA) reactor (Figure 1.2).^{11,12,13} CO_2 derived products could then be used to offset petroleum derived specialty chemicals necessary in medicines and high-performance materials - sufficing to say that reducing our dependence on fossil fuels will certainly require a lot of bottom-up chemistry. While Fischer-Tropsch processing and MTO/MTA reactors are currently powered by waste heat generated at oil refineries, the processes should operate at temperatures ($200\text{-}500\text{ }^\circ\text{C}$) accessible to sustainable sources like solar field arrays, and electric heaters.^{14,15}

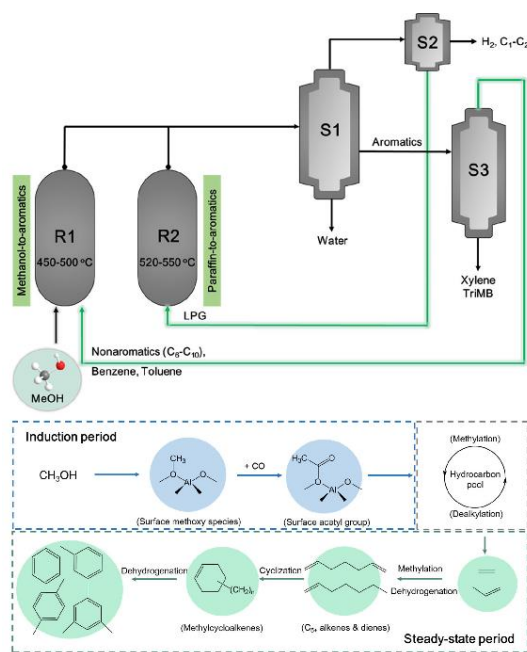


Figure 1.2 Methanol-to-aromatics schematic (top) and high-level formation scheme of aromatics from methanol (bottom).¹³

Even while the costs of solar-to-electric capture have fallen steadily,¹⁶ and despite rapid growth,¹⁷ solar-to-electric conversion necessitates large-scale battery systems for energy storage.¹⁸ If solar power is instead used to directly catalyze the formation of feedstocks, converting solar energy directly into chemical energy can present a unique opportunity to bypass ancillary storage systems¹⁹ and the flexibility to use the chemicals in other downstream applications.¹⁰ Apart from economic reasons, there are also academic and humanistic reasons for the study of artificial photosynthesis. Academically, the motivation to study artificial photosynthesis comes from a desire to better understand mother nature's brilliant chemistry. Developing physical models that describe the capture and utilization of photon energy is also useful for furthering knowledge about the universe and satisfies a natural humanistic curiosity. So far it is unclear if advances in artificial photosynthesis are imitations of mother nature, or if designs just happen to converge with hers, but the natural designs nonetheless elicit great respect due to their complexity and durability.

1.2 Nature's Photocatalyst Design

We can look to nature's photosynthetic pathways for inspiration to understand the mechanisms of light harvesting and charge transfer which may inform the design of artificial photosynthesis catalysts. At a high level, natural photosynthesis captures potential energy required to perform redox from sunlight by light harvesting antennae in the photosystem II (PS2) complex.²⁰ H₂O is oxidized to O₂ and H⁺ at PS2 and electrons are captured, transferred, and eventually used via the reduction of CO₂. Some organisms evolved processes that transfer the electronic potential energy to a second antennae, photosystem I (PS1), while others bypass the second step completely and undergo photosynthesis with light harvested within a single photosystem.²¹ Regardless of their pathway, the reaction center where reduction of CO₂ takes place must be activated by charge separation (CS) from the terminal photosystem.²² Figure 1.3 shows examples of one-step and two-step natural photosynthesis processes along with one-step and two-step processes in synthetic photosystems.²³

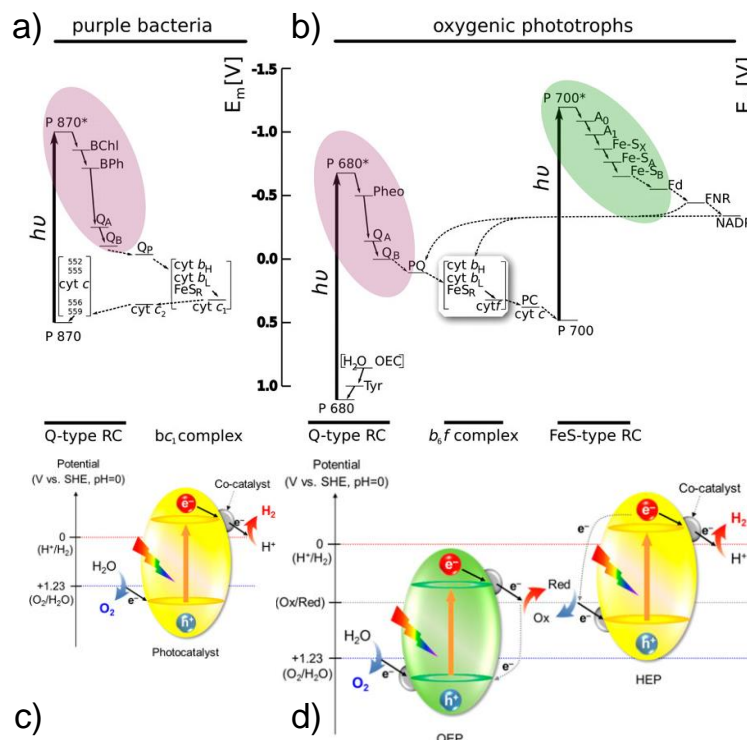


Figure 1.3 Diagram of (a) one-step, and (b) two-step *natural* photosynthesis process by purple and green bacteria, respectively.²² (c) one-step, and (d) two-step *artificial* photocatalytic processes are shown.²³

Natural and synthetic systems have diagrammatic similarities whereby light energy excites electrons that are transferred to a reaction center. Performance is thus greatly influenced by the amount of light absorption, the wavelength of light absorption, and the efficiency of energy transfer, which relates to why photosynthetic organisms evolved compounds that have high extinction coefficients.²⁴ The two-step systems (Figure 1.3b, 1.3d) each undergo second excitations which gives rise to the term “Z-scheme” as analogy to the shape of the diagram pathway. The most apparent natural/synthetic difference is natural photosynthesis involves numerous cascading electron transfer intermediaries whereas these pathways are much shorter in synthetic systems. This merits consideration of the structure, spatial distribution, and efficiency of light antennae and reaction centers, which is not well represented by the diagrams. On the one hand, nature evolved over eons to adapt systems of light harvesting chromophores that intelligently transfer energy exactly to where it is needed with efficiency approaching 100 percent. These systems even account for the diffusion of excess energy to heat when sunlight is abundant to avoid adverse effects.^{25,26} On the

other hand, excited states (electrons and holes) in synthetic semiconductor systems migrate depending on myriad factors and rely more on chance to reach a reaction center. This reliance on chance can negatively affect performance and beneficial strategies, like applying potential across the photocatalytic cell, increase complexity and reduce overall efficiency. Scholes et. al. summarizes this nicely in an excerpt from their work:²⁴ *“To utilize energy harvested from sunlight efficiently to promote photochemical reactions or to produce solar fuels, we must understand and improve both the effective capture of photons at a reactive site and the transfer of excitation energy. This would allow the design of molecular 'circuits' that can direct, sort, and respond in sophisticated ways to excitation energy.”* To implement designs in an elegant way it is important to first understand, on a molecular level, the strategies nature has developed to harvest light efficiently and get potential energy to where it can be used.

A model system suitable for studying nature's strategies for light harvesting and energy transfer is the light harvesting II complex (LH2) of purple bacteria (*Rhodospirillum rubrum*) shown in Figure 1.4a.²⁴ LH2 is comprised of two substructures (B800 and B850) named after their wavelength of maximal absorption (Figure 1.4b).²⁷ Interestingly, the substructures are collections of the same organic molecule, bacteriochlorophyll a (bca), meaning the difference in their function is largely determined by different arrangements of bca within each substructure.²⁸ Their relationship offers lessons about correlation between structure and function, particularly in terms of light harvesting and energy transfer. Consensus among the literature is that B850, whose bca molecules are packed close to one another, absorb lower energy light because the adjacent bca electronic transitions strongly couple to one another, thereby lowering the overall transition energy.^{24,29,30} For instance, ab initio calculations by Scholes, et. al. estimates the magnitude of the electronic coupling strength between dimeric bca units in B850 to be 320 cm^{-1} , up to ten times stronger than the predicted 30 cm^{-1} in B800.³¹ Arrangements of bca are precisely dictated by the structural environment of the proteins that hold them in place which in turn leads to differences in electronic coupling that have outsized impacts on the pathways of energy transfer.

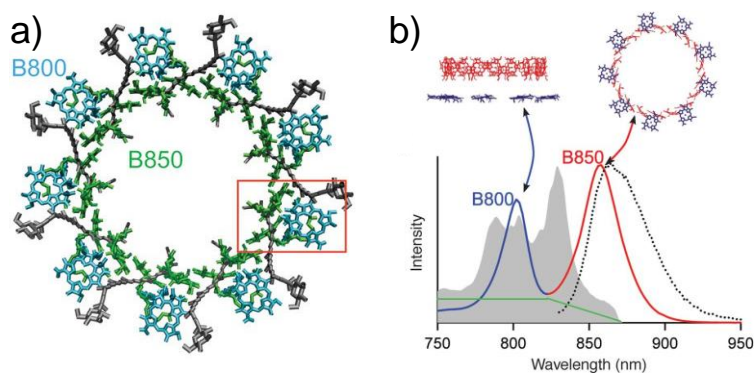


Figure 1.4 (a) Diagram of LH2 complex in purple bacteria (*Rhodospirillum rubrum*) highlighting the B800 and B850 subunits.²⁴ (b) Absorption spectrum of LH2 complex indicating peaks arising from B800 subunit and B850 subunit.²⁷ Gray region is the laser spectrum used to excite the complex. Dotted line shows emission from the LH2 complex.

1.3 Overview of Covalent Organic Frameworks

First reported in 2005 by the Yaghi group at the University of Michigan,³² Covalent Organic Frameworks (COFs) are polymers that arrange in an ordered, crystalline fashion. What sets COFs apart from typical polymers is that they are comprised of monomer(s) where the monomers are of high symmetry with functional groups at each terminal symmetry point. This distinction of higher order connectivity means that when COFs are properly formed, they will have void space, called a pore, that has a size and shape determined by the size and shape of the monomers. To illustrate, Figure 1.5a shows a simple example in which a linear monomer can combine with a quadrilateral or triangular monomer to form either a quadrilateral or hexagonal pore, respectively. Pre-determination of geometry is known as reticulation, and the resulting lattice is often termed a ‘net’ from the resemblance they share.³³ Nets are classified in terms of their topology, which in COFs defines the shape of the pore and is derived from the symmetry of the monomers. For instance, combining two monomers – each with three functional groups arranged with threefold C_3 symmetry – will result in a COF with a hexagonal pore and net topology denoted hcb having overall threefold C_3 symmetry (Figure 1.5b, right). But hexagonal pores with hcb topology can also be made with sixfold C_6 symmetry by combining two monomers – one with threefold C_3 symmetry, and the other with twofold C_2 symmetry (Figure 1.5b, left). Thus, the relationship between the symmetry of the monomers and the symmetry and topology of the COF are intrinsically linked, which with *a priori* knowledge of the monomers allows for prediction of the net topology and n-fold symmetry.

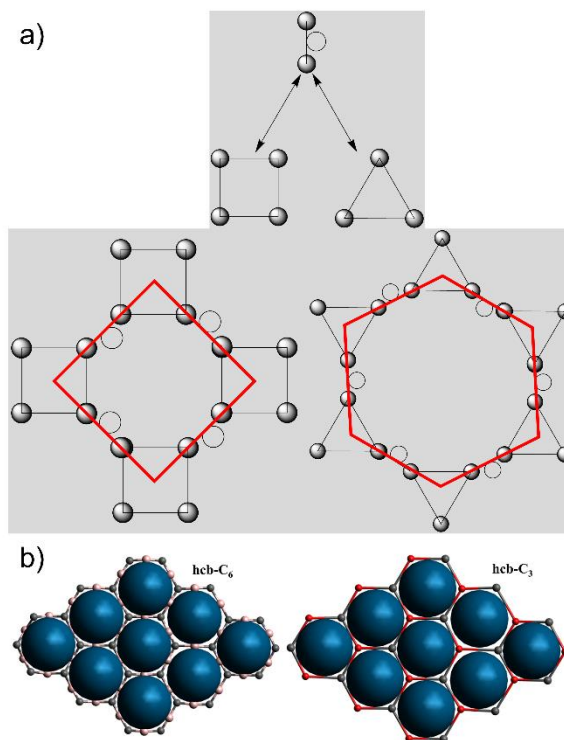


Figure 1.5 (a) Different topologies are available if a linear monomer is combined with a quadrilateral (left) or trigonal (right) monomer. The pore shape is highlighted in red. (b) Representations of hcb topology with C_6 and C_3 symmetry.

There are few limits to the topologies that can be formed by COFs, including their dimensionality. Examples in the previous paragraph outlined the formation of C_3 and C_6 symmetric hcb pores representing two-dimensional (2D) COFs, but the symmetry can also be readily extended to three-dimensions (3D) by including non-planar monomers. One such instance of a 3D COF can be achieved by using a tetrafunctional monomer arranged with tetrahedral T_d symmetry.³⁴ When combined with a linear monomer with C_2 symmetry, the resulting COF forms a net with dia topology, but the expansion of the pore caused by including the linear monomer leads to another factor to consider in three-dimensional pores, known as interpenetration. Interpenetration occurs predominantly in diamondoid structures like those of 3D COF with dia topology,³⁵ but even though it has implications on the properties of porous frameworks its origin is not fully understood.³⁶ If the co-monomer possesses tetrahedral T_d symmetry instead of C_2 symmetry the size of the pore is shrunk, and formation of a dia phase is avoided instead forming lon topology that is more dense than dia and the nature of interpenetration changes³⁷. Interestingly, it has been found that

interconversion between dia and lon topology is achievable in carbon allotropes under different pressure and shear conditions, but it has yet to be shown in COF materials (Figure 1.6).³⁸ So far, 3D COFs have been reported with a wide variety of topologies including ceq,³⁹ ctn,⁴⁰ bor,⁴⁰ ffc,⁴¹ srs,⁴² pts,⁴³ and more. The novelty of 3D COFs is that they can be synthesized as single crystals large enough to be studied by X-ray diffraction rather than the microcrystalline powders that 2D COFs usually form.⁴⁴ This makes 3D COFs extremely promising candidates for future study but is outside the scope of this work.

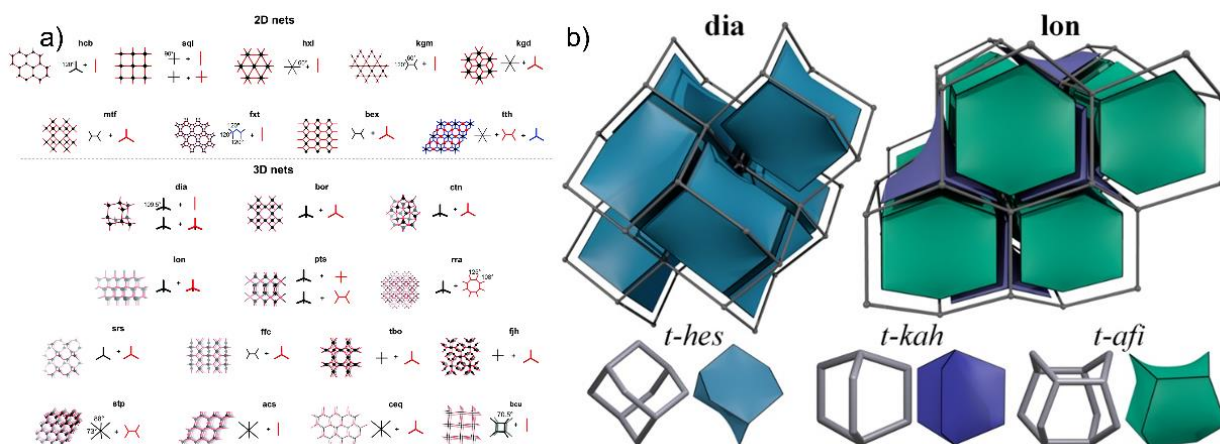
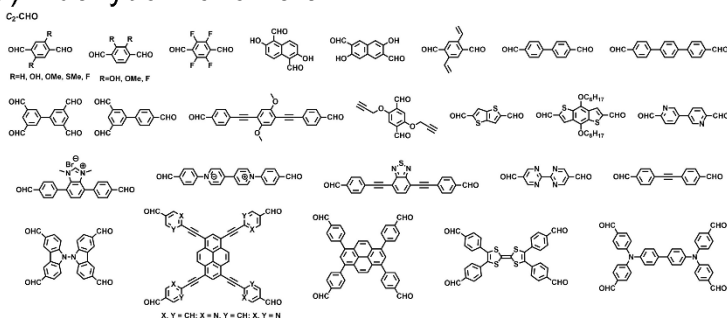


Figure 1.6 (a) The variety of COF topologies in two-dimensions (top) and three-dimensions (bottom).⁴⁴ (b) Space filling representations of dia and lon topologies.³⁸

Although they form the conceptual basis of symmetry and porosity in COFs, monomers are restricted by physical requirements to form ordered, crystalline structures. One such restriction is that monomers are typically rigid aromatic molecules that, after polymerization, resist undergoing dynamic conformational change (Figure 1.7).⁴⁵ This qualification is important for COFs because maintaining their porosity under ambient conditions would otherwise be a significant challenge if monomers were flexible. The property of aromatic monomers that allows them to form stable COFs is their propensity to aggregate due to attractive π interactions originating from delocalized p-orbitals, but there are other factors that can be designed into the COF to enhance their stability by selecting appropriate monomers; some such factors include the degree of ring twisting,⁴⁶ complementary dipolar interactions,⁴⁷ side-chain stabilization,⁴⁸ and hydrogen bonding.⁴⁹ These beneficial interactions resulting from simply choosing new building blocks are a part of what make COFs such an intriguing substrate for a variety of applications.

a) Aldehyde Monomers



b) Amine Monomers

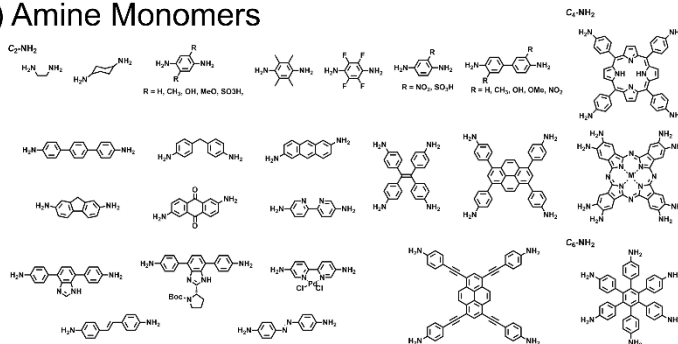


Figure 1.7 Representative examples of mainly aromatic monomers that can be used to form imine COFs from (a) aldehydes, and (b) amines.⁴⁵

Recognition of COFs as development targets can be attributed to the key benefits offered by combining the best parts of polymers and zeolites, shown by a three circle Venn diagram in Figure 1.8. Like polymers, the monomers that comprise COFs can be manipulated by traditional organic chemistry techniques and tailored to fit a given application. They're also reticulated into pores in the same way that gives zeolites the ability to act as molecular sieves or adsorb large quantities of gas onto their surface.

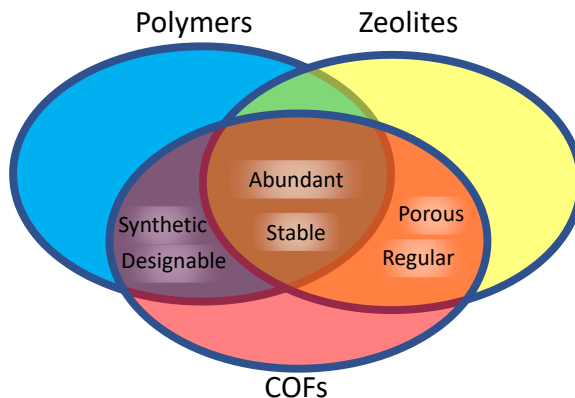


Figure 1.8 Venn diagram showing the similarities COFs have with polymers and zeolites.

Although COFs have many significant benefits there are many challenges to overcome until they see widespread usage. The main roadblock to widespread COF use rests on their intractable processing difficulties. Solubilizing COFs is nearly impossible due to their extended, aggregate structures, and even creating dispersions of COF can be difficult due to their propensity to form aggregates and crash-out of solution.⁵⁰ One rectification to this problem has been to create three dimensional (3D) COFs which provide the structural regularity to be grown into large crystals for single crystal x-ray diffraction studies.⁵¹ Beyond this, processing two dimensional (2D) COFs into consistent thin-films, where they may be useful in optoelectronic devices or size selective membranes, is difficult because the kinetics with which COF monomers polymerize, aggregate, and crash out of solution are difficult to control and not yet well understood.⁵² For many applications, however, large perfect crystals are simply unnecessary.

Of the diverse set of proposed applications for COFs the ones in which their powder form is suitable form offer the most immediately promising outlets. These include next-generation stationary phases for chromatography, gas storage, and as catalytic materials. COFs for catalysis are a promising way to combine advantages of homogeneous catalysis – like their large surface area which exposes a high number of active sites – with heterogeneous catalysts – like their simple separation from reaction mixtures. Additionally, the aromatic monomers COFs are constructed from often impart visible light absorption meaning that catalysis can be initiated by energy from solar radiation, making COFs great photosensitizers for photocatalysis. The precision with which nature crafts its protein structures to ensure proper electronic

coupling for energy transfer in PSI and PSII suggests its importance for natural photosynthesis. With COFs being reticulated macrostructures similar types of considerations can be made such that they enhance the energy transfer necessary to perform artificial photosynthesis.

1.4 Electronic Structure of Covalent Organic Frameworks

Much like how the structure of the LH2 complex is intricately linked to its light absorption, the structure of COFs has an implicit effect on their ability to harness energy. When COFs are formed, they arrange into periodic structures determined by the molecular geometries of the monomers they are comprised of. Depending on the monomers, COFs can be two-dimensional (2D) or three-dimensional (3D) and the shape formed by the free space within the COF is related to their overall topology. When a suitable bond is built between aromatic monomers, the COF forms extended electronic conjugation with delocalized π electrons along the structural backbone. Sheets of 2D COF can interact through London dispersion forces arising from the effects of overlapped π electrons, leading to the formation of aggregates, and on a larger scale - crystallites. In these 2D COFs, the pore becomes cylindrically shaped as the stacking of 2D sheets propagates in the transverse direction. Interestingly, the width of the pore can be on a similar scale to the LH2 complex in purple bacteria, and the monomers are in-plane like bca in B800. Conjugated 2D COFs are an area of particular interest because the in-plane conjugation and the interlayer π stacking may enable, within the strong coupling limit, the migration of charge carriers.^{53–56} These properties may ultimately aid in energy transfer to catalytic sites for $\text{H}_2\text{O}/\text{CO}_2$ redox but in a band transport mode different from the hopping mode in LH2 (Figure 1.9).⁵⁷ However, like LH2, the structure and its relationship with energy transfer must first be understood and considered before designing for energy transfer in photocatalysis.

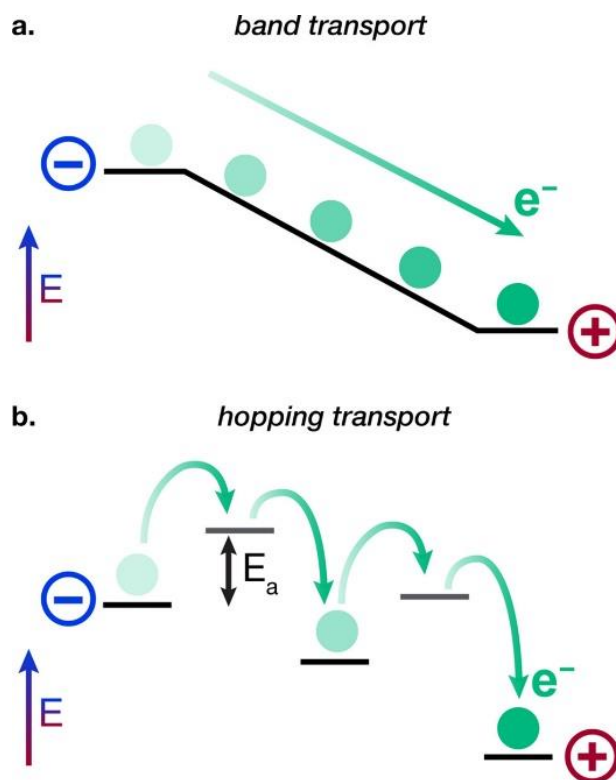


Figure 1.9 Band transport vs hopping transport⁵⁷

The topology of COFs has been studied by Zhu and Meunier⁵⁸ by changing the size of the pore with variable length spacers. Illustrated in Figure 1.9 is an example from the study of a COF with s-triazine as the trigonal monomer. The main finding is that the size of the pore inversely relates to the size of the band gap which the authors attribute to growing delocalization in the structure. This type of result is not completely unexpected, but it does establish the possibility for band edge tuning in COFs by careful selection of the monomeric units. Also important is the very low degree of band bending in the valence and conduction bands at each pore size. Band bending relates to the amount of mobility, i.e. dispersion, that charge carriers possess upon excitation of the semiconductor. In this case, because the band bending is so low it is likely that electron and hole populations would be immobile, at least within the plane of the COF. It is important to note that this type of energy transfer differs from LH2 (Section 1.2) because in this case the chromophores are directly linked by conjugated covalent bands implying that energy transfer occurs through bonds as opposed to through space like in LH2. Furthermore, the tight-binding model used to generate these insights may not consider effects past the interactions of nearest-neighbor or next-nearest-

neighbors. Lastly, although not claimed by the authors, the results also indirectly point to the interruption of conjugation at the s-triazine which helps to explain why the additional spacers have such a large impact on the band gap.

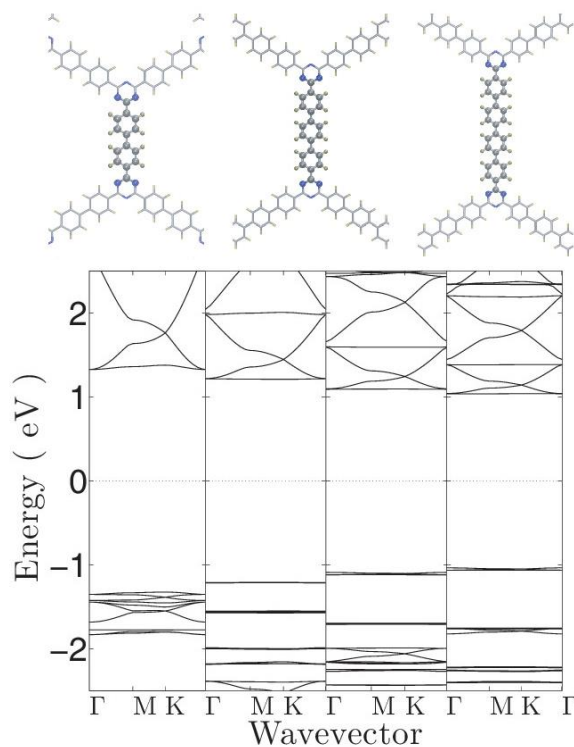


Figure 1.10 (top) Unit cells of COFs with variable pore size. (bottom) COF band structure with variable pore size illustrated by the diagram at the top. (a) Shows bands gap decreases with larger pore size. Dispersion in the valence and conduction bands seems to remain consistently negligible.⁵⁸

Another study by Thomas et. al.⁵⁹ found the topological symmetry to have a pronounced effect on the ability for charge carriers to migrate across the backbone through a band transport mode. Particularly, their main finding was that high symmetry can destroy the ability for electrons and holes to move within the plane of the COF due to destructive interference in the wavefunction at meta-substituted six-membered rings. The authors then specifically tune carrier mobility by lowering the symmetry of the COF structure. This effect is shown in Figure 1.11 that shows the band structure of compositionally identical but constitutionally varied COFs arranged in either an orthorhombic *pmm* or *pm* space group. The band

dispersion changes considerably when the placement of the N heteroatom is changed, suggesting symmetry modifications may be an elegant tool to direct energy transfer in COFs.

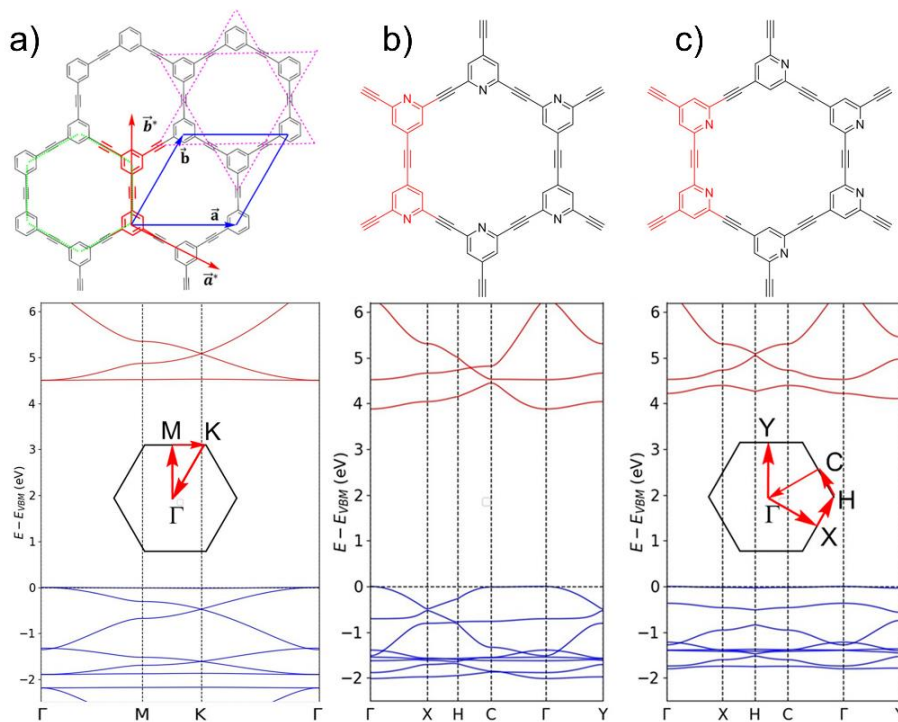


Figure 1.11 COF band structure with different topologies according to diagram at the top. (a) Shows valence and conduction bands with no dispersion (flat bands) in a P6m space group with sixfold rotational symmetry at benzene node. (b) Shows symmetry lowering that increases band dispersion due to placement of heteroatoms such that a pmm space group is formed. (c) Shows how band dispersion is affected when heteroatoms are placed such that a pm space group is formed. (d) Shows how removal of sixfold rotational symmetry in a P6 space group causes significant band bending.⁵⁹

Apart from in-plane and symmetry dependent carrier mobility 2D COFs can have band dispersion transverse to the plane of the framework. Meng et. al.⁵⁴ showed this in their COF constructed of a quadrilateral Ni porphyrin monomer linked to a linear pyrene monomer through a phenazine linker (Figure 1.12a). The superimposed Brillouin zone of the P4/mmm space group onto the COF structure (Figure 1.12b) shows the real space interpretation of the k-lines used to generate the band structure diagram (Figure 1.12c). Interestingly, the DFT predicted band structure not only has significant dispersion in the out-of-plane direction, but the valence band also crosses the Fermi level which indicates that ground state conductivity should theoretically be possible, although these types of interpretations need to be made with

care when using generalized gradient approximation (GGA) functionals as they can overstate delocalization and erroneously predict conductivity. The group finds a high degree of conductivity and exploits that property for gas sensing. Furthermore, their evidence shows that incorporation of Ni into the porphyrin array is not responsible for the conductivity in the stacked 2D COF, instead the density of states diagram (Figure 1.12c, right) shows C and N are primarily responsible.

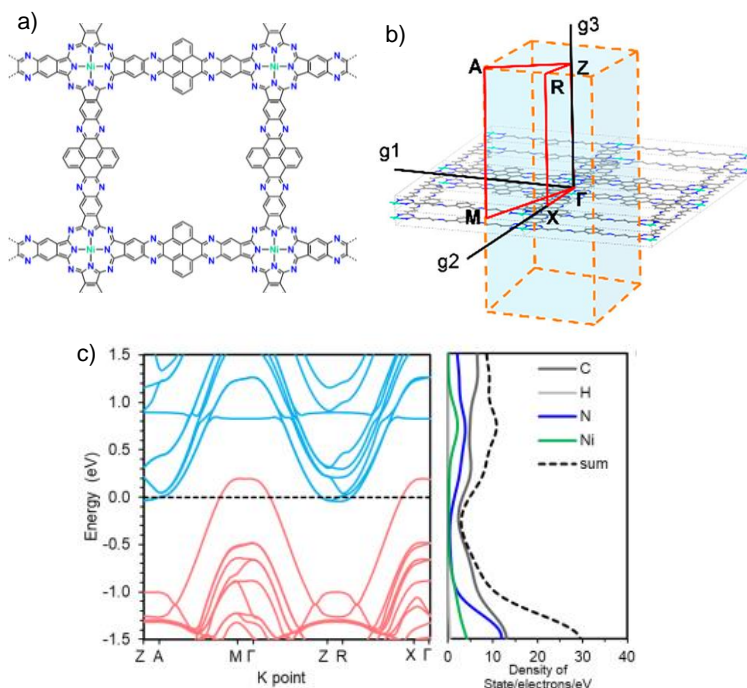


Figure 1.12 (a) COF structure showing the quadrilateral pore. (b) Brillouin zone superimposed to the COF structure showing the Fermi level crossing out of the plane of the framework. (c) Band structure crossing the Fermi level (0 eV) between A-M, G-Z, and R-X. Density of states shown on the right indicates conductivity primarily through C, N and H.⁵⁴

Between the strong electronic dipole coupling, low dielectric environment, and the possibility for extended conjugation, excitons formed in COFs can be bound at relatively long distances. Strong interlayer dipole coupling alone can lead to the formation of localized or delocalized Frenkel excitons,⁶⁰ intermolecular CT excitons,^{61,62} or excimer states.⁶³ Obfuscating the discovery of their nature, these types of excitons are deeply related and the threshold when one is created versus another is not clear.⁶⁴ On top of this, intralayer donor-acceptor coupling adds even more variety with ICT excitons and CS states that have their own relationships with interlayer dipole coupling.⁶⁵ Harnessing these excitons for photocatalysis

requires an understanding of how they form, how long they last, and how they migrate. Interchromophore Frenkel excitons in B850 can form as interlayer Frenkel excitons in COFs due to layer proximity and large ensuing dipole-dipole coupling.^{66,67} At intimate COF interlayer distances (typically $\sim 3.5\text{\AA}$) these Frenkel excitons can mix with CT states such that CT exciton formation may occur. In studies on CT exciton migration in organic semiconductors it was found that the propensity for electron/hole separation is related to the Coulombic forces in their dielectric environment.⁶⁸ Hestand et. al.⁶² outlines this relationship by constructing the Frenkel-CT Holstein Hamiltonian that includes integrals, t_e and t_h , which correspond to the probability of electron or hole transfer from one chromophore to another, respectively. When the magnitude of the integrals is on the same order or larger than the interlayer Coulombic forces CT between said chromophores is favored. CT favored interactions can lead to the CS process which extends the lifetime of excited states by preventing electron-hole recombination and enhances the probability of initiation of the photocatalytic process described above. With this knowledge, the strategy for manipulating systems to favor CT and CS becomes relatively straightforward from a theoretical point of view.

The first method for increasing probability of CT and CS is to lower the Coulombic forces, specifically the repulsive forces, between two adjacent chromophores. This strategy has been employed recently by functionalizing PMI chromophores with a hydrophilic carboxylate tail which attracts a positive counter-ion.⁶⁸ The inclusion of this ionic environment near the PDI chromophore lowers the dielectric screening, and hence the Coulombic forces in the organic crystal. Spectroscopically, the incorporation yielded a splitting in the absorption spectrum due to mixing between Frenkel and CT states (which are now favorable). Tailoring these properties offers an opportunity to promote efficient energy transfer but doing so while avoiding adverse effects poses a challenging task.

The periodic structure of COFs lends itself to the study of energy transfer through band structure calculations which make it clear that bidirectional charge transport is possible. While this macromolecular model of energy transfer is different from nature's supramolecular model, the overall goal to move energy where it can be used for photocatalysis remains the same. In fact, since there exists no straightforward way to build protein-like structures to immobilize chromophores into functional structures, topological band transport appears to be an elegant design for artificial photosynthesis. In contrast to Frenkel and CT

excitons, which form across identical adjacent chromophores, there is another type of exciton that forms between chromophores with different electron affinities. COFs are comprised of monomers linked through covalent bonds intralayer CT (ICT) excitons can also form whereby the hole localizes on the donor moiety whereas the electron localizes on the acceptor moiety. The key difference between interlayer CT and ICT in organic molecules is related to the potential energy of the donor and acceptor frontier orbitals. In interlayer CT the donor and acceptor pair are identical chromophores separated by a short enough distance for electron density to move to the adjacent unit. ICT on the other hand occurs when a donor and acceptor with different electron affinities are linked through a (typically conjugated) covalent bond. The different electron affinities lead to the electron from the donor moiety to localize on the excited state of the acceptor moiety. The rate of ICT is governed by Marcus theory which includes factors such as the reorganization energy, Gibb's free energy, electronic coupling between donor-acceptor, and the temperature.

1.5 Synthesis, Activation, and Characterization of Covalent Organic Frameworks

A wide variety of linker motifs have been used to form COFs like boronate esters, imines, azines, hydrazones, imidazoles, triazines, ethenes, and many more (Figure 1.13a). Typically, these COFs have been synthesized through solvothermal methods around 120°C in a sealed vessel for 72 hours. Solvent systems are chosen without a strong theoretical basis, but typically rely on a polar solvent in which the aromatic monomers are suitably soluble and a non-polar solvent that acts as a crystallization promoter. Oftentimes works in the literature settle on some ratio of 1,4-dioxane and mesitylene where 1,4-dioxane solubilizes the monomers and mesitylene aids crystallization. Other common solvent systems are n-butanol and o-dichlorobenzene, with instances of dimethyl acetamide, and methanol arising occasionally as well. This solvothermal method is often suitable to obtain COF powders for characterization by FTIR, PXRD, and BET but the fundamental understanding of reaction and crystallization kinetics are not fully understood. Initially it was believed that COFs formed first as amorphous polymers due to rapid chain-growth polymerization was proposed to be controlled by moderating the solubility of COF monomers to slow the chain-growth kinetics and allow reversible linker reaction dynamics to correct for errors. The rationale was that eventually the reversible COF linkers would end up reaching a favorable thermodynamic state with highly ordered structures stabilized by attractive π - π interactions. Instead, and in part due to the

formation of COFs with irreversible linkers, the consensus has moved towards preorganization of monomers in solution as the reason for COFs attaining crystalline structures (Figure 1.13b).

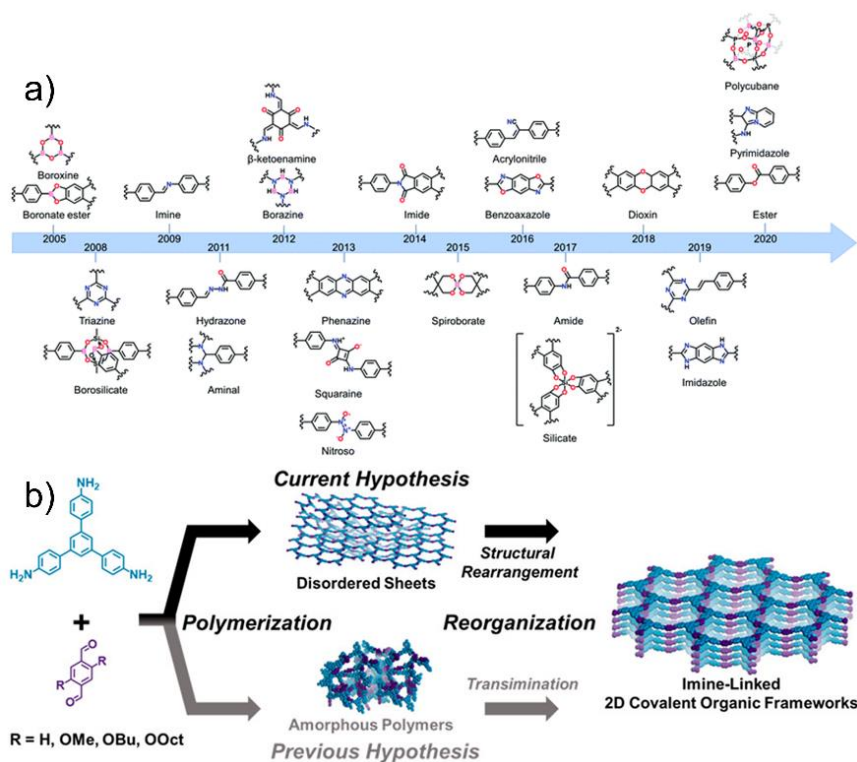


Figure 1.13 (a) Timeline of COF linkers. (b) Evolution of COF formation hypothesis.

Three major trends have emerged in the synthesis of COFs, each with complementary benefits that can enhance their properties, processability, or novelty. The first trend is the hunt for perfect crystallinity, which involves balancing polymerization and crystallization kinetics to achieve highly regular, defect free single crystal structures large enough for single crystal XRD measurement.⁶⁹ This has proven especially challenging for 2D COFs, but some crystals have been grown up to 5 μm that have thus far been shown to enhance their chromatographic properties from polycrystalline material (Figure 1.14a).⁷⁰ Defect-free COF crystals also represent ideal substrates to study mechanisms of energy transfer and charge transport, but doing so at scale remains an elusive challenge. The second trend in COF synthesis is applied polymerization that seeks to create COFs in novel, utilizable forms such as membranes, thin films, colloids, or pellets or via low-cost high-throughput procedures like sonochemical, mechanochemical, or microwave aided synthesis methods.^{71–78} Thin film formation on substrates is particularly relevant to utilization in

optoelectronic devices such as solar cells (Figure 1.14b), and along with colloidal particles they help enable spectroscopic studies. The third trend is multicomponent polymerizations that add functionality to COFs by taking advantage of one-pot organic reactions without sacrificing quality (i.e., porosity or crystallinity) that can be lost by performing the transformation separately from polymerization (Figure 1.14c).⁷⁹ These multicomponent polymerizations expand the scope of possible applications of COFs and are foundational to the idea of designability in COFs with implications in tailoring photophysical behavior and photocatalyst activation.

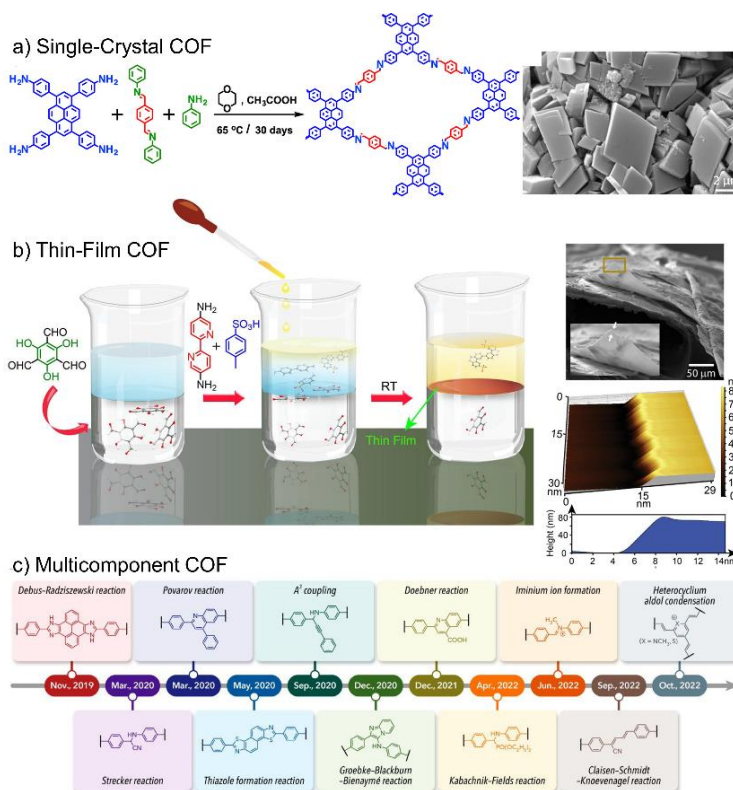


Figure 1.14 (a) An example of single crystal 2D COF synthesis.⁶⁹ (b) Formation of thin-film COF as an example of applied polymerization.⁷⁸ (c) Timeline of multicomponent COF reactions to form new types of linkages.⁷⁹

A significant advance in COF synthesis has been the development of methods to obtain them as colloidal nanoparticles in solution (Figure 1.15).^{70,76} The importance of colloidal COFs is that they are much easier to handle, deposit, and study and form relatively defect-free structures. So far only COFs with reversible linkages (boronate esters and imines) have been made colloidal and their preparation relies on

mediating the polymerization kinetics with an agent possessing a suitable reactive functional group and utilizing a solvent with sufficient dispersion power to keep the nanoparticles suspended. In imine colloidal COFs the agent used is aniline which is first reacted with the polyfunctional aldehyde before the addition of the polyfunctional amine (Figure 1.15b). The condensation between aniline and aldehyde proceeds via condensation reaction where water is released and is often initiated by the presence of an acid catalyst. Once the polyfunctional amine monomer is added the reaction depends on the reversibility of the imine to propagate chain-growth and because of this precipitation of oligomers is slowed, allowing the COF nanoparticles to achieve uniform sizes and shapes, sharp crystallinity, and high porosity. In addition, it is also likely that the uniform shape of colloidal COF nanoparticles is advantageous to their dispersion in solution.

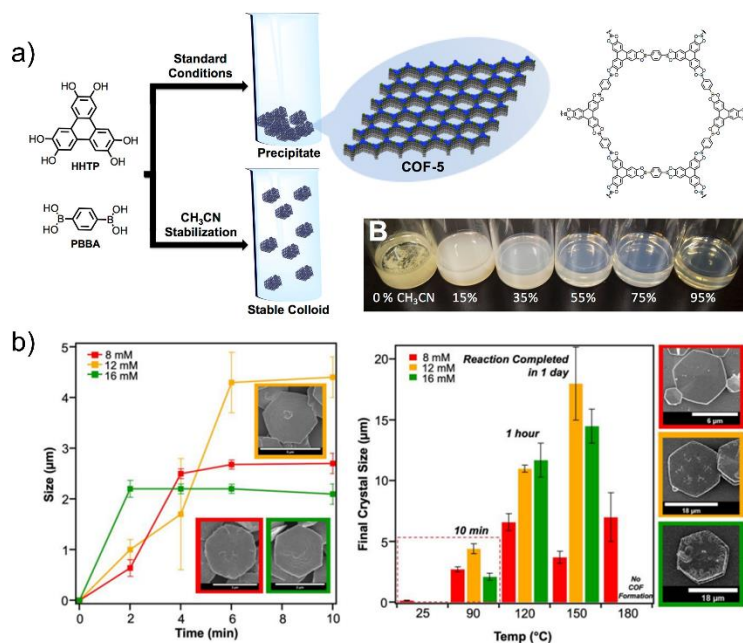


Figure 1.15 (a) Synthesis of boronate ester colloidal COF using acetonitrile as a stabilizing agent for the colloid nanoparticles.³²¹ (b) Synthesis of imine colloidal COF using benzonitrile as a stabilizing agent. (left) crystallite size as a function of time with varying amounts of aniline modulator. (right) crystallite size as a function of time and temperature with varying amounts of aniline modulator.⁷⁰

Once COFs are synthesized, they must often be handled with extreme care to avoid collapsing their pore structures, however some structures are more resistant to pore collapse than others. Advances in the understanding of pore collapse have improved greatly since the inception of COFs with clear

relationships between pore fragility, pore size, intermolecular interactions, and side groups being developed (Figure 1.16).⁸⁰ COFs with stable pores can be washed with low boiling solvents like ethanol, methanol, THF, or acetone and subsequently dried under heat and vacuum without affecting their quality. COFs with larger pores, less stabilizing intermolecular interactions, and no side groups are more susceptible to pore collapse and so a gentler drying method, otherwise known as activation, must be used. It has been shown that treatment of COFs possessing unstable pores with non-polar low boiling solvents like hexane, can help retain porosity where more polar solvents may destroy the pores, but even in many cases these non-polar solvents are too harsh. When the fragility of the pores is a concern and other activation methods do not work the gentlest activation one can use is critical point drying, otherwise known as supercritical CO₂ (scCO₂) activation. scCO₂ activation is often used to prepare fragile biological samples for imaging techniques like SEM, TEM, and the like, but also serves to evacuate COF pores without damaging them due to the extremely low surface tension of supercritical CO₂. In scCO₂ a room temperature liquid solvent is used to keep the COF sample from drying in open air, the sample is transferred in this solvent (typically absolute ethanol) to a chamber equipped to handle high pressures, high-purity liquid CO₂ (LCO₂) is then siphoned into the chamber and allowed to purge the ethanol. The sample is then soaked in LCO₂ so that any trapped ethanol can diffuse into the chamber before purging again with LCO₂. Once this process has been repeated numerous times the LCO₂ is brought to its critical point where it exists as scCO₂ (31°C, 1070 psi). scCO₂ has properties that allow it to act simultaneously as a liquid and a gas; namely the density of scCO₂ is high like that of a liquid, but the surface tension is low like that of a gas. Once the supercritical point has been reached the chamber is allowed to equilibrate its temperature and pressure and then slowly vented to yield the dried COF sample.

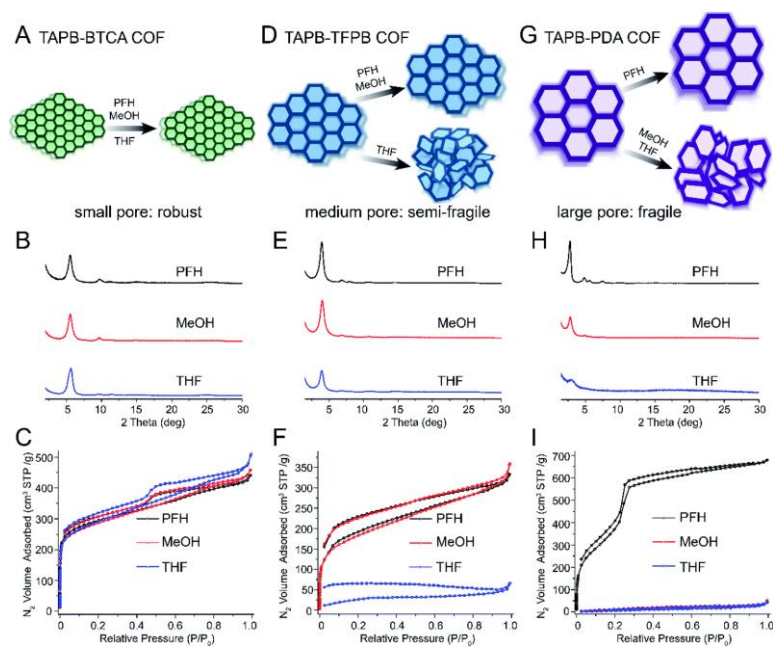


Figure 1.16 Effect of pore size on the stability of COFs. (a, b, c) small pore COF shows little change in PXRD or N₂ isotherm when dried from more polar solvents. (d, e, f) medium pore COF shows decrease in crystallinity and decrease in N₂ adsorption upon exposure to THF. (g, h, i) large pore COF shows high response to polar solvents.⁸⁰

Once the COF sample has been prepared either by vacuum drying or scCO₂ activation it must be characterized to ensure porosity, crystallinity, and proper bond formation. Porosity is measured by the adsorption isotherm of an inert gas (typically N₂ or Ar) at cryogenic temperatures. The way N₂ adsorption isotherms work is that a tube containing porous material is placed under high vacuum (<10 μ Torr) and kept at a consistent temperature by submerging it in liquid N₂. Then N₂ gas is added to the tube in microdoses and allowed to equilibrate through the porous sample, the pressure inside the tube is measured against the amount of gas added and the difference between expected pressure and measured pressure can be used to determine how many gas molecules have been adsorbed onto the surface of the porous material. This process is repeated according to a preset routine, typically until the relative pressure inside the tube is close to atmospheric pressure. The result from this measurement is the adsorption isotherm and can be analyzed according to the Brunauer-Emmett-Teller equation that assumes perfectly spherical gas molecules form a perfectly consistent monolayer over the surface of the pores. More information about the BET method can be found in the Appendices. For COFs their structures are expected to be microporous, which means that their pores are smaller than 10 nm. Micropores adsorb gases at very low pressures and so the adsorption

isotherm of a properly formed COF will have a sharp rise at these low pressures. As the relative pressure inside the tube increases the mesopores begin to be filled, because COFs often form microcrystalline nanoparticles with some amorphous regions, they often show increases in adsorption during the mesoporous filling portion of the adsorption isotherm (between 0.46 and 1). This does not disqualify their characterization as COFs, and there is no established standard in how porous a sample needs to be to be considered a COF.

Crystallinity of COFs is most often measured by powder x-ray diffraction (PXRD). PXRD relies on diffraction of Cu K α radiation off the crystal faces of the COF which yields a characteristic pattern based on the space group and stacking structure of the material. 2D COFs often have a low angle diffraction that corresponds to their large [1 0 0] pore facet, and since the facet distance is inversely related to diffraction angle according to the Bragg equation,

$$n\lambda = \frac{2d}{\sin \theta} \quad (1.1)$$

where n is the order of the diffraction plane, λ is the wavelength of x-ray radiation (1.5406 from Cu K α), d is the lattice spacing, and θ is the Bragg angle, very large pore COFs must be analyzed by specific small angle X-ray methods like small-angle x-ray scattering (SAXS). Due to the soft-matter nature of the all-organic structure of COFs their PXRD patterns are not infinitely intense and broaden due to the small size of or strain present within the crystallites. Size broadening generally follows the Scherrer equation,

$$\tau = \frac{K\lambda}{\beta \cos \theta} \quad (1.2)$$

Where τ is the mean crystallite size, K is a unitless shape factor, β is the amount of broadening of a diffraction plane measured as the full width at half-maximum, and θ is the Bragg angle. Uniform strain broadening across the entire diffraction pattern would result in uniform peak shifts across the diffraction pattern, as such it is reasonable to differentiate the Bragg equation with respect to the lattice spacing which yields the strain equation,

$$\epsilon = C_\epsilon \tan \theta \quad (1.3)$$

where ϵ is the broadening due to inhomogeneous strain, C_ϵ is a constant depending on the direction of the strain, and θ is again the Bragg angle. Thus, the overall broadening can be obtained by the summation of size and strain broadening in the form,

$$\beta + \epsilon = C_\epsilon \tan \theta + \frac{K\lambda}{\tau \cos \theta} \quad (1.4)$$

$$(\beta + \epsilon) \cos \theta = C_\epsilon \sin \theta + \frac{K\lambda}{\tau} \quad (1.5)$$

that has a linear relationship between total broadening at Bragg angles, $(\beta + \epsilon)\cos(\theta)$, and $\sin(\theta)$ where the crystallite size is related to the intercepts. Thus, size and strain broadening can be found by linear regression of total broadening versus Bragg angle under assumptions about the shape factor and strain direction. Broadening becomes important when attempting to obtain the structure of a crystalline lattice from a PXRD pattern by Reitveld refinement.

Bond formation in COFs is typically assessed by measuring the FTIR spectrum of monomers and the formed COF product. The functional groups of the monomers typically have signals corresponding to their stretching frequencies; in imine COFs the aromatic amines have frequencies around 3300 cm^{-1} and the aromatic aldehydes have frequencies around 1700 cm^{-1} . If the COF formed properly these frequencies should be attenuated and a new peak attributed to the polymer linker motif should appear; in imine COFs a conjugated imine stretching frequency is observable between $1620\text{-}1630 \text{ cm}^{-1}$.

1.6 Ultrafast Spectroscopy Studies of Covalent Organic Frameworks

As outlined in previous sections, nature optimizes its structures to enable electronic coupling that helps efficiently separate charges and theory predicts that the same can be done for COF systems.^{81,82} Elucidating experimental details about how excitations behave in COFs requires specialized ultrafast spectrometers to monitor their excited state dynamics. Transient absorption spectroscopy (TAS) has been used to study ultrafast phenomena like exciton diffusion,⁸³ singlet-singlet annihilation,⁸⁴ and charge separation in COFs,⁸⁵ and useful information about their structure-property relationships can be obtained.

TAS operates on a pump-probe principle in which the sample is exposed to a pump laser of a wavelength in which it absorbs and the response to the pump is monitored by a broadband probe laser with

wavelengths equal to the spectral region of interest. The spectral region of the probe is often used to specify the type of TAS being used; a UV-Visible probe is often termed optical TAS (OTA); synchrotron probes are termed X-ray TAS (XTA); infrared (IR) probes are termed time-resolved IR (TRIR); and terahertz probes are termed optical pump terahertz probe (OPTP). A distinction is also made about the timescale being monitored; these time resolved techniques can measure events occurring from an attosecond to millisecond timescale. Measurements cannot be accurately made within half of the pulse duration, so narrower pump laser pulse durations are required for faster measurement timescales (i.e. attosecond pump for attosecond measurements, femtosecond pump for femtosecond measurements, etc.). The primary drawback to using such ultrafast pulses is that the pulse duration is Fourier-transform limited, meaning that shortening the pulse duration will broaden the spectral bandwidth of the pump pulse according to the equation,

$$\Delta\omega = \frac{2\pi}{\Delta t}. \quad (1.6)$$

Short pulses with wide bandwidths are also susceptible to group velocity dispersion (GVD) inside media due to refraction that is dependent on the wavelength of light according to the equation,

$$v = \frac{c}{n'} \quad (1.7)$$

where n' is the refractive index of the medium where bluer wavelengths refract more than redder wavelengths. GVD can lead to a chirp in the measurement that is caused by some wavelengths of light reaching the detector sooner than others but can be compensated by making the redder wavelengths travel a longer distance to the detector.

To study the excited state dynamics relevant to artificial photosynthesis femtosecond OTA (fs-OTA) is a good candidate since most energy transfer, charge transfer, and charge separation processes take place within the fs to ns time window (Figure 1.17). In all cases involving excited state dynamics there are only three responses observable by the detector: excited state absorption (ESA), ground state bleach (GSB), and stimulated emission (SE). ESA occurs due to sample absorbing a photon from the pump laser which promotes an electron to a higher energy level, the excited electron can then absorb another photon from the probe laser that goes onto reach the detector. Because the probe photon was absorbed this results in less

transmission through the sample than there was prior to the pump photon excitation. Like absorption spectroscopy, TAS can be expressed as a difference in transmittance in which case ESA would be negative (i.e. $\%T_{\text{excited}} - \%T_{\text{ground}}$), but more commonly it is expressed as a difference in absorbance in which case ESA is positive. TAS results will be presented herein in as difference in absorbance (ΔA), unless noted otherwise. Conversely, GSB is the result of the vacancy left behind after the pump laser excited an electron to an excited state; this leads to less absorption of probe photons from the ground state and a corresponding decrease in ΔA , a negative signal. SE occurs due to photon emission from the excited sample resulting from the relaxation of the excited electron to the vacancy left in the ground state, but with the qualifier that the emission was in response to (i.e. stimulated by) the electric field of a probe photon. This phenomenon is the concept behind lasers (Light Amplification by Stimulated Emission of Radiation), but it is detectable in TAS because the stimulated emission of a photon from the sample is collinear with the probe that is bound for the detector. Because more light now reaches the detector SE is observable as a feature with negative ΔA and can be difficult to resolve from GSB.

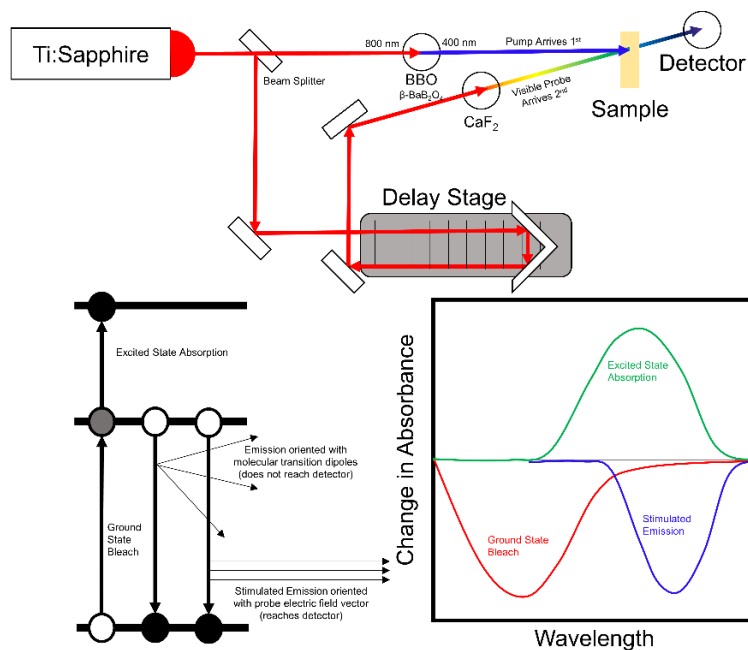


Figure 1.17 (top) Simplified diagram of OTA where the seed laser is split into pump and probe beams and the pump beam is frequency doubled in a BBO (β -barium borate) crystal while the probe beam is delayed and generates broadband white light in a CaF₂ crystal. (bottom) Three level energy diagram used to illustrate the processes responsible for signal in OTA and the changes in absorbance expected for these different processes.

While studies have thus far have proven useful, much is still left unknown about photophysics COFs. There is no agreement on how to treat interlayer interactions in COF – especially if there is no obvious effect of the effect of the strong coupling limit. Some literature references assume these effects are negligible,⁸⁶ while others seem to deduce that they are predominant (Figure 1.18).⁸⁷ Naturally, the answer may need to be arrived at on a case-by-case basis – some COFs maximize interlayer delocalization and charge transfer, while others suppress its effects.

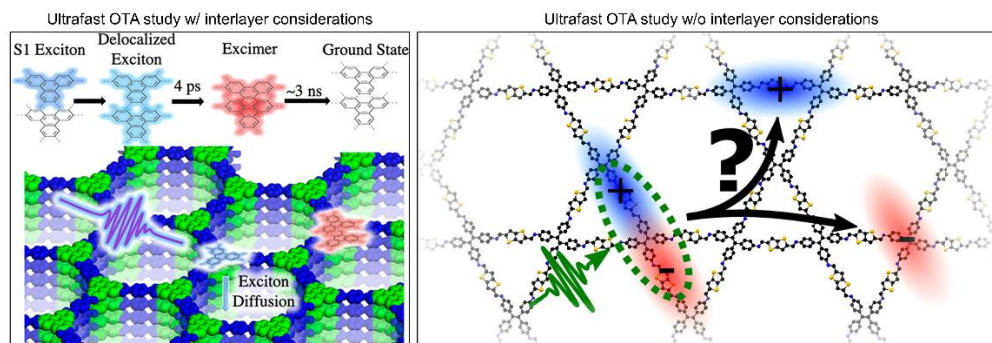


Figure 1.18 Figures from ultrafast OTA studies that either focus on (left)⁸³ or ignore interlayer interactions (right).⁸⁴

Some clues offered by one study on excited state (ES) dynamics of fully conjugated 2D COFs based on 1,1,2,2-tetrakis(phenyl)ethene and 1,3,5-triphenylbenzene cores shows that excitation results in CS by exciton delocalization and subsequent singlet-singlet annihilation.⁸⁴ This work compared TA data from different film thicknesses and different pump laser powers. Varying these parameters allowed the authors to arrive at the conclusion that generation of a higher density of excited states (by higher power and/or thickness) leads to the formation of more longer-lived excited state, which they attribute to singlet-singlet annihilation. Notably, this effect was only present in the COFs based on the tetrakisethene core and when analyzed through the lens of topological electronic structure effects, may result because dispersion across this core is possible while not as likely for the triphenylbenzene core.

More recently, the signature of delocalized excitons which relax to excimer states has been observed in COF-5 built from triphenylene monomers linked by boronate ester bonds.⁸³ This study differs than the one by Bein et. al. for fact that boronate esters are not conjugated aromatic species, ruling out ICT. Again, power dependence is used, but this time to identify the signature of excimer formation that is

present between dimers of adjacent triphenylene layers. These studies demonstrate the potential of COFs as light absorption and CS materials, but the variety in their photophysical properties leaves open the possibility for unexplained behaviors.

1.7 Photocatalysis by Covalent Organic Frameworks

COFs have emerged as photocatalytic materials due to a variety of benefits they possess over traditional molecular photocatalysts.⁸⁸⁻⁹⁰ First, COFs are inherently porous which imparts them with high surface areas that can enhance overall performance by increasing the number of available reaction sites, this porosity also helps confine molecules near these reaction sites which may help in kinetically challenging multistep reactions.^{88,91} Their periodic structure also offers very interesting possibilities to use structure based design much in the same way nature approaches the design of LH2 and other chromophore superstructures.⁵⁹ Additionally, accessible organic monomers allow for the precise insertion of catalytic sites⁹² and compositional flexibility opens avenues for molecular engineering.⁹³⁻¹⁰¹ Their covalently bound structures offer relatively high stability improve degradation resistance after multiple catalytic cycles that can improve turnover numbers (TON).^{53,102} Finally, the aromatic monomers they are often constructed from tend to have a good ability to capture ultraviolet (UV), visible, and even infrared (IR) radiation from the solar spectrum. There have been several reports of 2D COFs as photocatalytic materials encompassing a variety of different photocatalyst architectures. COFs with incorporated metal catalysts through post-synthesis modification¹⁰³ present a promising approach that allows full use of their high surface area. Similar strategies are COF photosensitizer/co-catalyst systems.^{95,104,105} These systems, instead of directly functionalizing the pore, utilize a phase separated homogeneous co-catalyst whereby the COF performs light harvesting and energy transfer. Certain COFs, on the other hand, have been reported with the ability to act as light harvesting unit and photocatalyst without metal atom incorporation.¹⁰⁶ Finally, COFs have been covalently bound to single semiconductor systems such that they form a Z-scheme type catalyst.¹⁰⁷

The artificial photosynthetic reaction that most closely mimics nature is the coupled H₂O oxidation/CO₂ reduction reaction. For more information on water oxidation and CO₂ reduction see the Future Directions section. While there are variations of artificial photosynthesis that rely on, for instance, hydride transfer to CO₂ or bimolecular metal-oxo interactions, the example presented in Figure 1.19 was selected for its relevance to artificial photosynthesis in COFs. Absorption of a photon promotes an electron

to a higher energy state generating an electron-hole pair with sufficient potential energy to activate the substrates. In the first step on the photoreduction side of the reaction CO_2 is bound to an active site (presented here as a general semiconductor interface) through its η^1 adduct mode. The electron transfer, which is coupled to a proton transfer, is made to CO_2 forming bound formate. This proton coupled electron transfer helps to lower the transition state energy of the intermediate and is particularly important to the reaction because this first step is the most thermodynamically challenging on the reductive side. Photooxidation in the first step results in an electron being transferred to the oxidative semiconductor from H_2O , quenching the hole and generating a bound hydroxide. A second photoexcitation leads to a second proton coupled electron transfer to the formate then dissociates H_2O and CO while the hydroxide is oxidized again to form an oxo-complex. For CO_2 reduction this dissociation of CO represents a full catalytic turnover and on subsequent cycles the previous two steps are repeated. The third photoexcitation is the most thermodynamically challenging on the water oxidation side of the reaction because the active site must now be oxidized a third time to activate the oxo-complex and form the O-O bond, if this is achieved there are primarily two subsequent pathways that can be followed. The first of these (not pictured here) involves two oxo-complexes that can interact to form an O-O bond and is bimolecular with respect to the active site. The second is unimolecular with respect to the active site due to a second water molecule that acts as a nucleophile, attacking the oxo-complex is termed water nucleophilic attack (WNA). WNA is presented here because in the bulk environment of a COF one would expect the insoluble macromolecular structure to be geometrically restricted from allowing two active sites from interacting. After WNA, the reaction is energetically downhill where after formation of the O-O bond two protons are removed and molecular O_2 is dissociated.

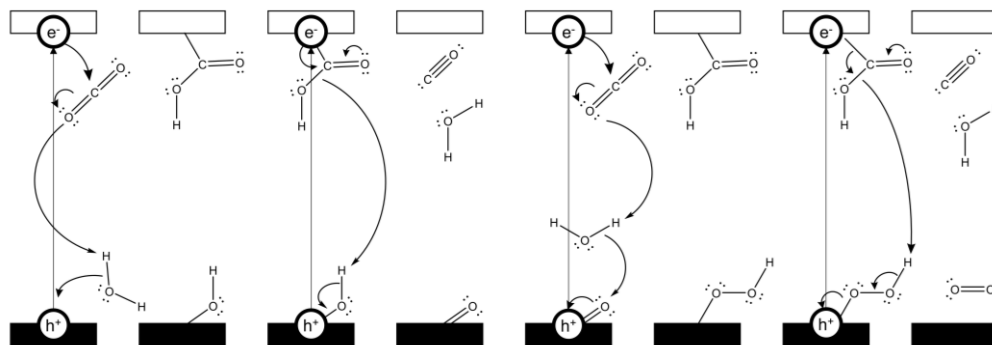


Figure 1.19 Simplified mechanism for coupled H₂O oxidation/CO₂ reduction driven by light. Note that the oxidation mechanism presented here is water nucleophilic attack (WNA). Also note the CO₂ adduct is binding in the η^1 mode and undergoes proton-coupled electron transfer in the first step of each CO₂ reduction reaction.

Even though WNA would seem the predominant pathway for water oxidation in COFs a recent example took advantage of the relative ease in which COFs can be engineered to facilitate the alternate two-interacting metallo-oxo (I₂M) pathway.¹⁰⁸ This 3D COF contained a Ru metal catalyst that was designed to take advantage of structural interpenetration to place Ru sites adjacent to one another at the precise distance necessary for I₂M to occur (Figure 1.20). Furthermore, they show that constitutionally identical non-porous material lacked the same activity which is strong evidence for the effect of structural engineering on performance and that the material was a suitable photocatalyst. This beautiful example of structural engineering in COFs is the best recent example of the untapped potential they hold as catalyst and photocatalyst substrates for kinetically challenging reactions like water oxidation.

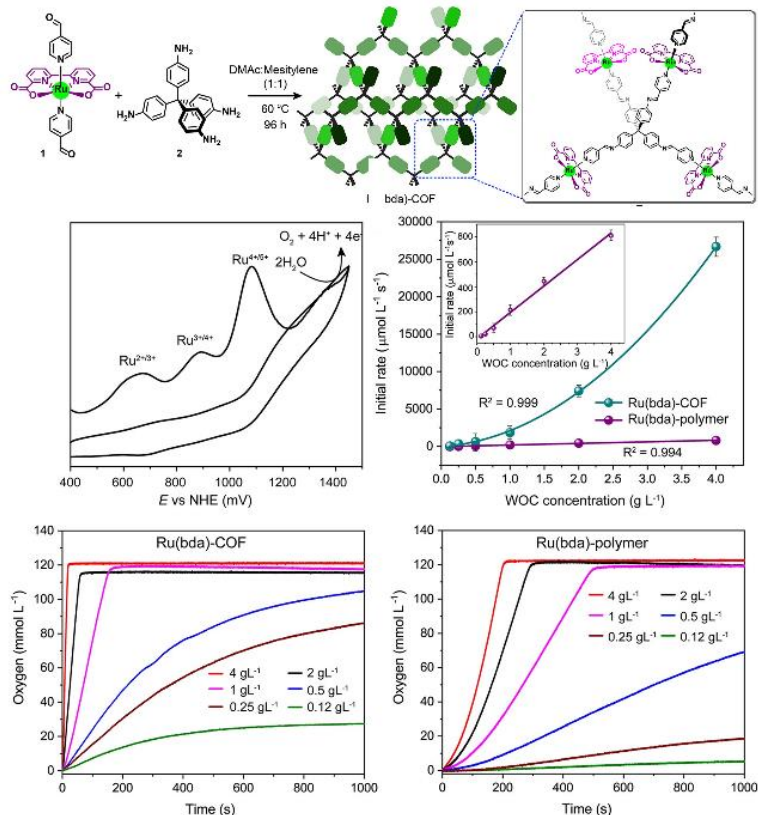


Figure 1.20 Covalent organic framework specifically designed for water oxidation by facilitating the I₂M pathway of embedded Ru=O metallo-oxo complexes.

Studying the photophysical properties of COFs is challenging but merits investigation based on the possibilities that exist to modify their electronic structures. Nature has spent eons fine-tuning the light harvesting abilities of chloroplasts for photosynthesis and it should be expected that doing the same in COFs will take time. The design advantage COFs have over other types of light harvesting systems is the predictable topological properties of their structures, and the direct influence of this topology on charge carrier mobility. Techniques to create COFs have come along way since their inception, and newfound understanding of their formation and stability mean that the most promising days are ahead for their utility as artificial photosynthesis platforms.

CHAPTER 2 – EXPERIMENTAL AND THEORETICAL METHODS & DETAILS

2.1 Experimental and Computational Methods for Chapter 3

2.1.1 Femtosecond transient absorption (fs-TA) measurements

The femtosecond TA spectroscopy is based on a regenerative amplified Ti-Sapphire laser system (Solstice, 800 nm, < 100 fs FWHM, 3.5 mJ/pulse, 1 kHz repetition rate). The tunable pump (235-1100 nm), chopped at 500 Hz, is generated in TOPAS from 75% of the split output from the Ti-Sapphire laser. The other 25% generated tunable UV-visible probe pulses by white light generation in a CaF₂ window (330-720 nm) on a translation stage. A Helios ultrafast spectrometer (Ultrafast Systems LLC) was used to collect the spectra. The film samples were continuously translated to avoid heating and permanent degradation.

2.1.2 Crystal Structure modeling and refinements

The crystal models for three imine COFs were modeled by using Materials Studio 5.0 software package (Accelrys Software Inc. (2009, now BIOVIA). Materials Studio 5.0: Modeling Simulation for Chemical and Material, San Diego, CA.). The lattice parameters and atomic positions were optimized under the universal force field and were further refined through the Pawley PXRD refinement conducted with the Reflex module until the Rwp value converging and a good agreement obtained between the refined profiles and the experimental ones. The parameters including peak broadening, peak asymmetry, and zero shift error were considered in the applied Pseudo-Voigt profile function for whole profile refinement.

2.1.3 Density Functional Tight Binding

A user-defined unit cell was constructed and optimized by self-consistent charge density functional tight-binding (SCC-DFTB) in the DFTB+ package.¹⁰⁹ SCC-DFTB was performed periodically to ensure the resulting structure was representative of the overall bulk structure. Slater-Kloster (SK) files (3ob-3-1)¹¹⁰ were used with D3 dispersion correction (a1=0.746, a2=4.191)¹¹¹ and Becke Johnson damping (s6=1.0, s8=3.209).¹¹² The structure was allowed to remain in its hexagonal lattice and optimized until forces on each of the atoms were no more than 1.0×10^{-5} eV/Å. Once the atomic positions were converged, a step of the lattice vectors was taken in the direction of the force acting upon them followed by another round of atomic position optimization until convergence. This process iterated until the maximum force acting on any of the lattice vectors was less than 1×10^{-4} Pa. Finite difference differentiation was used with a delta parameter of 1.22×10^{-4} and error in the SCC calculation was minimized with a Broyden density mixer

with mixing parameter set to 0.2, inverse Jacobi weight set to 1×10^{-2} and a weight factor of 1×10^{-2} . The Ewald parameters for unit cell optimization were determined automatically by DFTB+ and the Ewald tolerance was set to 1×10^{-9} . From these optimized structures the ends were capped with hydrogens and used for TDDFT.

2.1.4 Time-Dependent Density Functional Theory

TDDFT was performed in Gaussian16 with the range-separated global hybrid CAM-B3LYP¹¹³ functional to correctly model the charge transfer behavior with Pople's 6-311G** basis set.^{114–116} The first 10 transitions were calculated to obtain suitable convergence for our state of interest, which was the first singlet transition. It is important to note that for later transition density matrix analysis the keywords "iop(9/40=3)" "GFINPUT" and "Pop=Full" need to be included.

2.1.5 Analysis of Transition Density Matrix

The first singlet transition was analyzed by transition density matrix (TDM) analysis with the TheoDOR program^{117–120} to characterize and quantify the charge transfer in the system. More information about TDM analysis can be found in the Appendices. To analyze the transitions correctly it was important to define units of the structure critical to its charge transfer behavior so the transition density matrix would be projected onto a suitable basis. Units were selected as follows: the phenyl rings around the variable core (triazine, benzene, amine), the core itself, the imine, the BTPA pyridines, and the BTPA benzene.

2.2 Experimental and Computational Methods for Chapter 4

2.2.1 Transient Absorption (TA) Spectroscopy

Femtosecond TA spectroscopy in this chapter follows a similar procedure as outlined in Section 2.1 with a few exceptions. Sample solutions are analyzed in a 2 mm quartz cuvette with a septum and purged with N₂ atmosphere before TA measurements. A PTFE-coated stir bar in the cuvette allows continuous stirring during the measurements. pTCT-0P, pTCT-1P, pTCT-2P and donor samples are excited using 340 nm and 375 nm pump pulse (0.3 mW power), while the acceptor is excited using 300 nm pump pulse (0.3 mW). Global fitting analysis is performed using Glotaran 1.5.1.¹²¹

2.2.2 Computational Details

pTCT series molecules were initially optimized to their S₀ geometry using density functional theory (DFT) with the B3LYP functional,^{122–124} Grimme's D3 empirical dispersion with BJ damping (D3-BJ),¹²⁵ Pople's 6-311G** basis set,^{122,126} and a toluene ($\epsilon=2.38$, $\epsilon_{\infty}=2.238$) integral equation formalism polarizable continuum model (IEFPCM)¹²⁷ with the Gaussian16 program.¹²⁸ Diffuse functions were explored for use but ultimately exceeded resource constraints on compute nodes, particularly in frequency calculations on pTCT-2P. As for the ES, S₁ and T₁ geometries were found using time-dependent density functional theory (TDDFT) with B3LYP and CAM-B3LYP functionals, D3-BJ empirical dispersion, 6-311G** basis, and toluene IEFPCM. For each ground state geometry (S₀), two degenerate transitions are predicted to populate the S₁ and S₂ potentials, respectively; due to their degeneracy extra care was taken to optimize the molecule along the correct potential.

To accurately predict the frontier molecular orbital energies, we tuned the long-range corrected ω PBE functional¹²⁹ (LRC- ω PBE) at the S₀, S₁, and T₁ geometries. Tuning was performed without a solvent model by changing the amount of long-range Hartree-Fock exact exchange, represented by ω , until the sum-of-squares difference between the HOMO/LUMO gap and fundamental gap (ionization energy – electron affinity) was minimized, as in Equation 2.1.

$$\min(\omega) = [IP(\omega, N) + \epsilon_{HOMO}(\omega, N)]^2 + [IP(\omega, N + 1) + \epsilon_{LUMO}(\omega, N)]^2 \quad (2.1)$$

Tuning helps account for Coulomb interaction of the photoexcited hole and electron by minimizing self-interaction error and allowing for accurate ES energies to be obtained. Thus, vertical transitions were

solved using LR-TDDFT, LRC- ω PBE, D3-BJ empirical dispersion, 6-311G** basis set, and toluene PCM with equilibrium solvation for transitions at the S_1 and T_1 geometries, and non-equilibrium solvation at the S_0 geometries.

Error against experimental data increases with system size, possibly due to limitations of the adiabatic approximation in LR-TDDFT that becomes increasingly important for larger molecules. Nonetheless, the largest absorption energy error is 0.09 eV on pTCT-2P. We also find that LRC- ω PBE significantly improves predictions by global hybrids B3LYP (-0.52 eV) and CAM-B3LYP (0.60 eV) – strengthening our confidence in the model. Overall, emission was more accurately modeled by LRC- ω PBE at B3LYP S_1 geometries than CAM-B3LYP S_1 geometries, leading to its use in this work. However, we note pTCT-2P emission was better predicted using the CAM-B3LYP S_1 geometry.

ISC rates were modeled by adding the LRC- ω PBE transition energies to the S_1 and T_1 B3LYP SCF energies to determine ΔE_{ST} and related values. Spin-orbit coupling matrix elements (SOCME) were obtained using the screened one-electron Breit-Pauli Hamiltonian operator (as implemented in the pySOC program) on the LRC- ω PBE density but with 6 additional d-orbitals and 10 additional f-orbitals added to the 6-311G** basis set, as required by pySOC.^{130,131} Natural transition orbital (NTO) calculations¹³² were used to visualize transitions. Excited-state charge-transfer analysis was performed using TheoDORE¹¹⁸¹³³¹²⁰ and cclib¹³⁴ codes.

2.3 Experimental and Computational Methods for Chapter 5

2.3.1 Synthesis of TAT-COF

In a 20 mL autoclave, 2,7,12-Triformyl-5,10,15-triethyltriindole (TAT) (82mg) and Trimethyl-s-triazine (TMTA) (19.68mg) were dispersed in a mixture of mesitylene (8mL), MeOH (8mL) and NaOH (30mg). After being purged with N₂, the autoclave was heated to 180 °C for 4 days. The resulting solid was collected by centrifugation and washed with DCM and THF repeatedly to remove the trapped guest molecules. The powder was then dried under vacuum to produce TAT-COF with an isolated yield of 65%.

2.3.2 Synthesis of TPB-COF

In a 20 mL autoclave, 1,3,5-Tris(4-formaldehydephenyl)benzene (TFPB) (62.46mg) and Trimethyl-s-triazine (TMTA) (19.68mg) were dispersed in a mixture of mesitylene (8mL), MeOH (8mL) and NaOH (30mg). After being purged with N₂, the autoclave was heated to 180 °C for 4 days. The resulting solid was collected by centrifugation and washed with DCM and THF repeatedly to remove the trapped guest molecules. The powder was then dried under vacuum to produce TAT-COF with an isolated yield of 80%.

2.3.3 UV-Visible Absorption Spectroscopy

UV-Visible absorption spectra were taken using an Agilent 8453 spectrometer. To make COF films, the piranha etched glass was immersed in the COFs reaction tube during synthesis. The obtained thin layer of COF film was then washed with acetone to remove free ligands.

2.3.4 Powder X-Ray Diffraction

Powder X-Ray Diffraction (PXRD) measurements were taken on a Rigaku MiniFlex 2 utilizing CuK α ($\lambda=1.54$ Å) radiation source with 30 keV acceleration voltage and 15 mA current. The pattern was collected over the first 30° 2 θ in 0.05° 2 θ increments.

2.3.5 N₂ Adsorption Isotherm for Brunauer-Emmett-Teller Analysis

A dry, static-free sorption tube and SealFrit closure was weighed three times and the average was recorded. Then ~30 mg of COF sample was added to the sorption tube and re-weighed three times. A dewer containing a reference sorption tube was filled with liquid N₂ (LN₂) to ensure isothermal reference conditions. Over the sample sorption tube an isothermal jacket was placed to help wick LN₂ over the neck to ensure isothermal measurement conditions. The sample sorption tube was affixed to the ASAP-2020

(Micromeritics) and the pressure brought to 1×10^{-5} torr. A second dewer was filled with LN2 BET into which the evacuated sample sorption tube was placed. Microdoses of N₂ gas were incrementally fed into the sorption tube and the pressure within was monitored until the pressure within the tube reached ~0.95 torr. The calibrated microdoses allowed for quantitation of N₂ adsorbed by the sample yielding the N₂ adsorption isotherm. Analysis of N₂ adsorption isotherms was performed using the software provided by Micromeritics.

2.3.6 Femtosecond Transient Absorption (TA) Spectroscopy

Femtosecond TA spectroscopy in this chapter follows a similar procedure as outlined in Section 2.1.

2.3.7 Fabrication of LED strip

TAT-COF was dispersed in optical epoxy adhesive (Norland 63) through sonicating. The mixture was then dropped to the surface of LED strip. After that, Xe lamp was applied for 1 minute to cure the epoxy.

2.3.8 Quantum Yield measurement

Quantum yield of TAT-COF and TPB-COF were measured by using Coumarin-343 as reference. ZIF-8 (no absorption in the visible region) has been added to reference solution to account for the effect of scattering.

$$Q_s = Q_r \times \left(\frac{A_r}{A_s} \right) \left(\frac{E_s}{E_r} \right) \left(\frac{n_s}{n_r} \right)^2 \quad (2.2)$$

Where: Q is fluorescence quantum yield, A is absorption of solution, E is integrated fluorescence intensity of the emitted light, n is the refractive index of the solvent, subscripts 'r' and 's' refer to the reference and COFs, respectively

2.3.9 Structure simulation

Molecular modeling of COF for PXRD analysis was simulated using Materials Studio (2017) program. The initial lattice was created with space Group P1. The structure of TAT-COF is assumed to be analogous to that of COF 10,¹³⁵ where each edge of the hexagonal ring was substituted by the framework of (E)-2, -(2-(1,3,5-triazin-2-yl)vinyl)-9-ethyl-9H-carbazole. The geometry of COFs was optimized with MS DMol3 module and redundant atoms were deleted. After that, the symmetry was promoted to P6. The lattice model was then optimized using the MS Forcite module. Finally, Pawley refinement was applied to

define the lattice parameters, which produces the refined PXRD profile with lattice parameters of $a = b = 17.7452 \text{ \AA}$ and $c = 3.6403 \text{ \AA}$. R_{wp} and R_p values were converged to 2.23% and 1.75%, respectively. The same process was applied to TPB-COF, where after Pawley refinement, the lattice parameters of $a = b = 17.5590 \text{ \AA}$ and $c = 3.4520 \text{ \AA}$ were obtained with R_{wp} and R_p values of 1.83% and 1.47%, respectively.

2.3.10 DFTB Structure Optimization

The unit cell and atomic positions were optimized by SCC-DFTB as in Section 2.1 with a few exceptions. It was necessary to remove the hanging ethyl groups of the TAT monomer to achieve convergence which we assume will only lead to minute differences in the COF structure. The atomic structure was optimized until forces acting on any individual atom were less than 1×10^{-4} a.u.

2.3.11 TDDFT Calculations

TDDFT calculations were performed in a similar manner to those outlined in Section 2.1 with a few exceptions. To minimize computational costs of TDDFT calculations the final structures from DFTB (above) were decomposed into smaller units which retained the primary units for charge transfer. TAT-COF was truncated at the vertices of both the TAT monomer and the triazine unit with a hydrogen atom such that the two were connected via a C-C double bond. TPB-COF was decomposed in a similar manner. To simulate the effects of aggregation the substructures of TAT-COF and TPB-COF were built into supercells according to the DFTB optimized unit cell parameters. The selection for these smaller units was based on the important conjugation that exists across TAT. Because each indole unit is fused to the central benzene ring truncating the structure at the benzene would affect the predicted electronic properties. Additionally, because the three branches of TAT were preserved the decision was made to preserve the three branches of the TPB portion of TPB-COF, as well.

2.3.12 Transition Density Matrix Analysis

TDM analysis was performed using the TheoDORÉ software package.^{117,119,136} Fragment selection is crucial to developing reasonable insights from TDM analysis, and as such we selected three fragments – the triazine unit, the C-C double bond, and the TAT/TPB portions of the substructure. Importantly, TAT could not be broken down into smaller components as may be possible for TPB by selecting the individual rings which compromise its structure because the indole units of TAT are directly fused to the central

benzene ring. Also, by selecting the C-C double bond as a separate fragment instead of simply the donor and acceptor units the bridging effect of this linker was able to be considered.

2.4 Experimental and Computational Methods for Chapter 6

2.4.1 Synthesis of Isostructural Covalent Organic Frameworks

Following the literature procedure,⁹⁰ each COF was synthesized by taking a 1:1 molar ratio of linear monomer to trigonal monomer in a 5 mL 82:15:3 Toluene/Mesitylene/Glacial Acetic Acid mixture. The mixture was sonicated until all reactants were evenly dispersed or dissolved and then degassed and heated to 120°C in a 10mL pressure vial for 3 days. After the synthesis procedure, each COF was centrifuged, decanted, and soaked in methanol for a total of 3 times to remove solvent trapped in the pores.

2.4.2 Powder X-Ray Diffraction

PXRD measurements were collected in a similar manner to those outlined in Section 2.2 with a few exceptions. Strain parameters from the PXRD patterns were fitted according to the procedure from Molina et. al.¹⁰⁰ in GSAS-II¹³⁷ with slight modifications, as follows. First, the default U, V, W, and Gaussian components were accepted and refinement was performed from 2.0° to 12.0° 2θ. Background functions were Chebyshev polynomials where the order of the polynomial was selected from 5 to 8 to yield the best fit. The asymmetry parameter was not refined, and the peak positions were not refined after the initial position and intensity refinement. Predicted PXRD patterns from the DFTB optimized structures were generated by the Mercury software package¹³⁸ (version 4.1.3) from the Cambridge Crystallographic Structure Database (CCSD).

2.4.3 Diffuse Reflectance Measurements

Diffuse Reflectance Measurements were taken on a Agilent Cary 5000 spectrophotometer with a integration sphere. Raw data was processed by Kubelka-Munk transformation according to the following equation:

$$\frac{\text{Scattering}}{\text{Absorbance}} = \frac{2 \cdot \text{Reflectance}}{(1 - \text{Reflectance})^2}$$

2.4.4 Transient Absorption (TA) Measurements

Similar to the prior literature procedure⁹⁰ thin films of the COFs were made by drop-casting onto Pirhana-etched glass a dispersion of 1mg COF with 0.5 mL Nafion in 5% water and 1-propanol. The dispersion was formed by sonicating the mixture for 2h. Upon evaporation of the solvents a thin-film

suitable for TA measurements was formed. The collection of TA data was performed as outlined in Section 2.1.

2.4.5 DFTB Structure Optimization

Structure optimization using SCC-DFTB was performed in a similar manner to the procedure outlined in Section 2.1. with a few exceptions. Periodic SCC-DFTB optimizations were performed starting with a unit cell with a c-axis magnitude of 3.70 Å to replicate the bulk environment. The unit cell was obtained from a reference¹³⁹ in which the name of the fragment was “linker96_N_linker30_CH_hcb_relaxed.cif.” Additionally, three-body interactions (default cutoffs) and an additional H-H repulsion¹⁴⁰ correction were turned on.

To explore the possibility of different stacking modes periodic structures were optimized with a large vacuum separation to allow sufficient freedom for COFs to approach preferential interlayer arrangement. These periodic SCC-DFTB optimizations were performed starting with the single layer unit cell from above reoptimized with a 30 Å vacuum region above and below the layer. The optimization was performed isotropically, meaning both the atomic positions and unit cell parameters were optimized but each unit cell step was scaled proportionally with the other axes/angles, this was done to ensure significant vacuum separation remained present throughout. The same SK files (3ob-3-1) and dispersion parameters ($a_1=0.746$, $a_2=4.191$, $s_6=1.0$, $s_8=3.209$) from above were used as well as the same convergence criteria, density mixer and eigensolver. Once the single layer optimization was completed the layer was copied and translated 4.0 Å above and below the original layer to form a perfectly eclipsed three-layer system now with ~22 Å total vacuum separation. This three-layer system was then optimized as before yielding structures which preferentially adopted an inclined stacking arrangement. From these optimized three-layer geometries new unit cell angles were estimated according to location of each layers' center-of-mass.

2.4.6 Time-Dependent Density Functional Theory Calculations

TDDFT was performed in a similar manner to the procedure outlined in Section 2.1. To study multiple layers of COF the edge or star unit selected for analysis was duplicated and translated according to its unit cell parameters.

2.4.7 Transition Density Matrix Analysis

TDM analysis was performed in a similar manner to what was outlined in Section 2.1 with a few exceptions. We carefully select fragments which represent the most critical pieces of the COF structure involved in the CT transition. In the intralayer case we select four fragments – the tritopic core (s-triazine or benzene), the phenylene attached to the tritopic core, the imine linker formed through amine/aldehyde condensation, and the bridge (bipyridine or biphenyl). In the interlayer case our fragment selection is simply the separate layers in the system. By using these logical selections, we gain a clear two-dimensional picture of which portions or layers of the COF backbone participate in the CT transition as a donor, acceptor, or spectator.

2.4.8 Electronic Transitions at Various Interlayer Distances

To explore the impact of interlayer distance on transition intensity and exciton structure two approaches were taken to generate structures suitable for further analysis. First two-, three- and four-layer N2N3 edge fragment supercells were manually generated in Avogadro^{141,142} such that their interlayer distances ranged from 3.5 Å to 3.0 Å in 0.1 Å increments. TDDFT and TDM analysis were then performed on these “compressed” supercells and utilized in the main text discussion of the tail state phenomenon arising from lattice strain. To model any conformational change of N2N3 within strain defects, SCC-DFTB was performed with the c-axis constrained to 3.5 Å to 3.0 Å in 0.1 Å increments. Standard single-point DFT (B3LYP/6-311G**) was then performed on two-layer manually translated structures and constrained SCC-DFTB optimized structures.

2.5 Experimental and Computational Methods for Chapter 7

2.5.1 Synthesis of Covalent Organic Frameworks by Solvothermal Method

Synthesis of f-COF and Re-f-COF follows the previously reported method.⁹⁰ Newly designed r-COF is first synthesized by a similar solvothermal approach as f-COF; condensation of 2,2'-bipyridyl-5,5'-diamine (NH₂-bpy) and 4,4',4''-(1,3,5-triazine-2,4,6-triyl)tribenzaldehyde (CHO-TTA) at a 3:2 ratio in a 10mL N₂ purged Pyrex pressure tube with 6 mL 1:1 1,4-dioxane:mesitylene and 0.1 mL glacial acetic acid sealed, degassed by three freeze-pump-thaw cycles, and heated at 120°C for 3 days. r-COF is then washed by solvent exchange with methanol three times then ethanol five times and kept under ethanol for critical point drying.

2.5.2 Critical Point Drying

Critical point drying (CPD, also known as supercritical CO₂ activation) is done by exchanging ethanol with liquid CO₂ (LCO₂) three times at 0 °C, each with 3-5 hours of equilibration time. After the last equilibration, the LCO₂ is brought to supercritical temperature and pressure and slowly vented from the chamber yielding the dried (activated) material.

2.5.3 Brunauer-Emmett-Teller Analysis of Adsorption Isotherms

N₂ adsorption isotherms were collected in a similar manner to the procedure outlined in Section 2.3.

2.5.4 Solvent Screening for Solvothermal Synthesis of r-COF

Seeking to improve the BET area, we screen for optimal solvent conditions by varying the ratio of dioxane:mesitylene from 8:1 to 1:2. Trends in BET surface area follow solvent polarity, with polar solvent conditions yielding more accessible surface area (8:1 dioxane:mesitylene, 494 m²/g) than less polar solvent conditions (1:1 dioxane:mesitylene, 288 m²/g and 333 m²/g). Non-polar solvent conditions seemingly yield product with higher crystallinity than polar solvent conditions, contrary to what surface area measurements might suggest. When a solvent ratio of 1:2 dioxane:mesitylene is used noticeable peaks attributable to starting material became apparent leading to the conclusion that lower solvent polarities with poor monomer solvation allow pore blocking and cannot be resolved by solvent treatment with DCM, CHCl₃, or CCl₄. We also assess the viability of drying the material from a low surface tension solvent (hexane) by monitoring the crystallinity of PXRD patterns and found that hexane activation yielded semi-

crystalline samples. In terms of surface area, however, hexane activation allows almost no accessible porosity – indicating CPD is essential to maintain an accessible structure in r-COF. f-COF is found to retain some porosity after hexane activation, indicating its structure is less sensitive to processing conditions.

2.5.5 Synthesis of r-COF by Colloidal Synthesis Method

To achieve suitably high surface area samples of r-COF we modify a recently published synthetic method for colloidal imine linked COFs.⁷⁰ In this synthesis, a 20 mL scintillation vial is charged with 0.97 g of benzoic acid that is dissolved in benzonitrile at 120 °C followed by the addition of 1.43 mL of 48 mM CHO-TTA in benzonitrile (pre-heated to dissolve). Then, 0.35 mL of 0.7 M aniline in benzonitrile is added and allowed to react with CHO-TTA for 15 minutes while being sparged with N₂ (NH₂-bpy found to be prone to oxidation). After the CHO-TTA reaction with aniline 1.43 mL of 72 mM NH₂-bpy in N₂ purged benzonitrile is added, the vial sealed, and the polymerization proceeds at 120 °C for 4 hours under a positive pressure of N₂. The product is readily separable from solution, so it is centrifuged and placed into a teabag then washed with methanol in a Soxhlet extractor to remove solvent and benzoic acid before solvent exchange with absolute ethanol five times, under which it is kept for CPD. These conditions improve the BET surface area of r-COF (600 m²/g, Figure 1c) suggesting the utility of this synthetic procedure to enhance the quality of stubborn COF crystallites.

2.5.6 Transient Absorption Spectroscopy Measurements

As in Section 2.4, thin films COF were made by drop-casting onto Pirhana-etched glass a dispersion of 1mg COF with 0.5 mL Nafion in 5% water and 1-propanol. Collection of the TA data was carried out in a similar manner to Section 2.1.

2.5.7 CO₂ Photocatalysis Experiment Details

The 11 mL reaction vial was set up as specified in the main text and sealed with a tight-fitting rubber septum. As in reference 1, the amount of CO generated was quantified using Agilent 490 micro gas chromatograph (5 Å molecular sieve column) by removing the sample from the catalytic conditions and using a glass syringe to measure the composition of 200 µL of the headspace. To prevent substantial leakage of analyte gas through the rubber septum a maximum of three withdrawals were made from the reaction vial.

CHAPTER 3 – TUNING PHOTOEXCITED CHARGE TRANSFER AND NODAL SYMMETRY IN IMINE-LINKED TWO-DIMENSIONAL COVALENT ORGANIC FRAMEWORKS

3.1 Introduction

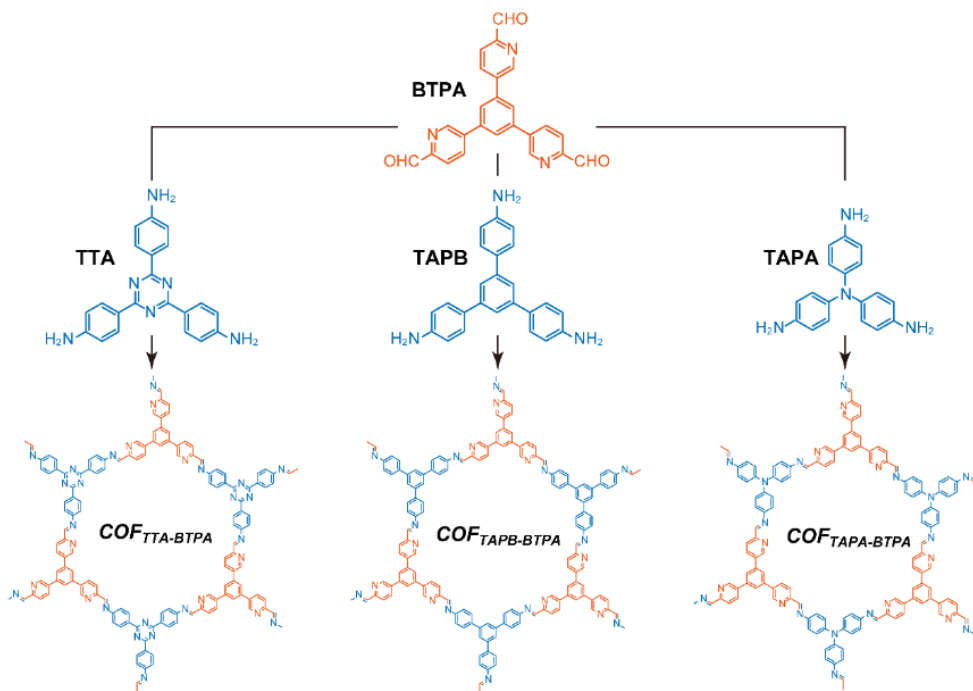
COFs are promising substrates for photocatalysis due to their visible light absorption, porous structure, and facile functionalization.^{90,98,143–146} The introduction of fully π -conjugated covalent linkages such as imines into 2D COFs enables the intralayer π -conjugation for extended photoabsorption to near-infrared regions and may help to generate long-lived charge carriers.^{84,85} Understanding how photoexcited charge carriers travel through COF material is not fully understood from a practical perspective and experimentally probing these properties is important to develop knowledge about how to design them for use as catalyst photosensitizers.

The topology of COFs has been shown to theoretically impact the mobility of charge carriers through modifications of their band structures. Thus, there is significant value in interrogating these impacts experimentally not only to establish the reliability of predictions, but to advance strategies for developing COFs for photocatalytic applications. Flat valence and conduction bands were observed in COFs with Kagome lattices which should limit the mobility of their charge carriers in the plane of the framework.⁵⁸ Thomas et. al. suggested that lowering the symmetry of the space group by modifying the position of heteroatoms on the trigonally branched six-membered ring (node) would produce band bending to assist the mobility of charge carrier.⁵⁹ This band bending was attributed to the avoidance of destructive wavefunction interference at the six-membered ring that would appear in COFs with symmetrical nodes. In the same work, Thomas also laid out another strategy to avoid destructive wavefunction interference by substituting the six-membered ring node with a tertiary carbon radical node that led to the prediction of a Dirac point in the band structure.

Modifying the symmetry of the node theoretically poses significant potential to increase charge carrier lifetime by charge separation. Designing an experimental approach to probe these differences is straightforward in COFs due to their designable nature by simply exchanging a nodal monomer with six-membered ring for one with a single atom at the nodal position. Once these COFs have been synthesized it is then pertinent to assess their charge separation capabilities and compare them against each other.

However, other factors relating to monomer selection such as electron donating ability, and physical structure need to be considered.

A systematic study is presented here on the photoexcited charge transfer dynamics of three imine-linked 2D COFs ($\text{COF}_{\text{TTA-BTPA}}$, $\text{COF}_{\text{TAPB-BTPA}}$, and $\text{COF}_{\text{TAPA-BTPA}}$, Scheme 3.1) constructed by the polycondensation of pyridine-containing 5,5',5''-(1,3,5-benzenetriyl)-tris(2-pyridine carboxaldehyde) (BTPA) with three aromatic triamine monomers with tunable electron-rich/deficient cores and different nodal symmetries. Using steady-state and transient absorption (TA) spectroscopies coupled with time-dependent density functional theory (TDDFT) calculations, we found that exciton relaxation dynamics and charge carrier lifetimes of these 2D COFs strongly depend on the electron affinities and nodal symmetries of the monomers.



Scheme 3.1 Construction of imine-linked $\text{COF}_{\text{TTA-BTPA}}$, $\text{COF}_{\text{TAPB-BTPA}}$, and $\text{COF}_{\text{TAPA-BTPA}}$ by polycondensation of BTPA with TTA, TAPB, and TAPA, respectively.

3.2 Synthesis and Characterization of BTPA COFs

Three imine-linked 2D COFs were synthesized by polycondensation of BTPA with 4,4',4''-(1,3,5-triazine-2,4,6-triyl)trianiline (TTA), 1,3,5-tris(4-aminophenyl)benzene (TAPB), and 4,4',4''-triaminotriphenylamine (TAPA), respectively, under convenient solvothermal conditions (Scheme 3.1, See experimental details in Section 2.1). The crystal structures of these COFs were characterized by PXRD. As

shown in Figure 3.1, the PXRD patterns of all three COFs exhibit prominent diffraction peaks. Based on the 3-fold symmetry of both amine- and aldehyde-based building blocks and the linear imine linkages, 2D layered topology (P1 space group) with hexagonal aperture is proposed for modeling the possible COF structures. The Pawley refinement demonstrates the good fit of the eclipsed stacking mode (AA stacking) for all three COFs, and this assignment is further confirmed by the precise match of diffraction angles with experimental data as well as later discussed porous surface area. The optimized unit cell parameters were $a = 25.9793 \text{ \AA}$, $b = 24.6632 \text{ \AA}$, $c = 3.6264 \text{ \AA}$, $\alpha = \beta = 90^\circ$, $\gamma = 120^\circ$ for COF_{TTA-BTPA} with good residual factors ($R_{wp} = 2.76\%$ and $R_p = 1.83\%$); $a = 25.1799 \text{ \AA}$, $b = 25.4141 \text{ \AA}$, $c = 3.7322 \text{ \AA}$, $\alpha = \beta = 90^\circ$, $\gamma = 120^\circ$ for COF_{TAPB-BTPA} ($R_{wp} = 4.12\%$ and $R_p = 2.95\%$); $a = 22.9347 \text{ \AA}$, $b = 23.6126 \text{ \AA}$, $c = 4.1407 \text{ \AA}$, $\alpha = \beta = 90^\circ$, $\gamma = 120^\circ$ for COF_{TAPA-BTPA} ($R_{wp} = 4.61\%$ and $R_p = 3.53\%$). The peaks at 4.03° , 7.02° , 8.12° , 14.75° and 25.42° in the PXRD patterns for COF_{TTA-BTPA} are attributed to the diffraction characters of (100), (110), (200), (120), (220), and (001) facets, respectively (Figure 3.1a). Similarly, the diffraction peaks in the PXRD patterns of COF_{TAPB-BTPA} can be indexed as in Figure 3.1b. The diffraction peaks for COF_{TAPA-BTPA} also indexes with the refinement (Figure 3.1c), whereas the diffraction peaks significantly shift to higher angles due to the smaller size of TAPA compared to TTA/TAPB. These results conclude the successful synthesis of these highly ordered imine-linker 2D COFs. The lower crystallinity of COF_{TAPA-BTPA} compared to the two other COFs can be attributed to the inferior planarity of TAPA. Notably, COF_{TAPB-BTPA} shows higher crystallinity with remarkably stronger diffraction intensity and narrower full width at half maximum (FWHM) with respect to that of COF_{TTA-BTPA}, although TTA is more planar than TAPB.¹⁴⁷ Thus, balancing the planarity of building blocks seems to facilitate the formation of highly ordered 2D COFs.

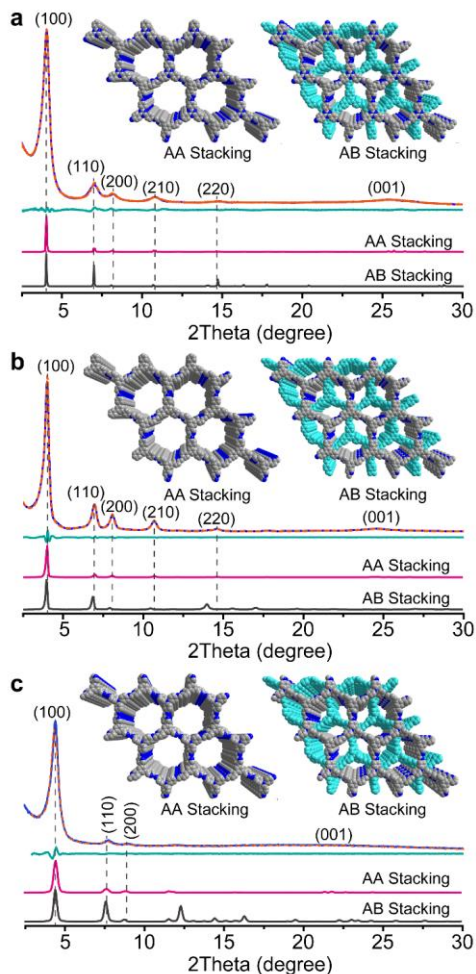


Figure 3.1 Experimental, refined, and simulated PXRD patterns of (a) $\text{COF}_{\text{TTA-BTPA}}$, (b) $\text{COF}_{\text{TAPB-BTPA}}$, and (c) $\text{COF}_{\text{TAPA-BTPA}}$. Inset represented the simulated eclipsed (AA) and staggered (AB) stacking models for the corresponding imine 2D COF.

The chemical structures of three imine-linked 2D COFs were characterized by Fourier transform infrared (FTIR) spectroscopy and solid-state ^{13}C NMR spectroscopy. As shown in Figure 3.2a, the characteristic FTIR peak at 1706 cm^{-1} is assigned to the typical $\text{C}=\text{O}$ stretching vibration mode of aldehyde groups in BTPA, and several sharp peaks around 3400 cm^{-1} are indexed as the N-H stretching vibration of amine building blocks. The disappear of those two kinds of peaks are accompanied by the emerging new peaks at $\sim 1620\text{ cm}^{-1}$ that can be attributed to the stretching mode of $\text{C}=\text{N}$ bonds, suggesting the formation of imine linkage in 2D COFs. COF formation is further supported by the characteristic peak at 159 ppm for $\text{COF}_{\text{TTA-BTPA}}$, 160 ppm for $\text{COF}_{\text{TAPB-BTPA}}$, and 155 ppm for $\text{COF}_{\text{TAPA-BTPA}}$ in the solid-state ^{13}C NMR spectra, respectively (Figure 3.2b), corresponding to the C of the imine bond.

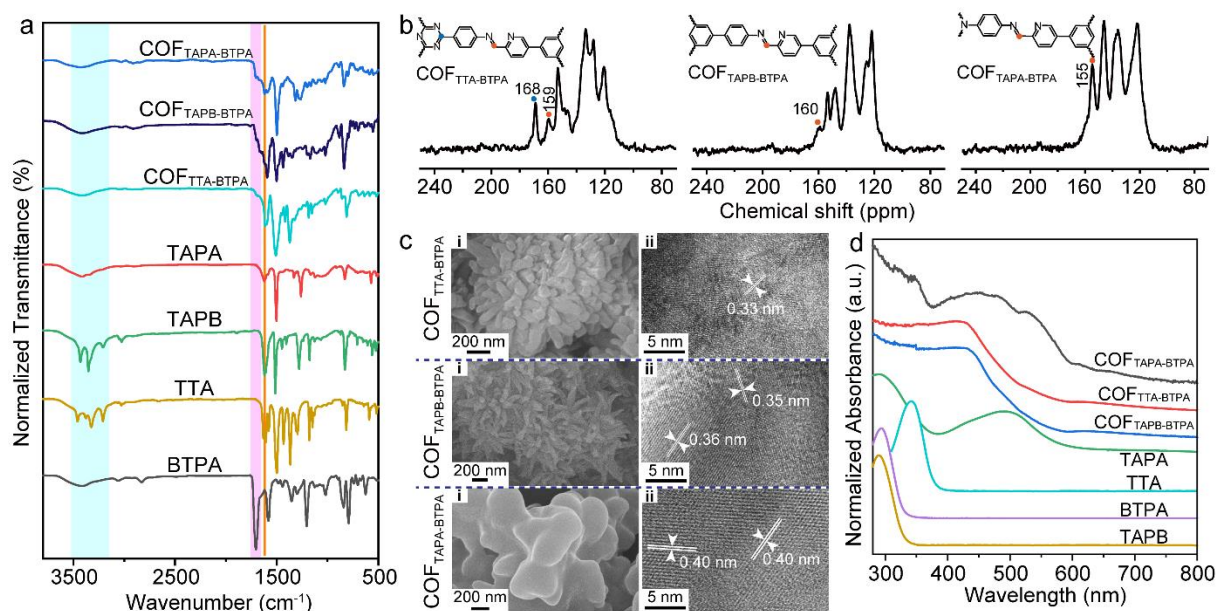


Figure 3.2 (a) FTIR spectra of COF_{TAPB-BTPA}, COF_{TTA-BTPA}, COF_{TAPA-BTPA}, and TAPA, TAPB, TTA, and BTPA; (b) solid-state ¹³C NMR spectra and (c) SEM (i) and high-resolution TEM (ii) images of COF_{TTA-BTPA}, COF_{TAPB-BTPA}, COF_{TAPA-BTPA}; (d) normalized diffuse reflectance spectra of COF_{TAPB-BTPA}, COF_{TTA-BTPA} and COF_{TAPA-BTPA} and UV-vis absorption spectra of their respective monomers measured in acetonitrile.

The morphologies of these COFs were recorded by scanning electron microscope (SEM). Both COF_{TTA-BTPA} and COF_{TAPB-BTPA} demonstrate aristate microparticles or micro-flakes consisting of flower-like nanosheets (Figure 3.2c, left panel). Well-defined lattice fringes for layered stacking are observed in transmission electron microscope (TEM) images with the distance of 3.3 Å for COF_{TTA-BTPA} and 3.6 Å for COF_{TAPB-BTPA}, respectively, confirming the highly ordered crystalline structure (Figure 3.2c, right panel). While COF_{TAPA-BTPA} appears as aggregates of irregular sheets and particles, the layered structures with the stacking distance of 4.0 Å are observed in the TEM image. These lattice distances are matched well with the (001) facets in the simulated models, which increases from COF_{TTA-BTPA} to COF_{TAPA-BTPA} due to the lower molecular planarity of the latter.

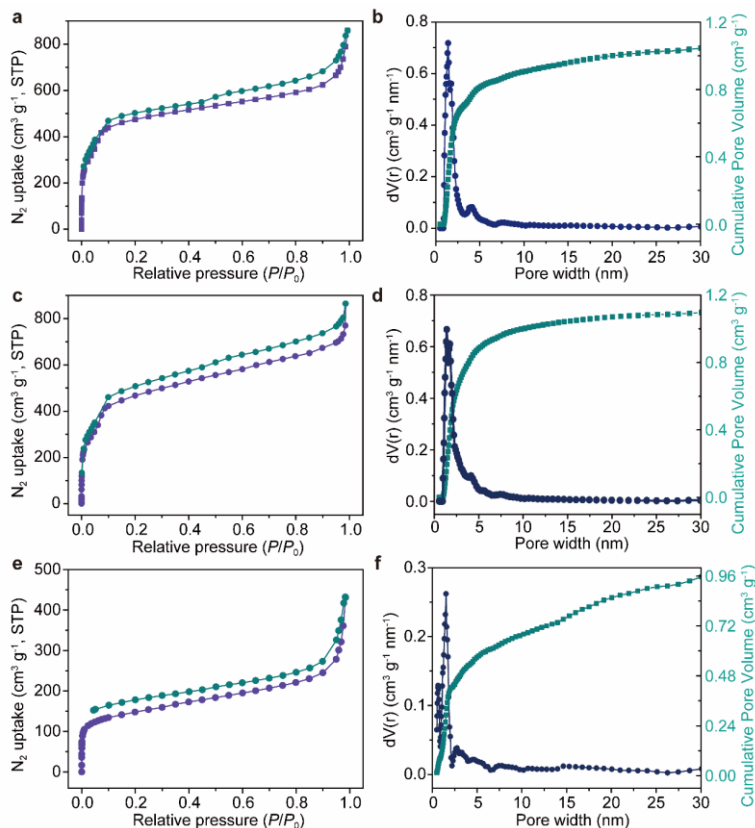


Figure 3.3 Nitrogen adsorption-desorption isotherms at 77 K, pore size distribution and cumulative pore volume for COF_{TTA-BTPA} (a, b), COF_{TAPB-BTPA} (c, d), and COF_{TAPA-BTPA} (e, f).

The porous structures of these COFs were investigated by nitrogen adsorption/desorption measurements at 77 K upon activation. All three COFs have the type I adsorption isotherms (Figure 3.3), implying the presence of micropores in these materials. The Brunauer–Emmett–Teller (BET) specific surface areas (SABET) are calculated to be 1842 m² g⁻¹ for COF_{TTA-BTPA} and 1463 m² g⁻¹ for COF_{TAPB-BTPA}. By using the nonlocal density functional theory (NLDFT) method, the pore sizes are evaluated as 1.75 nm for COF_{TTA-BTPA} and 1.77 nm for COF_{TAPB-BTPA}. The pore volumes are determined as 1.07 cm³ g⁻¹ for COF_{TTA-BTPA} and 1.11 cm³ g⁻¹ for COF_{TAPB-BTPA}. In contrast, COF_{TAPA-BTPA} demonstrates a pore size of 1.54 nm, comparable to the predicted value of 1.80 nm. A lower BET specific surface area (771 m² g⁻¹) and a smaller pore volume of 0.958 cm³ g⁻¹ are observed in the case of COF_{TAPA-BTPA} with respect to two other COFs due to the small domain size and structural defects of COF_{TAPA-BTPA} powders as revealed by relatively lower the lower PXRD intensity and broaden full width at half maximum of (100) diffraction peak.

To investigate the basic spectroscopic performance, the steady-state absorbance of $\text{COF}_{\text{TAPB-BTPA}}$, $\text{COF}_{\text{TAPA-BTPA}}$, and $\text{COF}_{\text{TTA-BTPA}}$ was measured using solid-state diffuse reflectance spectroscopy (Figure 2d). Each COF powder demonstrates significant visible light absorption with a trailing edge past 600 nm. Absorption maxima for all COFs are bathochromic compared with their monomers, which can be attributed to the extended π -conjugation of BTPA with TTA, TAPB, and TAPA. Particularly, $\text{COF}_{\text{TAPA-BTPA}}$ has the reddest peak maximum among the three, which is likely attributed to the strong donor nature of TAPA.

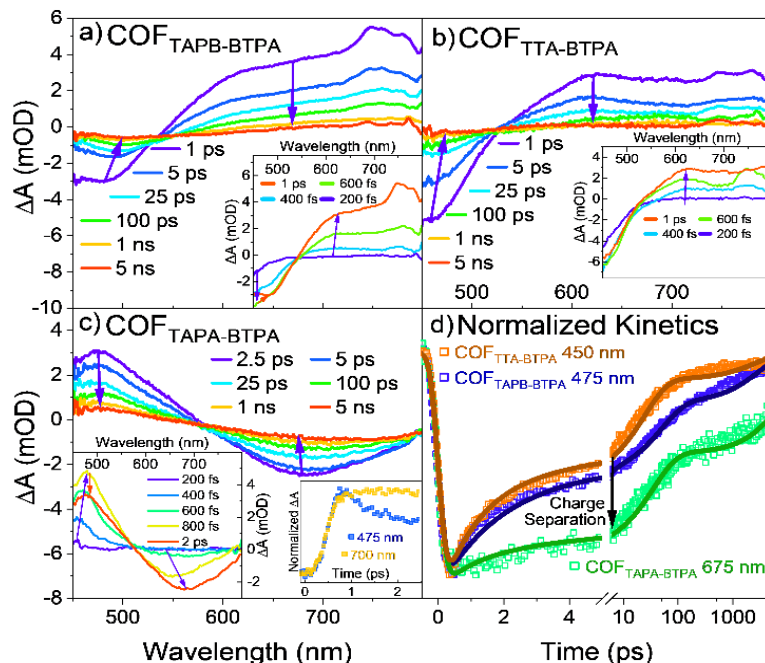


Figure 3.4 TA spectra of (a) $\text{COF}_{\text{TAPB-BTPA}}$, (b) $\text{COF}_{\text{TTA-BTPA}}$, and (c) $\text{COF}_{\text{TAPA-BTPA}}$ following 400 nm excitation. The early time spectra are shown in the insets. (d) The comparison of kinetic traces of TA spectra of $\text{COF}_{\text{TAPB-BTPA}}$, $\text{COF}_{\text{TTA-BTPA}}$, and $\text{COF}_{\text{TAPA-BTPA}}$ at the given wavelength.

3.3 Ultrafast Transient Absorption Spectroscopy of BTPA COFs

Femtosecond transient absorption (fs-TA) measurements were collected upon 400 nm excitation with thin-film samples formed by drop-casting onto a piranha etched glass slide. $\text{COF}_{\text{TAPB-BTPA}}$ (Figure 3.4a) displays an excited state absorption (ESA) at > 550 nm, which rises until 1 ps (inset of Figure 3.4a) and is completely quenched after 5 ns. The negative signal at < 550 nm reflects the inverse ground state diffuse reflectance spectrum (Figure 3.2d), leading to its assignment as ground state bleach (GSB). The positive ESA (> 550 nm) and negative GSB (< 550 nm) decayed concertedly with an isosbestic point at 480 nm, suggesting that they are related to the same relaxation process. The ESA spectral signature of $\text{COF}_{\text{TAPB-}}$

BTPA at 750 nm is somewhat similar in shape to ESA in the TA spectra of TAPB (Figure 3.5a, 3.5b), suggesting its origins from the TAPB portion of the framework.

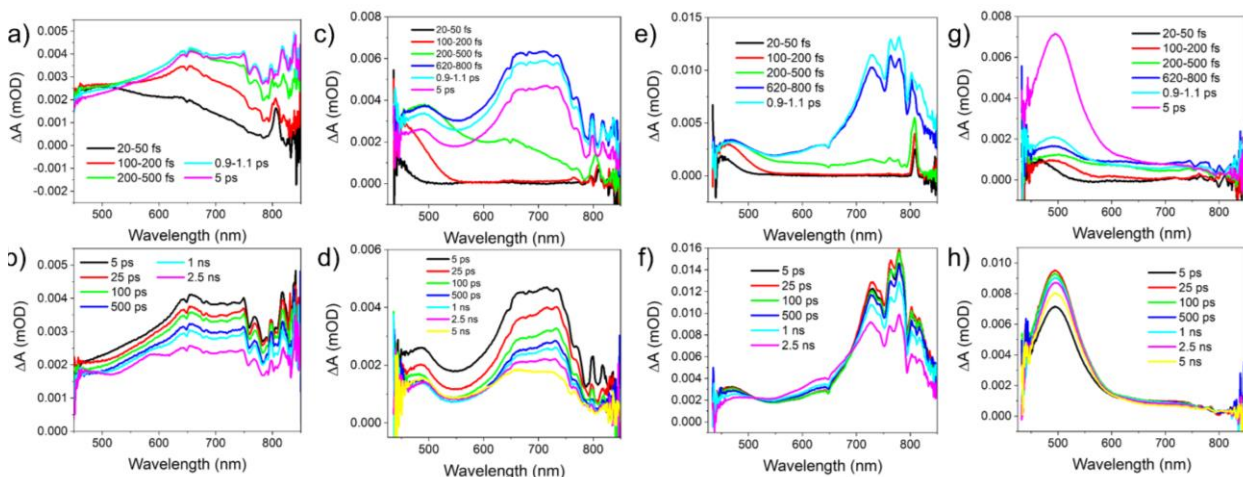


Figure 3.5 TA spectrum of TAPB at early time (a) and later time (b). TA spectrum of TTA at early time (c) and later time (d). TA spectrum of TAPA at early time (e) and later time (f). TA spectrum of BTPA at early time (g) and later time (h). All TA spectra collected after 400 nm excitation.

Optical signatures observed in the TA spectra of $\text{COF}_{\text{TTA-BTPA}}$ after 400 nm laser irradiation

(Figures 3.4b) are strikingly similar to those of $\text{COF}_{\text{TAPB-BTPA}}$. A 460 nm negative feature due to GSB is separated from the broad ESA by an isosbestic point around 550 nm which decays concertedly before 5 ns. Like $\text{COF}_{\text{TAPB-BTPA}}$, $\text{COF}_{\text{TTA-BTPA}}$ has an ESA spectral signature at 750 nm similar in shape to that of monomer TTA (Figure 3.5b, 3.5c), providing evidence for its emergence from the TTA portion of the COF structure.

Differences in ESA between $\text{COF}_{\text{TAPB-BTPA}}$ and $\text{COF}_{\text{TTA-BTPA}}$ and their constituent monomers can be explained based on what does – and doesn't – change because of connecting TAPB and TTA with BTPA. For instance, new π -conjugation is introduced between the COF monomers by imine π -bond formation that was not present prior; this leads to a 100 nm redshift of the 750 nm ESA spectral signatures for $\text{COF}_{\text{TTA-BTPA}}$ and $\text{COF}_{\text{TAPB-BTPA}}$ from monomeric TTA and TAPB, respectively. Continuing under the assumption that COF ESA redshifts ~ 100 nm from monomer ESA allows for the assignment of the 600 nm ESA peak in both $\text{COF}_{\text{TTA-BTPA}}$ and $\text{COF}_{\text{TAPB-BTPA}}$ to the BTPA portion of the framework (Figure 3.5g, 3.5h). We ascertain that π -conjugation formed in $\text{COF}_{\text{TAPB-BTPA}}$ and $\text{COF}_{\text{TTA-BTPA}}$ causes excited states to distribute closer in energy than in their respective monomers, causing the ESA redshift. This also indicates

only partial charge transfer (CT) between moieties with dissimilar electron affinities takes place as the excited state preserves ESA characteristics of both monomers.

In stark contrast to $\text{COF}_{\text{TAPB-BTPA}}$ and $\text{COF}_{\text{TTA-BTPA}}$, the TA spectra of $\text{COF}_{\text{TAPA-BTPA}}$ upon laser irradiation at 400 nm (Figure 3.4c) exhibits ESA at 475 nm, higher in energy than a negative signal at 675 nm and separated by an isosbestic point around 580 nm. Like $\text{COF}_{\text{TAPB-BTPA}}$ and $\text{COF}_{\text{TTA-BTPA}}$, the negative band in the TA spectrum can be attributed to GSB since the sample has absorption at these wavelengths (Figure 2d). In particular, the GSB above the 580 nm isosbestic point can be attributed to the hole localization on TAPA moieties of $\text{COF}_{\text{TAPA-BTPA}}$ since TAPA has significant steady-state absorption in this region. On the other hand, the ESA profile has very similar features to monomeric BTPA (Figure 3.5h), suggesting electron localization on the BTPA moiety in $\text{COF}_{\text{TAPA-BTPA}}$; but unlike $\text{COF}_{\text{TTA-BTPA}}$ and $\text{COF}_{\text{TAPB-BTPA}}$, $\text{COF}_{\text{TAPA-BTPA}}$ and monomeric BTPA have similarity in both shape and wavelength. This difference is rectified by considering the clear hole localization on TAPA units in $\text{COF}_{\text{TAPA-BTPA}}$, an indication of a much more pronounced CT with TAPA being oxidized (hole carrier, TAPA^+) and BTPA being reduced (electron carrier, BTPA^-). Thus, relatively well-separated charge carriers in $\text{COF}_{\text{TAPA-BTPA}}$ act somewhat independently of one another, causing ESA due to BTPA in $\text{COF}_{\text{TAPA-BTPA}}$ to resemble its monomeric form more closely than in $\text{COF}_{\text{TTA-BTPA}}$ and $\text{COF}_{\text{TAPB-BTPA}}$.

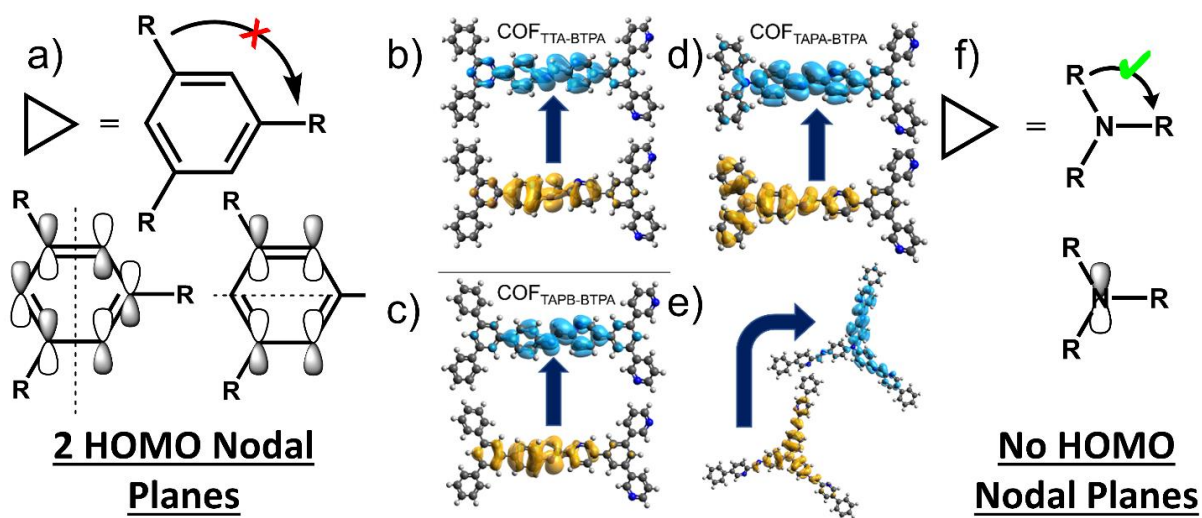


Figure 3.6 Diagram of nodal symmetry showing why exciton delocalization does not occur over symmetric six-member rings (a). Natural transition orbitals (CAM-B3LYP/6-311G**) of the S_1 transition of $\text{COF}_{\text{TTA-BTPA}}$ (b), $\text{COF}_{\text{TAPB-BTPA}}$ (c), and $\text{COF}_{\text{TAPA-BTPA}}$ (d). Due to delocalization across tertiary N in $\text{COF}_{\text{TAPA-BTPA}}$, the transition star fragment is shown (e). Isosurface values of the displayed orbitals are 0.02. Diagram for why exciton delocalization over tertiary N can occur (f).

The excited states of the three imine-linked COFs were further studied using time-dependent density functional theory (TDDFT) calculations (Figure 3.6). Natural transition orbitals (NTOs) of the S_1 transition on the edge fragments of $\text{COF}_{\text{TTA-BTPA}}$, $\text{COF}_{\text{TAPB-BTPA}}$, and $\text{COF}_{\text{TAPA-BTPA}}$ provide support for more complete CT in $\text{COF}_{\text{TAPA-BTPA}}$ compared to $\text{COF}_{\text{TTA-BTPA}}$ and $\text{COF}_{\text{TAPB-BTPA}}$, which helps explain the difference between the transient spectral features. In both $\text{COF}_{\text{TTA-BTPA}}$ and $\text{COF}_{\text{TAPB-BTPA}}$, the excitation is confined to the fragment between the central BTPA and TTA/TAPB rings, providing evidence that the meta substitution pattern prevents further delocalization (Figures 3.6a, 3.6e). In contrast, the excitation involves all the phenyl rings of the TAPA fragment (Figure 3.6d) shown by NTOs of $\text{COF}_{\text{TAPA-BTPA}}$ having greater hole delocalization in comparison to $\text{COF}_{\text{TTA-BTPA}}$ and $\text{COF}_{\text{TAPB-BTPA}}$. This can be more clearly seen from the star-shaped fragment (Figure 3.6e) illustrating the symmetry-breaking nature of the CT around the tertiary nitrogen in the TAPA portion of the COF.

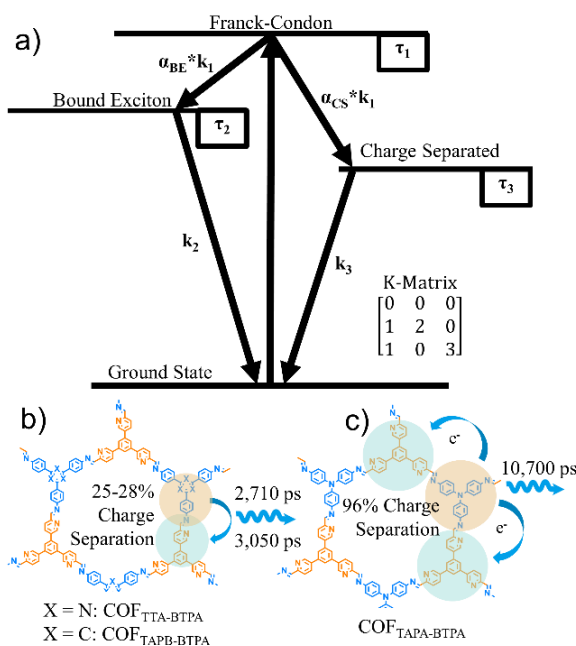


Figure 3.7 (a) Three-compartment model used for global target analysis and the K-matrix by which the model is defined. Diagonal elements represent those states decaying back to the ground state, off-diagonal elements represent the column index decaying to the row index state. (b) Schematic showing the excited state dynamics of $\text{COF}_{\text{TTA-BTPA}}$ and $\text{COF}_{\text{TAPB-BTPA}}$. (c) Schematic showing the excited state dynamics of $\text{COF}_{\text{TAPA-BTPA}}$.

Table 3.1 Exciton lifetimes of COF_{TTA-BTPA}, COF_{TAPB-BTPA}, and COF_{TAPA-BTPA}, where τ_1 represents the lifetime of the FC state as a weighted average of the decay rate to BE and CS, where α_{BE} and α_{CS} represent the weighting coefficients, respectively. These two FC decay rates were combined otherwise they would be too close to be meaningfully separated. τ_2 and τ_3 represent the average lifetime of BE and CS before returning to the GS, respectively.

	τ_1 (ps)	α_{BE}	τ_2 (ps)	α_{CS}	τ_3 (ps)
COF _{TTA-BTPA}	1.23 ± 0.01	75%	24.1 ± 0.11	25%	2710 ± 30
COF _{TAPB-BTPA}	1.92 ± 0.01	72%	49.4 ± 0.23	28%	3050 ± 20
COF _{TAPA-BTPA}	1.27 ± 0.01	4%	35.0 ± 0.24	96%	10700 ± 100

This assignment is further supported by the comparison of GSB recovery kinetics or ESA decay (Figure 3.4d), where the rate for COF_{TAPA-BTPA} is much slower than in COF_{TTA-BTPA} and COF_{TAPB-BTPA} due to better charge separation. Kinetic traces of the excited state decay are normalized to the maximum intensities and analyzed using global target analysis in Glotaran.¹²¹ For global target analysis a three-compartment model (Figure 3.7) was used in which the initial Franck-Condon (FC) state splits into two lower energy excited states that each return to the ground state – a bound excitonic (BE) state where the exciton is trapped, localizing on a single edge of the COF; and a charge separated (CS) state where electron and hole, either by intra- or interlayer CT, reside on separate edges that increases their exciton radius, reduces their coulombic attraction, and prolongs their persistence in the excited state. As summarized in Table 3.1, the FC lifetime, τ_1 , was determined by letting FC relaxation to both BE and CS share a rate constant and optimizing the proportion of that rate resulting from FC→BE relaxation and FC→CS relaxation, respectively. This method was necessary since treating these processes separately led to similar rate constants that could not be meaningfully separated, and forms τ_1 as a weighted average of the FC→BE rate and FC→CS rate with α_{BE} representing the weighting coefficient of FC→BE, and α_{CS} representing the weighting coefficient of FC→CS. In COF_{TAPA-BTPA} decay to the longer-lived CS state was found to comprise 96% of the τ_1 lifetime, but only 28% and 25% in COF_{TAPB-BTPA} and COF_{TTA-BTPA}, respectively. We propose that the initial excited state with the shortest lifetime (τ_1) corresponds to the TA rising component and is attributable to the FC state before nuclear rearrangement. From FC the exciton can either become trapped into a BE state with intermediate recombination lifetime (τ_2) or separate into a CS state with longer recombination lifetime (τ_3).

Notably, τ_1 is greatest for COF_{TAPB-BTPA} whereas COF_{TAPA-TAPA} and COF_{TTA-BTPA} have similar lifetimes. In COF_{TAPA-BTPA} this is because FC relaxation is dominated by FC \rightarrow CS (96%) that occurs more rapidly than FC \rightarrow BE (4%) due to FC possessing CS-like characteristics as predicted by TDDFT (Figure 3.6d). COF_{TTA-BTPA}, on the other hand, primarily undergoes rapid exciton trapping (75%) due to its FC possessing relatively poor, edge-confined intralayer CT resulting from the electron withdrawing, meta substituted triazine unit. This exciton trapping, however, is similarly prevalent in COF_{TAPB-BTPA} (72%) and cannot completely account for the τ_1 difference with COF_{TTA-BTPA}, leading to the interpretation that CS must also occur more slowly in COF_{TAPB-BTPA}, which is possibly related to its longer interlayer distance and subsequently sluggish interlayer CT. Altogether, we summarize our findings with a pictorial model illustrated in Figures 3.8b and 3.8c. Upon photoexcitation, little CS occurs between TTA and BTPA in COF_{TTA-BTPA} or TAPB and BTPA in COF_{TAPB-BTPA}, which is supported by the similar ESA in TA spectra of the COFs and their corresponding monomers. In contrast, prominent CS from TAPA to BTPA unit was observed in COF_{TAPA-BTPA} (Figure 3.8c), which is reflected by the much longer-lived ESA/GSB in TA spectra due to a well-separated CT state and retarded charge recombination. These experimental results are well supported by TDDFT calculations, which show that the excitation is confined to the portion of the fragment that is between the central BTPA and TTA/TAPB rings in COF_{TTA-BTPA} and COF_{TAPB-BTPA} but delocalized in COF_{TAPA-BTPA}.

Table 3.2 Charge transfer characteristics from analysis of the transition density matrices of COFs.

COF	CTC	EHSR	RMS _{eh} (Å)	ES Dipole (D)	GS Dipole (D)
COF _{TTA-BTPA}	0.625	0.913	4.219	5.0	2.5
COF _{TAPB-BTPA}	0.662	0.938	4.620	10.1	2.6
COF _{TAPA-BTPA}	0.660	0.932	5.726	14.1	2.9

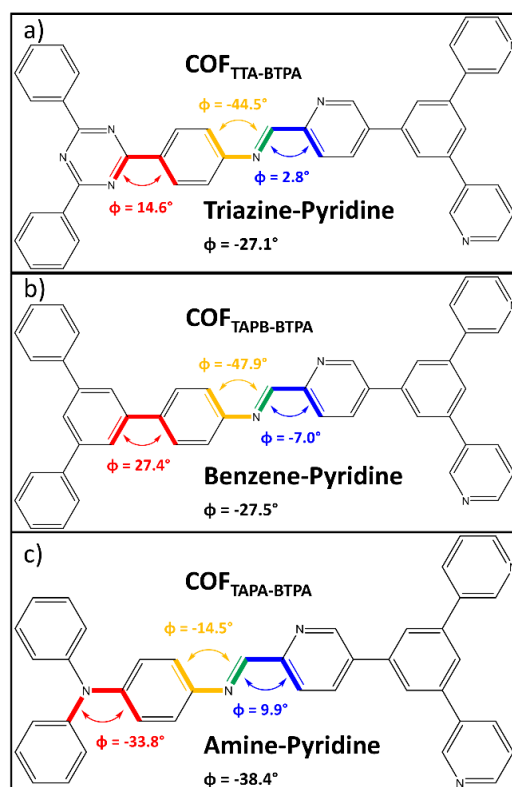


Figure 3.8 Representative dihedral angles for structures used in TDDFT of (a) COFTTA-BTPA, (b) COFTAPB-BTPA, and (c) COFTAPA-BTPA.

The trend observed in τ_1 FC lifetimes is consistent with τ_2 BE lifetimes, suggesting that BE persistence is related to intralayer CT characteristics. Surprisingly, COF_{TAPB-BTPA} has the longest-lived BE state, which implies it has more favorable intralayer CT characteristics than COF_{TAPA-BTPA}. Analysis of the TDM (Table 3.2) supports this interpretation, revealing that the same tertiary nitrogen that allows efficient charge separation also allows its adjacent phenylene to have relatively large dihedral angles (Figure 3.8), likely preventing a more complete intralayer CT in the BE state. Finally, τ_3 CS lifetimes in COF_{TAPA-BTPA} are much longer-lived, implying the redox species (TAPA⁺ and BTPA⁻) are well separated compared with those in COF_{TAPB-BTPA} and COF_{TTA-BTPA}. With evidence from TA and TDDFT (Figure 4c, bottom) we conclude that the tertiary nitrogen in COF_{TAPA-BTPA} instead of a meta substituted aromatic ring in COF_{TAPB-BTPA} or COF_{TTA-BTPA} is responsible for greater charge separation capabilities that ultimately prolong the excited state lifetime.

3.4 Conclusions

In summary, we designed and synthesized three imine-linked 2D COFs, and systematically investigated their photophysical properties and excited-state dynamics using steady-state absorption and femtosecond TA spectroscopy associated with TDDFT calculations. Excited state dynamics studied by TA spectroscopy and TDDFT calculations provided information on the charge transfer and separation processes of the 2D COF structures, where the excited CT state of COF_{TAPA-BTPA} is much longer lived than that of COF_{TTA-BTPA} and COF_{TAPB-BTPA}. The charge carriers on COF_{TAPA-BTPA} are generated freely across multiple edges that lead to a relatively sustained charge-separated state, whereas confinement of charge carriers on a single edge of COF_{TTA-BTPA} and COF_{TAPB-BTPA}. COF_{TAPA-BTPA} generated a pronounced CT state due to the extended π -conjugation and greater delocalization radius in COF_{TAPA-BTPA} with tertiary N instead of a meta-substituted aromatic ring. Our work paves the way for the rational design of fully conjugated 2D COFs with long-lived charge carriers for advanced organic optoelectronics and photochemistry, such as highly efficient organic light-emitter, photovoltaics, fluorescent bioimaging agents, and photocatalysts.

In the context of topological symmetry this work looks at the concept of band structures from a molecular orbital point of view and finds that the manifestation of destructive wavefunction interference is that excitons cannot delocalize across symmetric six membered rings. While other properties, like electron affinity, certainly play a role in excited state charge separation, or photophysical kinetic model shows that charge separation is enhanced in the COF with a tertiary amine node.

CHAPTER 4 – IMPACT OF π -CONJUGATION LENGTH ON THE EXCITED-STATE DYNAMICS OF STAR SHAPED CARBAZOLE- π -TRIAZINE ORGANIC CHROMOPHORES

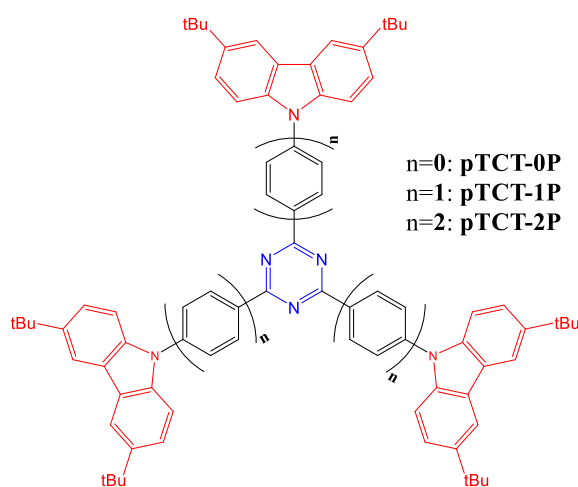
4.1 Introduction

Donor-bridge-acceptor (DBA) molecules have attracted research due to their potential utility as photocatalysts,^{148,149} photovoltaics,^{150,151} organic light emitting diodes (OLED),^{152,153} and thin-film transistors.¹⁵⁴ An interesting variation of DBA molecules have a star-shaped structure with donor groups attached around an aromatic core.^{155–159} While COFs have interesting photophysical properties it can be difficult to study their photophysical properties in depth due to their insolubility. Thus, it can be advantageous to study model systems like star-shaped organic molecules that resemble structural motifs present in COFs.

One particularly interesting star-shaped DBA system consists of an s-triazine acceptor surrounded by phenylene bridges, and 3,6-di-tert-butyl-carbazole donors which we denote the pTCT series. It has been previously shown that the key property dictating the photophysics of such pTCT molecules in photocatalysis¹⁶⁰ and optoelectronics^{161,162} is the presence of singlet intramolecular charge transfer (¹ICT) states preceding intersystem crossing (ISC) to ³ICT. When ¹ICT states have low lying energies, they can approach ³ICT energy levels, increasing the probability of ISC. Indeed, the use of triplet states in pTCT polymers have been used for ¹O₂ photogeneration,¹⁴⁸ which is directly related to triplet state formation, follows the trend of pTCT-0P > pTCT-1P > pTCT-2P. pTCT molecules have also been shown to display thermally-activated delayed fluorescence (TADF),¹⁶³ and that using a meta phenylene bridge drastically increases TADF versus a para phenylene bridge in pTCT-1P. Increased TADF in pTCT-1P was attributed to the constitutional isomers having either comparable or separated ¹ICT and ³ICT energy levels that strongly influence TADF.¹⁶³ Other works have also suggested that ICT is considerably affected by other structural characteristics of the molecule such as the length of the π -conjugated bridge,^{164,165} and the donor-acceptor (D-A) dihedral angle.^{166,167} These studies not only demonstrated the important roles ICT states play in photophysics of pTCT series but also their strong structural dependence, suggesting the necessity to develop a direct correlation of the ICT properties with molecular structure.

In this work, we report fundamental studies on ultrafast excited state (ES) dynamics of pTCT molecules with para phenylene bridges of different lengths (pTCT-0P, pTCT-1P, pTCT-2P, Scheme 1). By

using the combination of steady-state and transient absorption (TA) spectroscopy as well as computational modeling, we establish correlations between bridge length, structural conformation, ICT, and ISC. We show that pTCT-1P has favorable ISC characteristics in comparison to pTCT-0P and pTCT-2P that arise due to structural differences in the singlet manifold of the molecules. Insights generated from this work will help design next generation photoelectronic, photocatalytic, and OLED devices by providing a fundamental understanding of the photophysics possessed by star-shaped DBA type molecules.



Scheme 4.1 Star-Shaped DBA Molecules of the pTCT Series.

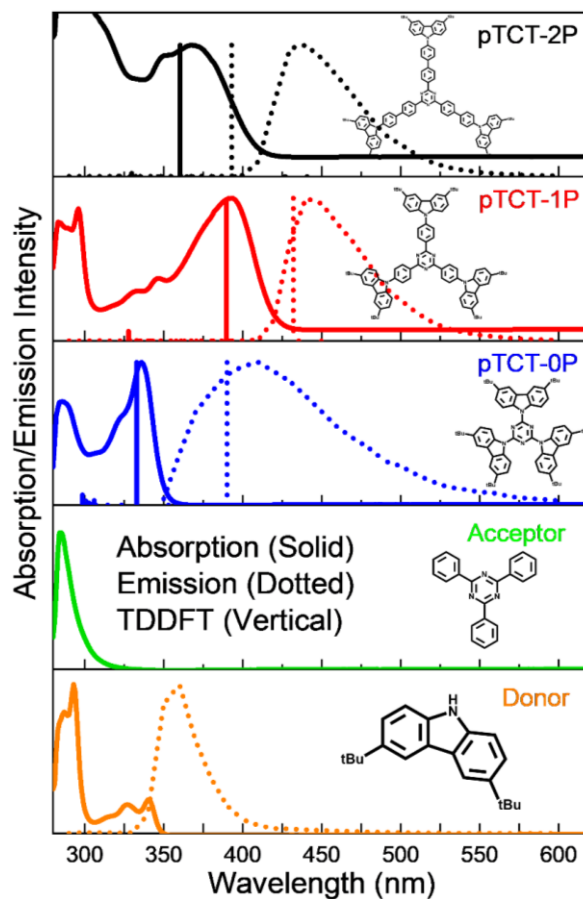


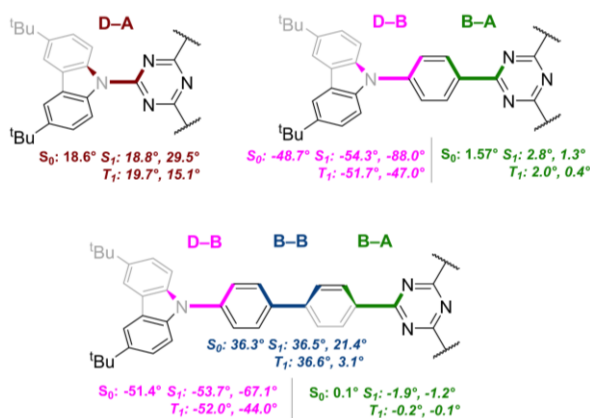
Figure 4.1 pTCT Series experimental absorption (solid line), emission (dotted line), and theoretical absorption (vertical line) with triazine absorption, and carbazole absorption & emission in toluene.

4.2 Steady State Spectroscopic Properties of pTCT Series

Figure 4.1 shows the steady state experimental, and theoretical (vertical lines) absorption (solid lines) and emission (dotted lines) of pTCT molecules as well as the triazine acceptor, and carbazole (3,6-di-tert-butyl-9-phenyl-9H-carbazole) donor. All spectra share a common absorption peak at ~280 nm that is thus attributed, in the pTCT molecules, to local excitation (LE) of the donor and acceptor units. An additional band (> 300 nm) in the pTCT molecules is attributed to intramolecular CT (ICT) from carbazole donor to triazine acceptor. This band is observed at 370 nm in pTCT-2P, 395 nm in pTCT-1P, and 340 nm in pTCT-0P. Evidently, the bathochromic shift of the ICT band from 340 nm in pTCT-0P to 395 nm in pTCT-1P must result from the phenylene bridges between the donor and acceptor.¹⁶⁸ However, since the absorption peak of pTCT-2P appears at shorter wavelength (370 nm) than pTCT-1P (395 nm), the spectral

trend is not directly related to the number of phenylene units. Because these trends are also observed in TDDFT absorption (Figure 4.1, solid vertical lines) – which highlights the validity of the computational model – key insights about the relationship between structure and photophysical properties can be drawn from the theoretical calculations.

4.3 Theoretical Relaxation Dynamics of pTCT Series



Scheme 4.2 Relevant dihedral angles for pTCT molecules at ground state (GS), S₁, and T₁ geometries calculated from DFT and TDDFT.

Comparing predicted transitions relative to GS/S₀ geometries (Scheme 4.2) provides evidence that D-B-A orthogonality, as measured by dihedral angles,^{167,169–171} significantly influences ICT. Structural optimization of pTCT-0P finds a GS stationary point with relatively small D-A dihedral (18.6°). From this geometry, LRC- ω PBE accurately predicts the ICT transition energy (3.67 eV) to be highest among pTCT molecules. In contrast, pTCT-2P has a lower ICT transition energy (3.57 eV) despite a smaller D-A dihedral (-15.0°), suggesting the long D-A distance and twisted D-B-A arrangement (Type-II¹⁷²) introduces D-B, B-B, and B-A orthogonality that each affect ICT. Finally, pTCT-1P has the lowest ICT transition energy (3.27 eV) and the largest D-A dihedral (-47.1°, b-Type¹⁷²). Altogether, these results indicate D-A orthogonality has a large influence on ICT, but the bridge also plays an important role.

Table 4.1 Charge transfer characteristics at S₀ and S₁ geometries for the pTCT series of molecules at the LRC- ω PBE/6-311G** level of theory.

Sample	pTCT-0P	pTCT-1P	pTCT-2P

Geometry	S0	S1	S0	S1	S0	S1
CTC	0.73	0.95	0.90	0.96	0.88	0.89
EHSR	0.97	0.94	0.83	0.88	0.69	0.89
RMS _{eh}	5.1 Å	6.4 Å	7.3 Å	7.1 Å	8.5 Å	8.0 Å

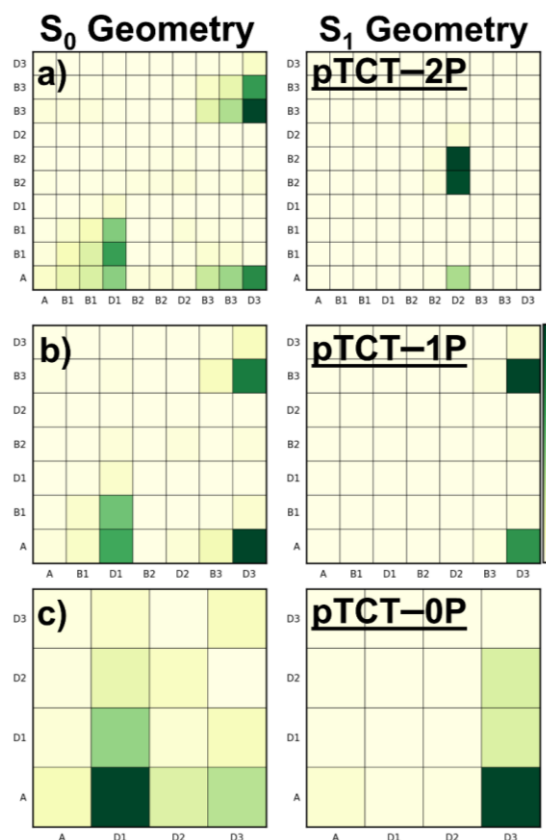


Figure 4.2 Electron-hole correlation plots at S_0 and S_1 geometries of (a) pTCT-0P, (b) pTCT-1P, and (c) pTCT-2P. Values of each matrix are normalized to largest value. Color bar is shown on the right. Cell labels are as follows: A=Acceptor, B=Bridge, D=Donor. Diagonal (lower-left to upper-right).

Based on the assignment of ICT in the steady-state absorption spectra, it is beneficial to quantify the amount of ICT to develop an understanding of ES populations. Transition density matrix (TDM) analysis (Table 4.1) shows that the S_0 ICT character (CTC) has an inverse relationship with transition energy. pTCT-0P has the smallest degree of CTC due to the adjacency of its D-A units, followed by pTCT-2P, and finally pTCT-1P. Interestingly, the S_0 e^-/h^+ separation ratio¹⁷³ (EHSR) in pTCT-0P approaches

unity, suggesting its charge carriers are well separated from one another. The contradiction of high EHSR and low CTC is rectified by observing the GS e^-/h^+ correlation plot (Figure 4.2, left) that shows while interbranch interactions are present to a miniscule degree in the larger pTCT molecules (Figure 2a, 2b), the donor branches interact through space significantly in pTCT-0P; an important feature that is observable in the intensity of off-diagonal elements corresponding to high EHSR, and that may also facilitate ISC by lowering the S_1/T_1 energy difference.¹⁷⁴ Nonetheless, TDM analysis confirms the population of ICT states from the S_0 of pTCT molecules and quantifies their behavior.

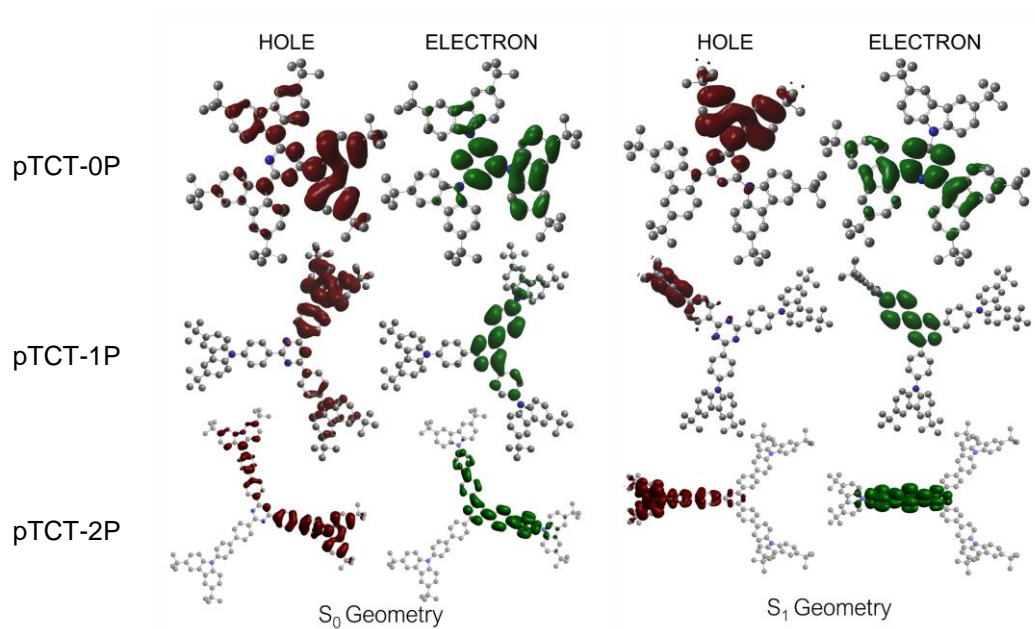


Figure 4.3 Natural transition orbitals of pTCT series molecules at their GS & S_1 geometries. Isosurface values are 0.02. Hydrogens removed for clarity.

Better understanding of the ICT population at the S_0 geometry can be gained by inspection of the natural transition orbitals (NTOs, Figure 4.3). For instance, all the pTCT molecules show varying degrees of ICT mixed with $\pi\pi^*$ character. This $\pi\pi^*$ mixing is likely responsible for the oscillator strength of the S_0 ICT transition, and indicates the excitation is not pure CT. Looking at pTCT-0P, the hole and electron orbitals overlap considerably, a result of the relatively small donor-acceptor dihedral, indicating the transition has small ICT character. Conversely, pTCT-1P has a visible disjunctive union between hole and electron orbitals on the donor and acceptor units, respectively, indicating the transition possesses high ICT character – in agreement with TDM analysis (Table 4.1) above. For pTCT-2P it can be clearly seen the

impact of the phenylene bridge units that have a large overlap between the electron and hole orbitals. Combined with the e^-/h^+ correlation plot (Figure 4.2a, left) this overlap suggests the donor makes its donation into the bridge, rather than directly into the acceptor. The S_0 ICT transition is the starting point for ES relaxation because it precedes structural relaxation to the minimum of the S_1 potential from which emission and ISC can occur.

The emission spectra of pTCT molecules at 340 nm (Figure 4.1, dotted lines) excitation show a Stokes shift that follows the trend of S_0 ICT transition energy; pTCT-1P shows the smallest redshift (0.32 eV), followed by pTCT-2P (0.53 eV), and finally pTCT-0P (0.60 eV). This trend is accurately reproduced for the smaller pTCT molecules by LRC- ω PBE transitions at the B3LYP S_1 geometry; pTCT-1P emission is predicted to Stokes shift 0.31 eV, followed by pTCT-0P with a 0.55 eV shift. pTCT-2P on the other hand is predicted to Stokes shift only 0.29 eV implying its long-range ICT behavior is incorrectly modeled with the B3LYP functional. Using CAM-B3LYP for S_1 optimization instead dramatically improves the Stokes shift of pTCT-2P (0.59 eV) but fails in the other two cases – 1.57 eV for pTCT-0P, 0.26 eV for pTCT-1P – leading to our decision to focus our discussion on the results obtained with B3LYP S_1 and T_1 geometries. Structurally, relaxation along the S_1 potential leads to conformational rearrangement of a single branch for each molecule of the pTCT series (Scheme 4.2). This “active branch” on the pTCT-0P S_1 potential undergoes rather small D-A orthogonalization to 29.5° while pTCT-1P relaxes -39.6° to -86.7° , and pTCT-2P changes by -31.9° to -46.9° . This orthogonalization affects delocalization between donor, bridge and acceptor moieties that correspond with ICT/ $\pi\pi^*$ transition mixing which in turn can affect D-A and spin-orbit coupling (SOC).

TDM analysis (Table 4.1) of the S_1 geometries reveal CTC grows for each entry of the pTCT series to varying degrees. pTCT-1P, like in the S_0 , still possesses the most CTC but is closely followed by pTCT-0P which undergoes a large CTC increase. Apart from CTC, other TDM quantities follow divergent patterns between pTCT-0P and the larger pTCT molecules. Notably, EHSR of pTCT-0P decreases at S_1 whereas the EHSR of pTCT-1P and pTCT-2P increases. These trends are inverted in RMSeh which grows in pTCT-0P but shrinks in pTCT-1P and pTCT-2P. The TDM results can be interpreted alongside the e^-/h^+ correlation matrix (Figure 4.2) to reveal that upon D-A orthogonalization the interbranch interactions in pTCT-0P are interrupted such that the active branch begins direct donation into inactive branches. This

causes RMSeh to increase due to the electron centroid moving towards those inactive branches, and EHSR to decrease due to less interbranch electron exchange. For pTCT-1P and pTCT-2P, D-A orthogonalization seems to isolate the transition from multiple branches in the S_0 to solely the active branch at S_1 . Now, with a clear picture of the ICT characteristics of the pTCT molecules in place the ES dynamics of the system can be unraveled.

4.4 Excited State Dynamics of pTCT series

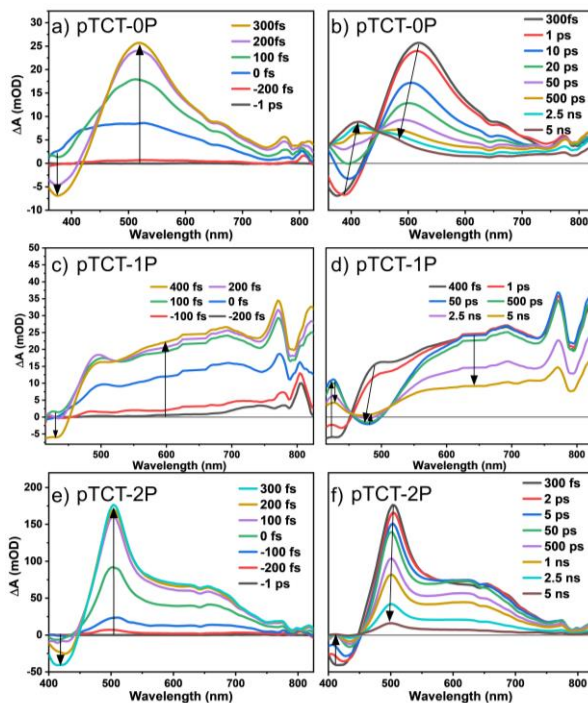
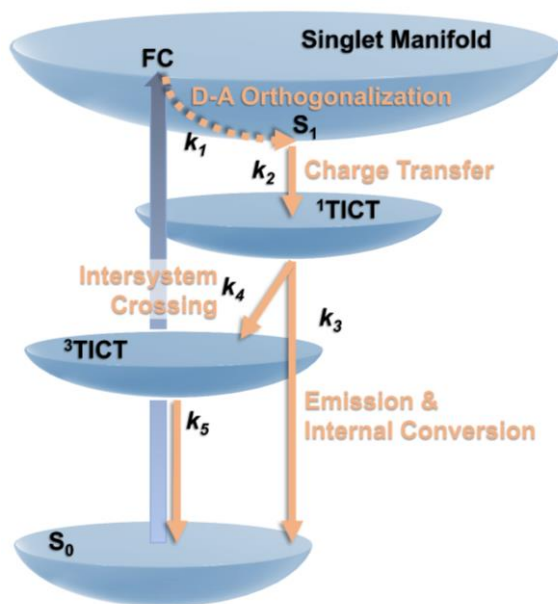


Figure 4.4 Transient absorption spectra of pTCT-0P following 340 nm excitation in toluene at early (a) and late time (b), pTCT-1P following 370 nm excitation in toluene at early (c) and late time (d), and pTCT-2P following 340 nm excitation in toluene at early (e) and late time (f). Chirp correction and 5 point adjacent averaging was performed.

To gain further insight on the impact of the bridge length on photophysical properties of the pTCT series, we examined the ES dynamics using TA spectroscopy following excitation of their respective ICT bands. As shown in Figure 3a, the TA spectra of pTCT-0P shows a rapidly rising broad band and negative feature in the spectral window at early time (< 0.5 ps, Figure 4.4a), featured by strong ES absorption (ESA) centered at 525 nm, a negative feature at 400 nm, and weaker ESA > 700 nm. After that, the ESA at 525 nm decays much faster than ESA > 700 nm (Figure 4.4b), resulting in distinct spectral features with more

persistent absorption > 700 nm than at 550 nm. The negative feature at 400 nm gives rise to a positive feature and displays a clear isosbestic point at 450 nm. The energetic diagram in Scheme 4.3 depicts the spectral evolution of the ES transients. Initial excitation promotes the system from its ground state (S_0) to its Franck-Condon (FC) state which quickly relaxes (k_1) to the bottom of the singlet manifold, undergoing a conformational twist along the way corresponding to the rapid early time rising component in Figure 3a. The donor and acceptor, now somewhat orthogonalized, undergo ICT (k_2) leading to a twisted ICT state ($^1\text{TICT}$) from which multiple deactivation pathways are available. Non-luminescent internal conversion or fluorescent recombination of the electron/hole pair returns the system directly to the ground state, or alternatively ISC can occur from $^1\text{TICT}$ to $^3\text{TICT}$ (k_4), which is followed by prolonged conversion from $^3\text{TICT}$ to S_0 (k_5), corresponding to the spectral evolution in Figure 4.4b.



Scheme 4.3 Photophysical model used to perform global target fitting on the pTCT series of molecules. Initial excitation is followed by a quick relaxation (0.2 – 1.2 ps) to the bottom of the singlet manifold. Relaxation causes donor-acceptor orthogonalization that precedes ICT (4 – 14 ps). From the ICT state relaxation back to the GS or ISC (1800 – 4100 ps) can take place. Finally, the triplet state will eventually undergo relaxation back to the GS (> 1 μs).

A single phenylene bridge between donor and acceptor moieties significantly changes the spectral features although similar relaxation dynamics are observed. As shown in Figure 4.4c, the TA spectra of pTCT-1P following 370 nm excitation shows the rapid formation of a broad absorption above 450 nm at

early time (< 0.6 ps), and a negative feature at 425 nm which can be assigned to the ultrafast relaxation from initially excited FC state to S_1 (k_1). After that, ICT occurs (S_1 to $^1\text{TICT}$), which is featured by the prominent decay at 475 nm to form a negative feature at the same region, the growth of a positive feature at 425 nm, and the decay of a portion of the positive feature at > 650 nm (~ 1 ps – 100 ps, Figure 4.4c).^{175,176} Because the GS of pTCT-1P has negligible absorption at 475 nm (Figure 4.1b), we attribute the observed negative feature in TA spectra to the stimulated emission (SE) of pTCT-1P, which is consistent with the emission spectrum of pTCT-1P shown in Figure 1b. The growth of the 425 nm ESA peak and 475 nm SE clearly show an isosbestic point at 450 nm. The growth and subsequent decay of the 425 nm ESA and 475 nm SE clearly show an isosbestic point that can be assigned to the formation of $^3\text{TICT}$. The formation of SE (k_3) accompanies the growth of $^3\text{TICT}$ absorption (k_4), which is consistent with our assignment earlier that multiple deactivation pathways from $^1\text{TICT}$ exist. The system then eventually relaxes from $^3\text{TICT}$ to S_0 (k_5) outside the time window of our instrument.

Like the TA spectra of pTCT-0P and pTCT-1P, the TA spectra of pTCT-2P (Figure 4.4e), where the donor and acceptor moieties are separated by two phenylene bridges, show the rapid formation of a broad absorption above 450 nm (< 0.3 ps) with a strong band centered at ~ 500 nm, a negative feature at 425 nm, and a weak but broad ESA centered at 650 nm. After that, ESA at 500 nm decays, accompanied by subtle spectral evolution of the broad ESA from 650 nm center to 625 nm center, corresponding to ISC from $^1\text{TICT}$ to $^3\text{TICT}$ which decays afterwards to S_0 .

4.5 Prediction of ISC Rates for pTCT Series Molecules

A key utility of the LRC- ω PBE functional is the prediction accuracy for singlet and triplet excitation energies. The difference between singlet and triplet energies, ΔE_{ST} , can thus be reliably calculated and used to find the free energy change of ISC. In the Arrhenius-type model used for modeling ISC rates (Equation 2)¹⁷⁷ the reorganization energy, λ , is related to the energy barrier overcome during ISC, and spin-orbit coupling matrix elements (SOCME, \hat{H}_{SO}) represent the connection between singlet and triplet manifolds based on changes in angular momentum necessary to accompany spin-flip. In our model we reduce λ to the state energy difference of T_1 at the S_1 geometry and the final T_1 geometry. ΔG (Equation 4.2), the change in free energy which drives the ISC process, is a crucial component in the estimation of ISC rates (Equation 4.1)¹⁷⁷. pTCT-0P has the highest ΔG of 0.025 eV due to its large λ of 1.12 eV from its

S₁ geometry to its T₁ geometry while pTCT-1P and pTCT-2P have ΔG of 0.0031 eV and 0.014 eV, and λ of 0.52 eV and 0.78 eV, respectively.

$$k_{ISC} = \frac{1}{h} \sqrt{\frac{\pi}{\lambda k_B T}} e^{\frac{-\Delta G}{RT}} |\langle S_1 | \hat{H}_{SO} | T_1 \rangle|^2 \quad (4.1)$$

$$\Delta G = \frac{\left((\Delta E_{S_1-T_1}) - \lambda \right)^2}{4\lambda} \quad (4.2)$$

Overall, of the ISC rates for the pTCT series (Table 4.2) pTCT-1P is predicted to have the fastest with $5.2 \times 10^7 \text{ s}^{-1}$ which is about 2.5 times faster than that of pTCT-0P with an ISC rate of $2.1 \times 10^7 \text{ s}^{-1}$, and 1.7 times faster than pTCT-2P with an ISC rate of $3.1 \times 10^7 \text{ s}^{-1}$. To determine the precision and accuracy of these rates predictions will need to be cross-referenced against a global target fitting model.

Table 4.2 ISC parameters for the pTCT series at the LRC- ω PBE/6-311G** level of theory.

Sample	pTCT-0P	pTCT-1P	pTCT-2P
$\Delta E_{ST} \text{ (eV)}$	0.14	0.055	0.67
$\lambda \text{ (eV)}$	1.12	0.52	0.78
SOCME			
$(S_1/T_1, \text{ cm}^{-1})$	0.48	0.40	0.43
$k_{ISC} \text{ (s}^{-1}\text{)}$	2.1×10^7	5.2×10^7	3.1×10^7

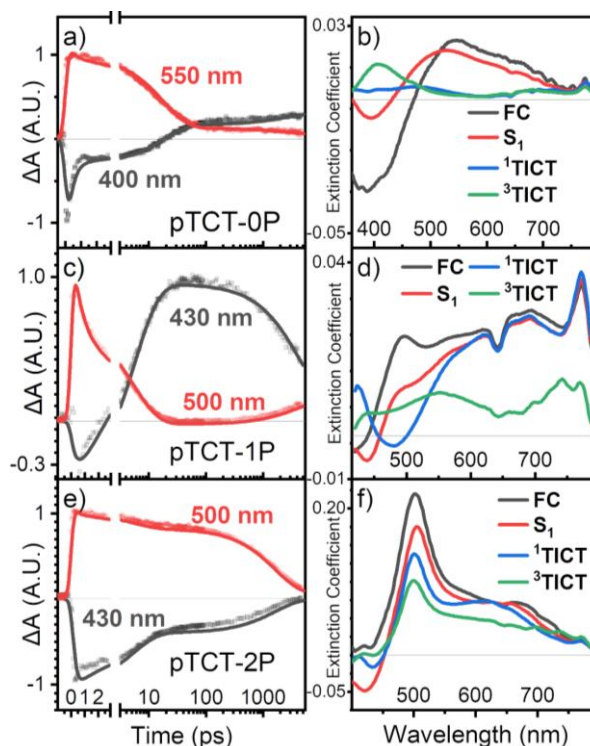


Figure 4.5 The kinetic traces of TA spectra with their fits from global target fitting at given wavelengths and the species associated spectra of pTCT-0P (a, b), pTCT-1P (c, d), and pTCT-2P (e, f). SAS is chirp corrected and adjacent averaging was performed.

Table 4.3 The fitting parameters resulting from the global analysis.

Rate Constant	pTCT-0P	pTCT-1P	pTCT-2P
* k_1 (ps ⁻¹)	3.16±0.02	1.68±0.03	6.44±0.17
* k_2 (ps ⁻¹)	0.0549±0.0002	0.178±0.001	0.189±0.001
* k_3 (ps ⁻¹)	1.92x10 ⁻⁴ ±9x10 ⁻⁶	1.46x10 ⁻⁴ ±1.0x10 ⁻⁵	5.43x10 ⁻⁴ ±1.4x10 ⁻⁵
* k_4 (ps ⁻¹)	1.96x10 ⁻⁴ ±1.1x10 ⁻⁶	9.30x10 ⁻⁵ ±1.05x10 ⁻⁵	6.24x10 ⁻⁵ ±1.54x10 ⁻⁵
** k_5 (ps ⁻¹)	1.00x10 ⁻⁷	1.00x10 ⁻⁷	1.00x10 ⁻⁷

*Rate constants correspond to the diagram in Scheme 3

** k_5 was fixed during target analysis

4.6 Global Fitting and ISC Rate Observation

Due to the spectral overlap between ¹TICT and ³TICT, a global target fitting model is used to analyze the TA data, which not only allows us to unravel the rate constants of the relaxation dynamics but also the extinction coefficients of ¹TICT and ³TICT in the species associated spectra (SAS, Figure 4.5b,

4.5d, 4.5f). The ES kinetics of pTCT molecules at different wavelengths are shown with their best fittings in Figure 4a, 4c, and 4e with fitting parameters listed in Table 3. To obtain global fitting results based on our target model, the $^3\text{TICT}$ decay rate ($1 \times 10^{-7} \text{ ps}^{-1}$) was fixed at a timescale well beyond our temporal window for each species. The SAS show excellent agreement with the corresponding TA spectra (Figure 4.4a to 4.4f), and the rate model fits the experimental data very well which strengthens the validity of the fitting model. Notably, pTCT-0P and pTCT-1P kinetics begin to diverge almost immediately after the rising component, and pTCT-2P kinetics diverge less so. This observation suggests that ICT and ISC vary drastically within the pTCT family (Figure 4.5a, 4.5c, 4.5e). Furthermore, it can be seen from Table 4.3 that the rising components (k_1) corresponding to internal conversion (IC) from FC to S_1 are 3.16 ps^{-1} , 1.68 ps^{-1} , and 6.44 ps^{-1} for pTCT-0P, pTCT-1P, and pTCT-2P, respectively. On the other hand, rate constants for ICT (k_2) are 0.0549 ps^{-1} for pTCT-0P, 0.178 ps^{-1} for pTCT-1P, and 0.189 ps^{-1} for pTCT-2P. The rate of $^1\text{TICT}$ which is depopulated by IC and emission to the ground state (k_3) is $1.92 \times 10^{-4} \text{ ps}^{-1}$ for pTCT-0P, $1.46 \times 10^{-4} \text{ ps}^{-1}$ for pTCT-1P, and $5.43 \times 10^{-4} \text{ ps}^{-1}$ for pTCT-2P. The $^1\text{TICT} \rightarrow ^3\text{TICT}$ ISC rate components (k_4) are $1.96 \times 10^{-4} \text{ ps}^{-1}$ in pTCT-0P, $9.30 \times 10^{-5} \text{ ps}^{-1}$ in pTCT-1P, and $6.24 \times 10^{-5} \text{ ps}^{-1}$ in pTCT-2P. $^1\text{TICT} \rightarrow S_0$ overall rates are in good agreement with those obtained by TCSPC (Figure 4.6, Table 4.4). ISC rates follow the order of pTCT-0P > pTCT-1P > pTCT-2P which does not match those made by TDDFT, reflecting a shortfall in the theoretical predictions. Nonetheless, the TDDFT predictions are consistently within an order of magnitude difference, suggesting they hold some predictive power. Importantly, ISC efficiency depends on the competition between ISC and $^1\text{TICT} \rightarrow S_0$, thus the ratio between them is relevant for comparison, where it is found that pTCT-0P has a ratio of 0.52, pTCT-1P has a ratio of 0.39, and pTCT-2P has a ratio of 0.10, altogether suggesting pTCT-0P and pTCT-1P generate $^3\text{TICT}$ most efficiently which generally agrees with previously reported oxygen sensitization abilities of pTCT polymers.¹⁴⁸ We note that the SAS of pTCT-2P (Figure 4.5f) have a high degree of spectral overlap between all four states (FC, S_1 , $^1\text{TICT}$, and $^3\text{TICT}$) which lowers our confidence in the above compartmental model when applied to the TA data for pTCT-2P. This may be the result of pTCT-2P populating $^3\text{TICT}$ rather inefficiently, or perhaps also due to a highly mixed $\pi\pi^*/\text{ICT}$ state which hampers the resolution of different states.

Table 4.4 Fitting constants for TCSPC data of pTCT series molecules in both O₂ containing toluene and air-free toluene.

Time Constant	pTCT-0P	pTCT-1P	pTCT-2P
IRF, fwhm (ns)	1.40	1.40	1.40
τ_1, O₂ (ns)	4.62 ± 0.08	4.28 ± 0.08	2.21 ± 0.04
k_1, O₂ (ns⁻¹)	0.217 ± 0.004	0.234 ± 0.004	0.452 ± 0.008
τ_1, N₂ (ns)	5.08 ± 0.08	5.22 ± 0.09	2.57 ± 0.03
k_1, N₂ (ns⁻¹)	0.197 ± 0.003	0.192 ± 0.003	0.389 ± 0.005
τ_1, N₂ – τ_1, O₂ (ns)	0.46 ± 0.11	0.94 ± 0.12	0.36 ± 0.02
k_1, O₂ – k_1, N₂ (ns⁻¹)	0.020 ± 0.005	0.042 ± 0.006	0.063 ± 0.007

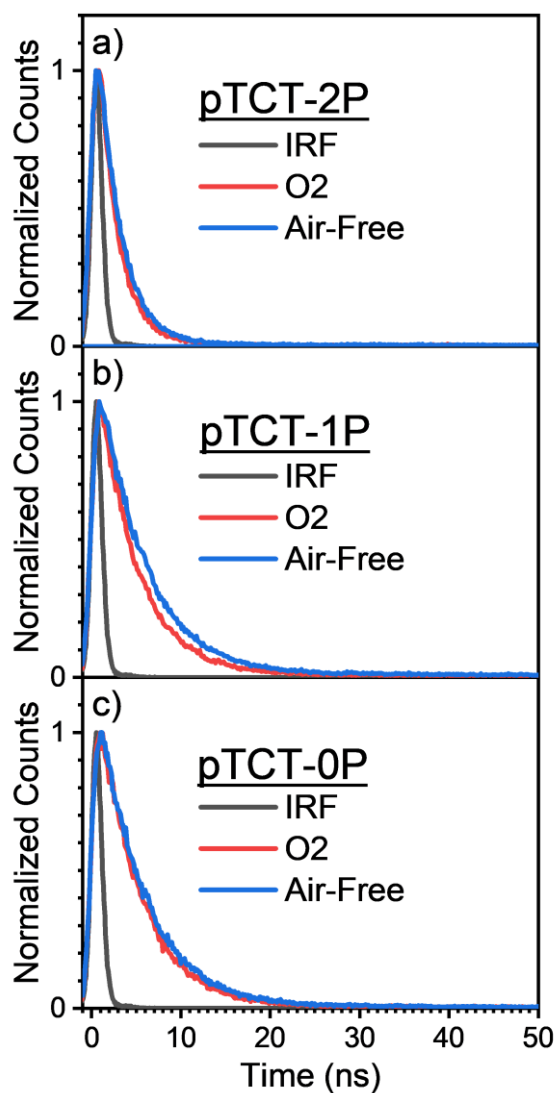


Figure 4.6 TCSPC data collected in O₂ containing toluene and air-free toluene of (a) pTCT-2P, (b) pTCT-1P, and (c) pTCT-0P.

From our analysis of the TA data, we can draw insight about the photodynamics of the pTCT series of molecules, which informs our understanding of the relationship between their structure and photophysical behavior. For instance, FC relaxation in pTCT-1P occurs slowly, which reflects the relatively longer reaction coordinate pTCT-1P must traverse before reaching its S₁ geometry – in line with results from TDDFT. The differences in ICT and emission rates are due to varying degrees of orthogonality and distance between the donor and the acceptor at the S₁ geometry as indicated by TDDFT (Table S1). pTCT-0P is an interesting case since its donor arms can strongly interact possibly providing an alternate through-space ICT mechanism that is not prevalent in the other molecules. ISC rates are interesting in that

a large D-A dihedral is beneficial for spin-crossover, which would seem to favor pTCT-1P over pTCT-0P, but TDDFT suggests SOCME of pTCT-0P is considerably larger which is reflected by its faster ISC rate and better ISC efficiency. Overall, however, SOCME must be balanced with ΔE_{ST} and the reorganization energy, λ , to yield efficient ISC which still allows pTCT-1P to exhibit more efficient ISC than pTCT-2P. From TDDFT and using Eq. 4.2, we find the S_1/T_1 ISC rates at the S_1 geometry to be $2.1 \times 10^7 \text{ s}^{-1}$, $5.2 \times 10^7 \text{ s}^{-1}$, and $3.1 \times 10^7 \text{ s}^{-1}$ for pTCT-0P, pTCT-1P, and pTCT-2P, respectively. These values are on par with those obtained from global target analysis and align with predictions made for the up-conversion ISC rates of known TADF emitters,¹⁷⁸ thus we conclude our results allow us to predict and identify the capabilities of the pTCT series of being able to produce triplet states in appreciable quantities with pTCT-0P being the most efficient.

4.7 Conclusions

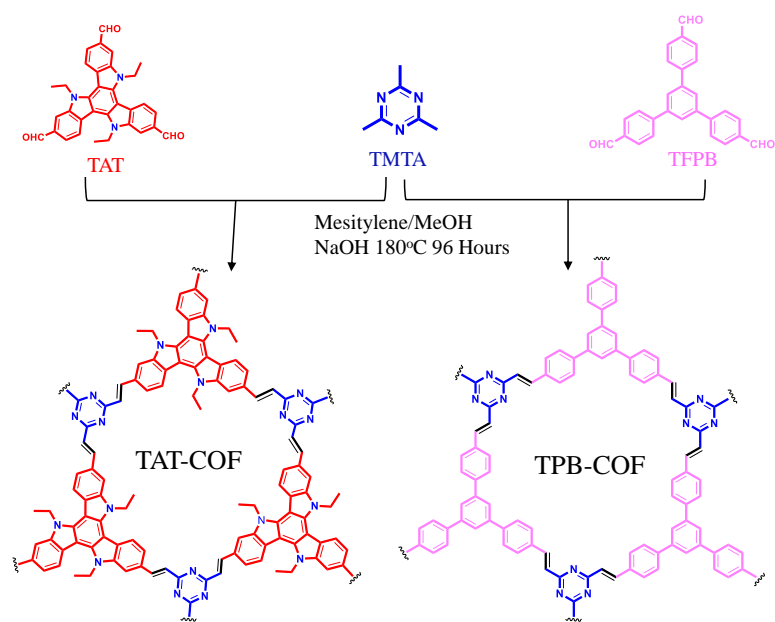
Star-shaped donor-bridge-acceptor molecules have recently begun to attract interest due to their great potential to deliver better performance in OLED devices and significant promise as photocatalysts. Developing a full understanding of their photophysical behavior is necessary to incorporate rational design elements to this class of molecules. In this work, we report a systematic photophysical study on a series of triazine-phenyl-carbazole (pTCT) star-shaped DBA molecules with 0, 1 and 2 bridging phenylene units using the combination of steady-state and time-resolved spectroscopy and TDDFT calculation. We find that the excited state relaxation pathways of these molecules are significantly dependent on the length of the bridge unit which governs the ground state D-A dihedrals and excited state conformational relaxation that ultimately dictates their propensity to undergo ISC or remain within the singlet manifold. Particularly, we were able to uncover and explain that pTCT-1P has ISC rates that are competitive with singlet emission resulting from a large conformational relaxation along the S_1 potential leading to a 1TICT state. This 1TICT has a narrow singlet-triplet energy gap, providing a mechanism for ISC through spin-orbit coupling. Furthermore, we were able to uncover that longer bridging units are unable to inhibit fast singlet electron-hole recombination, leading to poor ISC efficiency. The new fundamental insights gained from this work are essential for the future rational design of DBA molecules to facilitate their applications in OLED, photocatalysis, and optoelectronics.

CHAPTER 5 – CONJUGATION AND AGGREGATION DIRECTED DESIGN OF COVALENT ORGANIC FRAMEWORKS AS WHITE-LIGHT-EMITTING DIODES

5.1 Introduction

Photon emission by organic compounds is a process that is taken advantage of in various applications ranging from labelling biomarkers,¹⁷⁹ heavy ion sensing,¹⁸⁰ and as display or lighting devices.¹⁸¹ The photophysical properties that determine emission in COFs have not yet been settled,¹⁸² but 2D COFs are typically weakly fluorescent or non-fluorescent due to aggregation caused quenching due to π - π interactions that cause deactivation via excited state coupling.¹⁸³ It has been suggested that aggregation induced emission (AIE) can enhance emissive exciton recombination in COFs by restricting molecular motion thereby avoiding nonradiative internal conversion processes.^{184–186} AIE typically relies on polyarene units⁴³ or sterically frustrated units,^{187,188} however less is known about how to design planar COFs for photoluminescence and discovering the structural relationship to their properties is important for understanding this crucial relaxation pathway.

In this project, we synthesized two highly emissive COFs (TAT-COF and TPB-COF, Scheme 5.1) and investigated with the direct correlation of their structures and their light absorption, charge transfer (CT), and luminescent properties. TAT-COF and TPB-COF were synthesized by the reaction of 2,4,6-trimethyl-1,3,5-triazine (TMTA) with a star-shaped monomer, 2,7,12-Triformyl-5,10,15-triethyltriindole (TAT) and 1,3,5-Tris(4-formylphenyl)benzene (TFPB), respectively, via Knoevenagel condensation reaction. We hypothesize that the finely tuning the monomer structure in TAT with respect to TFPB alters the planarity, charge delocalization (conjugation), and π - π stacking (aggregation) of COF structure, which are anticipated to impact their photophysical properties. Using the combination of experimental spectroscopic and computational studies, we not only show that the designed COFs can be used to generate white light but also identify how the physical structure of COFs can modulate CT, exciton relaxation, and emission quantum efficiency.



Scheme 5.1 Synthesis Scheme of TAT-COF and TPB-COF

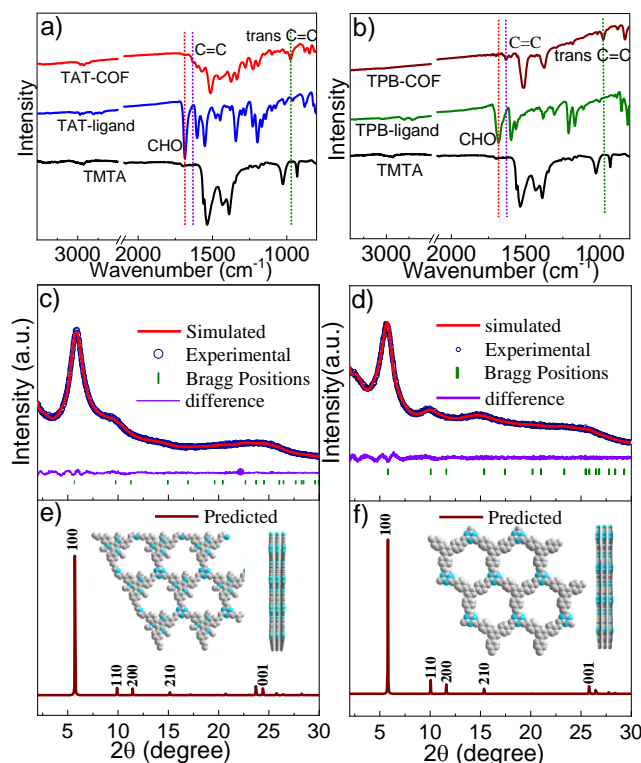


Figure 5.1 FTIR spectra of (a) TAT-COF and (b) TPB-COF with corresponding monomers. Powder XRD patterns of (c) TAT-COF and (d) TPB-COF: Pawley refinement of COFs (AA stacking) against the experimental data, the Bragg positions (green bar), and the refinement differences (purple). Simulated XRD of (e) TAT-COF and (f) TPB-COF. Inset are the top view and side view of structure modeling of TAT-COF and TPB-COF with AA stacking.

5.2 Synthesis and Structural Characterization of TAT-COF and TPB-COF

The details of synthetic procedure of TAT-COF and TPB-COF are described in Chapter 2.3 and follow the same procedure of TPB-COF reported previously.^{189,190} The formation of both COFs was confirmed by FTIR spectrum, PXRD, SEM, as well as diffuse reflectance (DR) and emission spectrum. The FTIR spectra of TAT-COF (Figure 5.1a) and TPB-COF (Figure 5.1b) show the absence of the aldehyde band (1689 cm^{-1}) which was present in TAT (Figure 5.1a) and TFTB (Figure 5.1b) ligand, and the characteristic vibrational stretching modes of $\text{C}=\text{C}$ *trans* configuration at 1630 cm^{-1} and 978 cm^{-1} , suggesting the complete condensation of the starting monomers to form the olefin linkages in both COFs. The XRD patterns of TAT-COF (Figure 5.1c) show peaks at 5.8° , 9.8° , 11.3° , 14.9° and 24.4° , and TPB-COF (Figure 5.1d) show distinguished peaks at 5.8° , 10.1° , 11.6° , 15.4° and 25.8° , which can be assigned to (100), (110), (200), (210) and (001) facets (Figure 5.1e and 5.1f), respectively. Pawley refinement of eclipsed (AA) stacking mode (inset of Figure 5.1e and 5.1f) modeled using Materials Studio yields XRD

patterns (red plot in Figure 5.1c and 5.1d) that show negligible difference from the experimental data. In contrast, a staggered (AB) mode cannot reproduce the experimental XRD patterns, suggesting that the condensation reaction of monomers leads to the formation of TAT-COF and TPB-COF with AA stacking mode.

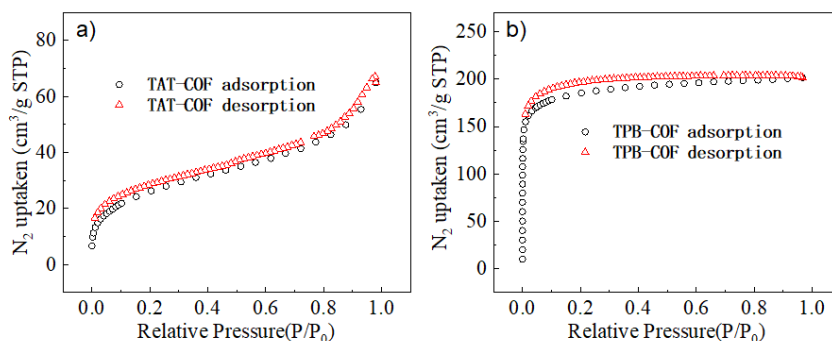


Figure 5.2 Nitrogen adsorption and desorption isotherms of (a) TAT-COF and (b) TPB-COF

The permanent porosity was investigated by N_2 sorption measurements at 77K. As illustrated in Figure 5.2, the Brunauer–Emmett–Teller (BET) surface area of TPB-COF is $703 \text{ m}^2/\text{g}$, which is comparable to the results reported previously.^{189,190} In contrast, the BET surface area of TAT-COF is only $91 \text{ m}^2/\text{g}$. The low surface area of TAT-COF can be attributed to the ultra-microporous pores resulting from the bulky ethyl group. This is further supported by the type II isotherms, which indicates their low porosity nature. Unlike TAT-COF, TPB-COF shows type-I reversible isotherms, implying their microporous characteristics.

5.3 Spectroscopic Characterization of TAT-COF and TPB-COF and Their Utility as WLEDs

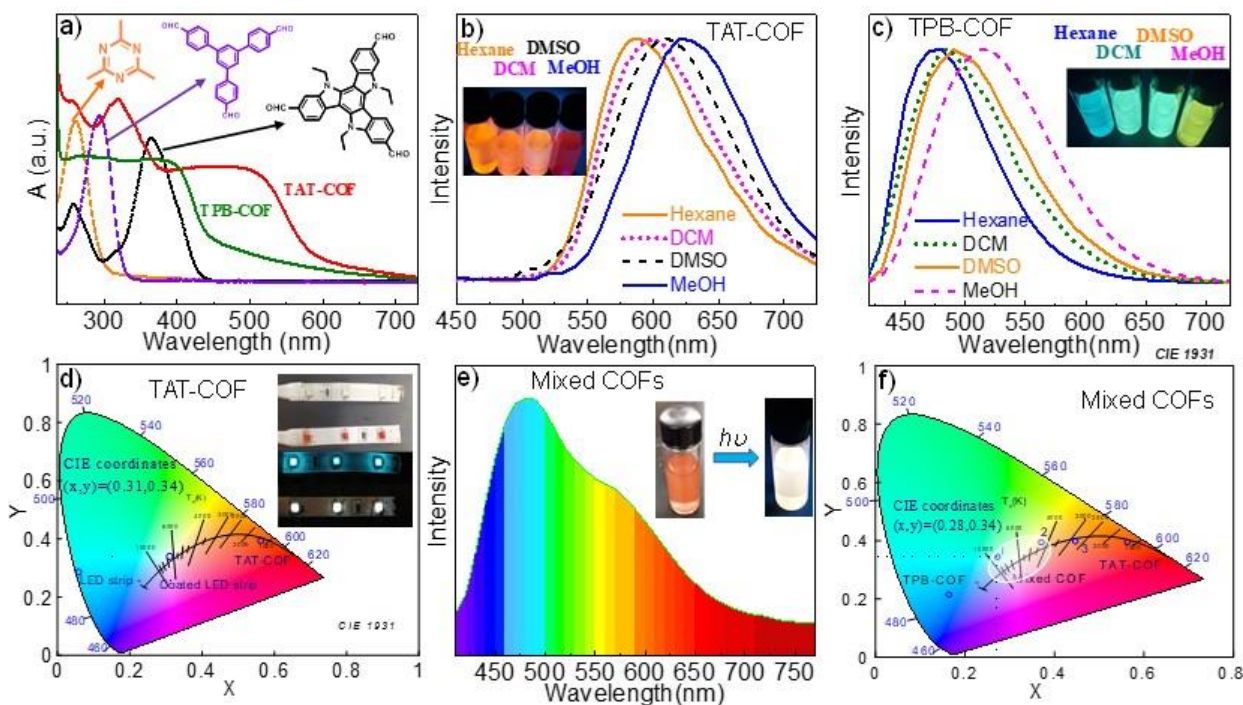


Figure 5.3 (a) Diffuse reflectance UV–visible spectra of TAT-COF and TPB-COF with corresponding monomers. Emission spectra of (b) TAT-COF and (c) TPB-COF in hexane, DCM, DMSO and MeOH. Insets are photographs of TAT-COF and TPB-COF suspensions in different solvents under UV light (365nm). (d) CIE-1931 diagram and the positions of coated LED strip, TAT-COF and LED strip. Insets are photographs of the LEDs. (e) Emission spectrum of mixed TAT-COF and TPB-COF suspension. Insets are photographs of suspensions with and without UV light. (f) CIE-1931 coordinate and the CCT diagram for mixed COF suspensions with different ratio.

The formation of COF structure was further supported by the DR and photoluminescence (PL) spectra. Compared to their corresponding monomers, the DR spectra of both COFs (Figure 5.3a) exhibit extended absorption in visible region, which can be attributed to the CT transition arising from the donor–acceptor pairs via π -conjugation in the skeleton and/or interlayer stacking. The emission spectra of TAT-COF and TPB-COF (Figures 5.3b, 5.3c) following 365 nm excitation show distinct emission band with significant red shift with respect to their single units, implying that the CT transition is responsible for the emission of COFs. In addition, the emission spectra of both samples show strong dependence on solvent polarity. When TAT-COF was dispersed in hexane, an orange light was emitted at 575 nm (Figure 5.3b). When more polar solvents were used, for which the solvent polarity increases in the order of DCM < DMSO < MeOH, the emission maxima shift to longer wavelength (from orange to red). A similar trend of bathochromic shift with increasing solvent polarity was observed in the emission spectrum of TPB-COF (Figure 5.3c), indicating the polar nature of the CT state of the COFs. Along with the bathochromic shift,

the PL quantum yield (PLQY) of the two COFs are also sensitive to the environment. As shown in Table 5.1, PLQY value of 17.82% was observed for TAT-COF in DCM and decreased to 5.29% and 2% in DMSO and MeOH, respectively. Compared to TAT-COF, TPB-COF exhibits much stronger emission with PLQY up to 62.17% in DCM. The different PLQY of TAT-COF and TPB-COF is correlated to the difference in transition dipole moment orientation and the geometrical effect of the framework, which will be discussed later.

Table 5.1 Quantum Yield of TAT-COF and TPB-COF in solvents of varying polarity

Solvent	TAT-COF QY (%)	TPB-COF (QY (%))
DCM	17.8	62.2
DMSO	5.3	43.7
MeOH	2.0	21.0

The tunable emission color as well as the high PLQY of TAT-COFs and TPB-COFs make them of interest in optical application such as white light-emitting diodes (WLEDs). RGB (red, green, blue) method and phosphor method are two conventional approaches to produce white light with LEDs by the proper mixture of LEDs with three primary colors (blue, green, red) or combining blue LED with yellow phosphor coating.¹⁹¹ As white light can be generated by mixing two complementary colors, we then explore the possibility to use TAT-COF for WLEDs. As shown in Figure 5.3d, white light was obtained by simply coating TAT-COF on the surface of cyan LED strip (~485 nm). The CIE coordinates were determined to be (0.31, 0.34) and found to be cold white (CCT 6500K). More interestingly, white light with variable temperature can be easily obtained by mixing the two COFs with certain ratios. Shown in Figure 5.3e is the emission spectrum of the mixed TAT-COF and TPB-COF dispersion in DCM with ratio of 3.5:1, which covers the entire visible spectrum. Upon illumination of the mixed suspension by UV light (365 nm), white light emission is clearly visible as shown in the inset of Figure 5.3e. The CIE coordinate of the mixed COFs (Figure 5.3f) was determined to be (0.28, 0.34), resulting in cold white light.

5.4 Excited State Dynamics of TAT-COF and TPB-COF

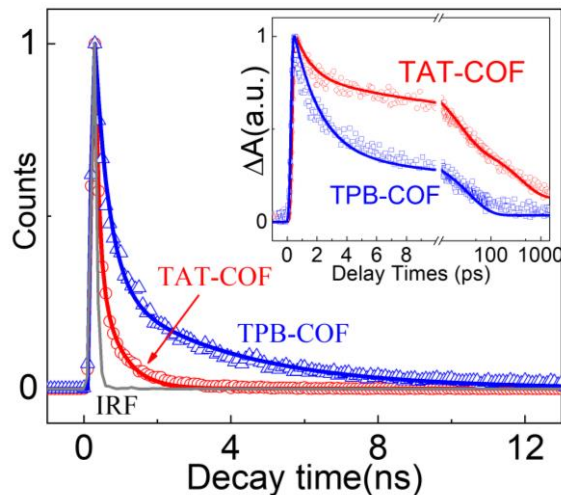


Figure 5.4 Comparison of emission decay (a) and electron absorption decay (inset) between TAT-COF and TPB-COF.

Table 5.2 Multiexponential fit parameters for TCSPC results of TAT-COF and TPB-COF.

Fit Component	TAT-COF	TPB-COF
A_1 (%)	84.1	73.2
τ_1 (ns)	0.134	0.389
A_2 (%)	15.8	26.8
T_2 (ns)	0.825	3.43

To gain insight on the origin of the observed emission behaviors of these COFs, we first measured the excited state (ES) lifetime of TAT-COF and TPB-COF by time resolved emission spectroscopy following 400 nm excitation. Figure 5.4 compares the emission decay of TAT-COF and TPB-COF collected at 580 nm and 450 nm, respectively, corresponding to their CT emission. The emission decay is much faster in TAT-COF than TPB-COF, suggesting that the CT state in the former has shorter emission lifetime than the latter, which is consistent with its lower PLQY and suggests “non-fluorescent J-type” aggregation behavior supported by later time dependent density functional theory (TDDFT) calculations. Each decay curve can be fit by a biexponential function, from which we obtained the amplitude weighted lifetime, which is 0.24 ns and 1.2 ns for TAT-COF and TPB-COF (Table 5.2), respectively.

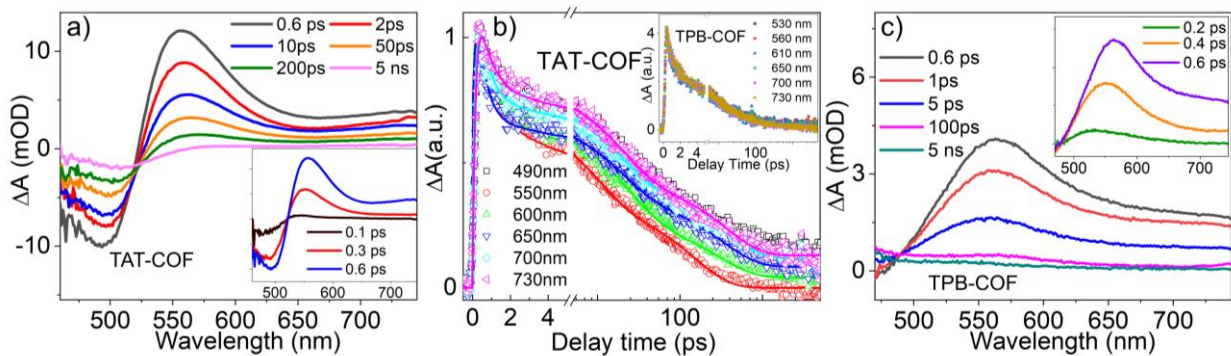


Figure 5.5 Transient absorption spectrum of TAT-COF (a) and TPB-COF (b) Comparison of TA kinetics of TAT-COF and TPB-COF (inset) at different wavelength. The solid lines are the fitting to the kinetic traces. (c) Transient absorption spectrum of TPB-COF following 400 nm excitation.

In addition to emission lifetime, we also examined the ES dynamics of these COFs using femtosecond transient absorption (TA) spectroscopy, which allows us to probe the early time dynamics that cannot be resolved by time resolved emission spectroscopy. Figure 5.5a shows the TA spectra of TAT-COF following 400 nm excitation. Immediately following the excitation, the TA spectra of TAT-COF show the formation of a negative feature centered around 500 nm and a broad positive absorption band from 525 nm to the red end of our spectral window (inset of Figure 5.5a). The negative feature can be assigned to ground state bleach (GSB) band due to the occupation of the conduction band (CB) by electrons following photoexcitation. The positive band can be attributed to the excited state absorption in the framework. The formation of both GSB and ESA bands shows a rising component within ~ 600 fs, which can be attributed to the relaxation of the electrons from the high to low energy CB. As shown in Figure 5.5b, the ESA of TAT-COF at 560 nm is found to decay faster with respect to the longer wavelength region. The similar probe wavelength dependent kinetics has been previously reported in other solid state materials and is likely associated with the presence of trap state.¹⁹² The similar spectral features, i.e. negative GSB and positive ESA (rises within 600 fs) were observed for TPB-COF (Figure 5.5c), although the negative band of TPB-COF is barely seen because of the limit of our TA window. Unlike TAT-COF, the kinetic traces for ESA at different probe wavelengths appear to be same for TPB-COF (inset of Figure 5.5c), suggesting different exciton relaxation dynamics from TAT-COF. More interestingly, we note that ESA kinetics of TPB-COF exhibits faster decay than TAT-COF (inset of Figure 3a), which conflicts with the time resolved

emission results, where its emission lifetime is longer compared to that of TAT-COF (Figure 5.4). This conflict further supports the fact that different exciton relaxation pathways are involved in these COFs.

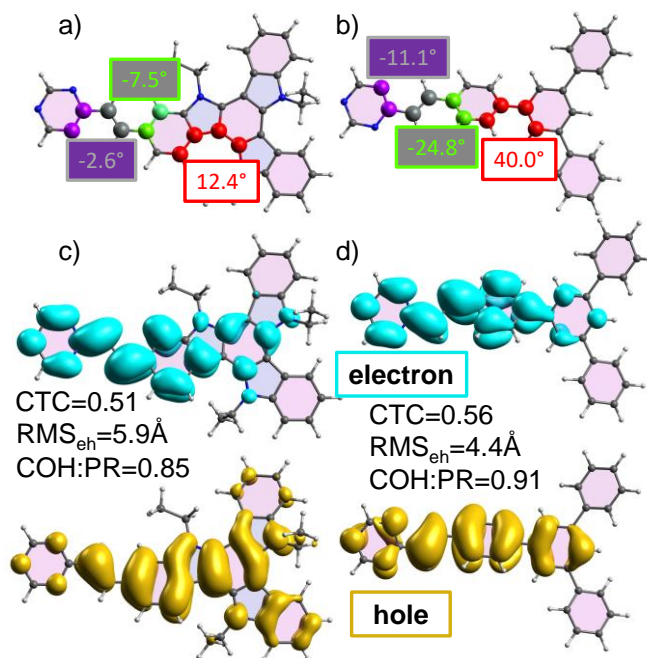


Figure 5.6 The representative units selected for TDDFT study including important dihedral angles of (a) TAT-COF, and (b) TPB-COF. Dihedrals in TPB-COF are larger than TAT-COF, demonstrating the difference in planarity. Natural transition orbitals and quantitative CT measures of (c) TAT-COF, and (d) TPB-COF.

5.5 Theoretical Modeling of TAT-COF and TPB-COF

To uncover the origins that result into distinct exciton relaxation dynamics in TAT-COF and TPB-COF, we turn to TDDFT (procedure outlined in the Chapter 2.3) to examine the direct correlation of optical properties of the COFs with their topology, structure, and composition, as these structural parameters are all expected to play a role in the photophysical properties of COFs. We prefix the computational work by acknowledging that although COFs polymerize into extended structures, the size of the systems that can be studied by TDDFT are limited by computational expense. As such, we decompose the extended COF structures into smaller units as a trade-off for reasonable timeliness and efficiency. The unit selection, however, is critical to ensure meaningful insight. In this work, the region including one triazine ring and one of either TAT or TPB is selected as the unit for study (Figure 5.6a and 5.6b). Finally, COFs readily form aggregated structures, which is especially important as our physical experiments herein are conducted

in the condensed phase. To account for aggregation, TDDFT is used to not only study single layers of COF but also the interlayer interactions between multiple layers (one to three) of our small units.

Table 5.3 Transitions of TAT-COF and TPB-COF predicted by TDDFT with one through three layers present.

	Layers	Allowed Transition	Transition Energy (nm)	Oscillator Strength (A.U.)
TAT-COF	1	S ₁	359.6	1.31
	2	S ₁	385.1	0.01
		S ₂	368.9	1.20
	3	S ₁	393.2	0.01
		S ₂	381.7	0.04
		S ₃	368.9	1.28
TPB-COF	1	S ₁	322.9	1.53
	2	S ₁	360.3	0.00
		S ₂	318.5	2.31
	3	S ₁	373.2	0.00
		S ₂	347.0	0.01
		S ₃	316.7	2.60

TDDFT is first used to examine the nature of electronic transitions of TAT-COF and TPB-COF. The predicted transitions indicate TAT-COF to possess lower energy absorption and oscillator strength than TPB-COF (Table 5.3), which directly reflects the DR spectrum above and suggests the validity of our computational model. The natural transition orbitals (NTOs) of the predicted electronic transitions indicate that the planarity of TAT-COF (Figure 5.6c and 5.6d) allows for significant delocalization, in contrast to the propeller-like structure of TPB-COF that prevents similar delocalization. In addition, branches of TPB are arranged meta- to one another around the benzene core, which is inconducive with their ortho-/para-electron directing nature.¹⁹³ On the other hand, TAT-COF possesses indole units which are directly attached to a benzene core, allowing more conjugation and lower energy electronic transitions than TPB-COF. These results agree well with the DR and emission spectra of COFs, where TAT-COF shows significantly red shifted absorption/emission, suggesting that in-plane conjugation plays an important role in extending the light absorption/emission properties of COFs into visible region.

Table 5.4 Quantitative CT measures of TAT-COF and TPB-COF in both the intralayer and interlayer directions (allowed transitions only).

	Layers	RMS _{eh}	Intralayer		Interlayer	
			CTC	COH:PR	CTC	COH:PR
TAT-COF	1	5.7	0.52	0.86	--	--
	2	5.9	0.53	0.87	0.380	0.95
	3	5.9	0.54	0.88	0.477	0.72
TPB-COF	1	4.6	0.54	0.89	--	--
	2	5.0	0.56	0.90	0.137	0.67
	3	5.3	0.58	0.92	0.271	0.61

In addition to conjugation, CT, and the effect of aggregation on the electronic structure needs to be considered to have a more complete picture on the correlation of COF structure with their light absorption properties. Due to the difficulties in using charge-transfer character (CTC) to describe the intermediate cases of CT,^{194,195} we also evaluated electron-hole separation (COH:PR) and exciton size (RMS_{eh}) as additional measures (Figure 5.6c, 5.6d, Table 5.4). Compared to TPB-COF, TAT-COF has less intralayer CTC and COH:PR but a larger overall exciton, which is due to the greater degree of electron delocalization in the ground state (GS) as shown in the NTOs (Figure 5.6). After aggregation to three layers, CTC does not change, but COH:PR decreases, and RMS_{eh} increases by 3% (Table 5.4). The transition energy decreases by 0.01 eV with oscillator strength increase by 0.2 A.U.

TPB-COF experiences a small increase of intralayer COH:PR, and a 7% in RMS_{eh} (Table 5.4). These increases correspond with an increase in the transition energy by 0.1 eV and in the oscillator strength by more than 1 A.U. These results suggest that TPB-COF exhibits more intralayer CT enhancement on aggregation as indicated by the growth of its exciton.

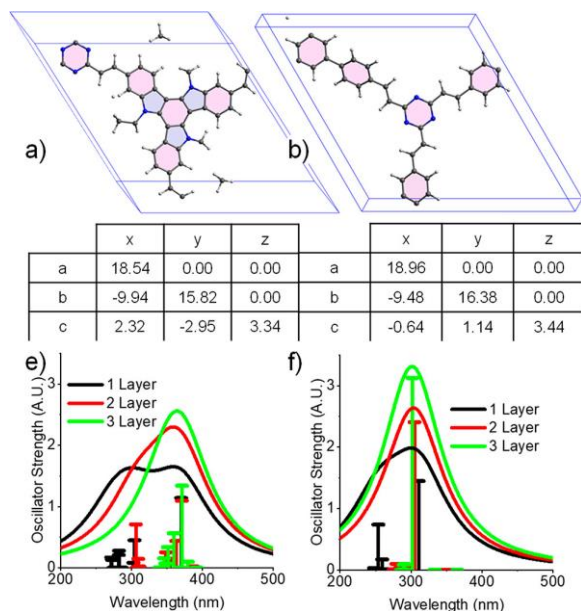


Figure 5.7 The interlayer arrangements of (a) TAT-COF, and (b) TPB-COF obtained from DFTB structure optimization. TDDFT predicted transition dipole moments of (c) TAT-COF, and (d) TPB-COF. Upon aggregation the TDDFT predicted absorption spectrum of (e) TAT-COF, and (f) TPB-COF.

To uncover why the exciton in TPB-COF grows and gains oscillator strength upon aggregation, we need to have an in-depth understanding of the exciton interactions,⁶⁶ for which structure, excited state polarizability,^{65,196–198} and superexchange CT (SECT) coupling need to be considered.⁶² First, it is important to note that TAT-COF and TPB-COF are predicted to have distinctly different aggregate structures. TAT-COF (Figure 5.7a) is offset in the x-direction by 2.32 Å and the y-direction by -2.95 Å while TPB-COF (Figure 5.7b) is -0.64 Å in the x-direction and 1.14 Å in the y-direction. We acknowledge that bulk COFs may assume various stacking patterns, but we assume our converged structures yield realistic representations. Nonetheless, the stacking geometries generally approach “card pack” and should lead to “H-type” aggregates, although TAT-COF may be more of an intermediate case within Kasha’s model of the exciton. However, since the transition energy of TAT-COF decreases with aggregation, we must consider other competing effects (Table 5.4). SECT coupling is the last piece considered here and can be gauged by the same CT measures above, but in the interlayer direction. For the two-layer system, TAT-COF observes almost 5 times as much CTC and ~35% more COH:PR than TPB-COF (Table 5.4). Notably, COH:PR of TAT-COF approaches 1 (0.73), which suggests that there is strong mixing of Frenkel and CT states. Moving to three layers, this quantity is tempered somewhat as COH:PR decreases to 0.55 but is still

45% more than the three-layer TPB-COF system. Overall, these results suggest that the fused, planar structure of TAT-COF yields more interlayer CT mixed into allowed transitions than TPB-COF.

Combining the computational results with the fundamental spectroscopic data above provides a robust explanation for experimental differences between exciton formation and relaxation dynamics in TPB-COF and TAT-COF. These comparative experimental observations in TAT-COF are (a) red-shifting of the absorption spectrum, (b) slower TA decay kinetics, (c) probe dependent TA decay kinetics, (d) shorter emission lifetime, and (e) lower PLQY. Delocalization and the CT stabilizing orientation of the transition dipole moment in TAT-COF contribute to the red-shift in the absorption spectrum. In turn, this narrows the exciton bandwidth and shortens the internal conversion channel. As shown in the model we proposed to illustrate these experimental and computational results (Figure 5.8), the photoexcitation of COFs promotes the electrons from their valence band (VB) to the high energy level of CB, which then quickly relax down to the edge of CB, corresponding to the rising component within 600 fs (k_1). Due to the presence of trap states in TAT-COF, some electrons relax down to this trap state (k_2), which is responsible for the probe dependent kinetics observed in TA spectra of TAT-COF. Because the electrons in trap states typically have longer lifetime, which coincides with the shortened internal conversion in TAT-COF, yielding the appearance of slower electron absorption decay in TAT-COF than TPB-COF, where the latter undergoes more internal conversion and barely populate trap states, and thus show negligible dependence of kinetic traces on probe wavelength. The trap state is a non-radiative state, which well explains that TPB-COF has much longer emission lifetime and higher PLQY than TAT-COF as time resolved emission spectroscopy only measures the emissive ES. While the origin of the trap state remain unclear, one possibility could arise from excimer formation,¹⁹⁹ which has also been recently reported to lead to probe dependent TA kinetics in COF-5.⁸³ However, further TA experiments using near IR probe does not show the spectral features of excimer, which may suggest that trap state herein may result from other factors rather than the formation of excimer.

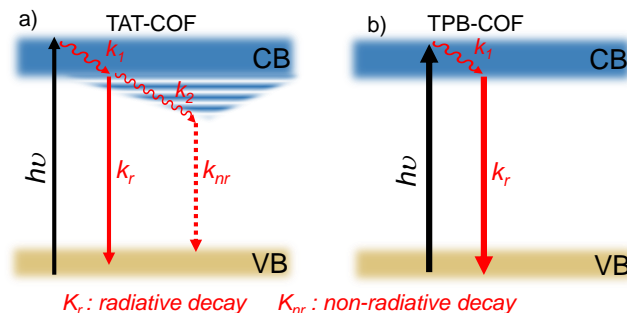


Figure 5.8 Energy diagram of TAT-COF (a) and TPB-COF (b) that illustrate exciton relaxation dynamics.

5.6 Conclusions

In summary, we examined the synthesis, white light emitting, and direct correlation of the structure (conjugation and aggregation) with the light harvesting, CT, and ES dynamics of two conjugated sp^2 -C-COFs with embedded donor-acceptor pairs. We show that both COFs are highly emissive, where white light can be obtained by simply coating COFs to LED strip. When adjusting the ratio of TAT-COF and TPB-COF in solution, the mixed COFs exhibit different colors across the visible spectrum. Using the combination of time resolved absorption and emission spectroscopy as well as TDDFT calculation, we show that the planar backbone of TAT-COF facilitates in-plane charge delocalization, resulting into broader absorption in the visible region with respect to TPB-COF. The transition dipoles interact with polarizable intramolecular CT states to narrow or widen exciton bandwidth, leading to shorter or longer internal conversion in TAT-COF and TPB-COF, respectively. In addition, the TAT-COF with a planar backbone exhibits stronger interlayer CT than TPB-COF with propeller-like monomers, which suppresses the fluorescence quantum yield. These results not only demonstrate the great potential of COFs as organic luminescent materials but also provided unprecedented insight on how the COF structure (conjugation and aggregation) should be considered for rational design of highly emissive COFs.

CHAPTER 6 – WAVELENGTH DEPENDENT EXCITONIC PROPERTIES OF COVALENT ORGANIC FRAMEWORKS EXPLORED BY THEORY AND EXPERIMENT

6.1 Introduction

For all the potential COFs have in optoelectronics and photocatalysis, without a fundamental understanding of their responses to external stimuli their utility may always be speculation and widespread adoption may never be realized. How COFs respond to photoexcitation is particularly important because the generation and persistence of excited states is directly related to performance.^{200–202} A topic that receives attention in COFs is the seemingly endless ways monomers can be combined to create new structures with unique properties, but not much is known about – from a photophysical point of view – how monomer swapping will affect their excited state dynamics.

Imine linked COFs are often considered fully conjugated systems, and as such they are good candidates to be able to finely tune donor-acceptor architectures to generate excitons with helpful properties in photocatalysis. Oftentimes, a fully conjugated nature in COFs can facilitate phenomena like exciton diffusion,^{83,203} singlet-singlet annihilation,⁸⁴ and charge separation.^{204,205} While studies of systematically modified donor-acceptor architectures have begun to emerge,²⁰⁴ little is known on how excess energy is dissipated in imine COFs, which is potentially essential for photocatalysis.

To probe the properties and photophysics of imine COFs, this study is designed to use time-dependent density functional theory (TDDFT) and fs-OTA on a series of COFs by permuting four monomers (two ditopic, two tritopic, Scheme 6.1) with varying D-A characteristics. The fs-OTA experiment is conducted to excite COF samples across their absorption spectrum to investigate how excitations above, at, and below the band edge are handled by COFs. Using TDDFT allows for analysis of the transition density matrix (TDM), which can quantify electron and hole particles to predict exciton properties. Theoretical analyses are then used to help guide the interpretation of fs-OTA data.

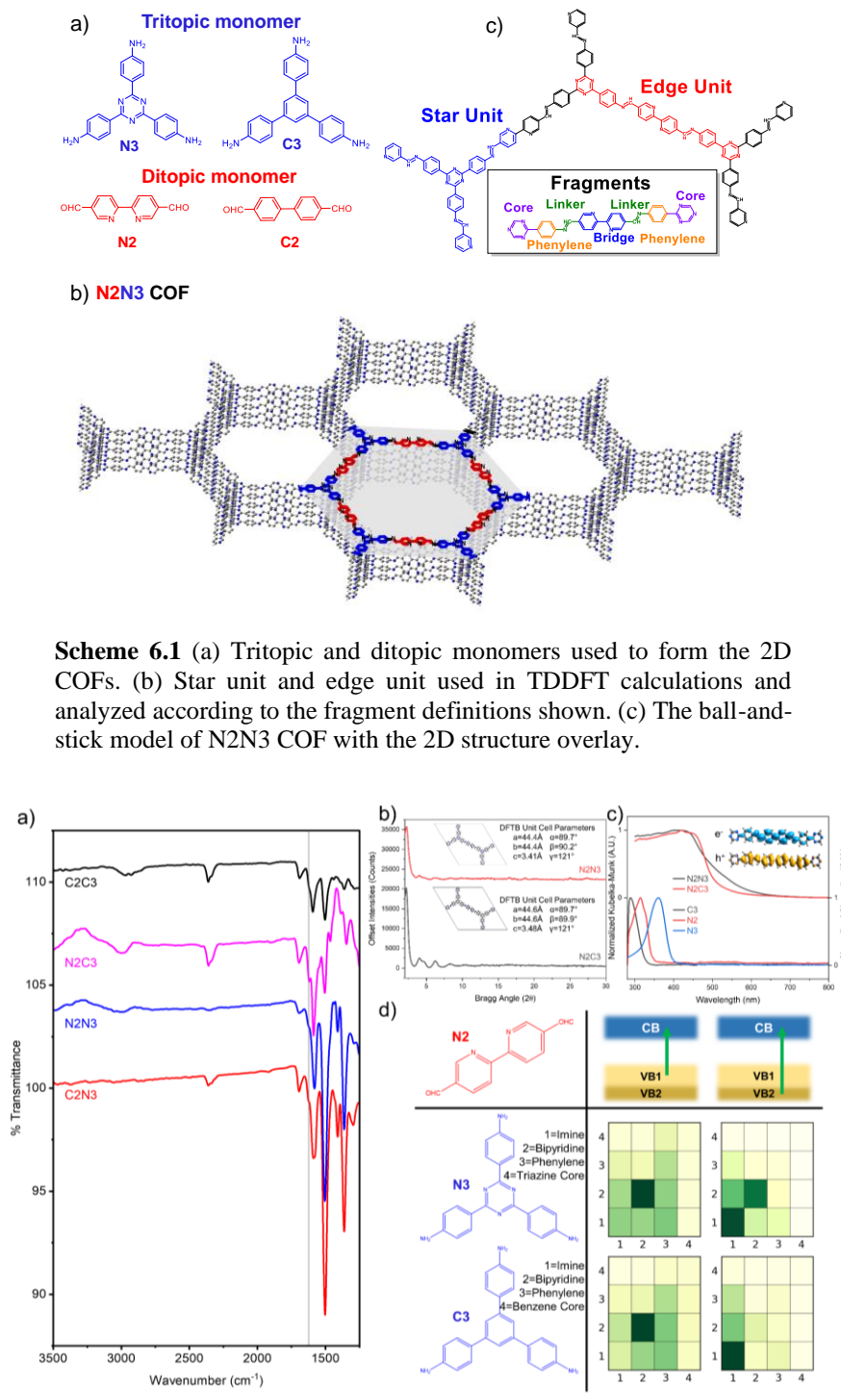


Figure 6.1 (a) FTIR spectra of the four COFs (b) Experimental PXRD patterns of N2N3 and N2C3 COF (background removed). (c) UV-visible absorption spectra of N2, N3, and C3 monomers in toluene and Kubelka-Munk transformed diffuse reflectance spectrum of N2N3 and N2C3 COFs; inset shows the major contribution (21.252) to the NTO of the VB1-CB transition of N2N3. (d) Normalized electron/hole correlation plots generated by TheoDORE showing the impact of tritopic core substitution on the VB1-CB (left) and VB2-CB (right) transitions.

6.2 Synthesis and Characterization of Isostructural 2D COFs

The synthesis of four 2D COFs with different combinations of tritopic and ditopic organic monomers follows previously reported procedures with minor modification,⁹⁰ and the details are described in Section 2.4. As shown in Scheme 6.1a, the tritopic monomers are 4,4',4''-(1,3,5-triazine-2,4,6-triyl)trianiline (denoted N3) and 1,3,5-tris(4-aminophenyl)benzene (denoted C3), and the ditopic monomers are [2,2-bipyridine]-5,5'-dicarbaldehyde (denoted N2) and [1,1'-biphenyl]-5,5'-dicarbaldehyde (denoted C2). The formation of these COFs is confirmed by FTIR spectra (Figure 6.1a), where the band between 1620-1626 cm^{-1} corresponds to the imine stretch. The powder X-Ray diffraction (PXRD) patterns of N2N3 and N2C3 COFs (Figure 6.1b) demonstrate their crystalline nature, where a strong diffraction peak $\sim 2.3^\circ$ can be attributed to the (100) diffraction plane, and two less intense diffraction peaks $\sim 4.0^\circ$ and $\sim 6.1^\circ$ can be assigned to (110) and (210) diffraction planes, respectively. The diffraction peaks in these PXRD patterns may be overtly broadened due to the distribution of crystallite size²⁰⁶ and strain defects.^{207–209} To quantify the amount of strain present in the microcrystalline powders, we utilize the refinement method used by Molina et. al.¹⁰⁰ over the first 10° in 2θ of the pattern (Figure 6.2a), with slight modifications (Section S2.4), which suggests that N2N3 has the highest amount of crystallite strain (51.8%) followed by C2C3 (49.3%), N2C3 (47.8%) and C2N3 (36.5%).

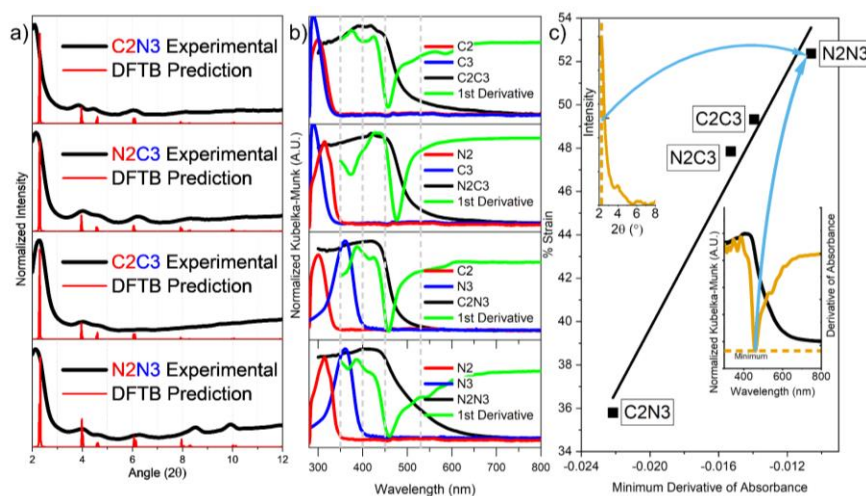


Figure 6.2 (a) First 12° 2θ of the PXRD patterns of the four COFs (b) Kubelka-Munk transformed diffuse reflectance spectra of the four COFs with their monomers and the derivative of their DR spectrum (c) Trendline showing the trend between peak broadening in the PXRD pattern with minimum of DR derivative.

Like many COFs, the Kubelka-Munk transformed diffuse reflectance (DR) spectra (Figures 6.2b) show broad absorption in the ultraviolet and visible regions (>400 nm).^{104,106,210–212} Because the monomers show negligible absorption in the visible region, we attribute the visible absorption for each COF to the charge transfer (CT) band, which is consistent with our previous report⁹⁰ and further supports the formation of COFs. Tails stretching from 450–700 nm are observed in each DR spectrum, but their steepness differs. By plotting the steepness of the tails (measured as the minimum slope) against the strain quantification of the PXRD peaks we observe a strong trend (Figure 6.2c, $R^2=0.964$).

Because interlayer packing is previously shown to have a drastic effect on the charge carrier mobility in organic semiconductors;^{213,214} we turn to computational methods to estimate the average^{75,215} interlayer distance. Starting from a reference unit cell,¹³⁹ SCC-DFTB as part of DFTB+^{109–111,125} is used to optimize both the structure and unit cell parameters of the COF series (Section 2.4). The optimized unit cells yield nearly hexagonal and eclipsed structure with an interlayer c-axis magnitude of 3.41–3.48 Å (Table 6.1). The predicted PXRD patterns show good agreement with experimental results (Figure 6.2a). By optimizing the atomic structure and unit cell parameters in tandem, we gain a reliable model of the bulk structure. Accordingly, we decomposed the predicted structures into edge and star units (Scheme 6.1c) for computational studies of the structure-property relationships of COFs in the current work.

Table 6.1 Unit cell parameters of COF structures predicted by SCC-DFTB

COF	a	b	c	α	β	γ
N2N3	44.4	44.4	3.41	89.7	90.2	121.
C2N3	44.6	44.6	3.42	89.8	90.0	121.
N2C3	44.6	44.6	3.48	89.7	89.9	121.
C2C3	44.7	44.7	3.46	90.0	90.0	120.

Table 6.2 Predicted and experimental transitions of COFs and monomers. TDDFT (CAM-B3LYP/6-311G**) predictions on single-layer edge units are the first transition with appreciable oscillator strength ($f > 0.01$). Experimental values determined at peak max for monomers, minimum of first derivative for COFs.

COF	Predicted			Experiment
	f (A.U.)	ΔE (eV)	ΔE (nm)	ΔE (nm)
N2	0.867	4.336	286.0	315
C2	0.884	4.351	285.0	300
N3	1.088	4.311	287.6	362
C3	0.088	4.764	260.2	290
N2N3	2.654	3.424	362.2	459
N2C3	3.110	3.294	376.4	476
C2N3	2.838	3.416	363.0	459
C2C3	2.646	3.442	360.2	456

Table 6.3 CT descriptors for N2N3 and N2C3.

		CTC (%)	COH:PR	RMSeh (Å)	Net Electron Gain (%)			
					Imine	Bipyridine	Phenylene	Tritopic Core
N2N3	VB ₁ -CB	57.7	0.88	5.148	7.5	6.6	-16.7	2.6
	VB ₂ -CB	46.0	0.88	3.946	-8.6	8.1	-0.7	1.2
N2C3	VB ₁ -CB	59.7	0.89	5.739	12.9	7.0	-15.0	-4.9
	VB ₂ -CB	49.6	0.91	3.495	-22.6	17.0	4.0	1.5

6.3 The Nature of Intralayer CT in Isostructural N2N3 and N2C3 COFs

Given that some CT-like state is populated in our COFs, its nature is important to understand the electronic correlation upon light absorption. We performed TDDFT and TDM analysis to gather information on the structure and energetics of the excitons. TDDFT is performed on an edge unit (Scheme 6.1c) of the optimized unit cell with branching carbons capped by hydrogen atoms. While the lowest energy allowed transitions predicted by TDDFT are ~0.7 eV higher in energy than experimental values, the trend of transition energies between COFs (Table 6.2) is accurately predicted, lending credibility to the model. The first and third lowest energy transitions of each COF correspond to transitions from the HOMO and HOMO-1 to the LUMO, respectively. These transitions are optically allowed and likely play primary

roles in the exciton dynamics so discussion of TDDFT and TDM analysis will primarily focus on these two transitions. Figure 6.3a shows the natural transition orbitals (NTOs)¹³² of N2N3 VB₁-CB and reveals that the exciton has $\pi\pi^*$ character and is delocalized across a majority of the edge unit.^{118,133,216} Visual inspection of the N2N3 VB₂-CB NTO (Figure 6.3b) reveals that the ES populates similar π^* orbitals as the VB₁-CB transition but the ground state (GS) originates partially from non-bonding N orbitals. From this evidence we attribute locally excited (LE) character to the VB₂-CB transition.

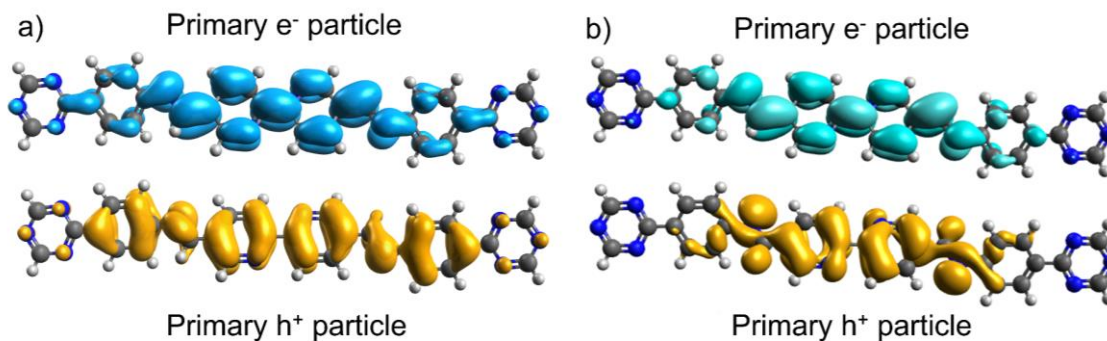


Figure 6.3 (a) NTO contributions of VB₁-CB transition for N2N3. (b) NTO contributions of VB₂-CB transition for N2N3.

Next, TDM analysis was performed in the TheoDORÉ package¹¹⁷ to understand the populated CT states^{217–219} and quantitatively predict the charge transfer character (CTC), electron-hole separation (COH:PR), and size of the exciton (RMSeh) along with generating electron correlation plots between user-defined fragments (Figure 6.1d). The selection of the molecular fragments is crucial to our TDM analysis and as such we carefully selected four fragments in the intralayer case - the tritopic core (N3 or C3), the phenylene attached to the tritopic core, the imine linker, and the bridge (N2 or C2).

Figure 6.1d presents the TDM analysis electron/hole correlation plots for the VB₁ & VB₂ to CB transitions of N2N3 and N2C3, which provide a visual representation of electron density movement between the specific fragments defined in our study (see Appendices for more information about TDM analysis). For instance, The bipyridine of the N2N3 VB₁-CB transition has significant local character (row 2, column 2). However, there is also significant electron correlation between the imine ES with the phenylene GS (row 1, column 3) and the bipyridine ES with the phenylene GS (row 2, column 3), indicative of CT like behavior. Notably, the lower triangular correlations are larger than their transposes which indicates that the CT is asymmetric favoring electron transfer (ET) towards bipyridine.¹³³ The VB₂-

CB transition exhibits more LE correlation at imine (row 1, column 1) and less phenylene/imine and phenylene/bipyridine correlation. For this transition, the upper triangular elements are larger than the lower triangular elements, suggesting hole transfer (HT) takes place away from bipyridine. Overall, the N2C3 VB₁-CB is similar to N2N3, but with noticeably less LE correlation at the imine, suggesting more CT takes place.

In the case of the VB₂-CB transition, the plots of N2N3 and N2C3 are considerably different. N2N3 is of mostly local transition character, but there is also correlation between the bipyridine ES and imine GS (#2, #1) that is larger than its transpose (#1, #2), indicating that HT from bipyridine to imine occurs. N2C3 also has significant correlation between the bipyridine ES (#2, #1) and phenylene ES (#3, #1) with the imine GS, again indicating HT originating from the bipyridine bridge to imine. However, unlike N2N3, there is less LE on the bipyridine, which suggests that the HT on N2C3 is much more pronounced.

CTC in N2N3 VB₁-CB (Table 6.3) is quantified as 0.577, RMSeh is found to be 5.148 Å, and COH:PR, which reflects the electron-hole separation, is 0.88, suggesting some degree of electron/hole separation and a moderate amount of CT. Upon excitation, electron density migrates to the imine linker and bipyridine bridge with 7.5% and 6.6% net electron gain, respectively, while phenylenes act as the electron donor netting 16.7% electron loss. The triazine core, which is expected to be strongly electron withdrawing due to its π -electron deficiency, surprisingly nets only 2.6% electron gain. In the N2N3 VB₂-CB transition, COH:PR is consistent with VB₁-CB (0.88) but other measures are smaller; CTC is 0.46 and the exciton size is 3.946 Å. In this case, the data indicates phenylene and triazine participate only marginally; imine nets 8.6% electron loss primarily to bipyridine that nets 8.1% electron gain.

In N2C3 the VB₁-CB transition has more CTC (0.597, Table 6.3) than N2N3 and comparable COH:PR (0.89), yet the size of the exciton (5.739 Å) is significantly larger. Electron density localization in the VB₁-CB transition of N2C3 nets 12.9% electron gain at the imine and 7.0% at the bipyridine. Like N2N3, the phenylene unit is the main electron donor netting 15% electron loss. However, the tritopic core acts as an electron donor with 4.9% net electron loss, an expected result of substituting for an electron donating group. The exciton created through the N2C3 VB₂-CB transition has more electron/hole separation with COH:PR of 0.91, but the other measures are considerably smaller than VB₁-CB; CTC is only 0.496, and exciton size is 3.495 Å. Tracking the migration of electron density, we find that the main

electron donor is the imine linker, consistent with N2N3. However, the magnitude of donation (22.6% net electron loss) is significantly larger than N2N3. This donation corresponds with a large localization (17.0% net electron gain) of electron density at the bipyridine bridge, and smaller electron gain at the phenylene, and tritopic core.

With these results, it is apparent that monomer selection is certainly important to CT. However, it is interesting to note that changing from electron withdrawing to donating tritopic core is predicted to lead to only a moderate increase of electron density at the bipyridine (the key unit for embedded molecular catalyst) after excitation of VB₁-CB, but a large increase of electron density after excitation of VB₂-CB with significant LE character. This can be explained by the bifurcation of the imine linker acting as either an electron donor or acceptor, suggesting it mediates CT which helps explain similar absorption energies in the COFs without a traditional electron acceptor group (e.g. C2C3).

Lastly, to ensure that the edge unit is a reliable representation of photophysical properties, we performed TDDFT on the star unit of the bulk model (Scheme 6.1c). Results on the star shaped units of the covalent organic frameworks indicate that the lowest ES is populated by two nearly degenerate transitions; one on a single branch of the tritopic core, the second on the other spread between two branches of the tritopic core. These transitions are slightly higher in energy than the lowest energy transition of the edge unit (3.69 eV vs. 3.42 eV). For both degenerate transitions, CTC is more pronounced in the star unit (0.62), and the exciton is better separated (COH:PR=0.93), but RMSeh is much smaller (3.998 Å) with respect to that of edge unit. The phenylene units lose 22.0% net electron density while pyridine and triazine units gain 13.3% and 6.6% net electron density, respectively. While the TDM statistics seem to provide results that show pronounced CT characteristics, the fragment selection is less representative of the true COF structure because the ratio of the fragments (3 imine, 3 pyridine, 3 phenylene, 1 triazine) causes the TDM metrics to overstate the importance of the tritopic triazine core. Finally, the transitions on separate branches have little interaction, as indicated by the small RMSeh. This conclusion is supported by studies on the band dispersion of 2D COFs with symmetric six-member tritopic cores.⁵⁹ Thomas, et. al. finds that in these Kagome lattice COFs the VB and CB are both completely flat, indicating little to no interaction occurs between branches due to destructive wavefunction interference at the *meta*- positions, leading to relatively

weak conjugation across the six-member core. A conclusion we also arrived to when triphenylamine was substituted for the aryl core.²⁰⁴

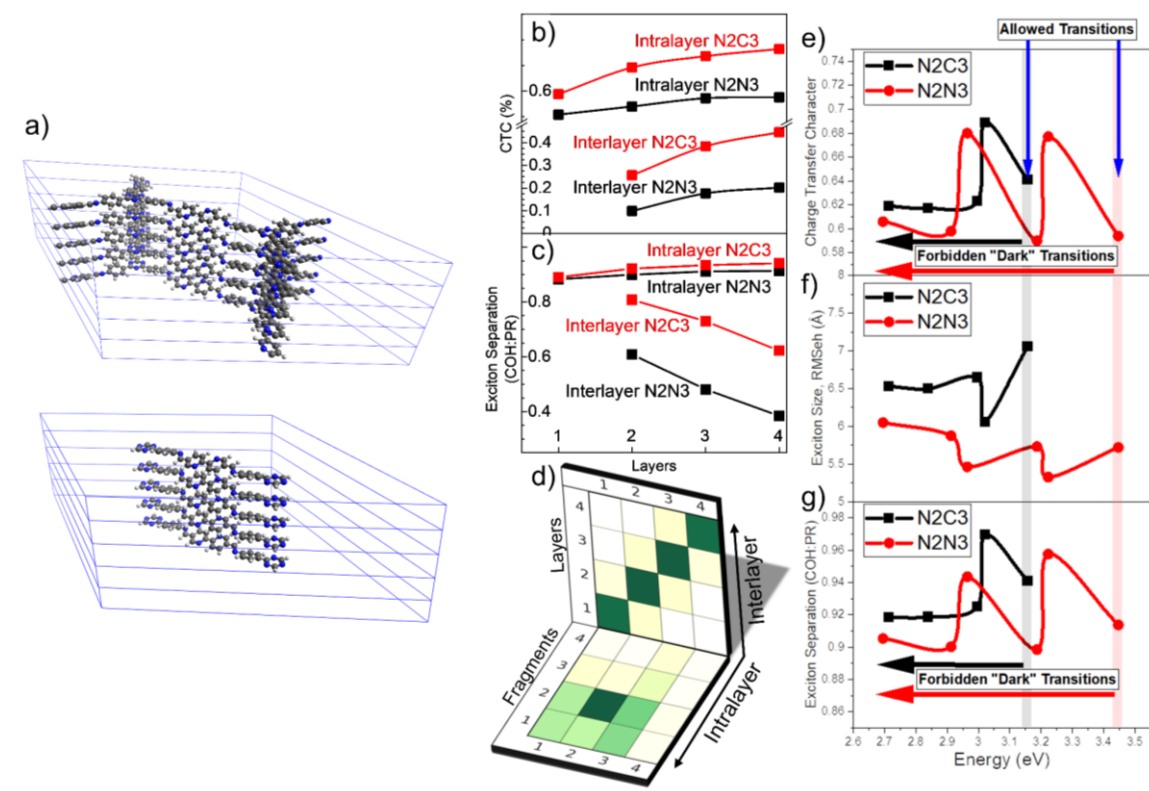


Figure 6.4 Bulk model used to analyze exciton properties upon aggregation (a). CTC (b) and COH:PR (c) of N2N3 (red) and N2C3 (black) as layers are added to the systems analyzed in the intralayer and interlayer directions. (d) Electron correlation plots of four-layer N2N3 in the intralayer and interlayer directions. Fragments are defined as: #1 = imine, #2 = bipyridine, #3 = phenylene, #4 = triazine.

6.4 The Role of Interlayer Interactions on CT in N2N3 COF

We also evaluate interlayer interactions in relation to electronic transitions by incrementally adding up to four layers of N2N3 and N2C3 edge units by replicating the unit cell along the c-axis and capping the branching carbons of the tritopic cores with hydrogens (Figure 6.4a). The multilayer electronic transitions are then calculated by TDDFT and analyzed by TDM analysis. To account for the possibility of bidirectional carrier mobility in 2D COFs, TDM analysis is performed by considering CT both amongst previously defined fragments (imine, bipyridine, phenylene, tritopic core) as well as between individual layers (Figure 6.4b-d).

TDM analysis of multilayer N2N3 uncovers that interlayer CTC increases as layers are added to the system (Figure 6.4b), but COH:PR decreases (Figure 6.4c). The inverse relationship between CT and

COH:PR suggests that intermolecular CT predominantly occurs between nearest neighbors, which is supported by the electron/hole correlation plot (Figure 6.4d) in line with previous works.⁵⁸ While the relationship of CTC to COH:PR is consistent in N2C3, the magnitude of this ratio is considerably different. For the four-layer case, N2N3 has COH:PR of only 0.38 with respect to 0.62 in N2C3. These results suggest that an exciton generated after photoexcitation in N2N3 may reside on only a few layers throughout its lifetime, indicating a lack of significant carrier mobility across layers. Conversely, the probability for the exciton to delocalize is greater for N2C3. The disparity in interlayer carrier mobility is attributable to the interplay between CS dynamics via super-exchange charge transfer (SECT) coupling and coulombic forces.⁶² SECT coupling is a process of exciton delocalization in which electron and hole wavefunctions transfer to adjacent layers.²²⁰ This process is adversely affected by coulombic forces, which can be especially strong in the low dielectric environment of an organic crystallite like a COF, although strategies have been developed to lower coulombic forces between organic layers.^{68,221} Since the amount of wavefunction interaction should be similar in both N2N3 and N2C3 due to their similar structures, the larger exciton in N2C3 (5.739 Å) than N2N3 (5.148 Å) may indicate more screening of intermolecular coulombic forces^{68,221–223} arising from cooperative polarizability,^{197,224} which is described by the essential states model^{225,226} that addresses some shortfalls in the dipolar Frenkel exciton model.^{65,198,227} This results in a larger exciton volume upon aggregation in N2C3 (7.06 Å) than N2N3 (5.72 Å), suggesting a relationship between the size of the intralayer exciton with delocalization of the interlayer exciton. Regardless, SECT coupling may not result in meaningful interlayer exciton separation in N2C3 since COH:PR (0.62) is well below 1.

Like the interlayer case, intralayer CTC increases when a layer is added, and more net electron gain is experienced at the N2 bridge with respect to the single layer (Figure 6.4d). Further stacking reveals that intralayer CTC and COH:PR continue to increase as layers are added (Figures 6.4b, 6.4c). In the four-layer case, dark states below the allowed transition of N2N3 (Figure 6.4e-g) have CTC oscillations between ~0.6 and ~0.68, whereas CTC below the allowed transition in N2C3 decreases monotonically. These results suggest that domains of ordered stacking may increase the activity of COFs for photocatalysis by activating the donor/acceptor pair through enhanced intralayer CT.

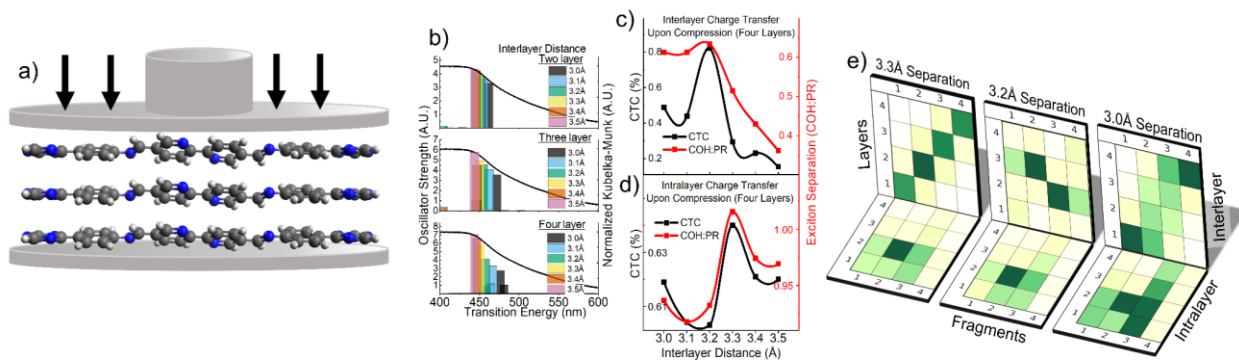


Figure 6.5 (a) Diagram of three-layer N2N3 edge unit being compressed. (b) TDDFT predicted absorption with varying levels of compression on two-, three-, and four-layer N2N3 COF systems. (c) Interlayer and (d) intralayer CTC and exciton separation of four-layer N2N3 at varying levels of compression. (e) Electron/hole correlation plots generated by TheoDORE in both the interlayer and intralayer directions. at varying levels of compression.

6.5 Tail State Analysis of Isostructural COFs

The TDDFT results to this point cannot explain the experimentally observed broad absorption tails in the DR spectrum of the COFs. To propose an explanation of these tail states, a computational model is proposed, in which layers of N2N3 are optimized under incrementally constrained conditions, illustrative of uniaxial inhomogeneous strain (i.e., compression), is conducted (Figure 6.5a). TDDFT is then performed on the structures and the transitions are plotted to align with the intramolecular CT peak at 444 nm. Figure 6.5b shows the predicted absorption of two-, three-, and four-layer N2N3 under varying levels of compression. Decreasing the interlayer distance significantly lowers the allowed transition energies and intensities, and the predicted absorption begins to resemble the measured one. These transitions occur because structural distortion, as suggested in prior literature⁸³, begins to mix allowed and forbidden transitions. As discussed in above, the trend in crystallite strain closely follows the broadness of the diffuse reflectance peaks (Figure 6.2), suggesting the correlation of crystallite strain with the broad absorption tails.¹⁰⁰ We note that the type of strain presented here represents only a hypothetical origin, and other explanations should be considered. Despite this, our results show that COF strain defects are a plausible source of tail states and merit further investigation.

To further assess the possible origin and nature of tail states, we perform TDM analysis on the four-layer N2N3 system at varying interlayer separation. The results reveal that interlayer CTC significantly increases as the layers are brought to proximity (Figure 6.5c). This coincides with increasing COH:PR – in agreement with a study that found decreasing the interlayer distance by solution shearing had

a significant effect on charge mobilities.²²⁸ However, COH:PR at 3.0 Å (COH:PR=0.67) remains significantly less than 1, suggesting that photoexcitation even under significant compression may not generate free carriers in N2N3. One noticeable feature of the CT characteristics is high CTC at 3.2 Å interlayer separation (0.821), suggesting that there exists an optimal balance between dispersion and coulombic forces for charge separation to occur. Compared to interlayer CT, the impact of interlayer separation on intralayer CTC and COH:PR follow the same pattern – however, the trend is less clear (Figure 6.5d). At 3.3 Å interlayer separation, CTC (0.64) and COH:PR (1.0) are maximized but decreased at shorter separation. Because Coulombic repulsion increases as $1/r^2$, when layers are very close to one another these forces dominate SECT coupling, preventing more effective CT.

Strain effects on CT of N2N3 edge units are visually depicted in the electron/hole fragment correlation plots in Figure 6.5e. The interlayer correlation plots show that the exciton changes from predominantly local transition character with nearest neighbour interactions at 3.3 Å interlayer distance to significant neighbour and next-nearest-neighbour CT at the compressed 3.2 Å, and 3.0 Å interlayer distance. Notably, the correlation plots are symmetric, suggesting that ET does not take place but instead charge delocalization or dissociation is more likely. Intralayer CTC correlation plots (Figure 6.5e) clearly show the activation of the phenylene donor units upon compression, which significantly correlate with the imine linker and bipyridine bridge. These results together suggest that if tail states arise from inhomogeneous strain in crystallites, studies probing the tail region by fs-OTA would show an outsized effect when measured under strain. According to this model, the shorter interlayer distance in COFs would not only enhance the light harvesting ability of COFs by extending the absorption spectrum further to the visible region but also facilitate charge separation, which could benefit photocatalysis.

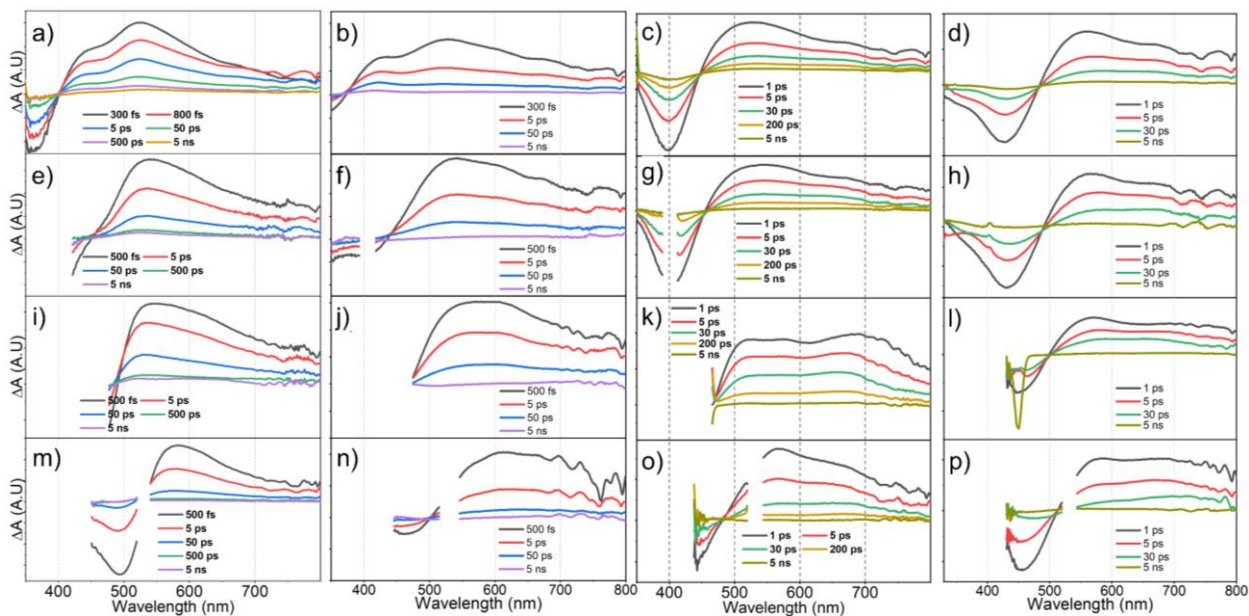


Figure 6.6 Optical transient absorption (OTA) spectra after 350 nm excitation (a) N2N3 (b) N2C3, (c) C2N3 (d) C2C3; OTA spectra after 400 nm excitation (e) N2N3, (f) N2C3 (g) C2N3, (h) C2C3; OTA spectra after 450 nm excitation (i) N2N3, (j) N2C3, (k) C2N3, (l) C2C3; OTA spectra after 530 nm excitation (m) N2N3, (n) N2C3, (o) C2N3, (p) C2C3.

6.6 Excited State Dynamics of CT Excitons in Isostructural COFs by fs-OTA Spectroscopy

To support our hypotheses based on the theoretical study of CT excitons and tail states, it is necessary to correlate our predictions with experiment. fs-OTA spectroscopy is conducted to gain a fundamental understanding of CT exciton dynamics in N2N3 and N2C3 while using the other isostructural COFs (C2C3, C2N3) as controls. To form a thin film suitable for analysis, the microcrystalline powder is evenly dispersed within a Nafion matrix through sonication and drop-casting. Selecting excitation wavelengths across the absorbance spectrum (350nm-530nm) allows us to probe multiple excitonic pathways and to gain an important understanding of the electronic structure below the CT band.

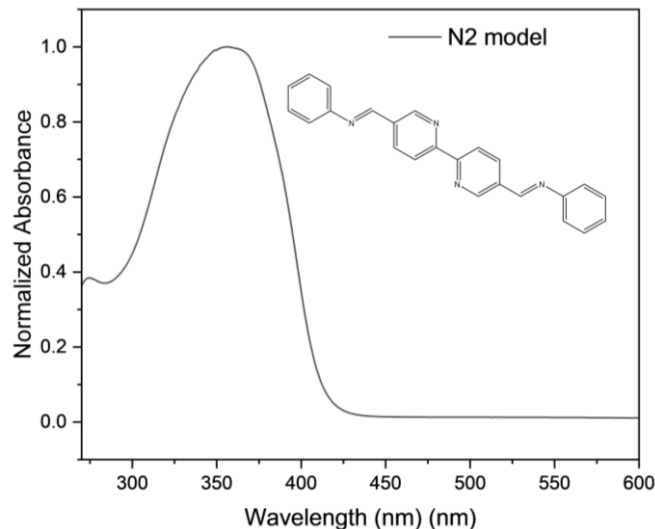


Figure 6.7 Absorption spectrum of N2 model in acetonitrile.

As shown in Figure 6.6a, when N2N3 is excited by a 350 nm pump pulse, a few noticeable features are immediately present. First, a negative feature centred at 360 nm corresponds to ground state bleach (GSB), which results from the reduced oscillation strength of the transition from the VB to the CB due to electrons filling the CB. Second, there is a broad positive feature from 400-800 nm attributable to excited state absorption (ESA). Inspection of the ESA band shows a distinct shoulder centred at 440 nm, which can be attributed to a transition with electrons localized at bipyridine. This is supported by the computational results which predicted that the VB₂-CB transition originates in part from non-bonding orbitals of imine and bipyridine and by the presence of the same shoulder in the OTA spectra of N2C3 (Figure 6.6b) yet absent in the spectra of C2C3 and C2N3 (Figure 6.6c, 6.6d). This shoulder occurs in bipyridine containing COFs because the N2 monomer has marginal absorption at 350 nm. For confirmation, an N2 model system made by condensation with benzaldehyde red shifts upon condensation (Figure 6.7), supporting the assignment. Conversely, the C2 monomer does not have absorption at 350 nm and thus this shoulder is noticeably absent in C2C3 and C2N3 COFs. With evidence from our TDDFT calculations and TDM analysis (vide supra), we ascertain that 350 nm excites the VB₂-CB transition, which includes a LE transition coupled to a CT transition (LE/CT) that results in a gain of oscillator strength observable in the OTA spectra. Furthermore, mixing LE character into the CT transition reduces the size of the exciton, resulting in greater coulombic attraction between the electron/hole pair and thus the higher

energy of the shoulder than the main peak. These assignments were further supported from the OTA spectra of N2C3, where the shoulder is blue shifted to 420 nm from 440 nm. This is consistent with our TDDFT results, which predicts that VB₂-CB transition generates a smaller exciton in N2C3 (3.459Å) than N2N3 (3.946Å). Besides this 440 nm shoulder, ESA above 500 nm can be generally attributed to the formation of a CT exciton that is common to all excitation energies in all COFs within this work. This CT exciton signature commonality implies that CT behaviours are similar regardless of monomer selection and indicates the importance of the imine linker.

Excitation of the COFs with 400 nm and 450 nm pump pulses which primarily excite the intramolecular CT bands yields similar ESA absorption above 500 nm (Figure 6.6e-6.6i), consistent with the assignment to CT. However, in contrast to 350 nm excitation, the ESA shoulder in N2N3 and N2C3 is no longer present. This absence is either due to the lack of VB₂-CB absorption at these excitation wavelengths or overlap with GSB. Notable red shift of the GSB band is observed with increasing excitation wavelength as evidenced by the bathochromic shift of the isosbestic points from ~400 nm, to ~445 nm, to ~485 nm for 350 nm, 400 nm, and 450 nm excitations, respectively. These experimental observations correlate well with the theoretically predicted VB₁-CB and VB₂-CB transitions of N2N3 and N2C3 by TDDFT, which demonstrates that the lowest allowed transitions arise from different GS (VB₁ and VB₂), i.e. the 400 nm and 450 nm likely involve excitation of VB₁-CB transition, resulting in GSB band depending on the excitation wavelength.

Besides the CT transition, the OTA spectra following the excitation of tail state transitions at 530 nm are also collected (Figure 6.6m-6.6p). Consistent with the spectra collected at higher energy excitation, the GSB band moves further to longer wavelengths. However, unlike the simultaneous GSB recovery and ESA decay upon higher energy excitation, the 530 nm pulse reveals the negative GSB recovery is significantly faster in N2N3 than the positive ESA decay. This similar asynchronous phenomenon is observed to a lesser degree in the 530 nm excitation kinetic traces of N2C3, C2C3, as well as previously reported conjugated polymers attributed to the formation of aggregates,²²⁹ leading us to believe it arises due to a delocalized nature in the tail states. Furthermore, the degree of asynchrony follows the trend of crystallite strain and tail state steepness established previously decreasing from N2N3 to C2C3 to C2N3 and N2C3. Additional experimental evidence arises from relative energies of the GSB and pump

wavelength; in the 530 nm excitation OTA spectra of the COFs (Figure 6.6n-6.6p) the GSB is higher in energy than the pump wavelength, indicating that excitation of tail states is directly related to higher energy transitions and suggesting the presence of delocalized sub-band gap states. Through the lens of delocalization, we propose that the tail state transition is initially delocalized over many framework layers, bleaching transitions that may have occurred within the exciton volume. The electron/hole pair, unable to escape their coulombic attraction then quickly localize to a trap at a strain site, defect site, or crystallite surface leading to fast recovery of the GSB.

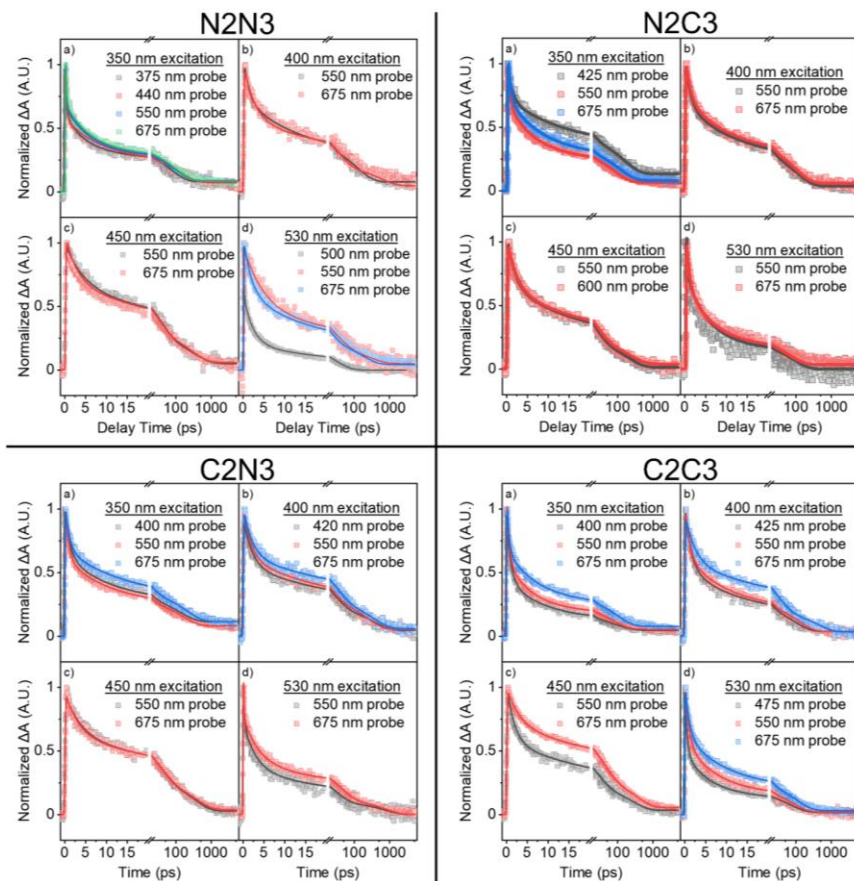


Figure 6.8 Normalized OTA kinetic traces of COFs at different probe wavelengths after different excitation energy pump pulses. N2N3 (top-left quadrant), N2C3 (top-right quadrant), C2N3 (bottom-left quadrant), and C2C3 (bottom-right quadrant). Excitation energies in each quadrant (a) 350 nm, (b) 400 nm, (c) 450 nm, and (d) 530 nm.

Shown in Figure 6.8 are the normalized kinetic traces of COFs probed at different wavelengths after 350 nm, 400 nm, 450 nm, and 530 nm excitation. In the 350 nm excitation kinetics (a in each quadrant of Figure 6.8), GSB recovery, LE/CT ESA decay, and CT ESA decays follow different trends for each COF. In N2N3 and C2N3 decays are synchronous, which together with a clear isosbestic point at 400 nm in

the OTA spectra, suggests that they correspond to the same relaxation process, i.e., recombination of the electron in the CB with the hole in VB₂. In N2C3 LE/CT ESA decay is slowed relative to CT ESA decay, suggesting its donor-acceptor architecture leads to a well-separated LE/CT state in line with TDDFT and TDM analysis. C2C3 on the other hand, possesses somewhat divergent kinetics within its CT ESA decay, suggesting the longer wavelengths of the spectral window may correspond to excitons with lower binding energies. Kinetic traces of the COFs after 400 nm and 450 nm excitation all show relatively synchronous decay within the CT ESA and (where applicable) the GSB recovery except for the previously noted C2C3 low binding energy excitons. At 530 nm excitation the previously mentioned trend in asynchronous GSB/ESA recovery/decay is clearly observable in N2N3 and to a lesser extent in C2N3 and C2C3.

Table 6.4 Fitting results for N2N3 at different excitation and probe wavelengths. A 150 fs instrument response factor was used to fit kinetic trace after 350 nm and 530 nm excitations and 250 fs instrument response factor used for 400 nm and 450 nm excitations due to a rising component in the 400 nm and 450 nm excitation kinetics that could not be otherwise fit.

N2N3	Excitation, nm (Probe, nm)	IRF (fs)	t1, ps (A1, %)	t2, ps (A2, %)	t3, ps (A3, %)	t4, ps (A4, %)	t _{1/2} , ps
	350 (375)	150	4.54 (24.91)	76.83 (20.42)	344.10 (48.17)	>5000 (6.51)	2.79
		Error	1.50 (3.93)	18.00 (2.48)	110.00 (9.04)	(0.84)	
	350 (440)	150	8.27 (25.66)	146.40 (16.44)	381.30 (51.86)	>5000 (6.03)	3.19
		Error	0.96 (1.31)	22.00 (1.11)	47.00 (3.77)	(0.42)	
	350 (550)	150	5.82 (24.77)	96.55 (16.84)	228.90 (52.14)	>5000 (6.24)	3.99
		Error	0.52 (0.97)	9.50 (0.82)	30.00 (5.83)	(0.27)	
	350 (675)	150	5.57 (24.15)	102.50 (17.06)	200.90 (53.14)	>5000 (5.65)	4.19
		Error	0.49 (0.93)	9.70 (0.76)	30.00 (7.62)	(0.28)	
	400 (550)	250	1.19 (29.85)	11.43 (36.03)	133.50 (26.75)	>5000 (7.37)	11.21
		Error	0.28 (3.23)	2.00 (2.93)	22.00 (2.44)	(0.59)	
	400 (675)	250	2.62 (43.29)	33.13 (37.05)	590.40 (14.85)	>5000 (4.81)	10.81
		Error	0.40 (2.98)	6.40 (2.79)	250.00 (2.59)	(1.20)	
	450 (550)	250	4.22 (32.62)	37.66 (42.23)	364.90 (20.00)	>5000 (5.15)	18.06
		Error	0.91 (4.01)	8.80 (4.07)	0.13 (4.54)	(0.94)	
	450 (675)	250	2.72 (33.38)	28.41 (38.38)	304.50 (22.16)	>5000 (5.67)	17.56
		Error	0.43 (2.53)	4.60 (2.52)	65.00 (2.74)	(0.65)	
	530 (500)	150	0.11 (74.79)	2.34 (16.83)	31.06 (8.39)	---	0.83
		Error	0.17 (17.98)	0.23 (0.76)	2.90 (0.54)	---	
	530 (550)	150	30.52 (5.03)	5.03 (35.08)	299.1 (12.96)	>5000 (5.35)	9.80
		Error	10.21 (1.50)	1.50 (29.00)	370.1 (11.40)	(1.82)	
	530 (675)	150	1.89 (40.18)	15.32 (37.40)	176.30 (18.20)	>5000 (4.22)	6.60
		Error	0.27 (3.21)	2.60 (2.90)	41.00 (2.33)	(0.54)	

Table 6.5 Fitting results for N2C3 at different excitation and probe wavelengths. A 150 fs instrument response factor was used to fit kinetic trace after 350 nm and 530 nm excitations and 250 fs instrument response factor used for 400 nm and 450 nm excitations due to a rising component in the 400 nm and 450 nm excitation kinetics that could not be otherwise fit.

N2C3	Excitation, nm (Probe, nm)	IRF (fs)	t1, ps (A1, %)	t2, ps (A2, %)	t3, ps (A3, %)	t4, ps (A4, %)	t _{1/2} , ps
	350 (425)	150	0.99 (29.91)	12.22 (30.53)	159.50 (26.75)	>5000 (12.80)	14.32
		Error	0.19 (2.53)	2.00 (2.17)	23.00 (1.94)	(0.55)	
	350 (550)	150	0.42 (40.27)	5.98 (33.68)	85.07 (20.52)	>5000 (5.53)	4.42
		Error	0.060 (2.97)	0.56 (1.43)	8.60 (1.13)	(0.33)	
	350 (675)	150	0.60 (34.69)	7.71 (36.06)	114.50 (21.89)	>5000 (7.36)	6.32
		Error	0.094 (2.35)	0.75 (1.62)	13.00 (1.23)	(0.38)	
	400 (550)	250	1.21 (37.01)	11.47 (34.36)	113.20 (25.13)	>5000 (3.50)	7.57
		Error	0.17 (2.47)	1.70 (2.29)	15.00 (2.17)	(0.42)	
	400 (675)	250	1.19 (32.07)	9.84 (34.59)	104.00 (27.82)	>5000 (5.52)	8.77
		Error	0.25 (3.33)	1.80 (3.03)	14.00 (2.40)	(0.49)	
	450 (550)	250	1.90 (37.77)	20.44 (41.22)	207.00 (19.67)	>5000 (1.34)	9.36
		Error	0.33 (3.02)	3.50 (2.95)	57.00 (3.17)	(0.67)	
	450 (675)	250	2.16 (38.16)	22.70 (39.65)	229.40 (18.30)	>5000 (3.88)	10.56
		Error	0.21 (1.75)	2.40 (1.73)	40.00 (1.89)	(0.39)	
	530 (550)	250	0.31 (42.90)	5.33 (41.90)	87.96 (15.20)	---	3.10
		Error	0.15 (13.61)	1.10 (3.93)	28.00 (2.79)	---	
	530 (675)	150	0.71 (37.63)	5.60 (43.17)	65.82 (19.21)	---	3.60
		Error	0.18 (4.56)	0.93 (3.90)	12.00 (2.23)	---	

Table 6.6 Fitting results for C2N3 at different excitation and probe wavelengths. A 150 fs instrument response factor was used to fit kinetic trace after 350 nm and 530 nm excitations and 250 fs instrument response factor used for 400 nm and 450 nm excitations due to a rising component in the 400 nm and 450 nm excitation kinetics that could not be otherwise fit.

C2N3	Excitation, nm (Probe, nm)	IRF (fs)	t1, ps (A1, %)	t2, ps (A2, %)	t3, ps (A3, %)	t4, ps (A4, %)	t _{1/2} , ps
	350 (400)	150	1.24 (38.515)	10.74 (32.344)	140.2 (18.139)	>5000 (11.002)	6.05
	Error		220 (3.375)	2.1 (3.101)	32 (2.161)	(0.576)	
	350 (550)	150	0.82 (43.094)	10.18 (31.372)	164.4 (18.046)	>5000 (7.488)	4.65
	Error		0.093 (2.11)	1.2 (1.66)	25 (1.23)	(0.258)	
	350 (675)	150	0.95 (34.457)	12.9 (33.157)	207.5 (21.454)	>5000 (10.932)	10.3
	Error		0.14 (2.6)	1.6 (1.999)	32 (1.634)	(0.507)	
	400 (420)	250	2.08 (42.249)	26.21 (34.677)	377.4 (18.169)	>5000 (4.905)	9.92
	Error		0.36 (3.28)	5.9 (3.09)	140 (3.059)	(1.072)	
	400 (550)	250	1.68 (39.227)	19.05 (33.065)	244.8 (22.466)	>5000 (5.241)	10.3
	Error		0.21 (2.231)	2.8 (2.025)	42 (1.914)	(0.556)	
	400 (675)	250	2.12 (37.106)	31.03 (35.997)	372.6 (20.99)	>5000 (5.908)	16.9
	Error		0.32 (2.46)	5.5 (2.635)	99 (2.909)	(0.835)	
	450 (550)	250	3.66 (34.427)	37.06 (38.041)	359.3 (24.56)	>5000 (2.972)	20.6
	Error		0.69 (3.366)	8.7 (3.741)	100 (4.291)	(0.89)	
	450 (675)	250	3.24 (35)	37.57 (37.85)	387.9 (23.159)	>5000 (3.991)	20.6
	Error		0.41 (2.095)	5.7 (2.42)	78 (2.744)	(0.646)	
	530 (550)	150	0.23 (48.622)	2.98 (26.826)	29.55 (18.003)	794.5 (6.549)	2.22
	Error		0.085 (13.3)	0.95 (3.847)	10 (3.008)	440 (1.684)	
	530 (675)	150	0.11 (64.511)	3.78 (17.468)	43.08 (12.776)	826.3 (5.246)	3.62
	Error		0.024 (22.909)	0.45 (0.934)	6.9 (0.859)	210 (0.729)	

Table 6.7 Fitting results for C2C3 at different excitation and probe wavelengths. A 150 fs instrument response factor was used to fit kinetic trace after 350 nm and 530 nm excitations and 250 fs instrument response factor used for 400 nm and 450 nm excitations due to a rising component in the 400 nm and 450 nm excitation kinetics that could not be otherwise fit.

C2C3	Excitation, nm (Probe, nm)	IRF (fs)	t1, ps (A1, %)	t2, ps (A2, %)	t3, ps (A3, %)	t4, ps (A4, %)	t _{1/2} , ps
	350 (400)	150	0.96 (56.998)	8.27 (28.263)	102.4 (10.237)	>5000 (4.502)	1.79
		Error	0.11 (3.067)	1.7 (2.828)	34 (1.955)	(0.481)	
	350 (550)	150	0.54 (49.193)	5.51 (31.399)	79.46 (14.824)	>5000 (4.585)	2.02
		Error	0.056 (2.15)	570 (1.642)	9.8 (1.02)	(0.289)	
	350 (675)	150	0.48 (41.691)	7.02 (32.247)	102.8 (19.436)	>5000 (6.626)	4.50
		Error	0.067 (2.785)	730 (1.513)	12 (1.215)	(0.364)	
	400 (425)	250	1.35 (48.755)	10.98 (29.446)	97.53 (18.361)	>5000 (3.438)	3.88
		Error	0.23 (4.286)	3.4 (4.053)	29 (3.856)	(0.635)	
	400 (550)	250	0.99 (40.957)	9.39 (35.543)	123.6 (20.106)	>5000 (3.395)	5.18
		Error	0.15 (2.741)	1.3 (2.413)	20 (1.71)	(0.459)	
	400 (675)	250	2.42 (39.245)	29.44 (40.289)	419.1 (16.916)	>5000 (3.55)	12.17
		Error	0.35 (2.646)	4.7 (2.524)	130 (2.524)	(0.867)	
	450 (550)	250	1.91 (43.568)	25.71 (34.864)	280.2 (18.225)	>5000 (3.343)	8.87
		Error	0.25 (2.574)	4.8 (2.719)	85 (3.038)	(0.755)	
	450 (675)	250	3.18 (29.556)	39.3 (42.143)	370.9 (22.808)	>5000 (5.493)	26.47
		Error	0.35 (1.554)	4.3 (2.063)	62 (2.392)	(0.509)	
	530 (475)	150	0.51 (57.199)	5.64 (28.04)	73.54 (13.249)	>5000 (1.511)	1.18
		Error	0.051 (2.489)	740 (1.758)	12 (1.273)	(0.332)	
	530 (550)	150	0.81 (45.452)	6.88 (35.299)	83.41 (17.393)	>5000 (1.856)	2.73
		Error	0.14 (3.571)	1.2 (3.2)	17 (2.095)	(0.486)	
	530 (675)	150	1.06 (38.86)	9.5 (36.066)	108.4 (22.031)	>5000 (3.043)	4.93
		Error	0.14 (2.464)	1.2 (2.203)	14 (1.722)	(0.388)	

Relevant to our study, there is a large body of work surrounding exciton dissociation and recombination in organic bulk heterojunction (BHJ) semiconductors for organic photovoltaics. Recent BHJ models stress the importance of considering thermalization of electrons,²³⁰ and hybridization between LE and CT states.^{231,232} According to the steady-state absorption spectrum of COF monomers, the 350 nm pump should excite LE states on N2 and N3 units and the 400 nm pump should excite LE states of N3 units that have intermonomer CTC. In the context of the BHJ literature excitation of LE states (350 nm) generates numerous thermalized LE/CT excitons in N2 containing COFs, which undergo fast non-radiative relaxation through the CT density of states. Upon increasing excitation wavelength from 350 nm to 400 and 450 nm, more CT transitions (less LE/CT transitions) are promoted, reducing non-radiative relaxation from

LE/CT, and correspond to slower EA decay for the normalized kinetics. Alternatively, excitation with higher pump energy may selectively excite regions of COF with more exciton splitting and longer internal conversion channels, manifesting the faster ES decay in the normalized TA kinetics. This explains the kinetics dependence at 400 nm excitation better than LE/CT coupling since there is no distinct feature attributable to LE N3 states in any OTA spectrum. Furthermore, TDDFT shows that the imine linker mediates CT, marginalizing the effect of N3 on the overall transition. Finally, the 350 nm excitation OTA kinetics have a faster rising component that can be best fit by a 150 fs IRF whereas the 400 and 450 nm excitation OTA kinetics require a 250 fs instrument response function (IRF) for suitable fitting results, suggesting the LE/CT state develops faster than the CT state. Moreover, this effect does not seem to be an artifact of the OTA instrument since the 530 nm kinetics also requires a 150 fs IRF for proper fitting.

To illustrate the effect of thermalization of electrons and LE/CT hybridization, the kinetic traces of GSB and ESA decay after higher energy (350, 400, 450 nm) are fit by a sequential four-exponential function (Figure 6.8, Tables 6.4-6.7). Helping to convey this information, a qualitative model for the relaxation process in the COFs based on our interpretation of the TDDFT, TDM, and OTA data is shown in Figure 6.9. The ultrafast time constant (τ_1) is attributed to the non-radiative relaxation process of thermalized electrons from a higher energy in the CB to the band edge. Depending on the excitation wavelength, this process may correspond to the relaxation from ${}^{\text{LE}}\text{CB}^*$ to ${}^{\text{LE}}\text{CB}$, ${}^{\text{CT}}\text{CB}^*$ to ${}^{\text{CT}}\text{CB}$, or ${}^{\text{LE}}\text{CB}$ to ${}^{\text{CT}}\text{CB}$. τ_2 , τ_3 and τ_4 represent the decay components that are beyond the typical timescale for internal conversion, and are ambiguously assigned to trapping, dissociation, or recombination of excitons. Due to the presence of a super-slow time constant (τ_4) which is beyond our OTA time window (5 ns), we cannot accurately determine the CT lifetime. Instead, the half lifetime ($\tau_{1/2}$), the time when the amplitude is reduced by 50%, is used for comparison. $\tau_{1/2}$ at the 550 nm probe wavelength is 4.0, 11.2, and 18.1 ps for 350 nm, 400 nm, and 450 nm excitation in N2N3, respectively, suggesting the exciton relaxation slows down with increasing excitation wavelength. This trend is similarly observed in the other COFs which suggests that in all cases thermalization of electrons by higher energy excitations plays a role in the exciton dynamics within the COFs.

In the lower energy excitation regime, the model for the delocalization process is qualitatively illustrated in Figure 6.9 – the tail state (TS) transitions occur between sub-bandgap energy levels and share the same VB ($^{\text{VB}}\text{TS}$) or CB ($^{\text{CB}}\text{TS}$). For example, excitation of the transition from the second tail state above the VB to the second tail state below the CB ($^{\text{VB}}\text{TS}_2 \rightarrow ^{\text{CB}}\text{TS}_2$) leads to the bleach of $^{\text{VB}}\text{TS}_1 \rightarrow ^{\text{CB}}\text{TS}_2$ which is responsible for the negative GSB band at 500 nm. $^{\text{VB}}\text{TS}_1 \rightarrow ^{\text{CB}}\text{TS}_2$ then quickly recovers due to the fast relaxation of electrons from $^{\text{CB}}\text{TS}_2$ to a trapped state. The trapped exciton exhibits EA before recombination leading to the persistence of this signal relative to EB.

In summary, we report a comprehensive computational analysis and OTA study of a series of 2D COFs which are constructed from a set of selective ditopic and tritopic monomers combined through an imine linker. OTA results are collected across the COF absorption region and correlated with an in-depth theoretical study quantifying the amount of CT present both in-plane and transverse to the plane of the

COF, the presence of transitions occurring from distinct valence bands, localization of excitons, and the effect of interlayer interactions. Using TDDFT and TDM analysis, we find that monomer selection and structural environment can have pronounced impacts on the photophysical properties of COFs, but linker chemistry has an outsized effect on exciton structure and these relaxation pathways and must be carefully considered when COFs are designed for photocatalysis. Moreover, we discover two distinct CT regimes originating from different VB, which arise from varying degrees of LE/CT mixing and are largely unaffected by interlayer interactions. In contrast, interlayer interaction plays an important role in modifying the energy levels, exciton volume, and electron density localization of the tail state, which is believed to correlate with strain present in the COF crystallites. Through OTA studies, we discovered an excitation wavelength dependence of GSB band and the ES decay kinetics, indicative of the presence of distinct VB bands and the relaxation of a thermalized electron in the CB, respectively. Further probing the tail state region by OTA reveals that the tail states are initially delocalized but quickly localize to a trapped state, which is consistent with the proposed computational model.

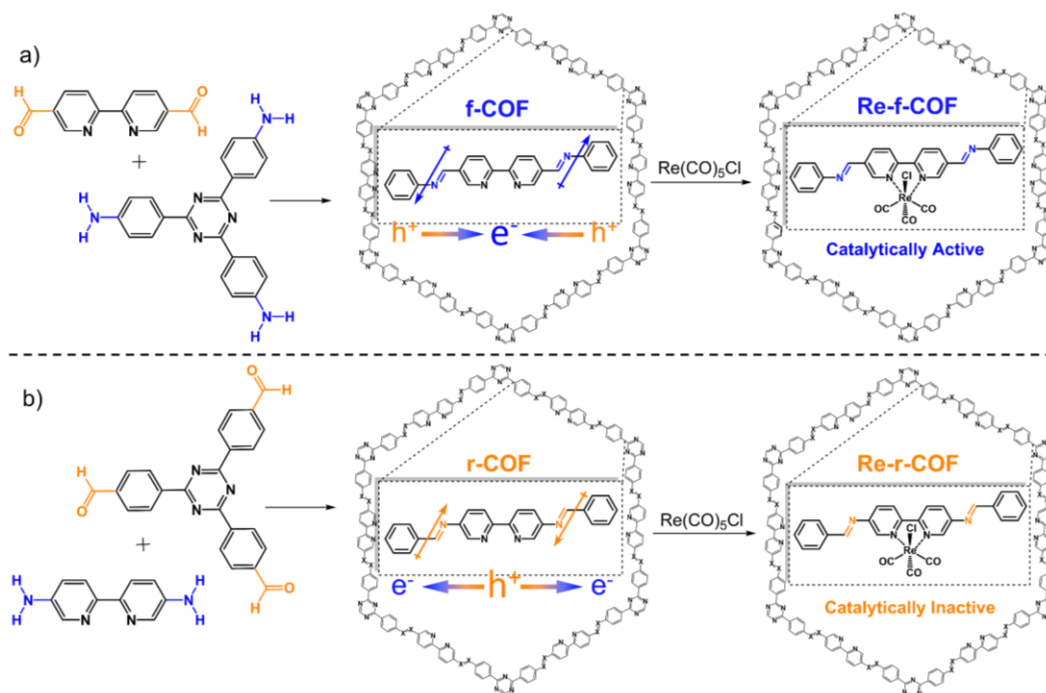
CHAPTER 7 – IMINE REVERSAL MEDIATES CHARGE SEPARATION AND CO₂ PHOTOREDUCTION IN COVALENT ORGANIC FRAMEWORKS

7.1 Introduction

The imine bond (-C=N- , Schiff base) is widespread amongst the field of COFs because of its facile formation and reversibility, but there is relatively little known about the photophysical implications of the bond beyond imparting extended π -conjugation between aromatic monomers. Baldwin et. al. discovered hints of photophysical differences in two COFs with reversed imine bonds by observing different responses to solvent polarity.²³³ Thomas et. al. dove deeper into the impact of imine reversal reporting changes in the absorption, band alignment, photoconductivity, and photocatalytic behavior,²³⁴ but the fundamentals for why imine reversal changes these properties remains elusive. A related trend in COF literature is the use of 5,5'-dicarbaldehyde-2,2'-bipyridine (CHO-bpy) as a MC docking site for the formation of photocatalytic COF structures with a variety of co-monomers.^{235–239} The structural diversity of co-monomers with 5,5'-diamino-2,2'-bipyridine (NH₂-bpy), however, is sparse.^{72,240–245} When NH₂-bpy does appear in the literature it is typically stabilized by hydrogen bonding interactions from 1,3,5-triformylphloroglucinol that undergoes keto-enol tautomerization to transform the imine bond into an amine and only a few references exist that polymerize NH₂-bpy without additional hydrogen bonding stabilization.^{246,247} Of these, the structures either make use of a tetratopic pyrene monomer that has been shown to be a beneficial crystallization agent,⁶⁹ or the crystallinity and porosity of the sample is low.³⁸ Despite these inherent structural challenges, discovering the electronic effects of imine reversal is important to understand how to maximize performance in COF photocatalysts.

In this work, in-depth theoretical and experimental studies on two imine COF isomers with reversed imine connectivity are reported. We show that the imine direction plays an outsized role in controlling excited state relaxation dynamics whether the COF is bare or coordinated to Re molecular catalyst (Re-COF). Photocatalytic CO₂ reduction performance of the Re-COFs, one of which has already been reported,⁹⁰ is starkly different – with the reversed imine COF isomer showing no significant photocatalytic activity. We go further to explain this finding by rationalizing that reversing the direction of the imine-linkage changes the behavior of 2,2'-bipyridine, switching it from an electron acceptor in the forward imine COF (f-COF, Scheme 7.1a) to an electron donor in the reversed imine COF (r-COF, Scheme

7.1b). This implies that the imine direction imparts directionality to intramolecular charge transfer (ICT), an effect we term “*ICT Tesla Valve*” in analogy to diodic one-directional fluidic flow devices.²⁴⁸ Upon Re incorporation, the impacts of imine reversal to Re/bpy orbital interactions are observable and drastically change the excited state (ES) and charge separation (CS) pathways. This interesting phenomenon suggests that linker directed ICT should be a key consideration when designing COFs for artificial photosynthesis and may also open doors to more efficient charge separation in COFs by taking advantage of other ICT linker directing abilities.



Scheme 7.1 Illustration of synthetic scheme of Re-COF from monomers having amine and aldehyde functional groups switched yielding a reversed imine linker. (a) Re-f-COF (b) Re-r-COF.

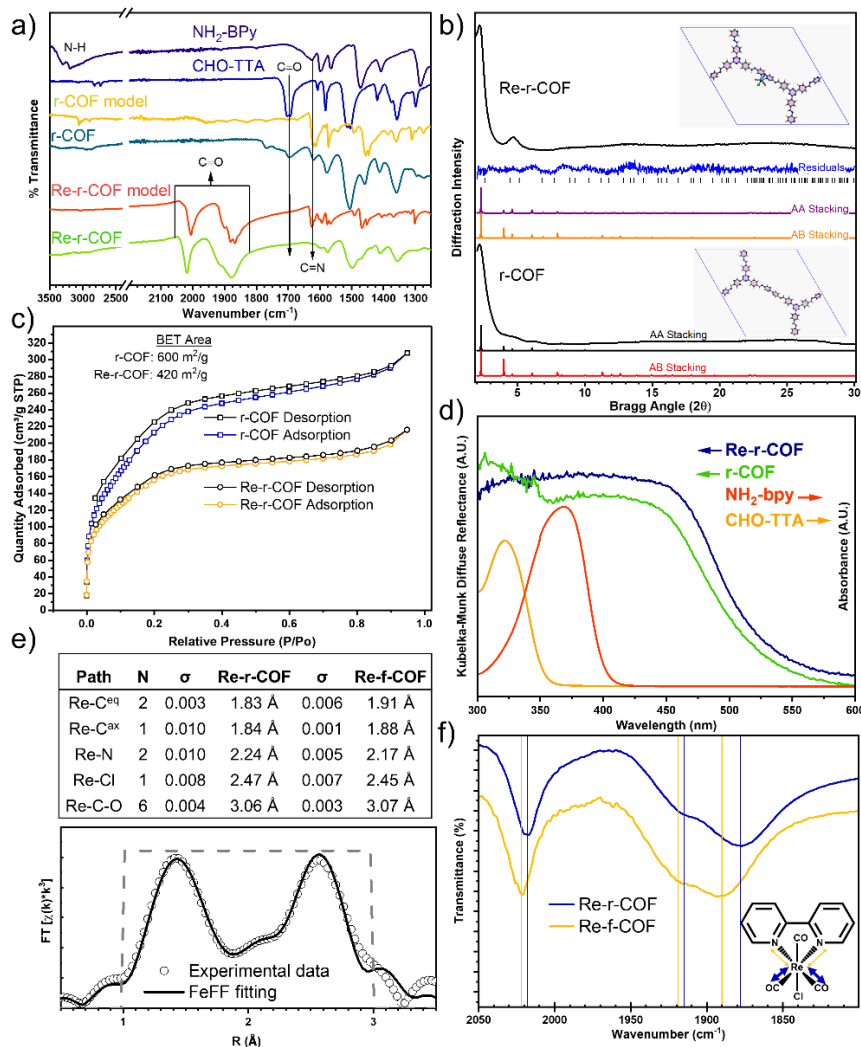


Figure 7.1 Characterization of r-COF and Re-r-COF. (a) FTIR spectrum of monomer, r-COF, Re-r-COF, and their model systems (b) PXRD patterns of r-COF and Re-r-COF with AA and AB stacking modes. (c) N₂ adsorption isotherms of r-COF and Re-r-COF with surface areas from BET calculation. (d) Diffuse reflectance of r-COF and Re-r-COF with the absorbance of the organic monomers in acetonitrile. (e) EXAFS fitting of Re-r-COF with fitting parameters (top) and R-space fitting (bottom). Note: Re-C-O forward scattering degeneracy of two. (f) FTIR of the (Re)-C≡O stretches in Re-f-COF and Re-r-COF with reference lines drawn through peaks determined by zero crossings of the derivatives.

7.2 Synthesis and Characterization of r-COF and Re-r-COF

Synthesis of f-COF and Re-f-COF (Scheme 7.1a) follows the previously reported method.⁹⁰

Newly designed r-COF (Scheme 7.1b) is first synthesized by a similar solvothermal approach as f-COF, and the experimental details can be found in Section 2.5. The product is carefully dried by critical point drying before collection of the N₂ adsorption isotherm and subsequent BET analysis performed. Powder X-

Ray diffraction (PXRD), Fourier-transformed infrared (FTIR) absorption, ^{13}C -CP-MAS NMR, and diffuse reflectance (DR) measurements are then made.

As shown in Figure 7.1a, the FTIR spectrum of r-COF shows an imine ($\text{C}=\text{N}$) stretching band at 1620 cm^{-1} , which is accompanied by attenuation of $-\text{NH}_2$ and $-\text{C}=\text{O}$ bands that are present in $\text{NH}_2\text{-bpy}$ and CHO-TTA , respectively, indicating the imine bond is formed by condensation of $-\text{NH}_2$ and $-\text{CHO}$. PXRD patterns (Figure 7.1b) of r-COF show noticeable diffraction intensity at $2.3^\circ 2\theta$, but have poorly pronounced higher order peaks, suggesting a semi-crystalline nature. The DFTB optimized unit cell is used as a lattice model (inset of Figure 7.1b) to cross-validate experimental and computational structures. In addition, a comparison of AA and AB stacking modes is made with AA appearing the most likely. BET area of r-COF synthesized through the solvothermal method is $333\text{ m}^2/\text{g}$, significantly less than what was achieved by the same procedure on f-COF.⁴ We screen for optimal solvent conditions in the solvothermal synthesis method (details in Section 2.5), but ultimately find optimal results by adapting a recent synthetic method for colloidal COF formation that uses aniline as a monofunctional polymerization mediator in benzonitrile with a benzoic acid catalyst (details in Section 2.5).²⁴⁹ This method yields r-COF with BET area of $600\text{ m}^2/\text{g}$ (Figure 7.1c). The Kubelka-Munk transformed diffuse reflectance spectra of r-COF (Figure 7.1d) shows broad absorption in the ultraviolet and visible regions ($>400\text{ nm}$), and because the monomers show negligible absorption in the visible region ($>400\text{ nm}$), we attribute the absorption in the visible region for r-COF to the intramolecular charge transfer (ICT) band, which further supports the formation of r-COF. Overall, the colloidal approach yields similar results by PXRD, FTIR, and DR.

Table 7.1 Analytic frequencies of the C≡O stretches from DFT and TDDFT calculations of Re-r-COF and Re-f-COF.

Re-r-COF	Energy (cm ⁻¹)	Intensity (a.u.)	Symm. Mode	Re-f-COF	Energy (cm ⁻¹)	Intensity (a.u.)	Symm. Mode
S ₀ Geometry (DFT Optimized)	2026	1234	A'(2)	S ₀ Geometry (DFT Optimized)	2029	1259	A'(2)
	2045	1323	A''		2052	1311	A''
	2136	977	A'(1)		2140	966	A'(1)
S ₁ Geometry (TDDFT Optimized)	2089	614	A''	S ₁ Geometry (TDDFT Optimized)	2096	689	A''
	2111	951	A'(2)		2114	971	A'(2)
	2189	760	A'(1)		2194	653	A'(1)
S ₄ Geometry (TDDFT Optimized)	2086	827	A''	S ₄ Geometry (TDDFT Optimized)	2097	1148	A''
	2185	498	A'(2)		2150	647	A'(2)
	2229	1657	A'(1)		2213	448	A'(1)
T ₁ Geometry (DFT Optimized)	2096	895	A''	T ₁ Geometry (DFT Optimized)	2092	969	A''
	2126	876	A'(2)		2131	755	A'(2)
	2189	999	A'(1)		2171	2303	A'(1)
T ₂ Geometry (TDDFT Optimized)	2029	1249	A'(2)	T ₂ Geometry (TDDFT Optimized)	2092	969	A''
	2047	1305	A''		2131	756	A'(2)
	2136	937	A'(1)		2171	2303	A'(1)

*All calculations are performed using the mixed basis set approach outlined in the main text

**S₀ geometry frequencies are calculated by KS-DFT using the B3LYP functional

***S₁, S₄, and T₁ geometry frequencies are calculated by TDDFT using the wB97XD functional

Refluxing r-COF with Re(CO)₅Cl in toluene under N₂ results in the formation of Re-r-COF (Scheme 7.1b). FTIR (Figure 7.1a) exhibits three new bands at 1878 cm⁻¹, 1910 cm⁻¹, and 2018 cm⁻¹. These bands correspond to the A'(2), A'', and A'(1) stretching modes of C≡O in *fac*-Re(bpy)(CO)₃Cl,²⁵⁰ respectively, and are in good agreement with the trend in analytic frequencies from DFT (Table 7.1). PXRD shows more prominent diffraction intensities which suggest possible enhancement of crystallinity upon incorporation of Re (Figure 7.1b). BET analysis of the N₂ isotherm (Figure 7.1c) of Re-r-COF from the colloidal synthesis indicates lower surface area (468 m²/g) than r-COF which is somewhat expected upon incorporation of Re MC onto the COF backbone. X-ray absorption spectroscopy (XAS) collected at the Re L₃ edge confirmed Re was incorporated into r-COF through bipyridine by fitting the extended X-ray absorption fine structure (EXAFS) R-space of Re-r-COF (Figure 7.1e).^{250–253} This fitting indicates that in Re-r-COF Re is coordinated by three C (C≡O), two N (bpy), and one Cl, which unambiguously confirms the presence of *fac*-Re(bpy)(CO)₃Cl. As shown in Figure 7.1e, fitting the EXAFS R-space using a Feff calculation based on a reported Re(bpy)(CO)₃Cl crystal structure (CCDC Deposition #649892) reveals a reduction of the Re-C bond (1.83 Å equatorial and 1.84 Å axial) in Re-r-COF with respect to Re-f-COF (1.91 Å equatorial and 1.88 Å axial). These Re-C bond reductions in Re-r-COF correspond with an increase

to the Re-N (2.24 Å) and Re-Cl (2.47 Å) bonds relative to those in Re-f-COF (2.17 Å for Re-N and 2.45 Å for Re-Cl, respectively). In contrast, Re→C→O forward scatterings only show slight change, which is 3.06 Å in Re-r-COF and 3.07 Å in Re-f-COF, leading to 0.07 Å and 0.03 Å net elongation of the equatorial and axial C≡O, respectively.

Differences in the EXAFS results between Re-f-COF and Re-r-COF are explained by π back-bonding from Re d-orbitals (π symmetry) to anti-bonding molecular orbitals of C≡O (π^*), which strengthens and shortens the Re-C bond while weakening and lengthening the C≡O bond. π back-bonding to equatorial C≡O is evidently more affected by imine reversal as indicated by larger C≡O net elongation relative to axial C≡O. These findings are supported by the lower frequency C≡O stretching modes in the FTIR spectra of Re-r-COF (1878 cm⁻¹, 1912 cm⁻¹ and 2018 cm⁻¹) in relation to Re-f-COF (1890 cm⁻¹, 1910 cm⁻¹ and 2021 cm⁻¹) due to increased Re(d π)→C≡O (π^*) back bonding in the former (Figure 7.1f). Together, results suggest that imine direction controls bipyridine π -acceptor characteristics in both f-COF and r-COF thus manipulating Re(d π)→bipyridine(π^*) back-bonding that is inversely related with back-bonding into the equatorial C≡O counterparts. The stronger Re(d π)→C≡O (π^*) back bonding in Re-r-COF is associated with weaker Re(d π)→bipyridine(π^*) back-bonding.

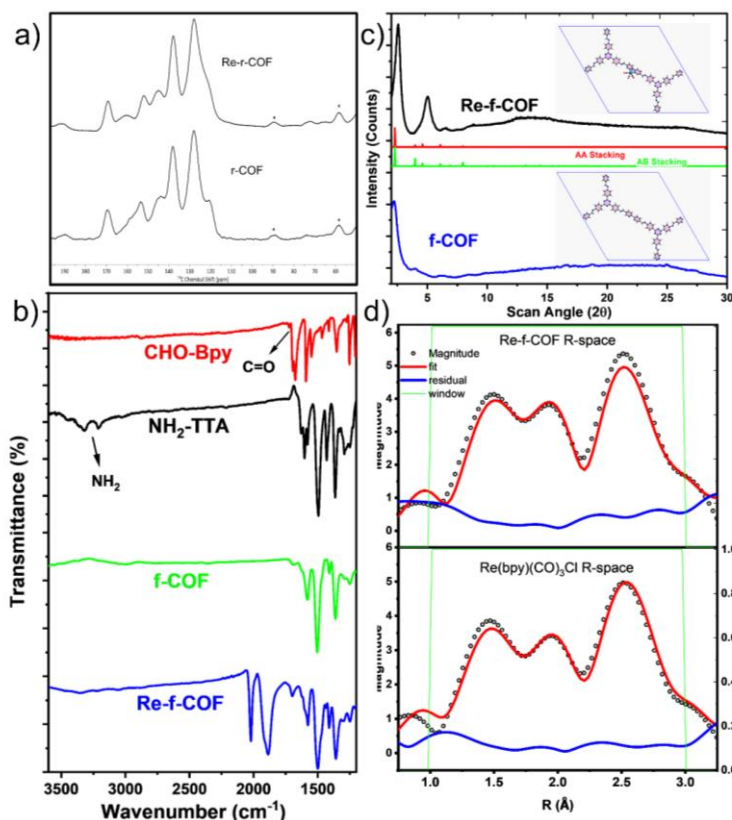


Figure 7.2 (a) ^{13}C -CP-MAS-NMR spectrum of r-COF and Re-r-COF. (b) FTIR of r-COF and Re-r-COF with its respective monomers NH_2 -TTA and CHO-bpy. (c) PXRD pattern of r-COF and Re-r-COF with insets showing DFTB optimized unit cells. (d) XAS fitting of Re-f-COF and $\text{Re}(\text{bpy})(\text{CO})_3\text{Cl}$.

In good agreement with f-COF,⁹⁰ the ^{13}C -CP-MAS NMR of r-COF shows a shoulder at a chemical shift of 159 ppm that we attribute to the imine C (Figure 7.2a). Additionally, a similar FTIR evolution is observed in the spectrum of f-COF and its monomers (Figure 7.2b), but the imine ($\text{C}=\text{N}$) stretching is found at 1626 cm^{-1} . In terms of PXRD, the patterns of r-COF and Re-r-COF resemble that of f-COF and Re-f-COF (Figure 7.2c), suggesting similar crystallinity and topology between r-COF and f-COF. Kubelka-Munk diffuse reflectance indicates that absorption is less red-shifted upon Re incorporation compared to f-COF and Re-f-COF.⁹⁰ Finally, the EXAFS R-space fitting of Re-r-COF is similar to that of $\text{Re}(\text{bpy})(\text{CO})_3\text{Cl}$ and Re-f-COF (Figure 7.2d).

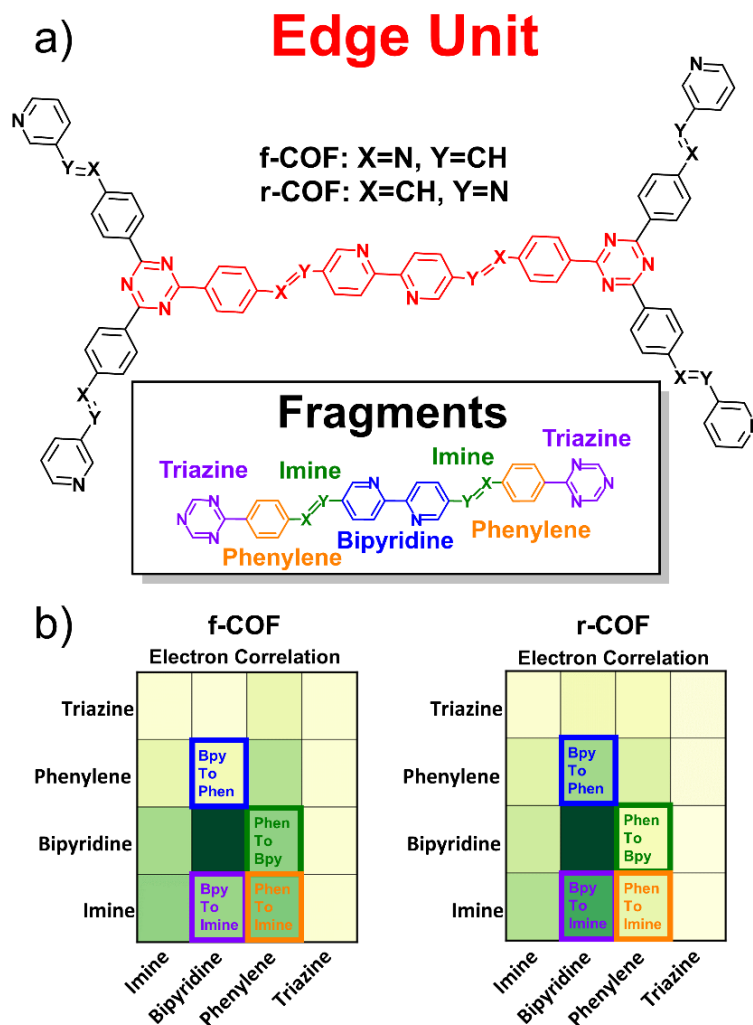


Figure 7.3 (a) Representative unit cell for COFs (implied hydrogens) with the edge unit outlined in red. Fragments used for TDM analysis are shown on the inset. (b) Electron-hole correlation plots of the optically allowed S_1 transition for f-COF (left) and r-COF (right) from TDM analysis.

7.3 Impact of Imine Direction on Ground State Transitions of f-COF and r-COF

To gain insight on the role imine direction plays on the electronic transitions and photophysical properties of f-COF and r-COF, we performed TDDFT on their edge units (Figure 7.3a) followed by TDM analysis to quantitatively unravel electronic correlation between fragments that contribute to ICT (Figure 7.3b). Selection of fragments is crucial to TDM analysis and as such we carefully selected four fragments - triazine, phenylene, imine, and bipyridine. The matrix elements shown in the electron correlation plot (Figure 7.3b) indicates that ICT favors some degree of electron transfer from phenylene to both imine and

bipyridine in f-COF. Reversing the direction of the imine linker leads to different behavior of the bipyridine, switching it from an electron acceptor to an electron donor, thus reversing the ICT direction. The electron correlation plot illustrates this by showing more correlation (darker green) in the bipyridine→imine and bipyridine→phenylene matrix elements, and less correlation (lighter green) in the phenylene→imine and phenylene→bipyridine matrix elements of r-COF and f-COF, respectively. This observation suggests an analogy to one-directional fluidic valves like the “Tesla Valve,” suggesting the key role imine direction plays on ICT in imine-linked COFs.²⁴⁸

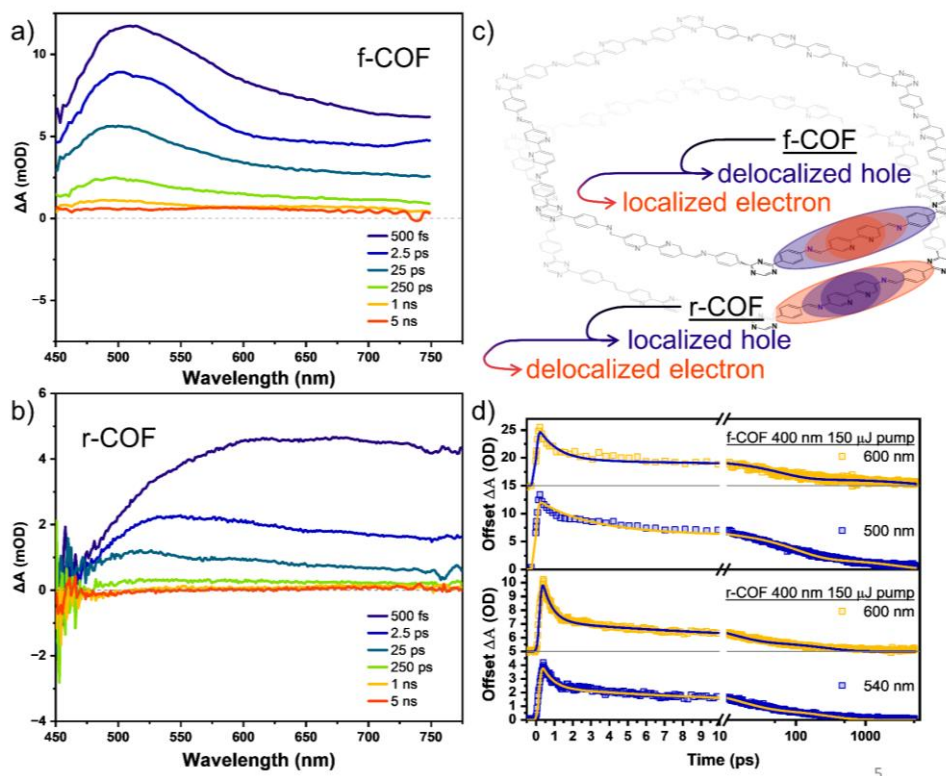


Figure 7.4 (a) fs-TA time slices of f-COF. (b) fs-TA time slices of r-COF. (c) Pictorial scheme of exciton localization in f-COF and r-COF. (d) fs-TA kinetic traces of f-COF (top) and r-COF (bottom) at various wavelengths.

7.4 Impact of Imine Direction on Excited State Dynamics of f-COF and r-COF

Visible transient absorption (TA) spectroscopy is used to assess the excited state (ES) properties and dynamics of f-COF and r-COF. ES properties are measured by pumping f-COF and r-COF samples with a 400 nm 150 μ J laser and using delayed visible light pulses to generate ES spectra. A distinct excited state absorption (ESA) peak at 500 nm is observed in the fs-TA spectrum of f-COF at 500 fs and persists until 1 ns (Figure 7.4a). The presence of a clearly defined peak indicates that ESA occurs from ground state

electrons being promoted to a relatively localized electronic ES. Notably, while this peak is no longer observable past 1 ns a broad positive feature persists, suggesting an underlying state is present. TDM analysis (vide supra) shows the exciton generated by the pump laser should localize electron density primarily at the bipyridine. In this case the hole density is delocalized, overlapping the bipyridine, imine and phenylene fragments. In contrast, r-COF seems to initially populate a rather electronically delocalized ES with a broad, featureless ESA profile that returns to GS within the fs-TA time window (Figure 3b). ESA in r-COF initially extends across the visible spectrum and shows no prominent peaks, but as time passes a peak is dynamically evident; the peak max arises at 525 nm in 2.5 ps, then migrates to 500 nm in 25 ps. Peak formation and migration represents exciton self-trapping of carriers, in this case electrons, that cannot escape Coulombic attraction to holes in the low dielectric environment of the framework. Thus, the initially delocalized state localizes relatively quickly before exciton recombination brings the system back to GS by 1 ns.

Table 7.2 Sequential multiexponential fitting components for f-COF and r-COF at representative wavelengths.

	IRF (ps)	τ_1 (ps)	A_1 (%)	τ_2 (ps)	A_2 (%)	τ_3 (ps)	A_3 (%)
f-COF (500 nm)	0.200	1.03	50.2 \pm 4.0	96.5	39.2 \pm 1.1	4540	10.6 \pm 0.4
f-COF (600 nm)	--	--	64.4 \pm 5.0	--	26.3 \pm 1.4	--	9.29 \pm 0.5
r-COF (525 nm)	0.200	0.515	39.2 \pm 3.1	10.9	36.8 \pm 3.3	212	24.0 \pm 1.1
r-COF (600 nm)	--	--	65.4 \pm 2.7	--	23.0 \pm 1.8	--	11.6 \pm 0.6

Theoretical and experimental results are thus in accordance with each other, allowing for summarization of the results in Figure 3c. f-COF initially generates a delocalized hole with localized electron while r-COF generates the opposite – a localized hole with delocalized electron. Figure 7.4d shows the kinetic traces of f-COF (top) and r-COF (bottom) that are fit by a finite three-component exponential decay for both COFs. It is difficult to definitively interpret what processes the time components correspond to without further study, but they are likely due to some combination of vibrational relaxation, exciton self-trapping, and recombination. The most distinct result is that the 600 nm probe in r-COF is comprised of a significantly higher proportion of the fastest component than the 525 nm probe ($\tau_1=515$ fs, $A_{1,600}=65.4\%$,

$A_{1,525}=39.2\%$, Table 7.2), suggesting the component, based on our interpretation, is related to exciton self-trapping.

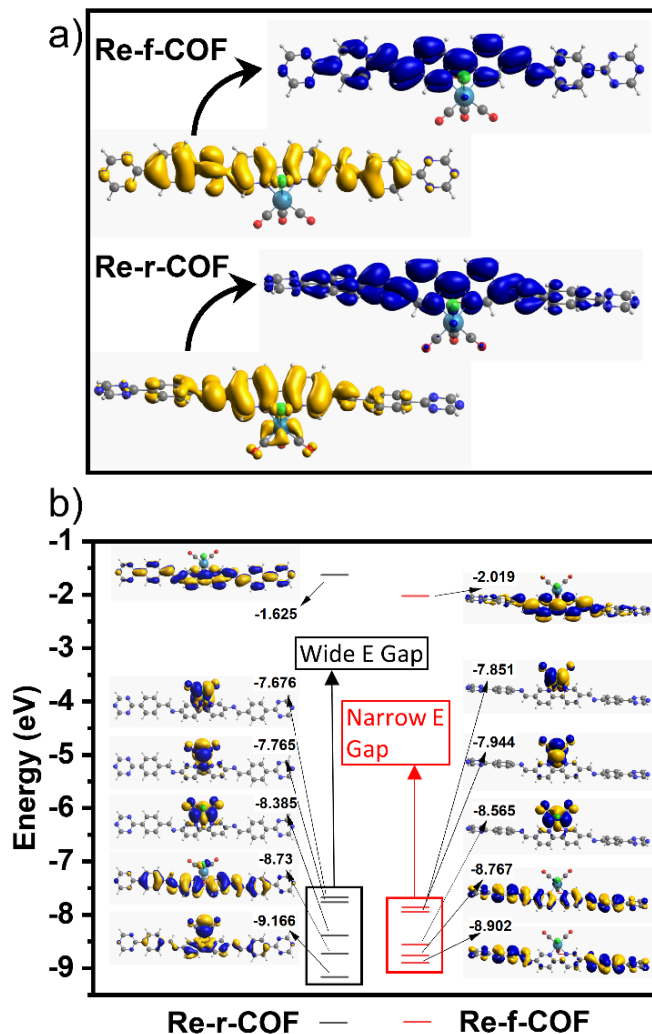


Figure 7.5 Theoretical electronic structure and experimental structural analysis of Re-f-COF and Re-r-COF. (a) NTO visualization of the lowest energy allowed singlet transition of Re-f-COF (S_4 , $f=1.86$) and Re-r-COF (S_4 , $f=1.96$) at the S_0 geometry. (b) Frontier orbitals of Re-f-COF and Re-r-COF at the S_0 geometry.

7.5 Impact of Imine Direction on Ground State Transitions of Re-f-COF and Re-r-COF

Reversal of the imine linker affects the ground state energetics and electronic structure of Re-COFs. The lowest energy transition with appreciable oscillator strength ($GS \rightarrow S_4$, Table 7.3), which should be the main absorbance peak in the visible portion of the DR spectrum for both Re-COFs, is 0.13 eV higher

in Re-r-COF than Re-f-COF. This absorption energy difference is reflected in the measured DR spectra of Re-COFs where Re-r-COF is centered around 450 nm (Figure 7.1d) and Re-f-COF is centered around 475 nm.⁹⁰ Natural transition orbitals (NTOs, Figure 7.5a) of this GS→S₄ transition shows that Re-f-COF possesses a COF centered hole particle and mixed Re/f-COF electron particle. This suggests that a small degree of ligand-to-metal charge transfer (LMCT) may take place initially after excitation but is primarily intraligand charge transfer (ILCT) in nature. In contrast, the Re-r-COF NTO of the S₄ transition shows a hole particle with mixed Re/r-COF orbital contributions (Figure 7.5a, bottom), in line with some degree of metal-to-ligand charge transfer (MLCT) typically observed in Re(bpy)(CO)₃Cl.²⁵² Frontier orbitals (Figure 7.5b) illustrate the effect of imine reversal on Re/bipyridine energetic overlap in Re-COFs. In Re-r-COF the occupied MOs localizing electron density on Re (HOMO, HOMO-1, HOMO-2) and those localized on COF (HOMO-3) are energetically separated relative to those of Re-f-COF. This disparity results from a relatively electron-rich bipyridine ground state in Re-r-COF, causing energy lowering that prevents Re(dπ) and bipyridine(π*) orbitals from mixing and is consistent with stronger Re(dπ)→C≡O (π*) back bonding in Re-r-COF (Figure 1e, 1f) and C≡O stretching frequencies predicted by DFT calculation (Table 7.1).

Table 7.3 First ten triplet and first ten singlet transitions of Re-r-COF and Re-f-COF from the S₀ geometry with wB97XD functional.

Re-r-COF	Energy (nm)	Osc. Strength (a.u.)	Re-f-COF	Energy (nm)	Osc. Strength (a.u.)
T ₁	484.21	0.0000	T ₁	510.54	0.0000
T ₂	455.08	0.0000	T ₂	473.15	0.0000
T ₃	433.80	0.0000	S ₁	472.70	0.0002
T ₄	419.03	0.0000	T ₃	470.93	0.0000
S ₁	417.32	0.0001	T ₄	462.14	0.0000
T ₅	408.62	0.0000	S ₂	448.59	0.0343
S ₂	397.18	0.0452	T ₅	414.55	0.0000
T ₆	362.27	0.0000	T ₆	373.54	0.0000
T ₇	342.14	0.0000	S ₃	370.82	0.0075
S ₃	338.93	0.1337	T ₇	370.00	0.0000
S ₄	333.28	1.9626	T ₈	346.37	0.0000
T ₈	332.96	0.0000	S ₄	345.03	1.8623
T ₉	329.72	0.0000	T ₉	344.91	0.0000
T ₁₀	328.50	0.0000	T ₁₀	331.32	0.0000
S ₅	309.46	0.0234	S ₅	329.05	0.0177
S ₆	303.32	0.0183	S ₆	324.12	0.0171
S ₇	300.46	0.0204	S ₇	313.31	0.0135
S ₈	293.87	0.0002	S ₈	303.33	0.0451
S ₉	293.72	0.0002	S ₉	301.58	0.0079
S ₁₀	291.59	0.0138	S ₁₀	295.64	0.0815

*All calculations are performed using the mixed basis set approach outlined in Section 2.5

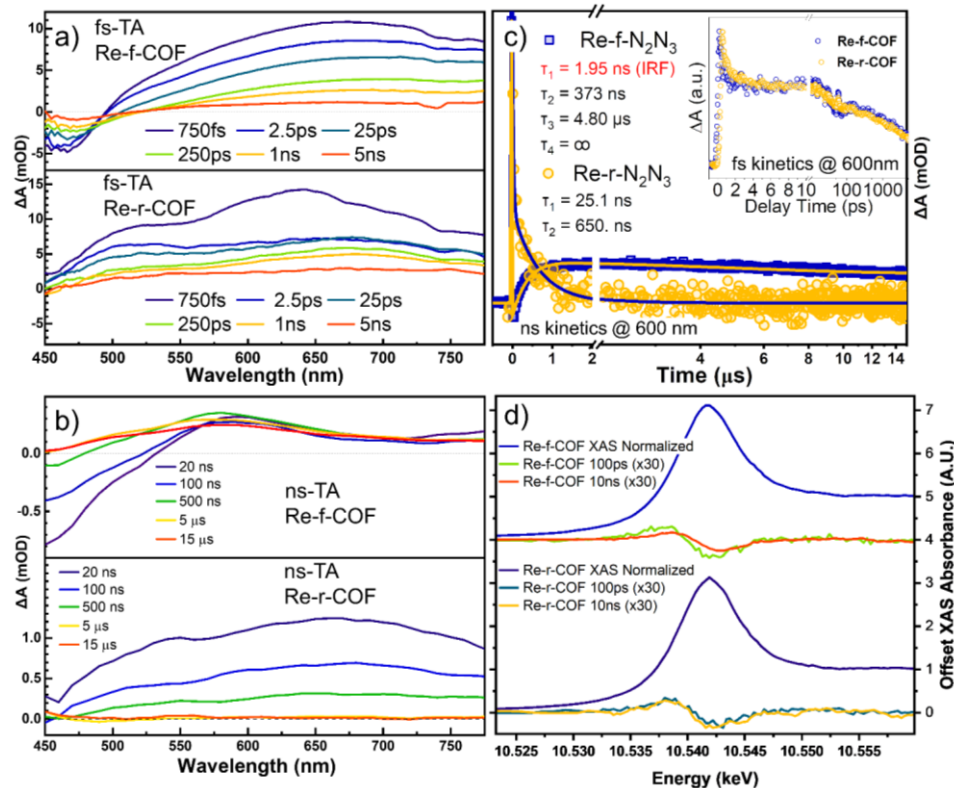


Figure 7.6 fs-TA (a) and ns-TA (b) spectra of Re-f-COF (top) and Re-r-COF (bottom) excited by 400 nm and 355 nm pump pulse, respectively. (c) Normalized kinetic traces of Re-f-COF and Re-r-COF from ns-TA and from fs-TA (inset). (d) XTA spectra of Re-f-COF (top) and Re-r-COF (bottom) after 100 ps and 10 ns.

7.6 Impact of Imine Direction on Excited State Dynamics of Re-f-COF and Re-r-COF

Visible TA and synchrotron X-ray TA (XTA) spectroscopies are used to examine the excited state (ES) and CS dynamics of Re-f-COF and Re-r-COF. Femtosecond (fs-TA) and nanosecond TA (ns-TA) spectroscopies are used to probe the dynamics of these Re-COFs in the visible region, and synchrotron XTA spectroscopy is used to probe dynamics of the Re metal center at the L_3 edge. Figure 7.6a compares the fs-TA spectra of Re-f-COF and Re-r-COF following 400 nm excitation. The fs-TA spectrum of Re-f-COF (top panel) possesses a ground state bleach (GSB) at ~ 470 nm, a broad ES absorption (ESA) centered at 675 nm, and an isosbestic point at 500 nm. It is interesting to note that before 250 ps the isosbestic point shifts by ~ 25 nm and the GSB broadens, suggesting the system relaxes to form a new intermediate state. Re-r-COF has a significantly different initial fs-TA spectra from Re-f-COF, displaying a bimodal ESA across the entire spectral window with peaks at 630 nm and 525 nm, and no observable GSB. Spectral evolution is minimal, in the form of a red-shifting of the 630 nm peak to 675 nm, suggesting the relaxation

of an intermediate excited state in Re-r-COF. By the end of the fs-TA time window, the profiles of Re-f-COF and Re-r-COF somewhat resemble one another, except for the persistent GSB in Re-f-COF. At the beginning of the ns-TA window, Re-f-COF (Figure 7.6b, top panel) still exhibits a GSB towards the blue and an ESA centered at 600 nm, resembling the signature at the end its fs-TA. Prominent spectral evolution takes place where the GSB decays into ESA by 5 μ s then the whole ESA persists past 15 μ s. After recovery of the GSB, the broad ESA appears relatively unchanged, suggesting the recovery or interconversion of an intermediate species in Re-f-COF on a ns timescale. In contrast, the ns-TA spectra of Re-r-COF (Figure 7.6b, bottom panel) has a single broad ESA spectral feature with maximal ΔA at 675 nm that decays monotonically back to the ground state within 15 μ s.

The kinetic traces of the visible TA measurements are shown in Figure 7.6c. On a fs timescale the decay of the normalized 600 nm signal is comparable between the Re-COFs (inset of Figure 7.6c), suggesting the broad ESA corresponds to the population of a similar excited state. The GSB in Re-f-COF recovers within 5 μ s and the ESA grows, indicating it either overlapped GSB or that a new state is populated (Figure 7.6c). Regardless, ES population persisting well after the 15 μ s time window of the ns-TA measurement is evidence of an exceptionally long-lived ES in Re-f-COF. In fact, an attempt to find the end of this lifetime was unsuccessful as significant signal remained after 4 ms which is in stark contrast to the ESA of Re-r-COF which completely decays within 6 μ s. Since the ESA of r-COF is completely decayed by the end of the fs-TA time window we can rule out r-COF exciton recombination from possible ESA contributions in ns-TA. For more information on the nature of the Re-COF states in the visible TA we turn to XTA spectroscopy to probe the dynamics of the Re center.

Evidence of different Re participation in the excited states of Re-COFs is drawn from XTA spectroscopy (Figure 7.6d). Both Re-COFs have nearly identical signatures at 100 ps, but while Re-r-COF shows no evolution at 10 ns the spectrum of Re-f-COF does, suggesting the interconversion observed in ns-TA is related to Re. Ground state XAS of both Re-COFs show a strong white line that arises due to the promotion of 2p core electrons to unoccupied 5d orbitals. Since the $5d_{xy}$, $5d_{xz}$, and $5d_{yz}$ orbitals are occupied in the ground state these unoccupied 5d orbitals correspond to $5d_{x^2-y^2}$ and $5d_z^2$ orbitals. These unoccupied 5d orbitals have σ character and it has been suggested by Chergui et. al. that a shoulder on the high energy side of the white line indicates they split into different energy levels due to low molecular

symmetry.²⁵⁴ The 100 ps XTA spectrum of both Re-COFs resembles the $^3\text{MLCT}$ state reported in the same work by Chergui et. al. which they attribute to depletion of $5d_{xy}$, $5d_{xz}$, and $5d_{yz}$ orbitals allowing a new pre-edge transition (i.e., $2p_{3/2} \rightarrow 5d_{xy}$). The corresponding negative feature is attributed to an upwards shift in the edge energy due to partial oxidation of the Re center by $^3\text{MLCT}$. A further positive feature may be present above 10.546 keV caused by the $^3\text{MLCT}$ increasing the Re effective nuclear charge, and hence the edge energy, but this is difficult to claim in Re-COFs. At 10 ns the pre-edge and negative features in Re-f-COF all decrease in intensity but shift to higher energy. We attribute this shift to relaxation of the Re centered hole to the HOMO, and an electron occupying $5d\sigma$ orbital. To further develop a hypothesis for Re-f-COF having a longer-lived excited state we can turn to TDDFT to help describe differences the Re-COFs have in their $^3\text{MLCT}$ manifold.

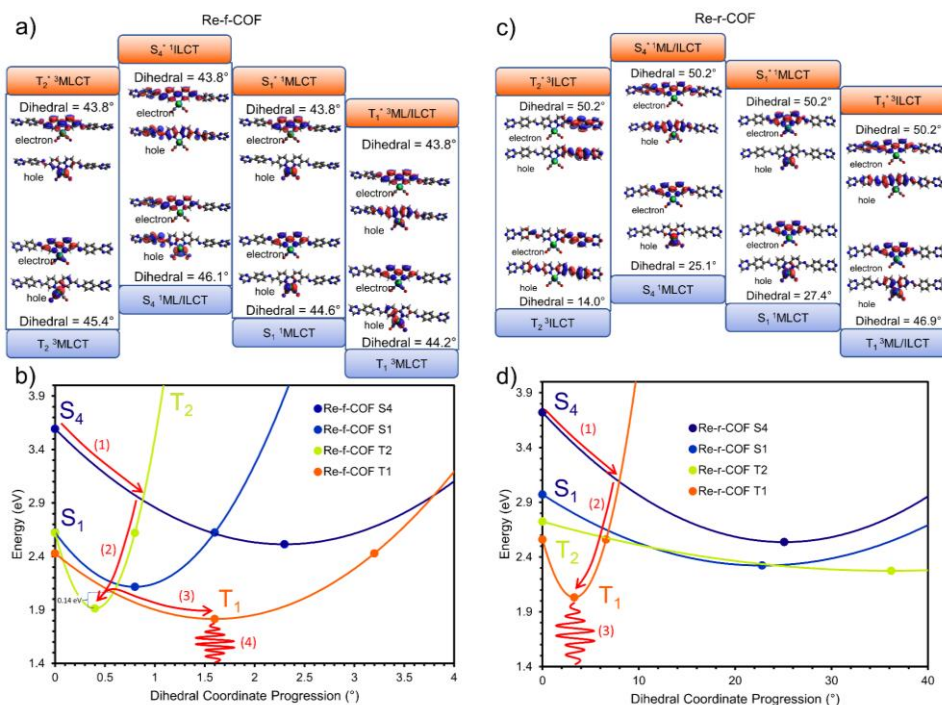


Figure 7.7 (a) TDDFT predicted NTOs of excited states at the S_0 geometry (top) and optimized geometry (bottom) of Re-f-COF. (b) Excited state potential energy surfaces of Re-f-COF as a function of the phenyl-bipyridine dihedral angle assuming parabolic surfaces. (c) TDDFT predicted NTOs of excited states at the S_0 geometry (top) and optimized geometry (bottom) of Re-r-COF. (d) Excited state potential energy surfaces of Re-r-COF as a function of the phenyl-bipyridine dihedral angle assuming parabolic surfaces.

7.7 Modeling Excited State Pathways of Re-f-COF and Re-r-COF

Starting from the GS geometry the transitions predicted by TDDFT can be inspected by generating the NTOs (top of Figures 7.7a and 7.7b). Re-f-COF has an optically allowed vertical transition to the S_4 state which has $^1\text{ILCT}$ character ($f=1.86$, vide supra). The optically forbidden ($f=0.00$) $\text{GS} \rightarrow S_1$ transition has $^1\text{MLCT}$ character, $\text{GS} \rightarrow T_2$ is $^3\text{MLCT}$, and $\text{GS} \rightarrow T_1$ is mixed $^3\text{ML}/\text{ILCT}$. Re-r-COF has a mixed $^1\text{ML}/\text{ILCT}$ character for its optically allowed $\text{GS} \rightarrow S_4$ transition ($f=1.96$), $^1\text{MLCT}$ for $\text{GS} \rightarrow S_1$, and $^3\text{ILCT}$ for $\text{GS} \rightarrow T_1$ and $\text{GS} \rightarrow T_2$.

TDDFT optimization of excited states is performed under the constraint that the two triazines of the edge fragments remain planar to replicate the bulk environment of the COFs. At their respective optimized geometries, the S_4 state of Re-f-COF takes on mixed $^1\text{ML}/\text{ILCT}$ character, the S_1 state remains $^1\text{MLCT}$, while T_2 and T_1 both remain $^3\text{MLCT}$. In Re-r-COF the S_4 state becomes $^1\text{MLCT}$, S_1 remains $^1\text{MLCT}$, T_2 remains $^3\text{ILCT}$, and T_1 becomes mixed $^3\text{ML}/\text{ILCT}$. The relationship between state identity and dihedral angle is best represented by plotting potential energy surfaces under the assumption they are parabolic (Figures 7.7c, 7.7d). In Re-f-COF the small dihedral progressions should allow for a variety of pathways through the ES manifold, but the most prominent is outlined by three steps (Figure 7.7c). The first step involves relaxation of the S_4 state until ISC to T_2 occurs; ISC has been suggested by studies on Re-bpy complexes to occur quickly.²⁵⁵ Next, the system relaxes along the T_2 potential to its energetic minima; we infer that crossing to the T_1 state can be reasonably well avoided due to the mixed $^3\text{ML}/\text{ILCT}$ character of the latter which would require hole transfer to f-COF. At the T_2 minima a thermal equilibrium with the T_1 state ($\Delta G^\ddagger=0.14$ eV under parabolic PES assumption) can be established. Finally, once the T_1 minima has been reached relaxation back to the GS can take place. Re-r-COF has a larger bipyridine-phenylene dihedral progression than Re-f-COF; but notably, the dihedral progression for the T_1 relaxation in Re-r-COF is much smaller than its other investigated transitions. The dihedral progression of Re-r-COF proceeds towards planarization and is evidently due to delocalization of electron density in the excited state, as observed in fs-OTA measurements of r-COF, which may be key to its rapid excited state deactivation. The generally large dihedral progression, and energetic isolation of the S_4 state offers fewer pathways through the ES manifold (Figure 7.7d). The likely pathway would follow relaxation along the S_4 potential until crossing onto the T_1 potential where the excitation is resides until relaxation back to the GS can occur.

Putting the TA and TDDFT results together, we propose an ES relaxation hypothesis that can explain the observed experimental data. The pump initially excites Re coordinated sites from GS to $^1\text{ILCT}$ in Re-f-COF or mixed $^1\text{ML}/\text{ILCT}$ in Re-r-COF. Conversely, excitons at bare sites underlie $^1\text{MLCT} \rightarrow ^3\text{MLCT}$ at Re coordinated sites and recombine within 5 ns. Both Re-COFs initially undergo intersystem crossing to $^3\text{MLCT}$ states, but this lifetime is decreased in Re-r-COF due to more metal-ligand mixing in the T_1 than Re-f-COF that experiences slow interconversion of T_2 state to the T_1 . This interconversion is observable by the recovery of GSB into ESA in ns-TA and in XTA by shifting $d\sigma$ occupation at 10 ns. Re-N bond distances support shifting occupation into $d\sigma$ orbitals. At T_2 the Re-N(1) distance is 2.19 Å and the Re-N(2) distance is 2.09 Å while at T_1 Re-N(1) is 2.17 Å and Re-N(2) is 2.14 Å. This interpretation suggests that the T_2 state is being probed at 10 ns before significant interconversion to T_1 can take place. Unfortunately, the later time XTA scans were obfuscated due to decreasing ES concentration from sample movement under jet conditions and could not be resolved.

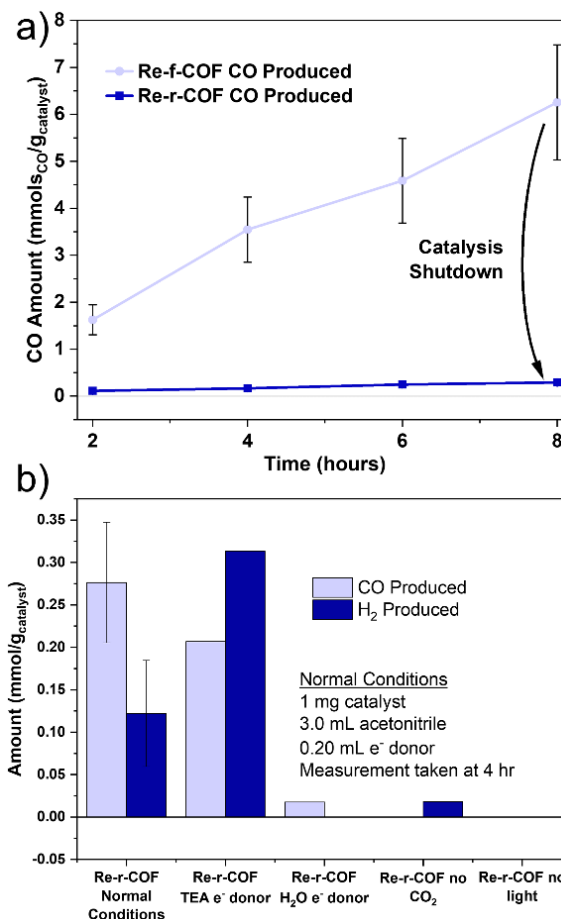


Figure 7.8 (a) Time profile of CO production from CO₂ per gram of COF catalyst by Re-f-COF, and Re-r-COF. Error bars represent 90% CI (n=3). (b) Control experiments performed on Re-r-COF.

7.8 Impact of Imine Direction on Photocatalytic Performance

With fundamental insight about the distinct electronic structure and ICT difference due to imine reversal between f-COF and r-COF, and Re-f-COF and Re-r-COF, we proceed to examine their catalytic performance for light driven CO₂→CO reduction (Figure 7.8a). Control studies were performed without catalyst, without CO₂, with ¹³CO₂, without light, and with TEA or H₂O as electron donors (Figure 7.8b). Additionally, model compounds of the Re-COFs were synthesized by performing Schiff base condensation between CHO-bpy with aniline, and NH₂-bpy with benzaldehyde followed by refluxing with Re(CO)₅Cl in toluene (Supporting Information). The typical reaction vial was purged with CO₂ for 15 minutes then exposed to a focused Xe lamp with a cut off filter (>420 nm) and a one-foot water filter to remove IR light and simulate solar radiation passing through water vapor in the atmosphere. Percent mass of Re in Re-

COFs is determined from ICP-MS to be 6.2% Re in Re-f-COF and 7.4% Re in Re-r-COF (Figure 7.9a). As shown in Figure 7.8a, under the same experimental conditions, Re-f-COF can generate 6.3 ± 1.2 mmol CO per gram Re-f-COF catalyst within 8 hours whereas Re-r-COF can only produce 0.30 ± 0.05 mmol CO per gram Re-r-COF catalyst within the same period. Furthermore, no ^{13}CO could be detected by GC-MS suggesting the CO detected previously may be due to decomposition of the catalyst or a side reaction with TEOA. These findings suggest that imine reversal from Re-f-COF to Re-r-COF significantly or entirely reduces catalytic activity for $\text{CO}_2 \rightarrow \text{CO}$ photoreduction. These results were also reflected by model systems of Re-f-COF and Re-r-COF which also showed that reversal of the imine linker significantly hinders or entirely shuts off CO_2 photoreduction (Figure 7.9b).

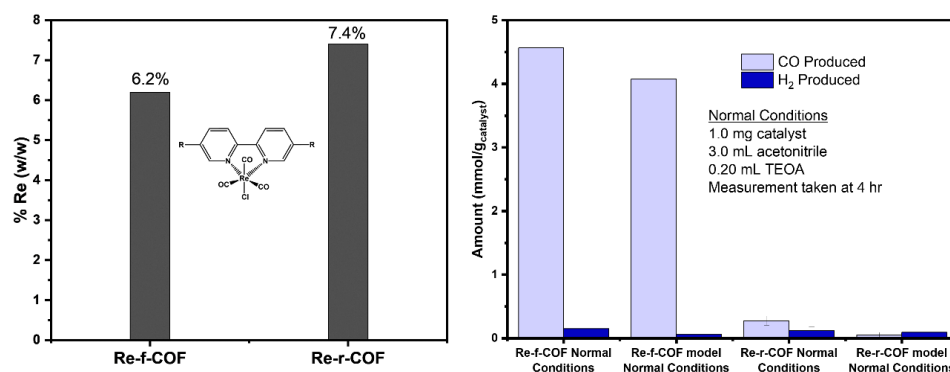


Figure 7.9 (a) Mass percentage of Re in Re-f-COF and Re-r-COF measured by ICP-MS. (b) Control experiments performed on Re-r-COF and Re-f-COF compared with their model compounds.

7.9 Conclusion

In summary, we report the design, synthesis, photophysical properties, and photocatalytic performance of two constitutional COF isomers with reversed imine connectivity, that demonstrate distinct relationships between their structure, properties, and function. Using theoretical predictions to lead our investigation by advanced spectroscopic methods, we show that the imine-linker acts as an electron mediator and imparts directionality to ICT. Re-f-COF constructed from CHO-bpy and NH_2 -TTA can drive ICT from TTA to bipyridine, which facilitates CS to Re MC, and thus functions as an efficient and selective CO_2 photoreduction catalyst. In contrast, its sibling Re-r-COF, which is constructed from CHO-TTA and NH_2 -bpy (reverse imine direction), favors ICT away from bipyridine which inhibits CS and significantly slowing down or altogether shutting down its photocatalytic activity. This finding – that the imine linker plays a key role in ICT by mediating the direction of electron donation – is unprecedented and

provides a unique approach to design photocatalysts that might be capable of performing both reductive and oxidative half reactions in artificial photosynthesis. For example, f-COF can direct electron density toward the bipyridine ligand that has an integrated CO₂ reduction or H₂ evolution MC while of r-COF may have the potential, in other systems, to drive hole density toward bpy and to the desired MC to perform the OER half-reaction.

CHAPTER 8 – CONCLUSIONS & FUTURE DIRECTIONS

8.1 Topology, Aggregation, and Charge Transfer Make COFs Unique Photocatalyst Platforms

A multitude of approaches are needed to solve Earth's climate crisis. Artificial photosynthesis is one such approach that mimics nature to capture solar energy and uses it to convert greenhouse gases into useful products. Over millennia, nature has adapted chloroplasts to absorb photons of visible wavelengths to complete photosynthesis in a way that takes advantage of supramolecular arrangements to facilitate charge transfer and energy transfer to reaction sites where CO₂ and H₂O are turned into carbohydrates and breathable O₂. Taking inspiration from these arrangements, COFs seem to have potential to operate by similar principles as chloroplasts due to their regular arrangement of organic repeating units in space. However, instead of being supramolecular arrangements of chromophores like Nature's chloroplasts, COFs are covalently linked polymers that lead to important distinctions in their basic photophysical properties. One such distinction is the extended macromolecular nature of COFs that affects how electrons and holes persist within their photoexcited states. Certain macromolecular arrangements, or topologies, are quite suitable for moving charge carriers through the structure and allowing them to potentially reach a reaction site. But even within COFs of identical topologies, monomer symmetry can play a significant impact on the ability for COFs to separate charges. This effect was shown in Chapter 3 and is the first experimental confirmation that monomer symmetry, particularly at the node, can facilitate exciton trapping or dissociation in COFs. Another distinction that exists between chloroplasts and COFs is the existence of extended π -conjugation and stronger intermolecular interactions between adjacent COF layers than the chromophores in chloroplasts. When a fully conjugated C=C bond is formed between COF monomers, luminescent excited state decay becomes available as an excitonic recombination pathway that can be creatively tuned to generate white light. This was shown in Chapter 5 which also uncovers a clear effect that planar monomers allow more intimate intermolecular interactions to partially quench their luminescence. Chromophores in chloroplasts are held in very specific arrangements by protein scaffolds, but COFs rely on π - π interactions between their aromatic units to maintain long-range order. Because π - π interactions can be relatively weak and susceptible to fluctuations, disorder may easily be introduced into COFs and this disorder may correlate with the formation of sub-bandgap states that have implications on the excited state relaxation dynamics in COFs. In fact, it was found in Chapter 6 that many relaxation

pathways exist in COFs in response to various wavelengths of light; and they show signatures of thermalized carriers and LE/CT hybridization. Chapter 6 also explores the effect of using a conjugated C=N imine bond to form four COFs from monomers with various electron affinities; ICT bands are formed in these COFs, but evidence arises that the polarized bond imparts some of its own ICT properties onto the visible light absorption and relaxation dynamics of the different COFs. C=N imine bonds are ubiquitous in COF research worldwide, and thus its effect on excited state dynamics becomes an extremely important topic. In Chapter 7 this effect is explicitly explored by reversing the imine bond direction which, apart from causing structural sensitivity, is found to mediate ICT by increasing the electron donating ability of the monomer containing the N. Due to this ICT directing effect, when a well-known CO₂ reduction catalyst is attached to the forward and reverse imine COFs the forward COF can reduce CO₂ to CO, but the reverse imine COF cannot. Overall, as synthesis strategies are improved, COFs will become easier to study by ultrafast spectroscopy and more of their potential will be unlocked. Already we have shown that the aggregation, topology and covalency of COFs separate them from other types of organic polymers and impart them with unique characteristics that may lead to their utility in artificial photosynthesis.

8.2 Future Directions for Covalent Organic Framework Research in Catalysis and Optoelectronics

Overall, the most promising feature of COFs is the ability to combine chemical functionality with a high degree of mass transport through their porous structure. Size dependent sieving is one such application that takes advantage of this mass transport and should theoretically be possible in COFs. However, recent research suggests tempering expectations regarding the multitude of reports of membrane action in COFs – size exclusive sieving can be quite difficult to achieve because of their propensity to form as polycrystalline materials.⁷⁷ This motivates the need for versatile designs to generate customized structures with suitable long-range order, which in turn requires fundamental understanding of why and how COFs form the way they do. This also has implications on the utility of COFs in other applications where mass transport is important – size selective catalysis or ion conduction, for instance. None of these limitations rule out the use of COFs as membranes or sieving materials, but unless long-range order can be proven and better understood, COFs should be thought of as disordered materials without columnar pore structures. Recent colloidal synthetic approaches seem to be a promising route obtaining such long-range order, but it remains to be seen how broadly these approaches are successful in making ordered COFs.

The most probable immediate use for COFs is for use as either thermocatalysts or photocatalysts in high-value organic transformations where size selectivity is not required, and active sites can be directly attached to the COF backbone. One such area where COF catalysts may be suitable is in flow reactors where packed bed catalysts are typically used.²⁵⁶ This is likely limited to cases where using a high-surface area, heterogeneous catalyst is preferable to a homogeneous catalyst. A scenario where packed bed COF catalysts may be useful is in organic transformations of pharmaceuticals when use of toxic or precious metal catalysts cannot be avoided. Anchoring these catalysts to a COF could prove useful to help separate them from products if there are low enough levels of leaching. Since COFs are relatively stable, precious metal catalysts could be reused in subsequent reactions, saving resources in the process.

There could be distinct possibilities in using COFs for solar fuel production, but for now the barriers seem inherent to the material and more challenging to overcome than competing strategies. A successful solar fuel cell has the requirement that no sacrificial agents should be used and is a severe limitation for COFs. Currently it takes a highly designed system to achieve efficient water oxidation in COF catalysts.¹⁰⁸ It is then more likely that COFs for solar fuel production would need be integrated as part of device that can separately facilitate oxidation half-reactions, but this is hampered by poor adhesion of COFs to semiconductor substrates. A potential method to bypass these limitations is to use COF for reductive half-reactions (CO_2 reduction, hydrogen evolution reaction) and nanoparticle catalysts (potentially RuO_2 ,²⁵⁷ Co_3O_4 ,²⁵⁸ or CoMnP ²⁵⁹) for water oxidation. In this case, the nanoparticles should be small enough to diffuse into COF pores ($\sim 1\text{-}2$ nm diameter), yet still allow mass transport of H_2O and CO_2 . Of course, this would again require development of COFs with sufficient long-range order to allow diffusion of nanoparticles into the pores. If this challenge were able to be overcome, one could try to influence secondary sphere effects to enhance the kinetics of water oxidation. This could exist in the form of incorporating appropriate functional groups on the COF backbone to act as a proton relay to help facilitate WNA. A promising strategy to achieve this is one-pot imine formation and phosphonylation²⁶⁰ where the H_2PO_3 groups can help to provide a proton rich local environment to drive acidic OER which has been shown possible with RuO_2 nanoparticles.²⁵⁷ Developing COFs that can perform full water splitting or artificial photosynthesis redox cycles is nonetheless still a worthy area of research, especially if earth abundant elements can be used for water splitting or artificial photosynthesis.

Using COFs in optoelectronics faces some of the same barriers as in solar fuel production. It is very challenging to integrate COFs into devices to properly enable their unique advantages particularly because of issues with long range order. The unique advantage COFs have is ambipolar charge transport²⁶¹ and can result in band transport.²⁶² Many reports indicate oriented COF growth through interfacial synthesis,²⁶³ but scalable ink depositions usually do not result in orientation of COFs with suitably large grain sizes.²⁶⁴ In most cases, it would be more straightforward to use typical polymers, but certain research suggests that methoxy groups on the ditopic linker of the COF can help create better orientation of COF films,²⁶⁵ and similar motifs in state of the art hole transport layers like spiro-OMeTAD in organic solar cells suggest these functional groups are crucial in determining their function.²⁶⁶

Overall, there is reason to believe that COFs are on the cusp of finding commercial applications, and the next wave in development may be geared towards these end uses. However, to truly unlock benefits from COFs there should be more fundamental understanding of their crystallization kinetics to generate applicable forms (powders, and films) with long-range order. In the context of this work, it may be the case that long-range order could hold interesting photophysical properties in response to photoexcitation and photocatalysis.

CHAPTER 9 – APPENDICES

9.1 Density Functional Tight-Binding

Obtaining COF structures which are physically meaningful requires using methods that can model their aggregated structure in the bulk phase in a computationally efficient, yet accurate way. The issue that arises is that COFs effectively extend infinitely in two- or three-dimensions which would be impossible to model with typical DFT or wavefunction methods. The solution to develop reasonable structures which agree well with experimental data is twofold – optimize atomic positions within a unit cell that may be infinitely translated to form extended structures and utilize an efficient approach that incorporates electronic and dispersion forces. In this section a high-level overview of the computational procedures used by DFTB is given, followed by the specific parameters. Theoretical concepts are covered in section 2.1.2.

In optimizing the atomic positions within a unit cell, a few computational tools need to be employed so its translation leads to a realistic extended structure. First, the atoms near the edges of the unit cell need to be accounted for such that they connect with their counterpart on the opposite side – this accounting is known as enforcing periodic boundary conditions (PBCs). Note that we will not cover the theoretical derivation of periodic boundary conditions, but helpful references are provided.²⁶⁷ Second, because 2D COF layers are held together through relatively weak $\pi\pi$ interactions, they likely do not form perfect eclipsed, highly symmetric unit cells as is often assumed in many literature references. Lowering symmetry by dislocation of COF layers from one another will likely lead to the prediction of different optical properties later in the computational workflow and is thus a particularly important piece to consider. Introducing the possibility for layer dislocation necessitates the incorporation of unit cell parameters (lengths and angles) as degrees of freedom into the structure optimization. This is done by optimizing the atomic structures within a static unit cell until some convergence criteria is met, then the hydrostatic strain can be derived from forces acting on the atoms. Finally, the unit cell parameters can be stepped down the strain gradient and the atomic positions are again optimized within the new, static unit cell. This process is repeated until a second convergence criteria, some specified strain present in the unit cell, is achieved and the resulting structure is output.

For the atomic positions that are optimized within the unit cell the density functional tight-binding model employs a self-consistent charge (SCC) correction to interatomic charge transfer. The SCC correction can be applied either to nearest-neighbor or nearest-and-next-nearest-neighbor (three-body) interactions. Construction of the Kohn-Sham orbitals begins from parameterized values contained within a set of Slater-Koster (SK) files.¹¹⁰ To address shortfalls in the DFTB method, parameterized dispersion forces¹¹¹ with appropriate damping¹¹² are also included in the structure optimization. The dispersion forces, as well as the SCC correction are applied both on the interactions between atoms within the unit cell but also to the implied interactions resulting from the enforcement of PBCs.

The main discussion about theoretical concepts of DFTB are adapted from the works by Hourahine, et. al.^{109,268} and Elstner et. al.,²⁶⁹ and Koskinen.²⁶⁷ DFT itself forms the basis of DFTB as the total energy expression, E^{total} , is also initially a functional of the electron density, $\rho(\mathbf{r})$, having a one-to-one mapping to the external potential created by the atomic nuclei in the Born-Oppenheimer approximation. The total energy expression can be simplified as a Kohn-Sham system of non-interacting electrons,

$$E^{\text{total}}[\rho(\mathbf{r})] = T_s + E_{\text{ext}} + E_H + E_{\text{XC}} + E_{\text{II}}, \quad 9.1$$

accounting for the kinetic energy, T_s , interaction with the external potential, E_{ext} , Hartree energy, E_H , the exchange-correlation energy, E_{XC} , and the ion-ion interaction, E_{II} . A more expressive form of this equation can be used including the occupation, f_a , of single-particle states, ψ_i ,

$$E^{\text{total}}[\rho(\mathbf{r})] = \sum_a f_a \langle \psi_a | -\frac{1}{2} \nabla^2 + V_{\text{ext}}(\mathbf{r}) + V_H[\rho(\mathbf{r})] | \psi_a \rangle + E_{\text{XC}}[\rho(\mathbf{r})] + E_{\text{II}}. \quad 9.2$$

However, when the total energy equation is formed in this manner the density is non-interacting and cannot account for charge reorganization based on electronegativities, and thus the density does not yield a minimum energy, or energy stationary point. In DFTB the density is then considered as a sum of some initial reference density with a density fluctuation, $\delta\rho(\mathbf{r})$, acting as a perturbation,

$$\rho(r) = \rho_0(r) + \delta\rho(r). \quad 9.3$$

The density fluctuation can be expanded to an N-order term around the reference density, in our case we expand to the quadratic,

$$\begin{aligned} E^{total}[\delta\rho(r)] \approx & \sum_a f_a \langle \psi_a | \underbrace{-\frac{1}{2}\nabla^2 + V_{ext}(r) + V_{xc}[\rho_0(r)] + V_H[\rho_0(r)]}_{\hat{H}^0[\rho_0(r)]} | \psi_a \rangle \\ & + \frac{1}{2} \iint \frac{\delta^2 E_{xc}[\rho_0(r)]}{\delta\rho(r)\delta\rho(r')} + \frac{1}{|r-r'|} \delta\rho(r)\delta\rho(r') \\ & - \frac{1}{2} \int V_H[\rho_0(r)](r) * \rho_0(r) d^3r \\ & + E_{xc}[\rho_0(r)] + E_{II} \\ & - \int V_{xc}[\rho_0(r)](r) * \rho_0[r] d^3r. \end{aligned} \quad 9.4$$

The first line yields the total energy without considering any charge reorganization or electrostatic repulsion. In the second line the charge reorganizations are accounted for by including Coulomb and exchange-correlation interactions. And the rest of the equation lead to the repulsive energies of the system. From this point approximations need to be made to arrive at the total DFTB energy. Firstly, the repulsion interactions can be approximated by only considering the atomic number and the interatomic distance for all atom-atom pairs. This is justified due to $\rho_0(r)$ being spherically symmetric for the non-interacting atoms and is similarly accounted for in the ion-ion repulsion term. Next, the Hamiltonian matrix elements, $\langle \psi_{a\mu} | \hat{H}^0[\rho_0(r)] | \psi_{a\mu} \rangle$, can be expressed in a minimal basis that only utilizes a single radial function for each angular momentum state of the valence atomic orbitals. This relationship is shown where μ represents the radial function within the atomic basis of atom a,

$$\psi_a(r) = \sum_{\mu} c_{\mu}^a \phi_{\mu}(r) . \quad 9.5$$

Thus, the Hamiltonian matrix elements $H_{\mu\nu}^0$ are the free, neutral atoms for the diagonal elements $H_{\mu\mu}^0$, and the off-diagonal elements are simply calculated within a two-body approximation,

$$H_{\mu\nu}^0 = \langle \phi_\mu | \hat{T}_s + (V_H + V_{XC} + V_{ext}) [\rho_{i0}(r) + \rho_{j0}(r)] | \phi_\nu \rangle. \quad 9.6$$

Formally then, by accepting the parameterized diagonal Hamiltonian matrix elements an efficiency gain is enabled since the elements are known *a priori*, speeding up construction of the Hamiltonian. In addition, from the interatomic distances and the overlap integral, $S_{\mu\nu}$, can be formed as we will soon discuss.

To introduce charge self-consistency into the calculation such that the adjacent atoms which have different electronegativities can transfer charge amongst themselves, the change in electron distribution around the atoms needs to be found in the volume occupied by each atom, V_i . The charge redistribution on atom i is represented by,

$$\Delta q_i \approx \int_V \delta \rho(r) d^3r, \quad 9.7$$

which can be recast into the atomic contributions of the normalized density perturbation,

$$\delta \rho(r) = \sum_i \Delta q_i \delta \rho_i(r) \quad 9.8$$

$$\Delta q_i \approx \int_V \delta \rho(r) d^3r = 1. \quad 9.9$$

In turn allowing for the Coulombic portion of the energy to be converted from the integral over all space to the sum over atom pairs and integrals over their volumes. When I and J share their atomic identity the density fluctuation perturbation depends on the quadratic term,

$$\frac{1}{2} \Delta q_i^2 \int_{V_i} \int_{V_i}' \frac{\delta^2 E_{xc}[\rho_0(r)]}{\delta \rho(r) \delta \rho(r')} + \frac{1}{|r - r'|} \delta \rho_i(r) \delta \rho_i(r'). \quad 9.10$$

This on-site Coulombic energy is readily available in the form of Hubbard parameters, U_i . On the other hand when I and J are different atoms the only interaction is electrostatic,

$$\gamma_{ij}(R_{ij}) = \frac{1}{2} \Delta q_i \Delta q_j \int_{V_i} \int_{V_j} \frac{\delta \rho_i(r) \delta \rho_j(r')}{|r - r'|}, \quad 9.11$$

and by assuming they maintain their spherical symmetry the integrals can be evaluated, and the extra Coulomb energy from the charge redistribution from two interacting Gaussian charge distribution can be calculated analytically,

$$\gamma_{ij}(R_{ij}) = \int_{V_i} \int_{V_j} \frac{\delta \rho_i(r) \delta \rho_j(r')}{|r - r'|} = \frac{\text{erf}(C_{ij} R_{ij})}{R_{ij}}. \quad 9.12$$

So, the final energy expression for the DFTB formalism is self-consistent – the energy depends on the charges $q_{i,j}$ which are dependent on the orbital coefficients,

$$E = \sum_{ab} f_a \sum_{\mu\nu} c_\mu^{a*} c_\nu H_{\mu\nu}^0 + \frac{1}{2} \sum_{ij} \gamma_{ij}(R_{ij}) \Delta q_i \Delta q_j + \sum_{i < j} V_{repulsion}^{ij}(R_{ij}). \quad 9.13$$

9.2 Overview of Theoretical Background of DFT and TDDFT

Discussion of the following theoretical concepts behind DFT and TDDFT were made with input from the text by Ullrich.²⁷⁰ The total energy operator Hamiltonian for an N-electron system is comprised of a kinetic energy term, \hat{T} , potential energy term, \hat{V} , and an electron-electron interaction energy term, \hat{W} , as shown by

$$\hat{H} = \hat{T} + \hat{V} + \hat{W} = \sum_{i=1}^N \left(-\frac{\nabla_i^2}{2} + v(r_i) \right) + \frac{1}{2} \sum_{\substack{i,j \\ i \neq j}}^N \frac{1}{|r_i - r_j|}. \quad 9.14$$

Solving for the total energy of a system requires the assumption that nuclear positions are fixed such that the total external potential generated by the nuclei remains constant. According to the Hohenberg-Kohn theorem the single-particle density of the electronic ground state has a one-to-one mapping with the external potential. This arises because the ground state density is obtained from the wavefunction and must thereby obey Schrödinger's equation, making the ground state density a functional of the wavefunction, $\rho_0[v_{ext}](r)$ or $v_{ext}[\rho_0](r)$. The proof of this rule will not be detailed herein but relies on the Rayleigh-Ritz variational principle to yield a proof through contradiction (*reductio ad impossibile*). Furthermore, because the nuclear positions are fixed and the system is a single-particle density the kinetic energy and electron interactions are also fixed, implying that the Hamiltonian is itself a functional of the ground state density, $\hat{H}[\rho_0]$, and its eigenstates. The interpretation of this is that the one-particle ground state density tells us everything we need to know about the system at hand. Connecting the ground state wavefunction with its density that uniquely maps to an external potential also means that the energy functional, $E_{v_0}[\rho]$, obeys the variational principal,

$$E_{v_0}[\rho] > E_0 \text{ for } \rho(r) \neq \rho_0(r) \quad 9.15$$

$$E_{v_0}[\rho] = E_0 \text{ for } \rho(r) = \rho_0(r), \quad 9.16$$

which states that the ground state energy can be found without solving the Schrödinger equation by Euler's equation,

$$\frac{\delta}{\delta \rho(r)} \left[E_{v_0}[\rho] - \mu \int d^3r' \rho(r') \right] = 0. \quad 9.17$$

The factor, μ , ensures that all the N electrons are accounted for in the equation. This cannot be solved exactly because the functional, $E_{v_0}[\rho]$, relies on the unknown universal functional, $F[\rho]$.

To solve the one-particle ground state density a practical and iterative approach is taken. This approach takes advantage of the Rayleigh-Ritz variational principle to minimize energy until self-consistency is achieved. Doing this would require an impossible searching of all wavefunctions that yield the density (wavefunction to density is not one-to-one, external potential is) and the lowest energy density would be the ground state. Instead, a different approach is followed constructing the Kohn-Sham density that lends itself to efficient minimization.

In the Kohn-Sham equations a non-interacting system is chosen such that the Hamiltonian of this system is,

$$\hat{H}_s = \hat{T} + \hat{V}_s = \sum_{i=1}^N \left(-\frac{\nabla_i^2}{2} + v_s(r_i) \right). \quad 9.18$$

The one-to-one correspondence still holds, and the total energy can be solved for. However, the unknown universal functional is now expressed in terms of kinetic energy only because the system is non-interacting. Casting this to Euler's equation yields the exact ground state density, $\rho_{0s}(r)$, of the non-interacting system,

$$\frac{\delta E_{v_s}[\rho(r)]}{\delta \rho(r)} = \frac{\delta T_s[\rho]}{\delta \rho(r)} + v_s(r) = \mu. \quad 9.19$$

This can be solved within a Slater determinant with one-particle orbitals, $\phi_i(r)$, that can be summed into the exact ground state density,

$$\rho_s(r) = \sum_{i=1}^N |\phi_i(r)|^2. \quad 9.20$$

Now the density, when plugged into the Euler equation again, yields

$$v_s[\rho(r)](r) = v(r) + \int d^3r' \frac{\rho(r')}{|r-r'|} + v_{xc}[\rho(r)](r), \quad 9.21$$

and the ground-state density of the interacting system can be solved via the single-particle Schrödinger equation,

$$\left(-\frac{\nabla^2}{2} + v_s[\rho(r)](r) \right) \phi_i(r) = \epsilon_i \phi_i(r). \quad 9.22$$

Finally, the density is arrived at by summing the squared of the single-particle orbitals,

$$\rho_0(r) = \sum_{i=1}^N |\phi_i(r)|^2. \quad 9.23$$

Yielding good results requires an accurate exchange-correlation functional since the rest of the solution is exact. Difficulties arise in obtaining accurate exchange-correlation because the interactions are all swept into the functional and rely on approximations which trade-off accuracy for speed. Developing good solutions to this problem is an entire field of active study that we will not cover here.

Within a time-dependent external potential there exists a one-to-one correspondence between the potential and time-dependent wavefunction of a system as shown by the time-dependent Schrödinger equation,

$$i \frac{\delta}{\delta t} \Psi(x_{1..N}, t) = \left(\hat{T} + \sum_{i=1}^N v(r, t) + \hat{W} \right), \quad 9.24$$

where,

$$v(r, t) = v_0(r) + v_1(r, t)\theta(t - t_0). \quad 9.25$$

The above equations state that the wavefunction propagates starting at some initial state, Ψ_0 , to a final state at time t . Instead of using the Hamiltonian operator to solve the time-dependent Schrödinger equation, a time evolution operator can be used instead,

$$\Psi(t) = \hat{U}(t, t_0)\Psi_0. \quad 9.26$$

the properties of this time evolution operator allow for norm conservation and a composition of two or more states – implying that the wavefunction can propagate through some intermediate state. These properties will not be explored further herein, but the result in the linear approximation to the time evolution operator is as follows,

$$\hat{U}(t, t_0) \approx e^{-iH_0(t-t_0)} \left[1 - i \int_{t_0}^t dt' F(t') \hat{\beta}(t' - t_0) \right]. \quad 9.27$$

$\hat{\beta}$ is an observable which is present with $F(t')$, an external field that is responsible for the perturbation to the static time Hamiltonian operator. This linear approximation will become important in the discussion about linear response TDDFT later in this section. Before linear response TDDFT can be covered, the basics of TDDFT must be established. From the one-to-one correspondence of a time-dependent external potential to the time-dependent wavefunction an extension can be made whereby the external potential also corresponds to a time-dependent density, $\rho(r, t)$. This extension was made by Runge-Gross theorem that shows two different time-dependent potentials will always yield two different time-dependent potentials.

Additionally, the potentials are structured such that they are much larger than the system and can be expanded in a Taylor series,

$$v(r, t) = \sum_{i=0}^{\infty} \frac{1}{i!} v_i(r) (t - t_0)^i. \quad 9.28$$

This type of potential is useful to describe monochromatic radiation acting on our system. Thus, the time-dependent density is a unique functional of the external potential and the case can thereby be reversed such that the potential is a unique functional of the time-dependent density, much in a same manner to DFT.

Unlike DFT, however, another step, known as the van Leeuwen theorem, must be taken so that the interacting density can be replaced by a non-interacting, readily solvable density.

The van Leeuwen theorem proves that from a different initial state the same time-dependent density can be created by a different external potential when the different system has differing particle-particle interactions. To accomplish this the theorem utilizes the constraint that both potentials, $v(r, t)$ and $v'(r, t)$, vanish at infinity and the conditions that the initial states yield the same densities, and the time-derivative of the densities are equal at t_0 . Advantageously, the van Leeuwen theorem thus states that given the non-interacting ground state density, $\rho_{s0}(r, t)$ with a suitable time-derivative, a unique time-dependent potential, $v_s(r, t)$ will yield the same density at time t as the interacting ground state density. This allows for the solution to the time-dependent Schrödinger equation using the same type of method as the Kohn-Sham, discussed earlier.

Time-dependency in the KS approach expresses the potential as a functional of the density, initial state, and non-interacting state,

$$v_s[\rho, \Psi_0, \Phi_0](r, t). \quad 9.29$$

From the ground state at time zero the time-dependent potential can be written as a sum of the ground state external potential with the time-dependent potential applied,

$$v(r, t) = v_0(r) + v_1(r, t). \quad 9.30$$

After $t = 0$, the time dependent density changes under the external time-dependent potential as the ground state KS orbitals in the time domain,

$$\rho(r, t) = \sum_{i=1}^N |\phi_i(r, t)|^2 \quad 9.31$$

$$\left[-\frac{\nabla^2}{2} + v_s[\rho(r)](r, t) \right] \phi_i(r, t) = i \frac{\delta}{\delta t} \phi_i(r, t) \quad 9.32$$

$$v_s[\rho(r)](r, t) = v(r, t) + \int d^3r' \frac{n(r', t)}{|r - r'|} + v_{xc}[\rho(r)](r, t). \quad 9.33$$

Now the exchange-correlation must be approximated to yield realistic result for the time-dependent density and related energies. Next, we move ahead into linear response TDDFT, the most widely accepted practical approach to solving the time-dependent Schrödinger equation for large systems in a relatively accurate manner.

Linear response TDDFT leads to better performance in the prediction of transition energies because it can capture many-body effects and introduce mixing between the KS eigenstates. Much of the performance, however, rests in the exchange-correlation functional, f_{xc} . Linear response theory captures the small deviations that arise due to a (relatively) weak electric field as is typically the case in spectroscopic experiments. Considering a static, ground state observable and its time-dependent variation, the response to the time-dependent perturbation is defined as the difference of the density at a short time after the electric field perturbation, t , and the density at time zero, $\hat{o}(t) - \hat{o}$. When the external potential field is expanded to N-orders,

$$\hat{o}(t) - \hat{o} = \hat{o}_1(t) + \hat{o}_2(t) + \hat{o}_3(t) + \dots, \quad 9.34$$

where increasing n represents a higher order response to the electric field (e.g. first order is the linear response, second is the quadratic response, etc.). These responses each have physical interpretations, like the polarizability and hyperpolarizabilities. Then the first-order response is a linear approximation to the difference caused by perturbation, and it can serve as a simplification to make the solution tractable. The linear response function and the response of the density is respectively,

$$\hat{o}_1(t) = \int_{-\infty}^{\infty} dt' \chi_{\alpha\beta}(t-t') F(t') \quad 9.35$$

$$\rho_1(r, t) = \int_{-\infty}^{\infty} dt' \int d^3r' \chi_{nn}(r, r', t-t') v_1(r', t'). \quad 9.36$$

The variable χ_{nn} is the density-density response function that links the unperturbed and perturbed states,

$$\chi_{nn}(r, r', t-t') = -i\theta(t-t') \langle \Psi | [\hat{\rho}(r, t-t'), \hat{n}(r')] | \Psi_0 \rangle. \quad 9.37$$

and since the linear responses to the time-dependent potential perturbations are all separate from each other they can be independently combined. In this manner the Hamiltonian can be perturbed from its ground state formulation to yield a time-dependent term that gives a density response to be integrated over all space.

Because time-dependent potential perturbations are typically envisioned as radiation with energies scaled to their frequency, the time domain is changed to frequency via a Fourier transform,

$$F(t) = \int_{-\infty}^{\infty} \frac{d\omega}{2\pi} F(\omega) e^{-i\omega t} \quad 9.37$$

$$F(\omega) = \int_{-\infty}^{\infty} dt F(t) e^{i\omega t}, \quad 9.38$$

where $F(t)$ and $F(\omega)$ are the fields perturbing the system under study. This transform yields, through the equivalency $\int_{-\infty}^{\infty} dt' e^{it'(\omega-\omega')} = 2\pi\delta(\omega - \omega')$ the linear response to the observable, $\hat{o}_1 = \chi_{ab}(\omega)F(\omega)$.

The response function, $\chi_{ab}(\omega)$, couples the ground state, a (α), to the excited state, b (β) through,

$$\chi_{\alpha\beta}(\omega) = -i \sum_{n=1}^{\infty} \int_{-\infty}^{\infty} d\tau \theta(\tau) e^{i\omega\tau} [\langle \Psi_0 | \hat{a} | \Psi_n \rangle \langle \Psi_n | \hat{\beta} | \Psi_0 \rangle e_n^{-i\Omega\tau} - \langle \Psi_0 | \hat{\beta} | \Psi_n \rangle \langle \Psi_n | \hat{a} | \Psi_0 \rangle e_n^{i\Omega\tau}]. \quad 9.39$$

This response function can then be transformed used within the frequency-dependent density response,

$$\rho_1(r, \omega) = \int d^3r' \chi_{nn}(r, r', \omega) v(r', \omega). \quad 9.40$$

From here the observables for the time-dependent system such as oscillator strength and transition energy can be calculated.

For a noninteracting KS system with the time-dependent external potential,

$$v_s[\rho(r)](r, t) = v(r, t) + \int d^3r' \frac{\rho(r', t)}{|r - r'|} + v_{xc}[\rho(r)](r, t), \quad 9.41$$

can, by the Runge-Gross theorem, be expressed as the functional of time-dependent density,

$$\rho(r, t) = \rho[v_s](r, t). \quad 9.42$$

Like above, the density can be expanded to the first order of the time-dependent external potential,

$$\rho_1(r, t) = \int dt' \int d^3r' \chi_s(r, t, r', t') v_{s1}(r', t'). \quad 9.43$$

And the density-density response in the noninteracting KS lens is,

$$\chi_s(r, t, r', t') = \frac{\delta \rho[v_s](r, t)}{\delta v_s(r', t')} \Big|_{v_s[\rho_0(r)]}. \quad 9.44$$

Finally, the time-dependent external potential is,

$$v_{s1}[\rho](r, t) = v_1(r, t) + \int d^3r' \frac{\rho_1(r', t)}{|r - r'|} + v_{1xc}(r, t) \quad 9.45$$

And the exchange-correlation potential term contains the exchange-correlation kernel by expansion,

$$f_{xc}(r, t, r', t') = \frac{\delta v_{xc}[\rho(r)](r, t')}{\delta \rho(r', t')} \quad 9.46$$

that is crucial to the accuracy of TDDFT calculations calculated by the Casida equation,

$$\begin{bmatrix} A & B \\ B & A \end{bmatrix} \begin{bmatrix} X \\ Y \end{bmatrix} = \Omega \begin{bmatrix} -1 & 0 \\ 0 & 1 \end{bmatrix} \begin{bmatrix} X \\ Y \end{bmatrix}. \quad 9.47$$

A and B can be broken into their matrix elements in the form,

$$A_{ia\sigma, i', a', \sigma'}(\Omega) = \delta'_{ii'} \delta'_{aa'} \delta_{\sigma\sigma'} \omega_{a' i' \sigma'} + K_{ia\sigma, i' a' \sigma'} \quad 9.48$$

$$B_{ia\sigma, i' a' \sigma'}(\Omega) = K_{ia\sigma, i' a' \sigma'}(\Omega), \quad 9.49$$

And Ω is the excitation frequency.

9.3 Orbital Configurations and Natural Transition Orbitals

Natural Transitions Orbitals (NTOs) were first described by Martin²⁷¹ to compactly describe orbital transitions in terms of their origin before excitation, and destination after excitation. To accomplish this succinct description of electron particles and hole particles Martin relies on a principal component analysis (PCA) which is an ordering and selection of the principal orthogonal contributions to transition density fluctuations found by the decomposition of the transition density matrix (TDM). This decomposition breaks the TDM into an eigenvector-eigenvalue pair where the vectors represent a relationship between two separate molecular orbitals, and the eigenvalue represents the importance of that relationship to the electronic transition.

The TDM is a rectangular matrix with dimensions, $n \times m$, where n is the number of occupied orbitals and m is the number of unoccupied orbitals. These orbitals themselves are described by orthogonal vectors of the unperturbed system, v_o and v_u and their coefficients, c_o and c_u . In his description, Ullrich et. al.²¹⁶ then define the time independent operator that connects occupied orbitals to unoccupied orbitals in terms of the one particle densities of two states of the same external (one with perturbation and one without, in terms of the single particle densities $\hat{\psi}(r)$ and $\hat{\psi}(r')$ as,

$$\hat{\rho}(r, r') = \hat{\psi}^T(r') \hat{\psi}(r) \quad 9.50$$

and dependence on time requires the use of a phase factor to form the TDM,

$$T(r, r', t) = \langle \Psi(t) | \hat{\rho}(r, r') | \Psi_0 e^{-iE_0 t} \rangle, \quad 9.51$$

that can be written with the eigenstate coefficients, c_k^* , based on the superpositioned eigenstates, k , of the steady-state TDM, $T_k(r, r')$,

$$T(r, r', t) = \sum_k c_k^*(t) T_k(r, r') e^{i(E_k - E_0)t}. \quad 9.52$$

In this TDM the diagonal elements describe fluctuations in the transition density. It is these elements that can be used to form new orbitals by solving the eigenvalue problem,

$$TT^T u_i = \lambda_i u_i \quad 9.52$$

$$T^T T v_i = \lambda_i' v_i \quad 9.53$$

and are ordered by the values of the λ_i and λ_i' and the eigenvectors u_i and v_i represent the hole particle and electron particle densities of a given transition i . These densities can be visualized and analyzed to assess the physical origin of holes and electrons in an electronic transition.

In the time-dependent Kohn-Sham formalism the KS orbitals can differ from the many body wavefunction considerably. This makes the choice of exchange-correlation functional an important factor, particularly those that don't correct for correlation (like PBE), or range-separation (like B3LYP) can lead to results that over delocalize or over separate transitions.

9.4 Transition Density Matrix Analysis

TDM analysis focuses on the one-electron transition density matrix generated by TDDFT which considers the populations of the predominant orbital configurations that contribute to the one electron transition.^{118,133,216} Tracking orbital populations from the GS to the ES allows the movement of electron density between orbitals to be represented by an orbital correlation matrix. Summation over blocks – representing the orbitals belonging to each atom – in the orbital correlation matrix yields the atom correlation matrix for which each index represents the CT number, Ω_{ij} , between each pair of atoms. Further summation over all atoms yields the total CT number, Ω_{Tot} , which in the norm conserved MO basis of TDDFT will be a value close to 1. The diagonal elements of the atom correlation matrix represent the CT numbers which are completely local to the atom. Conversely, the off-diagonal blocks represent the correlation between the GS and ES of separate atoms, respectively; put simply, the movement of electron density from one atom to another.

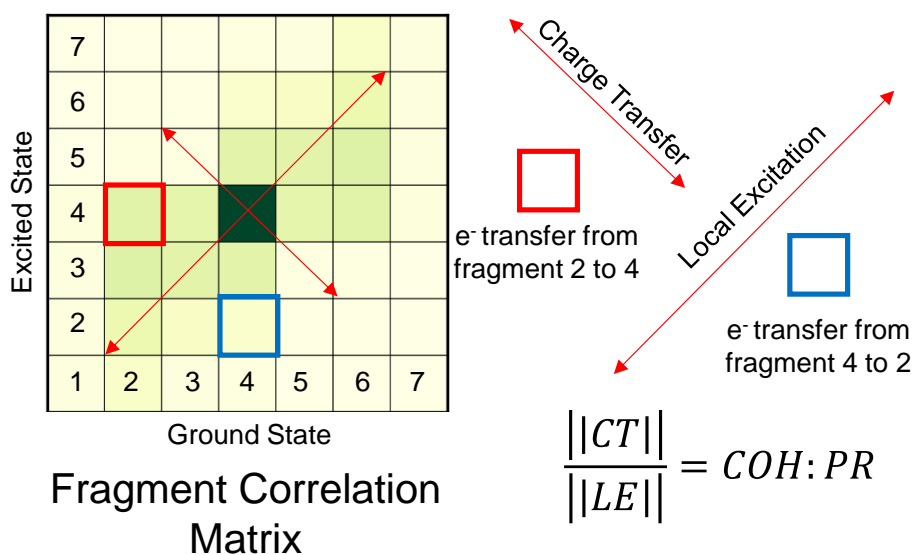


Figure 9.1 Example of the fragment correlation matrix showing key points to its

Because TDM analysis is not simply focused on CT between individual atoms, we consider the CT numbers and CTC among groups of atoms termed “fragments”. The fragments are used to group atoms

from the atom correlation matrix to form a new matrix with blocks defined by the user (fragment correlation matrix). From this new block matrix, the CTC and other corresponding TDM statistics can be calculated. Fragment selection is highly important to the reliability of the TDM analysis; thus, we carefully select fragments which represent the most critical pieces of the structure involved in the CT transition. By using logical selections, we gain a clear two-dimensional picture of which portions or layers of the structure participate in the CT transition as a donor, acceptor, or spectator.

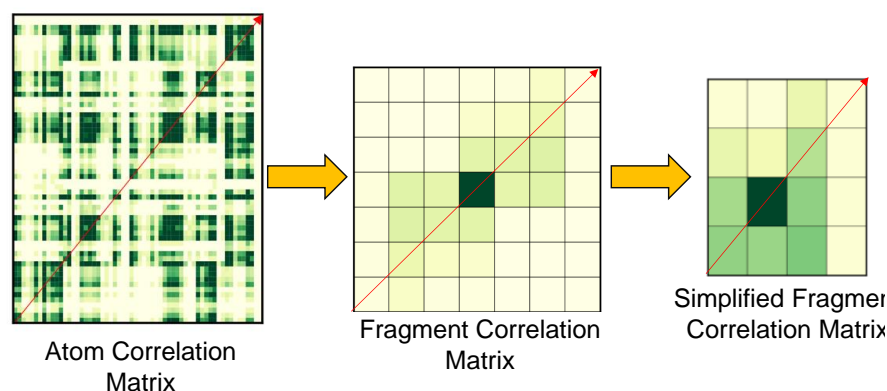


Figure 9.2 Diagram showing the effects of projecting the electronic correlation to the atomic and fragment bases.

From the total sum of the off-diagonal blocks, the total charge transfer character (CTC) is determined. This measure is a useful high-level descriptor for the quantity of CT in an electronic transition, however, it does not completely encompass the nature of the exciton. For instance, CTC does not consider spatial orthogonality,¹¹⁷ or spatial separation between atoms' orbitals¹¹⁸ and thus may lead to spurious conclusions¹⁹⁵ if other measures are not considered.¹⁹⁴ To help cover the shortfalls of the CTC statistic, the root-mean-squared distance between the electron and hole centroids (RMSeh) can be used.²¹⁷ Because RMSeh is derived from the difference in location of orbitals in the GS (hole centroid) versus the location of orbitals in the ES (electron centroid), it provides a statistic which is independent of orbital correlations and the orbital correlation matrix. This is useful because, as we soon discuss, RMSeh is also independent of fragment selection.

CTC and RMSeh describe the amount of CT and the size of the photogenerated exciton, respectively. However, even together these two useful characteristics do not offer a complete description of the exciton. Perhaps a more informative metric than CTC is the proportion of coherence length (COH) to participation ratio (PR), COH:PR. Like CTC, COH:PR depends on the selection of fragments and the CT numbers, ΩF , of said fragments. Unlike CTC, COH:PR is a clearer measure of spatial overlap that indicates separation of the electron/hole pair.^{118,133} To start, PR quantifies delocalization calculated as the weighted arithmetic mean of the number of fragments involved in the GS (hole), and the number of fragments involved in the ES (electron). Especially with conjugated π -systems like the COFs in this work, the PR can be quite large and incorporates both local excitation (LE) and CT. Concomitant with PR, COH is also a spatial measure but instead of delocalization relates to the separation of the electron/hole pair, that is, the number of fragments with off-diagonal correlation. Diagonal elements in this matrix represent local transitions of electron density – that is, GS and ES orbitals that reside on the same fragment and off-diagonal elements represent correlation of electron density between different units. A larger value of COH (measured in number of fragments) typically indicates better separation of the exciton but should be compared with PR to maintain consistency across systems. In the extreme case, if no diagonal matrix elements are populated, then COH:PR (i.e. COH/PR)=1 and the exciton would be considered completely separated.

9.5 Brunauer-Emmett-Teller Theory

The theory for which porosity and surface area measurements are determined is named after the founders of the method – Brunauer-Emmett-Teller (BET).²⁷² BET theory relies on data collected from adsorption isotherms. In an adsorption isotherm, gas is introduced to the sample at a particular temperature such that the amount delivered is dependent on the gas pressure applied. To complete the measurement, the pressure is then reduced until the initial pressure is reached. If the pressure swing follows the same pathway, then the adsorption isotherm of the porous sample is considered reversible. Depending on the size of the pore, and the distribution of pore sizes multiple sharp increases or large plateaus in gas uptake may be observed. Figure 9.3 shows the different types of adsorption isotherms illustrating the difference which depend on the nature of the sample porosity.²⁷³

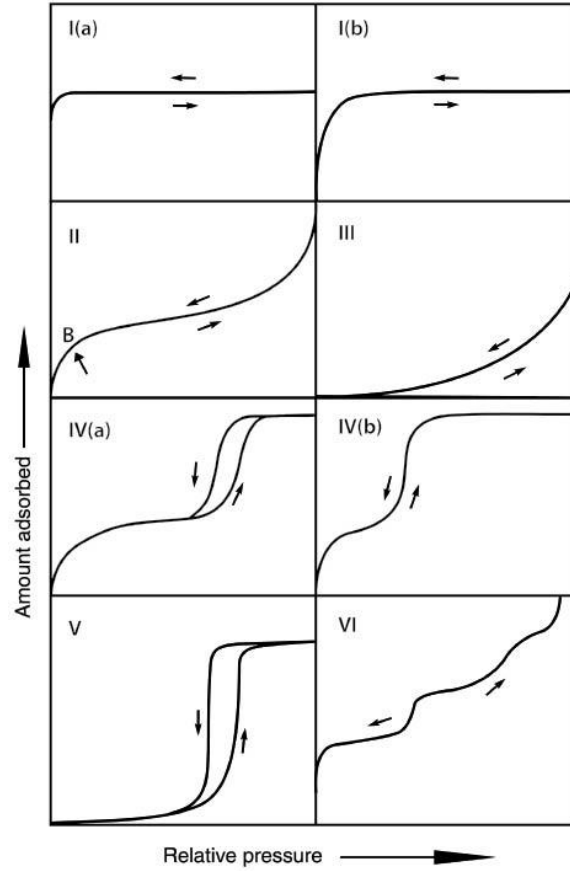


Figure 9.3 Chart showing the types of adsorption isotherms. Permanent porosity is confirmed by the swing following the same

Once the adsorption isotherm is collected analysis by BET theory yields the surface area starting from the linear equation,²⁷³

$$\frac{\frac{p_o}{p}}{n \left(1 - \left(\frac{p_o}{p} \right) \right)} = \frac{1}{n_m C} + \frac{C-1}{n_m C} \left(\frac{p_o}{p} \right) \quad (9.54)$$

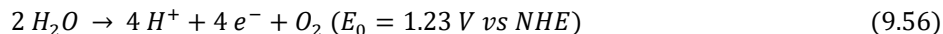
where n is the number of moles of gas adsorbed onto the surface of the COF at a particular relative pressure. n_m represents the capacity of the COF if an even monolayer forms at the surface and is used to calculate the surface area from the equation,²⁷⁴

$$A = n_m \sigma_0 N_{avo} \quad (9.55)$$

where N_{avo} is Avogadro's number, and σ_m is the area density of the adsorbate in its liquid phase. For the commonly used N_2 adsorbate this area density is 16.2 \AA .

9.6 Fundamentals of Water Oxidation

In order to lay out a clear path forward for overall artificial photosynthesis artificial it is essential to carefully consider the water oxidation couple. This oxidation reaction is often termed water oxidation (WO) by chemists but can often be referred to as the oxygen evolution reaction (OER) in other scientific communities; WO will be used for the duration of this work. The overall reaction for WO involves two water molecules that overall lose 4 H^+ and 4 e^- and come together to form an O-O bond (Equation 9.56).



WO is by nature a challenging reaction due to the kinetics involved in bringing two water molecules together at the same reaction site while removing 2 e^- from each and successively dissociating their four protons. Indeed, it is a wonder that nature has developed a scheme to do this in quantities that allow for life on earth. Yet despite its relevance to artificial photosynthesis, examples of pure photocatalytic WO using MC remain rare and limited in scope because of the added difficulty of harnessing and directing photonic potential energy (hole, h^+) to the oxidative site on the reaction time scale.^{275–277} As such, most works on WO are performed electrochemically which can be used to elicit mechanistic pathways relevant to photochemical WO and can help inform design decisions for photochemical WO catalysts. In electrochemical WO electrons are removed from the catalyst to the anode via the flow of electrolyte when a suitably positive potential is applied; this is mimicked in photochemical WO by removing electrons from the catalyst via some sacrificial electron acceptor. These have traditionally been rather strong chemical oxidizing agents like Ce(IV), but more recently have been replaced by some like Ru(III) that can itself be photogenerated in the presence of another, less harsh oxidizing agent to achieve the same function.²⁷⁸ Photochemically relevant discussions often start from the basis of electrochemistry and the two techniques are quite complementary when used in unison.²⁷⁹

When an electron is moved into a higher energy state by a system's absorption of a photon it leaves a vacancy in the ground state, this vacancy is commonly referred to as a hole – a term probably originating from Heisenberg^{280,281} in 1931 but not popularized until work on semiconductors in the late 1930s and early 1940s by Schottky,²⁸² Mott,²⁸³ and Jones²⁸⁴ as a way to rationalize charge movement in crystalline lattices. The hole has oxidative potential assumed equal to the ionization potential (IP) of the ground state molecule. IP can be accurately measured through advanced techniques like ultraviolet

photoemission spectroscopy (UPS) under high vacuum, but oftentimes the value is substituted for the oxidation potential measured electrochemically via cyclic voltammetry (CV) against a known standard. Since UPS is performed under high vacuum the substrate must either be in the gaseous or solid state. CV, on the other hand, imposes the limitation of being conducted in a solution which is acceptable as the conditions are more experimentally relevant.

Water Nucleophilic Attack vs. Two Interacting Metallo-Oxyls

Generally, in WO the hole is quenched by the first oxidation of bound H_2O , releasing H^+ , e^- , and leaving hydroxyl (OH^\cdot) bound to the oxidative reaction site. To complete WO and generate O_2 the system must then associate another water molecule, undergo three more oxidations and three proton dissociations, and finally form the desired O-O bond before dissociating O_2 . Mechanistically, the way by which these steps occur is the subject of much debate and is likely system dependent.²⁸⁵ Some reports²⁷⁸ outline a single-site process known as water nucleophilic attack (WNA) in which the metal- OH^\cdot undergoes a second oxidation and proton dissociation to form a metal-oxyl radical or a metal-oxo complex. From here the system may be oxidized a third time, and in some cases an additional fourth time, before the oxygen atom of a second water molecule attacks the electron deficient metal-oxyl or metal-oxo and loses a proton to form a metal bound hydroperoxide (M-O-O-H). Finally, the fourth oxidation (if it has not occurred yet) and proton dissociation can occur leaving metal-peroxido (M-O_2) that can dissociate O_2 upon replacement by H_2O . Catalyst regeneration in this scenario is achieved when two electrons are transferred to the catalytic metal site upon WNA, and two more upon O_2 dissociation.

Other reports find an O-O radical coupling between two interacting metallo-oxyl radicals, termed I_2M . The I_2M mechanism can occur either intra- or intermolecularly, but many systems utilizing dual-site catalysts have been found to enhance turnover frequency (TOF) due to faster intramolecular kinetics. In intermolecular I_2M the two-interacting metallo-oxyl originates from concerted oxidization of metal bound water and dissociation of the water's two protons. At this point the resonance between metallo-oxyl radical and metallo-oxo helps to stabilize the intermediate state allowing a homologous bimolecular reaction forming the peroxido bridged bimetallic intermediate that then decomposes in the presence of water to dissociate O_2 , regenerating the separate catalysts. Intramolecular I_2M differs in that the peroxido bridge is

cleaved by water to form a terminal peroxido intermediate that instead dissociates O_2 in the presence of water.

Kinetic & Thermodynamic Challenges

Kinetic challenges of electrochemical WO by MC are the same as photochemical WO.

Understanding the mechanisms by which important WO intermediates form helps face these kinetic challenges. For instance, the discovery of the formation of a bimetallic bridging peroxido in I_2M suggested that ligands can judiciously be designed to pre-organize the catalyst to help rapidly form the desired intermediate. An example of this prearrangement is the use of a 3,5-bis-(2-pyridyl)pyrazolate to bind two Ru(II) atoms in close proximity.²⁸⁶ H^+ dissociation in both WNA and I_2M as well as any proton-coupled electron transfer (PCET) in these mechanisms are influenced heavily by second coordination sphere effects and have been found to be more favorable in the presence of pendant Brønsted basic groups^{287,288}. These design schemes will be particularly relevant to the discussion in *Chapter 9 – Future Directions* and how they can be installed and improved in Covalent Organic Frameworks but altogether show the type of design schemes that have been used for WO.

Particularly, the discovery that 2,2'-bipyridine-6,6'-dicarboxylate (bda) aids I_2M by prearranging the bimolecular metallo-oxyl intermediates while also facilitating PCET was a breakthrough for WO by MC allowing TOF comparable to PSII (300 s^{-1} vs $100\text{--}400\text{ s}^{-1}$) when isoquinoline is used as the axial ligand.^{288,289} These pendant Brønsted base designs have been furthered by incorporating phosphonate groups instead of carboxylate groups,^{290,291} mixing-and-matching carboxylates and phosphonates,²⁹² and substituting 2,2'-bipyridine-6,6' derivatives for 2,2':6',2''-terpyridine-6,6' derivatives.^{287,293} This class of polypyridyl groups with pendant Brønsted bases have become known as Flexible Adaptive Multidentate Equatorial (FAME) ligands and represent a burgeoning field for further study.²⁹⁴ Of the multitude of designs that have been achieved for WO by MC a significant number use Ru(II) as the catalytic center, partially due to its ability to expand coordination from 6 to 7 once it reaches the fourth oxidation state, Ru(IV).²⁸⁸ The role that 7-coordinate Ru plays in WO, and whether it forms, is still up for debate,^{294,295} but so far it seems likely that FAME ligands can take advantage of this coordination expansion to enhance activity.

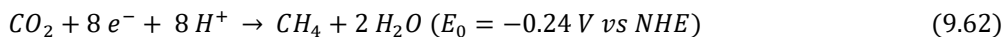
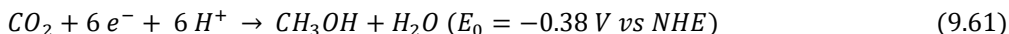
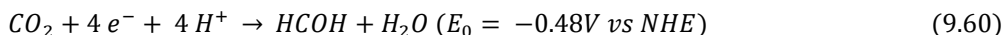
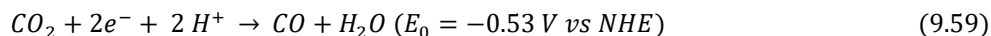
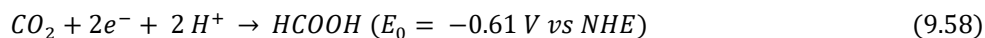
9.7 Fundamentals of CO₂ Reduction for Artificial Photosynthesis Using Molecular Catalysts

For the products that may be harvested from water splitting and CO₂ reduction, the combination of H₂ and O₂ can be used within a hydrogen fuel cell to produce clean electricity. Alternatively, CO with H₂ (syn gas) can be converted into a huge array of chemical products through well-known methods like the Fischer-Tropsch process,^{296,297} the Haber process,²⁹⁸ among others.²⁹⁹ Notably, there can be significant competition between H₂ and CO generation at the cathodic reaction site⁸⁸ and while this is beneficial to produce syn gas, pure CO is seen as a more economically viable alternative.^{300,301}

Artificial photosynthesis can be designed in two overlapping ways – by using photovoltaics to capture solar energy and generate a current that drives an electrochemical reaction, or by absorbing solar energy with molecules that directly use it to perform a photochemical reaction. The two most environmentally relevant forms of artificial photosynthesis are the oxidation of water (H₂O) to oxygen (O₂), and the reduction of carbon dioxide (CO₂) to various products like carbon monoxide (CO), formaldehyde (HCOH) methanol (CH₃OH), formic acid (HCOOH), and methane (CH₄).^{302–304} Together these half-reactions form a reduction/oxidation (redox) couple in which electrons from the anodic H₂O oxidation can be used by the cathodic CO₂ reduction.^{304–306} Each half-reaction, however, poses distinct challenges making studies on overall artificial photosynthetic systems difficult, especially for molecular catalysts (MC) at high efficiencies. Thus, reports of overall artificial photosynthesis are rare with researchers instead focusing on understanding each side of the redox reaction separately. While electrochemical studies have provided a huge number of details about the factors controlling the thermodynamics and kinetics of both water oxidation (WO) reactions and CO₂ reduction reactions (CO₂RR), photochemical artificial photosynthesis is particularly interesting due to the overall efficiency, and the direct analogy it has with natural photosynthesis. Together, however, they provide rich details surrounding the relationship between structures and performance, and strategies to improve them are relatively similar. Due to its unique challenges photochemical WO titles are sparse, but photochemical CO₂RR has a large footprint in the literature. Of the redox couple CO₂RR bears more relevance to this dissertation, but discussions, examples, and future directions of WO will be covered. To gain a fundamental understanding of the factors controlling CO₂RR the thermodynamics and kinetics of the reaction will be discussed while introducing

relevant examples that alter ligand structure and photosensitizer abilities to improve the performance of CO₂ electro- and photoreduction catalysts.

As outlined in Equations 9.57-9.62 CO₂RR varies from needing 1 e⁻ to form a CO₂ radical at E₀ = -1.90V vs. NHE to 8 e⁻ and 8 H⁺ to form CH₄ at -0.24V vs. NHE.



The formation of highly reduced products like CH₃OH and CH₄ requires a lower overall thermodynamic driving force, but as the number of components involved in these reactions increases so does the kinetic barrier. Photochemical CO₂RR must occur within the lifetime of a photogenerated e⁻/h⁺ pair, setting up a race between reaction kinetics and photodynamic relaxation that makes achieving highly reduced products by photochemical methods challenging. As such, this dissertation will focus primarily on photochemical CO production.

Thermodynamic control of intermediate pathways in CO₂RR is especially important because of competing reactions that hinder selectivity of the overall reaction. The primary side reaction that occurs in lieu of CO₂RR is the 2 e⁻ reduction of 2 H⁺ to H₂ at 0.00 V vs NHE (Equation 9.63).



Despite reasonable accessibility of photo- or electrochemical CO₂RR to CO, the 2 e⁻/2 H⁺ reaction is even more favorable thermodynamically. Because of this, mechanisms and intermediates involved in CO/H₂ production are crucial to understanding how selectivity is governed. The energetic landscape of intermediates varies depending on their chemical environment, and the stability of each intermediate will determine the selectivity and activity of the catalytic cycle overall. So far, the study of selectivity in CO₂RR has centered around two reaction pathways – known as the protonation-first, and reduction-first pathways.^{307–309}

Hydride-First Pathway

The hydride-first pathway is often referred to as the protonation-first pathway, but the latter has taken on a distinct meaning and is first hypothesized based on the requirement that Ni(II) and Co(II) tetraazamacrocycles under a CO₂ atmosphere would only generate CO and H₂ when a protic solvent was included in the reaction mixture.³¹⁰ Conducted under inert atmosphere achieved the same overall Faradaic efficiency (FE), but only H₂ production took place – illustrating not only that CO₂ is the source of CO, but also that there is competition between CO and H₂ production. This competitive CO/H₂ production suggested that in a protic solvent a metal hydride intermediate was generated and was necessary to reduce both H⁺ and CO₂ substrates. At first, the role of the metal hydride in CO₂RR was unknown until it was later shown that the hydride intermediate was necessary to lower the free energy of the CO₂ adduct by facilitating CO₂ insertion at the catalytic site. Over time, the necessity of metal hydride for CO₂RR to proceed became somewhat obfuscated by the possibility of pathways that proceed via proton-coupled electron transfer (PCET), and so the definition of “protonation-first” became less clear. Particularly, a study on Ni(II) cyclam found that the intermediate formed in CO₂RR was likely not a metal hydride since activity towards H₂ generation was very low.³¹¹ Instead, protonation of the cyclam amine helped to facilitate CO₂ binding by serving as a PCET agent and forming an intramolecular hydrogen bond between the CO₂ O and ammonium H, leading to lowered overpotential and selective CO production. Modern discussions involving the protonation-first pathway oftentimes assume some type of PCET takes place after reduction of the catalyst. Instead, protonation-first now often refers to protonation of metal bound formate (M-HCO₂⁻) that then dissociates H₂O. To distinguish these pathways from one another the one involving hydride will be referred to as the hydride-first pathway.

In the hydride pathway, the first thermodynamic factor to consider is favorability of metal center protonation.³⁰⁷ Metal hydride formation free energy is the sum of conjugate base protonation free energy with that of metal hydride deprotonation (Equation 9.64).³¹²

$$\Delta G \left(M^- + HA \rightarrow MH + A^- \right) = \Delta G \left(A^- + H^+ \rightarrow AH \right) + \Delta G \left(MH \rightarrow M^- + H^+ \right) \quad (9.64)$$

This free energy can be expressed in terms of pKa by Equation 9.68,³⁰⁷

$$\Delta G = -2.303 RT \log \left(\frac{[HA]}{[H^+][A^-]} \right) - 2.303 RT \log \left(\frac{[M^-][H^+]}{[MH]} \right) \quad (9.65)$$

$$\Delta G = 2.303 RT \log \left(\frac{[H^+][A^-]}{[HA]} \right) - 2.303 RT \log \left(\frac{[M^-][H^+]}{[MH]} \right) \quad (9.66)$$

$$\Delta G = -2.303 RT \text{pK}_a^{\text{acid}} + 2.303 RT \text{pK}_a^{\text{metal hydride}} \quad (9.67)$$

$$\Delta G = -2.303 RT (\text{pK}_a^{\text{acid}} - \text{pK}_a^{\text{metal hydride}}) \quad (9.68)$$

and is interpreted to mean that nucleophilicity increases with pKa upon protonation (M-H, stronger Brønsted base). Thus, since electron rich metals tend to require more negative potential to reduce, a negative linear relationship between pKa and reduction potential is expected. This relationship illustrates the link between the reduction potential and the M-H bond dissociation free energy which is helpful to explain CO₂RR selectivity.³¹³ Modeling the selectivity of the metal hydride towards H₂ or intermediate formate production in CO₂RR one must consider not only the pKa of the metal hydride, but also its two-electron reduction potential and that of H⁺/H⁻. These factors combine to form the measure of hydricity, ΔG_{H^-} (Equation 9.72).³¹⁴



The change in free energy in the formation of H₂ is the sum of the hydricity with the free energy of acid deprotonation minus the cleavage energy of H₂ (C_{H_2}) from the metal center (Equation 9.72).

$$\Delta G(H_2) = \Delta G (MH \rightarrow M^+ + H^-) + \Delta G (HA \rightarrow H^+ + A^-) - \Delta G (MH_2 \rightarrow M + H_2) \quad (9.70)$$

$$\Delta G(H_2) = -2.303 RT \log \left(\frac{[M^+][H^-]}{[MH]} \right) - 2.303 RT \log \left(\frac{[H^+][A^-]}{[HA]} \right) + 2.303 RT \log \left(\frac{[H_2][M]}{[MH_2]} \right) \quad (9.71)$$

$$\Delta G(H_2) = \Delta G_{H^-} + 2.303 RT \text{pK}_a^{\text{acid}} - C_{H_2} \quad (9.72)$$

On the other hand, the formation of formate intermediate is simply the free energy of insertion of CO₂ into the metal hydride bond (Equation 9.74).



$$\Delta G(MCO_2H) = -2.303 RT \log \left(\frac{[MCO_2H]}{[MH][CO_2]} \right) \quad (9.74)$$

The binding mode for CO₂ insertion depends heavily on the ligand environment. Previous examples of structurally similar Ni(II) tetraazamacrocycles and Ni(II) cyclams showed the presence of an aliphatic amine enhanced the CO:H₂ selectivity.^{310,311} More will be discussed about binding modes later in

this section. Nonetheless, some catalysts favor the binding of CO₂ in such a way that promotes formation free formate (Equation 9.75),



and includes a term of formate analogous to hydricity (Equation 9.78).

$$\Delta G(HCO_2^-) = \Delta G_{H^-} + 2.303 RT \log \left(\frac{[M^+][HCO_2^-]}{[MH][CO_2]} \right) \quad (9.76)$$

$$\Delta G(HCO_2^-) = \Delta G_{H^-} - 2.303 RT pK_a^{HCO_2^-} \quad (9.77)$$

$$\Delta G(HCO_2^-) = \Delta G_{H^-} - \Delta G_{H^-}(HCO_2^-). \quad (9.78)$$

While the production of H₂ is dependent on the pK_a of the acid, the formate intermediate and free formate formations are not, thus if the pK_a of the acid is less than the pK_a of metal hydride then H₂ formation will be favored.³⁰⁷ As such, the reaction of metal hydride with CO₂ can be exothermic in suitably acidic conditions because it is a 1 H⁺/2 e⁻ process whereas H₂ production requires 2 H⁺. Finally, if the metal-formate adduct is too stable it will resist HCO₂⁻ release; this will inhibit catalyst turnover of CO₂ even though it may mean that selective CO₂RR takes place. Sabatier's principle then comes into play suggesting that a CO₂RR MC should be sufficiently electron rich to form hydrides but have a low enough formate hydricity to allow catalytic turnover. Overall, the hydride-first pathway is a straightforward way to perform CO₂RR, but it lacks some distinct advantages of the protonation first pathway.

Protonation-First Pathway

There is debate over what follows in the next step;³¹⁵ some studies make the claim that electron transfer to CO₂ occurs in sync with proton (H⁺) transfer by a process known as proton coupled electron transfer (PCET);^{316,317} other studies claim that either a CO₂ anion radical is formed, followed by subsequent protonation.^{301,318} Considering the thermodynamic barrier to CO₂ radical formation, it seems that since PCET is more feasible (-0.53V vs -1.90V vs NHE @ pH 7) and thus should be considered the preferred target mechanism for CO₂ reduction.^{319,320}

H⁺ from the OH⁻ oxidation then either initiates a second PCET step or protonates the carboxylic acid radical anion resulting in the dissociation of H₂O from the desired CO product. Thermodynamically, the complete redox requires a potential of 1.35V at neutral pH, but when considering the complex kinetics and/or an unavoidable CO₂ anion radical intermediary the reaction does not typically proceed unless an

additional overpotential is applied.^{88,301} Regardless, the populated excited state must have a potential energy of -0.53V to catalyze CO₂ reduction, and the unpopulated ground state must have a potential energy of 0.82V to catalyze H₂O oxidation. The redox potentials highlight the need for an appropriate band gap in the photocatalyst and the kinetic requirements require intelligent and efficient energy transfer.

REFERENCES

- (1) Shaftel, H.; Jackson, R.; Callery, S.; Bailey, D. Global Climate Change: Vital Signs of the Planet climate.nasa.gov (accessed Apr 10, 2020).
- (2) IEA (2020). *Key World Energy Statistics 2020*; Paris, 2020.
- (3) Ritche, H. Sector by Sector: Where Do Global Greenhouse Gas Emissions Come From? 2020.
- (4) Levi, P. G.; Cullen, J. M. Mapping Global Flows of Chemicals: From Fossil Fuel Feedstocks to Chemical Products. *Environ Sci Technol* **2018**, *52* (4), 1725–1734.
- (5) Yoon, J.; Baca, A. J.; Park, S.-I.; Elvikis, P.; Geddes, J. B.; Li, L.; Kim, R. H.; Xiao, J.; Wang, S.; Kim, T.-H.; Motala, M. J.; Ahn, B. Y.; Duoss, E. B.; Lewis, J. A.; Nuzzo, R. G.; Ferreira, P. M.; Huang, Y.; Rockett, A.; Rogers, J. A. Ultrathin Silicon Solar Microcells for Semitransparent, Mechanically Flexible and Microconcentrator Module Designs. *Nat Mater* **2008**, *7* (11), 907–915.
- (6) Knott, B. C.; Erickson, E.; Allen, M. D.; Gado, J. E.; Graham, R.; Kearns, F. L.; Pardo, I.; Topuzlu, E.; Anderson, J. J.; Austin, H. P.; Dominick, G.; Johnson, C. W.; Rorrer, N. A.; Szostkiewicz, C. J.; Copié, V.; Payne, C. M.; Woodcock, H. L.; Donohoe, B. S.; Beckham, G. T.; McGeehan, J. E. Characterization and Engineering of a Two-Enzyme System for Plastics Depolymerization. *Proceedings of the National Academy of Sciences* **2020**, 202006753.
- (7) De Luna, P.; Hahn, C.; Higgins, D.; Jaffer, S. A.; Jaramillo, T. F.; Sargent, E. H. What Would It Take for Renewably Powered Electrosynthesis to Displace Petrochemical Processes? *Science (1979)* **2019**, *364* (6438), eaav3506.
- (8) Nitopi, S.; Bertheussen, E.; Scott, S. B.; Liu, X.; Engstfeld, A. K.; Horch, S.; Seger, B.; Stephens, I. E. L.; Chan, K.; Hahn, C.; Nørskov, J. K.; Jaramillo, T. F.; Chorkendorff, I. Progress and Perspectives of Electrochemical CO₂ Reduction on Copper in Aqueous Electrolyte. *Chem Rev* **2019**, *119* (12), 7610–7672.
- (9) He, J.; Janáky, C. Recent Advances in Solar-Driven Carbon Dioxide Conversion: Expectations versus Reality. *ACS Energy Lett* **2020**, *5* (6), 1996–2014.
- (10) Nørskov, J. K.; Weckhuysen, B.; Centi, G.; others. Research Needs towards Sustainable Production of Fuels and Chemicals. *Energy X* **2019**.
- (11) Olah, G. A. Beyond Oil and Gas: The Methanol Economy. *Angewandte Chemie International Edition* **2005**, *44* (18), 2636–2639.
- (12) Tian, P.; Wei, Y.; Ye, M.; Liu, Z. Methanol to Olefins (MTO): From Fundamentals to Commercialization. *ACS Catal* **2015**, *5* (3), 1922–1938.
- (13) Li, T.; Shoinchorova, T.; Gascon, J.; Ruiz-Martínez, J. Aromatics Production via Methanol-Mediated Transformation Routes. *ACS Catal* **2021**, *11* (13), 7780–7819.
- (14) Grätzel, M. Photoelectrochemical Cells. *Nature* **2001**, *414* (6861), 338–344.
- (15) Lindsey, R. Climate and Earth's Energy Budget <https://earthobservatory.nasa.gov/features/EnergyBalance> (accessed Apr 10, 2020).
- (16) IRENA (2020). Renewable Power Generation Costs In 2019. International Renewable Energy Agency: Abu Dhabi 2020.
- (17) Feldman, D.; Margolis, R. *Q1/Q2 2020 Solar Industry Update*; 2020.
- (18) *Solar-Plus-Storage 101*; U.S. Department of Energy: Washington D.C., 2019.

- (19) Roy, S. C.; Varghese, O. K.; Paulose, M.; Grimes, C. A. Toward Solar Fuels: Photocatalytic Conversion of Carbon Dioxide to Hydrocarbons. *ACS Nano* **2010**, *4* (3), 1259–1278.
- (20) Blankenship, R. E. *Molecular Mechanisms of Photosynthesis*; John Wiley & Sons, 2014.
- (21) Björn, L. O.; Govindjee. The Evolution of Photosynthesis and Chloroplasts. *Curr Sci* **2009**, *96* (11), 1466–1474.
- (22) Blankenship, R. E. Early Evolution of Photosynthesis. *Plant Physiol* **2010**, *154* (2), 434 LP – 438.
- (23) Wang, Y.; Suzuki, H.; Xie, J.; Tomita, O.; Martin, D. J.; Higashi, M.; Kong, D.; Abe, R.; Tang, J. Mimicking Natural Photosynthesis: Solar to Renewable H₂ Fuel Synthesis by Z-Scheme Water Splitting Systems. *Chem Rev* **2018**, *118* (10), 5201–5241.
- (24) Scholes, G. D.; Fleming, G. R.; Olaya-Castro, A.; van Grondelle, R. Lessons from Nature about Solar Light Harvesting. *Nat Chem* **2011**, *3* (10), 763–774.
- (25) Terazono, Y.; Kodis, G.; Bhushan, K.; Zaks, J.; Madden, C.; Moore, A. L.; Moore, T. A.; Fleming, G. R.; Gust, D. Mimicking the Role of the Antenna in Photosynthetic Photoprotection. *J Am Chem Soc* **2011**, *133* (9), 2916–2922.
- (26) Niyogi, K. K. Safety Valves for Photosynthesis. *Curr Opin Plant Biol* **2000**, *3* (6), 455–460.
- (27) Hildner, R.; Brinks, D.; Nieder, J. B.; Cogdell, R. J.; van Hulst, N. F. Quantum Coherent Energy Transfer over Varying Pathways in Single Light-Harvesting Complexes. *Science (1979)* **2013**, *340* (6139), 1448 LP – 1451.
- (28) Fowler, G. J. S.; Visschers, R. W.; Grief, G. G.; van Grondelle, R.; Hunter, C. N. Genetically Modified Photosynthetic Antenna Complexes with Blueshifted Absorbance Bands. *Nature* **1992**, *355* (6363), 848–850.
- (29) Koolhaas, M. H. C.; Frese, R. N.; Fowler, G. J. S.; Bibby, T. S.; Georgakopoulou, S.; van der Zwan, G.; Hunter, C. N.; van Grondelle, R. Identification of the Upper Exciton Component of the B850 Bacteriochlorophylls of the LH2 Antenna Complex, Using a B800-Free Mutant of Rhodobacter Sphaeroides. *Biochemistry* **1998**, *37* (14), 4693–4698.
- (30) Cogdell, R. J.; Gall, A.; Köhler, J. The Architecture and Function of the Light-Harvesting Apparatus of Purple Bacteria: From Single Molecules to in Vivo Membranes. *Q Rev Biophys* **2006**, *39* (3), 227–324.
- (31) Scholes, G. D.; Gould, I. R.; Cogdell, R. J.; Fleming, G. R. Ab Initio Molecular Orbital Calculations of Electronic Couplings in the LH2 Bacterial Light-Harvesting Complex of Rps. Acidophila. *J Phys Chem B* **1999**, *103* (13), 2543–2553.
- (32) Côté, A. P.; Benin, A. I.; Ockwig, N. W.; O’Keeffe, M.; Matzger, A. J.; Yaghi, O. M. Porous, Crystalline, Covalent Organic Frameworks. *Science (1979)* **2005**, *310* (5751), 1166 LP – 1170.
- (33) Diercks, C. S.; Yaghi, O. M. The Atom, the Molecule, and the Covalent Organic Framework. *Science (1979)* **2017**, *355* (6328), eaal1585.
- (34) Uribe-Romo, F. J.; Hunt, J. R.; Furukawa, H.; Klöck, C.; O’Keeffe, M.; Yaghi, O. M. A Crystalline Imine-Linked 3-D Porous Covalent Organic Framework. *J Am Chem Soc* **2009**, *131* (13), 4570–4571.
- (35) Blatov, V. A.; Carlucci, L.; Ciani, G.; Proserpio, D. M. Interpenetrating Metal–Organic and Inorganic 3D Networks: A Computer-Aided Systematic Investigation. Part I. Analysis of the Cambridge Structural Database. *CrystEngComm* **2004**, *6* (65), 377–395.
- (36) Park, I.-H.; Mulijanto, C. E.; Lee, H.-H.; Kang, Y.; Lee, E.; Chanthapally, A.; Lee, S. S.; Vittal, J. J. Influence of Interpenetration in Diamondoid Metal–Organic Frameworks on the Photoreactivity and Sensing Properties. *Cryst Growth Des* **2016**, *16* (5), 2504–2508.

- (37) Ma, T.; Wei, L.; Liang, L.; Yin, S.; Xu, L.; Niu, J.; Xue, H.; Wang, X.; Sun, J.; Zhang, Y.-B.; Wang, W. Diverse Crystal Size Effects in Covalent Organic Frameworks. *Nat Commun* **2020**, *11* (1), 6128.
- (38) Blatov, V. A.; Yang, C.; Tang, D.; Zeng, Q.; Golov, A. A.; Kabanov, A. A. High-Throughput Systematic Topological Generation of Low-Energy Carbon Allotropes. *NPJ Comput Mater* **2021**, *7* (1), 15.
- (39) Li, Z.; Sheng, L.; Wang, H.; Wang, X.; Li, M.; Xu, Y.; Cui, H.; Zhang, H.; Liang, H.; Xu, H.; He, X. Three-Dimensional Covalent Organic Framework with Ceq Topology. *J Am Chem Soc* **2021**, *143* (1), 92–96.
- (40) El-Kaderi, H. M.; Hunt, J. R.; Mendoza-Cortés, J. L.; Côté, A. P.; Taylor, R. E.; O’Keeffe, M.; Yaghi, O. M. Designed Synthesis of 3D Covalent Organic Frameworks. *Science (1979)* **2007**, *316* (5822), 268–272.
- (41) Lan, Y.; Han, X.; Tong, M.; Huang, H.; Yang, Q.; Liu, D.; Zhao, X.; Zhong, C. Materials Genomics Methods for High-Throughput Construction of COFs and Targeted Synthesis. *Nat Commun* **2018**, *9* (1), 5274.
- (42) Yahiaoui, O.; Fitch, A. N.; Hoffmann, F.; Fröba, M.; Thomas, A.; Roeser, J. 3D Anionic Silicate Covalent Organic Framework with Srs Topology. *J Am Chem Soc* **2018**, *140* (16), 5330–5333.
- (43) Lin, G.; Ding, H.; Yuan, D.; Wang, B.; Wang, C. A Pyrene-Based, Fluorescent Three-Dimensional Covalent Organic Framework. *J Am Chem Soc* **2016**, *138* (10), 3302–3305.
- (44) Bourda, L.; Krishnaraj, C.; Van Der Voort, P.; Van Hecke, K. Conquering the Crystallinity Conundrum: Efforts to Increase Quality of Covalent Organic Frameworks. *Mater Adv* **2021**, *2* (9), 2811–2845.
- (45) Geng, K.; He, T.; Liu, R.; Dalapati, S.; Tan, K. T.; Li, Z.; Tao, S.; Gong, Y.; Jiang, Q.; Jiang, D. Covalent Organic Frameworks: Design, Synthesis, and Functions. *Chem Rev* **2020**, *120* (16), 8814–8933.
- (46) Ascherl, L.; Sick, T.; Margraf, J. T.; Lapidus, S. H.; Calik, M.; Hettstedt, C.; Karaghiosoff, K.; Döblinger, M.; Clark, T.; Chapman, K. W.; Auras, F.; Bein, T. Molecular Docking Sites Designed for the Generation of Highly Crystalline Covalent Organic Frameworks. *Nat Chem* **2016**, *8* (4), 310–316.
- (47) Chen, X.; Addicoat, M.; Irle, S.; Nagai, A.; Jiang, D. Control of Crystallinity and Porosity of Covalent Organic Frameworks by Managing Interlayer Interactions Based on Self-Complementary π -Electronic Force. *J Am Chem Soc* **2013**, *135* (2), 546–549.
- (48) Fang, Q.; Pang, Z.; Ai, Q.; Liu, Y.; Zhai, T.; Steinbach, D.; Gao, G.; Zhu, Y.; Li, T.; Lou, J. Superior Mechanical Properties of Multilayer Covalent-Organic Frameworks Enabled by Rationally Tuning Molecular Interlayer Interactions. *Proceedings of the National Academy of Sciences* **2023**, *120* (15), e2208676120.
- (49) Alahakoon, S. B.; Tan, K.; Pandey, H.; Diwakara, S. D.; McCandless, G. T.; Grinffiel, D. I.; Durand-Silva, A.; Thonhauser, T.; Smaldone, R. A. 2D-Covalent Organic Frameworks with Interlayer Hydrogen Bonding Oriented through Designed Nonplanarity. *J Am Chem Soc* **2020**, *142* (30), 12987–12994.
- (50) Nguyen, V.; Grünwald, M. Microscopic Origins of Poor Crystallinity in the Synthesis of Covalent Organic Framework COF-5. *J Am Chem Soc* **2018**, *140* (9), 3306–3311.
- (51) Ma, T.; Kapustin, E. A.; Yin, S. X.; Liang, L.; Zhou, Z.; Niu, J.; Li, L.-H.; Wang, Y.; Su, J.; Li, J.; Wang, X.; Wang, W. D.; Wang, W.; Sun, J.; Yaghi, O. M. Single-Crystal x-Ray Diffraction Structures of Covalent Organic Frameworks. *Science (1979)* **2018**, *361* (6397), 48 LP – 52.

- (52) Wang, H.; He, B.; Liu, F.; Stevens, C.; Brady, M. A.; Cai, S.; Wang, C.; Russell, T. P.; Tan, T.-W.; Liu, Y. Orientation Transitions during the Growth of Imine Covalent Organic Framework Thin Films. *J Mater Chem C Mater* **2017**, *5* (21), 5090–5095.
- (53) Wu, Y.; Yan, D.; Zhang, Z.; Matsushita, M. M.; Awaga, K. Electron Highways into Nanochannels of Covalent Organic Frameworks for High Electrical Conductivity and Energy Storage. *ACS Appl Mater Interfaces* **2019**, *11* (8), 7661–7665.
- (54) Meng, Z.; Stolz, R. M.; Mirica, K. A. Two-Dimensional Chemiresistive Covalent Organic Framework with High Intrinsic Conductivity. *J Am Chem Soc* **2019**, *141* (30), 11929–11937.
- (55) Wan, S.; Guo, J.; Kim, J.; Ihee, H.; Jiang, D. A Belt-Shaped, Blue Luminescent, and Semiconducting Covalent Organic Framework. *Angewandte Chemie International Edition* **2008**, *47* (46), 8826–8830.
- (56) Jin, S.; Ding, X.; Feng, X.; Supur, M.; Furukawa, K.; Takahashi, S.; Addicoat, M.; El-Khouly, M. E.; Nakamura, T.; Irle, S.; Fukuzumi, S.; Nagai, A.; Jiang, D. Charge Dynamics in A Donor–Acceptor Covalent Organic Framework with Periodically Ordered Bicontinuous Heterojunctions. *Angewandte Chemie International Edition* **2013**, *52* (7), 2017–2021.
- (57) Xie, L. S.; Skorupskii, G.; Dincă, M. Electrically Conductive Metal–Organic Frameworks. *Chem Rev* **2020**, *120* (16), 8536–8580.
- (58) Jakowetz, A. C.; Hinrichsen, T.; Ascherl, L.; Sick, T.; Calik, M.; Auras, F.; D. Medina, D.; H. Friend, R.; Rao, A.; Bein, T. Excited-State Dynamics in Fully Conjugated 2D Covalent Organic Frameworks. *J Am Chem Soc* **2019**, *0* (0), null-null.
- (59) Thomas, S.; Li, H.; Zhong, C.; Matsumoto, M.; R. Dichtel, W.; Bredas, J.-L. Electronic Structure of Two-Dimensional π -Conjugated Covalent Organic Frameworks. *Chemistry of Materials* **2019**, *31* (9), 3051–3065.
- (60) Spano, F. C. The Spectral Signatures of Frenkel Polarons in H- and J-Aggregates. *Acc Chem Res* **2010**, *43* (3), 429–439.
- (61) Hestand, N. J.; Spano, F. C. Molecular Aggregate Photophysics beyond the Kasha Model: Novel Design Principles for Organic Materials. *Acc Chem Res* **2017**, *50* (2), 341–350.
- (62) Hestand, N. J. J.; C. Spano, F.; Spano, F. C.; C. Spano, F.; Spano, F. C. Expanded Theory of H- and J-Molecular Aggregates: The Effects of Vibronic Coupling and Intermolecular Charge Transfer. *Chem Rev* **2018**, *118* (15), 7069–7163.
- (63) Schubert, A.; Settels, V.; Liu, W.; Würthner, F.; Meier, C.; Fink, R. F.; Schindlbeck, S.; Lochbrunner, S.; Engels, B.; Engel, V. Ultrafast Exciton Self-Trapping upon Geometry Deformation in Perylene-Based Molecular Aggregates. *J Phys Chem Lett* **2013**, *4* (5), 792–796.
- (64) Bae, Y. J.; Shimizu, D.; Schultz, J. D.; Kang, G.; Zhou, J.; Schatz, G. C.; Osuka, A.; Wasielewski, M. R. Balancing Charge Transfer and Frenkel Exciton Coupling Leads to Excimer Formation in Molecular Dimers: Implications for Singlet Fission. *J Phys Chem A* **2020**, *124* (41), 8478–8487.
- (65) Zhong, C.; Bialas, D.; Spano, F. C. Unusual Non-Kasha Photophysical Behavior of Aggregates of Push–Pull Donor–Acceptor Chromophores. *The Journal of Physical Chemistry C* **2020**, *124* (3), 2146–2159.
- (66) Kasha, M. Energy Transfer Mechanisms and the Molecular Exciton Model for Molecular Aggregates. *Radiat Res* **1963**, *20* (1), 55–70.
- (67) Scholes, G. D.; Rumbles, G. Excitons in Nanoscale Systems. *Nat Mater* **2006**, *5* (9), 683–696.
- (68) Hestand, N. J.; Kazantsev, R. V.; Weingarten, A. S.; Palmer, L. C.; Stupp, S. I.; Spano, F. C. Extended-Charge-Transfer Excitons in Crystalline Supramolecular Photocatalytic Scaffolds. *J Am Chem Soc* **2016**, *138* (36), 11762–11774.

- (69) Kang, C.; Yang, K.; Zhang, Z.; Usadi, A. K.; Calabro, D. C.; Baugh, L. S.; Wang, Y.; Jiang, J.; Zou, X.; Huang, Z.; Zhao, D. Growing Single Crystals of Two-Dimensional Covalent Organic Frameworks Enabled by Intermediate Tracing Study. *Nat Commun* **2022**, *13* (1), 1370.
- (70) Natraj, A.; Ji, W.; Xin, J.; Castano, I.; Burke, D. W.; Evans, A. M.; Strauss, M. J.; Ateia, M.; Hamachi, L. S.; Gianneschi, N. C.; AlOthman, Z. A.; Sun, J.; Yusuf, K.; Dichtel, W. R. Single-Crystalline Imine-Linked Two-Dimensional Covalent Organic Frameworks Separate Benzene and Cyclohexane Efficiently. *J Am Chem Soc* **2022**, *144* (43), 19813–19824.
- (71) Zhao, W.; Yan, P.; Yang, H.; Bahri, M.; James, A. M.; Chen, H.; Liu, L.; Li, B.; Pang, Z.; Clowes, R.; Browning, N. D.; Ward, J. W.; Wu, Y.; Cooper, A. I. Using Sound to Synthesize Covalent Organic Frameworks in Water. *Nature Synthesis* **2022**, *1* (1), 87–95.
- (72) Shinde, D. B.; Aiyappa, H. B.; Bhadra, M.; Biswal, B. P.; Wadge, P.; Kandambeth, S.; Garai, B.; Kundu, T.; Kurungot, S.; Banerjee, R. A Mechanochemically Synthesized Covalent Organic Framework as a Proton-Conducting Solid Electrolyte. *J Mater Chem A Mater* **2016**, *4* (7), 2682–2690.
- (73) Díaz de Greñu, B.; Torres, J.; García-González, J.; Muñoz-Pina, S.; de los Reyes, R.; Costero, A. M.; Amorós, P.; Ros-Lis, J. V. Microwave-Assisted Synthesis of Covalent Organic Frameworks: A Review. *ChemSusChem* **2021**, *14* (1), 208–233.
- (74) Yuan, S.; Li, X.; Zhu, J.; Zhang, G.; Van Puyvelde, P.; Van der Bruggen, B. Covalent Organic Frameworks for Membrane Separation. *Chem Soc Rev* **2019**, *48* (10), 2665–2681.
- (75) Medina, D. D.; Petrus, M. L.; Jumabekov, A. N.; Margraf, J. T.; Weinberger, S.; Rotter, J. M.; Clark, T.; Bein, T. Directional Charge-Carrier Transport in Oriented Benzodithiophene Covalent Organic Framework Thin Films. *ACS Nano* **2017**, *11* (3), 2706–2713.
- (76) Evans, A. M.; Castano, I.; Brumberg, A.; Parent, L. R.; Corcos, A. R.; Li, R. L.; Flanders, N. C.; Gosztola, D. J.; Gianneschi, N. C.; Schaller, R. D.; Dichtel, W. R. Emissive Single-Crystalline Boroxine-Linked Colloidal Covalent Organic Frameworks. *J Am Chem Soc* **2019**, *141* (50), 19728–19735.
- (77) Fenton, J. L.; Burke, D. W.; Qian, D.; Olvera de la Cruz, M.; Dichtel, W. R. Polycrystalline Covalent Organic Framework Films Act as Adsorbents, Not Membranes. *J Am Chem Soc* **2021**, *143* (3), 1466–1473.
- (78) Dey, K.; Pal, M.; Rout, K. C.; Kunjattu H, S.; Das, A.; Mukherjee, R.; Kharul, U. K.; Banerjee, R. Selective Molecular Separation by Interfacially Crystallized Covalent Organic Framework Thin Films. *J Am Chem Soc* **2017**, *139* (37), 13083–13091.
- (79) Guan, Q.; Zhou, L.-L.; Dong, Y.-B. Construction of Covalent Organic Frameworks via Multicomponent Reactions. *J Am Chem Soc* **2023**, *145* (3), 1475–1496.
- (80) Zhu, D.; Zhang, J.-J.; Wu, X.; Yan, Q.; Liu, F.; Zhu, Y.; Gao, X.; Rahman, M. M.; Yakobson, B. I.; Ajayan, P. M.; Verduzco, R. Understanding Fragility and Engineering Activation Stability in Two-Dimensional Covalent Organic Frameworks. *Chem Sci* **2022**, *13* (33), 9655–9667.
- (81) Smieja, J. M.; Kubiak, C. P. Re(Bipy-TBu)(CO)₃Cl-improved Catalytic Activity for Reduction of Carbon Dioxide: IR-Spectroelectrochemical and Mechanistic Studies. *Inorg Chem* **2010**, *49* (20), 9283–9289.
- (82) Zhu, S.; Wang, D. Photocatalysis: Basic Principles, Diverse Forms of Implementations and Emerging Scientific Opportunities. *Adv Energy Mater* **2017**, *7* (23), 1700841.
- (83) C. Flanders, N.; S. Kirschner, M.; Kim, P.; J. Fauvell, T.; M. Evans, A.; Helweh, W.; P. Spencer, A.; D. Schaller, R.; R. Dichtel, W.; X. Chen, L. Large Exciton Diffusion Coefficients in Two-Dimensional Covalent Organic Frameworks with Different Domain Sizes Revealed by Ultrafast Exciton Dynamics. *J Am Chem Soc* **2020**, *142* (35), 14957–14965.

- (84) Jakowetz, A. C.; F. Hinrichsen, T.; Ascherl, L.; Sick, T.; Calik, M.; Auras, F.; D. Medina, D.; H. Friend, R.; Rao, A.; Bein, T. Excited-State Dynamics in Fully Conjugated 2D Covalent Organic Frameworks. *J Am Chem Soc* **2019**, *141* (29), 11565–11571.
- (85) Zhang, X.; Geng, K.; Jiang, D.; Scholes, G. D. Exciton Diffusion and Annihilation in an Sp²Carbon-Conjugated Covalent Organic Framework. *J Am Chem Soc* **2022**, *144* (36), 16423–16432.
- (86) Jakowetz, A. C.; Hinrichsen, T. F.; Ascherl, L.; Sick, T.; Calik, M.; Auras, F.; Medina, D. D.; Friend, R. H.; Rao, A.; Bein, T. Excited-State Dynamics in Fully Conjugated 2D Covalent Organic Frameworks. *J Am Chem Soc* **2019**, *141* (29), 11565–11571.
- (87) Flanders, N. C.; Kirschner, M. S.; Kim, P.; Fauvell, T. J.; Evans, A. M.; Helweh, W.; Spencer, A. P.; Schaller, R. D.; Dichtel, W. R.; Chen, L. X. Large Exciton Diffusion Coefficients in Two-Dimensional Covalent Organic Frameworks with Different Domain Sizes Revealed by Ultrafast Exciton Dynamics. *J Am Chem Soc* **2020**, *142* (35), 14957–14965.
- (88) Lin, S.; Diercks, C. S.; Zhang, Y.-B.; Kornienko, N.; Nichols, E. M.; Zhao, Y.; Paris, A. R.; Kim, D.; Yang, P.; Yaghi, O. M.; Chang, C. J. Covalent Organic Frameworks Comprising Cobalt Porphyrins for Catalytic CO₂ Reduction in Water. *Science (1979)* **2015**, *349* (6253), 1208 LP – 1213.
- (89) Behar, D.; Dhanasekaran, T.; Neta, P.; Hosten, C. M.; Ejeh, D.; Hambright, P.; Fujita, E. Cobalt Porphyrin Catalyzed Reduction of CO₂. Radiation Chemical, Photochemical, and Electrochemical Studies. *J Phys Chem A* **1998**, *102* (17), 2870–2877.
- (90) Yang, S.; Hu, W.; Zhang, X.; He, P.; Pattengale, B.; Liu, C.; Cendejas, M.; Hermans, I.; Zhang, X.; Zhang, J.; Huang, J. 2D Covalent Organic Frameworks as Intrinsic Photocatalysts for Visible Light-Driven CO₂ Reduction. *J Am Chem Soc* **2018**, *140* (44), 14614–14618.
- (91) Ma, L.; Falkowski, J. M.; Abney, C.; Lin, W. A Series of Isorecticular Chiral Metal–Organic Frameworks as a Tunable Platform for Asymmetric Catalysis. *Nat Chem* **2010**, *2* (10), 838–846.
- (92) Bunck, D. N.; Dichtel, W. R. Internal Functionalization of Three-Dimensional Covalent Organic Frameworks. *Angewandte Chemie International Edition* **2012**, *51* (8), 1885–1889.
- (93) Diercks, C. S.; Yaghi, O. M. The Atom, the Molecule, and the Covalent Organic Framework. *Science (1979)* **2017**, *355* (6328), eaal1585.
- (94) Huang, N.; Wang, P.; Jiang, D. Covalent Organic Frameworks: A Materials Platform for Structural and Functional Designs. *Nat Rev Mater* **2016**, *1* (10), 16068.
- (95) Vyas, V. S.; Haase, F.; Stegbauer, L.; Savasci, G.; Podjaski, F.; Ochsenfeld, C.; Lotsch, B. v. A Tunable Azine Covalent Organic Framework Platform for Visible Light-Induced Hydrogen Generation. *Nat Commun* **2015**, *6*, 8508.
- (96) Bunck, D. N.; Dichtel, W. R. Postsynthetic Functionalization of 3D Covalent Organic Frameworks. *Chemical Communications* **2013**, *49* (24), 2457–2459.
- (97) Waller, P. J.; Lyle, S. J.; Osborn Popp, T. M.; Diercks, C. S.; Reimer, J. A.; Yaghi, O. M. Chemical Conversion of Linkages in Covalent Organic Frameworks. *J Am Chem Soc* **2016**, *138* (48), 15519–15522.
- (98) Kandambeth, S.; Dey, K.; Banerjee, R. Covalent Organic Frameworks: Chemistry beyond the Structure. *J Am Chem Soc* **2019**, *141* (5), 1807–1822.
- (99) Zhao, W.; Xia, L.; Liu, X. Covalent Organic Frameworks (COFs): Perspectives of Industrialization. *CrystEngComm* **2018**, *20* (12), 1613–1634.
- (100) Vazquez-Molina, D. A.; Mohammad-Pour, G. S.; Lee, C.; Logan, M. W.; Duan, X.; Harper, J. K.; Uribe-Romo, F. J. Mechanically Shaped Two-Dimensional Covalent Organic Frameworks Reveal

- Crystallographic Alignment and Fast Li-Ion Conductivity. *J Am Chem Soc* **2016**, *138* (31), 9767–9770.
- (101) Li, X.; Zhang, C.; Cai, S.; Lei, X.; Altoe, V.; Hong, F.; Urban, J. J.; Ciston, J.; Chan, E. M.; Liu, Y. Facile Transformation of Imine Covalent Organic Frameworks into Ultrastable Crystalline Porous Aromatic Frameworks. *Nat Commun* **2018**, *9* (1), 2998.
- (102) Huang, N.; Chen, X.; Krishna, R.; Jiang, D. Two-Dimensional Covalent Organic Frameworks for Carbon Dioxide Capture through Channel-Wall Functionalization. *Angewandte Chemie International Edition* **2015**, *54* (10), 2986–2990.
- (103) Fu, Z.; Wang, X.; Gardner, A. M.; Wang, X.; Chong, S. Y.; Neri, G.; Cowan, A. J.; Liu, L.; Li, X.; Vogel, A.; Clowes, R.; Bilton, M.; Chen, L.; Sprick, R. S.; Cooper, A. I. A Stable Covalent Organic Framework for Photocatalytic Carbon Dioxide Reduction. *Chem Sci* **2020**, *11* (2), 543–550.
- (104) Stegbauer, L.; Schwinghammer, K.; Lotsch, B. V. A Hydrazone-Based Covalent Organic Framework for Photocatalytic Hydrogen Production. *Chem Sci* **2014**, *5* (7), 2789–2793.
- (105) Pachfule, P.; Acharjya, A.; Roeser, J.; Langenhahn, T.; Schwarze, M.; Schomäcker, R.; Thomas, A.; Schmidt, J. Diacetylene Functionalized Covalent Organic Framework (COF) for Photocatalytic Hydrogen Generation. *J Am Chem Soc* **2018**, *140* (4), 1423–1427.
- (106) Bhunia, S.; Das, S. K.; Jana, R.; Peter, S. C.; Bhattacharya, S.; Addicoat, M.; Bhaumik, A.; Pradhan, A. Electrochemical Stimuli-Driven Facile Metal-Free Hydrogen Evolution from Pyrene-Porphyrin-Based Crystalline Covalent Organic Framework. *ACS Appl Mater Interfaces* **2017**, *9* (28), 23843–23851.
- (107) Zhang, M.; Lu, M.; Lang, Z.-L.; Liu, J.; Liu, M.; Chang, J.-N.; Li, L.-Y.; Shang, L.-J.; Wang, M.; Li, S.-L.; Lan, Y.-Q. Semiconductor/Covalent-Organic-Framework Z-Scheme Heterojunctions for Artificial Photosynthesis. *Angewandte Chemie International Edition* **2020**, *n/a* (n/a).
- (108) Karak, S.; Stepanenko, V.; Addicoat, M. A.; Keßler, P.; Moser, S.; Beuerle, F.; Würthner, F. A Covalent Organic Framework for Cooperative Water Oxidation. *J Am Chem Soc* **2022**, *144* (38), 17661–17670.
- (109) Aradi, B.; Hourahine, B.; Frauenheim, Th. DFTB+, a Sparse Matrix-Based Implementation of the DFTB Method. *J Phys Chem A* **2007**, *111* (26), 5678–5684.
- (110) Gaus, M.; Goez, A.; Elstner, M. Parametrization and Benchmark of DFTB3 for Organic Molecules. *J Chem Theory Comput* **2013**, *9* (1), 338–354.
- (111) Grimme, S.; Antony, J.; Ehrlich, S.; Krieg, H. A Consistent and Accurate Ab Initio Parametrization of Density Functional Dispersion Correction (DFT-D) for the 94 Elements H-Pu. *J Chem Phys* **2010**, *132* (15), 154104.
- (112) Johnson, E. R.; Becke, A. D. A Post-Hartree–Fock Model of Intermolecular Interactions. *J Chem Phys* **2005**, *123* (2), 24101.
- (113) Yanai, T.; Tew, D. P.; Handy, N. C. A New Hybrid Exchange–Correlation Functional Using the Coulomb-Attenuating Method (CAM-B3LYP). *Chem Phys Lett* **2004**, *393* (1–3), 51–57.
- (114) Petersson, G. A.; Al-Laham, M. A. A Complete Basis Set Model Chemistry. II. Open-shell Systems and the Total Energies of the First-row Atoms. *J Chem Phys* **1991**, *94* (9), 6081–6090.
- (115) Krishnan, R.; Binkley, J. S.; Seeger, R.; Pople, J. A. Self-consistent Molecular Orbital Methods. XX. A Basis Set for Correlated Wave Functions. *J Chem Phys* **1980**, *72* (1), 650–654.
- (116) McLean, A. D.; Chandler, G. S. Contracted Gaussian Basis Sets for Molecular Calculations. I. Second Row Atoms, Z=11–18. *J Chem Phys* **1980**, *72* (10), 5639–5648.

- (117) Plasser, F. TheoDORE: A Toolbox for a Detailed and Automated Analysis of Electronic Excited State Computations. *J Chem Phys* **2020**, *152* (8), 84108.
- (118) Plasser, F.; Lischka, H. Analysis of Excitonic and Charge Transfer Interactions from Quantum Chemical Calculations. *J Chem Theory Comput* **2012**, *8* (8), 2777–2789.
- (119) Plasser, F.; Wormit, M.; Dreuw, A. New Tools for the Systematic Analysis and Visualization of Electronic Excitations. I. Formalism. *J Chem Phys* **2014**, *141* (2), 24106.
- (120) Plasser, F. TheoDORE 2.0: A Package for Theoretical Density, Orbital Relaxation, and Exciton Analysis.
- (121) Snellenburg, J. J.; Liptenok, S.; Seger, R.; Mullen, K. M.; van Stokkum, I. H. M. Glotaran: A Java-Based Graphical User Interface for the R Package TIMP. *J Stat Softw* **2012**, *49* (3 SE-Articles), 1–22.
- (122) Becke, A. D. Density-functional Thermochemistry. III. The Role of Exact Exchange. *J Chem Phys* **1993**, *98* (7), 5648–5652.
- (123) Lee, C.; Yang, W.; Parr, R. G. Development of the Colle-Salvetti Correlation-Energy Formula into a Functional of the Electron Density. *Phys Rev B* **1988**, *37* (2), 785–789.
- (124) Stephens, P. J.; Devlin, F. J.; Chabalowski, C. F.; Frisch, M. J. Ab Initio Calculation of Vibrational Absorption and Circular Dichroism Spectra Using Density Functional Force Fields. *J Phys Chem* **1994**, *98* (45), 11623–11627.
- (125) Grimme, S.; Ehrlich, S.; Goerigk, L. Effect of the Damping Function in Dispersion Corrected Density Functional Theory. *J Comput Chem* **2011**, *32* (7), 1456–1465.
- (126) Ditchfield, R.; Hehre, W. J.; Pople, J. A. Self-Consistent Molecular-Orbital Methods. IX. An Extended Gaussian-Type Basis for Molecular-Orbital Studies of Organic Molecules. *J Chem Phys* **1971**, *54* (2), 724–728.
- (127) Tomasi, J.; Mennucci, B.; Cammi, R. Quantum Mechanical Continuum Solvation Models. *Chem Rev* **2005**, *105* (8), 2999–3094.
- (128) Frisch, M. J.; Trucks, G. W.; Schlegel, H. B.; Scuseria, G. E.; Robb, M. A.; Cheeseman, J. R.; Scalmani, G.; Barone, V.; Mennucci, B.; Petersson, G. A. Gaussian 09, Revision D. 01; Gaussian, Inc: Wallingford, CT, 2013.
- (129) Rohrdanz, M. A.; Herbert, J. M. Simultaneous Benchmarking of Ground- and Excited-State Properties with Long-Range-Corrected Density Functional Theory. *J Chem Phys* **2008**, *129* (3), 34107.
- (130) Gao, X.; Bai, S.; Fazzi, D.; Niehaus, T.; Barbatti, M.; Thiel, W. Evaluation of Spin-Orbit Couplings with Linear-Response Time-Dependent Density Functional Methods. *J Chem Theory Comput* **2017**, *13* (2), 515–524.
- (131) Chiodo, S. G.; Leopoldini, M. MolSOC: A Spin–Orbit Coupling Code. *Comput Phys Commun* **2014**, *185* (2), 676–683.
- (132) Martin, R. L. Natural Transition Orbitals. *J Chem Phys* **2003**, *118* (11), 4775–4777.
- (133) Tretiak, S.; Mukamel, S. Density Matrix Analysis and Simulation of Electronic Excitations in Conjugated and Aggregated Molecules. *Chem Rev* **2002**, *102* (9), 3171–3212.
- (134) O’boyle, N. M.; Tenderholt, A. L.; Langner, K. M. Cclib: A Library for Package-Independent Computational Chemistry Algorithms. *J Comput Chem* **2008**, *29* (5), 839–845.
- (135) Doonan, C. J.; Tranchemontagne, D. J.; Glover, T. G.; Hunt, J. R.; Yaghi, O. M. Exceptional Ammonia Uptake by a Covalent Organic Framework. *Nat Chem* **2010**, *2* (3), 235–238.

- (136) Plasser, F.; Lischka, H. Analysis of Excitonic and Charge Transfer Interactions from Quantum Chemical Calculations. *J Chem Theory Comput* **2012**, 8 (8), 2777–2789.
- (137) Toby, B. H.; Von Dreele, R. B. *{\it GSAS-II}*: The Genesis of a Modern Open-Source All Purpose Crystallography Software Package. *J Appl Crystallogr* **2013**, 46 (2), 544–549.
- (138) Macrae, C. F.; Sovago, I.; Cottrell, S. J.; Galek, P. T. A.; McCabe, P.; Pidcock, E.; Platings, M.; Shields, G. P.; Stevens, J. S.; Towler, M.; Wood, P. A. *{\it Mercury 4.0}*: From Visualization to Analysis, Design and Prediction. *J Appl Crystallogr* **2020**, 53 (1), 226–235.
- (139) Mercado, R.; Fu, R.-S.; Yakutovich, A. V.; Talirz, L.; Haranczyk, M.; Smit, B. In Silico Design of 2D and 3D Covalent Organic Frameworks for Methane Storage Applications. *Chemistry of Materials* **2018**, 30 (15), 5069–5086.
- (140) Řezáč, J.; Hobza, P. Advanced Corrections of Hydrogen Bonding and Dispersion for Semiempirical Quantum Mechanical Methods. *J Chem Theory Comput* **2012**, 8 (1), 141–151.
- (141) Avogadro: An Open-Source Molecular Builder and Visualization Tool.
- (142) Hanwell, M. D.; Curtis, D. E.; Lonie, D. C.; Vandermeersch, T.; Zurek, E.; Hutchison, G. R. Avogadro: An Advanced Semantic Chemical Editor, Visualization, and Analysis Platform. *J Cheminform* **2012**, 4 (1), 17.
- (143) Wang, H.; Wang, H.; Wang, Z.; Tang, L.; Zeng, G.; Xu, P.; Chen, M.; Xiong, T.; Zhou, C.; Li, X.; Huang, D.; Zhu, Y.; Wang, Z.; Tang, J. Covalent Organic Framework Photocatalysts: Structures and Applications. *Chem Soc Rev* **2020**, 49 (12), 4135–4165.
- (144) Pan, Q.; Abdellah, M.; Cao, Y.; Lin, W.; Liu, Y.; Meng, J.; Zhou, Q.; Zhao, Q.; Yan, X.; Li, Z.; Cui, H.; Cao, H.; Fang, W.; Tanner, D. A.; Abdel-Hafiez, M.; Zhou, Y.; Pullerits, T.; Canton, S. E.; Xu, H.; Zheng, K. Ultrafast Charge Transfer Dynamics in 2D Covalent Organic Frameworks/Re-Complex Hybrid Photocatalyst. *Nat Commun* **2022**, 13 (1), 845.
- (145) Li, S.-Y.; Meng, S.; Zou, X.; El-Roz, M.; Teleguev, I.; Thili, O.; Liu, T. X.; Zhu, G. Rhenium-Functionalized Covalent Organic Framework Photocatalyst for Efficient CO₂ Reduction under Visible Light. *Microporous and Mesoporous Materials* **2019**, 285, 195–201.
- (146) Yadav, R. K.; Kumar, A.; Park, N.-J.; Kong, K.-J.; Baeg, J.-O. A Highly Efficient Covalent Organic Framework Film Photocatalyst for Selective Solar Fuel Production from CO₂. *J Mater Chem A Mater* **2016**, 4 (24), 9413–9418.
- (147) Halder, A.; Kandambeth, S.; Biswal, B. P.; Kaur, G.; Roy, N. C.; Addicoat, M.; Salunke, J. K.; Banerjee, S.; Vanka, K.; Heine, T.; Verma, S.; Banerjee, R. Decoding the Morphological Diversity in Two Dimensional Crystalline Porous Polymers by Core Planarity Modulation. *Angewandte Chemie International Edition* **2016**, 55 (27), 7806–7810.
- (148) Luo, J.; Lu, J.; Zhang, J. Carbazole–Triazine Based Donor–Acceptor Porous Organic Frameworks for Efficient Visible-Light Photocatalytic Aerobic Oxidation Reactions. *J Mater Chem A Mater* **2018**, 6 (31), 15154–15161.
- (149) Clough, A. J.; Yoo, J. W.; Mecklenburg, M. H.; Marinescu, S. C. Two-Dimensional Metal-Organic Surfaces for Efficient Hydrogen Evolution from Water. *J Am Chem Soc* **2015**, 137 (1), 118–121.
- (150) Chen, X. Q.; Yao, X.; Bai, T.; Ling, J.; Xiao, W. J.; Wang, J.; Wu, S. C.; Liu, L. N.; Xie, G.; Li, J.; Lu, Z.; Visoly-Fisher, I.; Katz, E. A.; Li, W. S. Donor–Acceptor Photovoltaic Polymers Based on 1,4-Dithienyl-2,5-Dialkoxybenzene with Intramolecular Noncovalent Interactions. *J Polym Sci A Polym Chem* **2018**, 56 (7), 689–698.
- (151) Mei, C. Y.; Liang, L.; Zhao, F. G.; Wang, J. T.; Yu, L. F.; Li, Y. X.; Li, W. S. A Family of Donor-Acceptor Photovoltaic Polymers with Fused 4,7-Dithienyl-2,1,3-Benzothiadiazole Units: Effect of Structural Fusion and Side Chains. *Macromolecules* **2013**, 46 (19), 7920–7931.

- (152) Chang, C. H.; Kuo, M. C.; Lin, W. C.; Chen, Y. T.; Wong, K. T.; Chou, S. H.; Mondal, E.; Kwong, R. C.; Xia, S.; Nakagawa, T.; Adachi, C. A Dicarbazole-Triazine Hybrid Bipolar Host Material for Highly Efficient Green Phosphorescent OLEDs. *J Mater Chem* **2012**, *22* (9), 3832–3838.
- (153) Youn Lee, S.; Yasuda, T.; Nomura, H.; Adachi, C. High-Efficiency Organic Light-Emitting Diodes Utilizing Thermally Activated Delayed Fluorescence from Triazine-Based Donor-Acceptor Hybrid Molecules. *Appl Phys Lett* **2012**, *101* (9), 1–5.
- (154) Yuen, J. D.; Fan, J.; Seifter, J.; Lim, B.; Hufschmid, R.; Heeger, A. J.; Wudl, F. High Performance Weak Donor-Acceptor Polymers in Thin Film Transistors: Effect of the Acceptor on Electronic Properties, Ambipolar Conductivity, Mobility, and Thermal Stability. *J Am Chem Soc* **2011**, *133* (51), 20799–20807.
- (155) Ren, S.; Zeng, D.; Zhong, H.; Wang, Y.; Qian, S.; Fang, Q. Convergent Synthesis and Multifunctional Properties. *J. Phys. Chem. B* **2010**, *114*, 10374–10383.
- (156) Weiss, E. A.; Ahrens, M. J.; Sinks, L. E.; Ratner, M. A.; Wasielewski, M. R. Solvent Control of Spin-Dependent Charge Recombination Mechanisms within Donor-Conjugated Bridge-Acceptor Molecules. *J Am Chem Soc* **2004**, *126* (31), 9510–9511.
- (157) Ricks, A. B.; Solomon, G. C.; Colvin, M. T.; Scott, A. M.; Chen, K.; Ratner, M. A.; Wasielewski, M. R. Controlling Electron Transfer in Donor-Bridge-Acceptor Molecules Using Cross-Conjugated Bridges. *J Am Chem Soc* **2010**, *132* (43), 15427–15434.
- (158) Matulaitis, T.; Kostiv, N.; Grazulevicius, J. V.; Peciulyte, L.; Simokaitiene, J.; Jankauskas, V.; Luszczynska, B.; Ulanski, J. Synthesis and Properties of Bipolar Derivatives of 1,3,5-Triazine and Carbazole. *Dyes and Pigments* **2016**, *127*, 45–58.
- (159) Reghu, R. R.; Grazulevicius, J. V.; Simokaitiene, J.; Matulaitis, T.; Miasojedovas, A.; Kazlauskas, K.; Jursenas, S.; Data, P.; Lapkowski, M.; Zassowski, P. Glass Forming Donor-Substituted s-Triazines: Photophysical and Electrochemical Properties. *Dyes and Pigments* **2013**, *97* (3), 412–422.
- (160) Sun, Z.; Jiang, Y.; Zeng, L.; Huang, L. Intramolecular Charge Transfer and Extended Conjugate Effects in Donor– Π –Acceptor-Type Mesoporous Carbon Nitride for Photocatalytic Hydrogen Evolution. *ChemSusChem* **2019**, *12* (7), 1325–1333.
- (161) Pan, J. Y.; Zuo, L. J.; Hu, X. L.; Fu, W. F.; Chen, M. R.; Fu, L.; Gu, X.; Shi, H. Q.; Shi, M. M.; Li, H. Y.; Chen, H. Z. Star-Shaped D-A Small Molecules Based on Diketopyrrolopyrrole and Triphenylamine for Efficient Solution-Processed Organic Solar Cells. *ACS Appl Mater Interfaces* **2013**, *5* (3), 972–980.
- (162) Wu, H. C.; Zhang, J.; Bo, Z.; Chen, W. C. Well-Defined Star-Shaped Donor-Acceptor Conjugated Molecules for Organic Resistive Memory Devices. *Chemical Communications* **2015**, *51* (75), 14179–14182.
- (163) Matulaitis, T.; Imbrasas, P.; Kukhta, N. A.; Baronas, P.; Bučiūnas, T.; Banevičius, D.; Kazlauskas, K.; Gražulevičius, J. V.; Juršėnas, S. Impact of Donor Substitution Pattern on the TADF Properties in the Carbazolyl-Substituted Triazine Derivatives. *The Journal of Physical Chemistry C* **2017**, *121* (42), 23618–23625.
- (164) Davis, W. B.; Ratner, M. A.; Wasielewski, M. R. Conformational Gating of Long Distance Electron Transfer through Wire-like Bridges in Donor–Bridge–Acceptor Molecules. *J Am Chem Soc* **2001**, *123* (32), 7877–7886.
- (165) Albinsson, B.; Eng, M. P.; Pettersson, K.; Winters, M. U. Electron and Energy Transfer in Donor–Acceptor Systems with Conjugated Molecular Bridges. *Physical Chemistry Chemical Physics* **2007**, *9* (44), 5847–5864.

- (166) Daub, J.; Engl, R.; Kurzawa, J.; Miller, S. E.; Schneider, S.; Stockmann, A.; Wasielewski, M. R. Competition between Conformational Relaxation and Intramolecular Electron Transfer within Phenothiazine–Pyrene Dyads. *J Phys Chem A* **2001**, *105* (23), 5655–5665.
- (167) Seok Oh, C.; de Sa Pereira, D.; Hyun Han, S.; Park, H.-J.; F. Higginbotham, H.; P. Monkman, A.; Yeob Lee, J. Dihedral Angle Control of Blue Thermally Activated Delayed Fluorescent Emitters through Donor Substitution Position for Efficient Reverse Intersystem Crossing. *ACS Applied Materials & Interfaces* **2018**, *10* (41), 35420–35429.
- (168) Liang, X.; Zhang, Q. Recent Progress on Intramolecular Charge-Transfer Compounds as Photoelectric Active Materials. *Sci China Mater* **2017**, *60* (11), 1093–1101.
- (169) Zhang, Q.; Kuwabara, H.; J. Potscavage, W.; Huang, S.; Hatae, Y.; Shibata, T.; Adachi, C. Anthraquinone-Based Intramolecular Charge-Transfer Compounds: Computational Molecular Design, Thermally Activated Delayed Fluorescence, and Highly Efficient Red Electroluminescence. *J Am Chem Soc* **2014**, *136* (52), 18070–18081.
- (170) Kuang, Z.; He, G.; Song, H.; Wang, X.; Hu, Z.; Sun, H.; Wan, Y.; Guo, Q.; Xia, A. Conformational Relaxation and Thermally Activated Delayed Fluorescence in Anthraquinone-Based Intramolecular Charge-Transfer Compound. *The Journal of Physical Chemistry C* **2018**, *122* (7), 3727–3737.
- (171) Hirata, S.; Sakai, Y.; Masui, K.; Tanaka, H.; Lee, S. Y.; Nomura, H.; Nakamura, N.; Yasumatsu, M.; Nakanotani, H.; Zhang, Q.; Shizu, K.; Miyazaki, H.; Adachi, C. Highly Efficient Blue Electroluminescence Based on Thermally Activated Delayed Fluorescence. *Nat Mater* **2014**, *14*, 330.
- (172) Zhang, Q.; Kuwabara, H.; J. Potscavage, W.; Huang, S.; Hatae, Y.; Shibata, T.; Adachi, C. Anthraquinone-Based Intramolecular Charge-Transfer Compounds: Computational Molecular Design, Thermally Activated Delayed Fluorescence, and Highly Efficient Red Electroluminescence. *J Am Chem Soc* **2014**, *136* (52), 18070–18081.
- (173) Tanaka, S.; Miyata, K.; Sugimoto, T.; Watanabe, K.; Uemura, T.; Takeya, J.; Matsumoto, Y. Enhancement of the Exciton Coherence Size in Organic Semiconductor by Alkyl Chain Substitution. *The Journal of Physical Chemistry C* **2016**, *120* (15), 7941–7948.
- (174) Han, G.; Hu, T.; Yi, Y. Reducing the Singlet–Triplet Energy Gap by End-Group Π – π Stacking Toward High-Efficiency Organic Photovoltaics. *Advanced Materials* **2020**, *32* (22), 2000975.
- (175) Lu, J.; Pattengale, B.; Liu, Q.; Yang, S.; Shi, W.; Li, S.; Huang, J.; Zhang, J. Donor–Acceptor Fluorophores for Energy-Transfer-Mediated Photocatalysis. *J Am Chem Soc* **2018**, *140* (42), 13719–13725.
- (176) Hosokai, T.; Matsuzaki, H.; Nakanotani, H.; Tokumaru, K.; Tsutsui, T.; Furube, A.; Nasu, K.; Nomura, H.; Yahiro, M.; Adachi, C. Evidence and Mechanism of Efficient Thermally Activated Delayed Fluorescence Promoted by Delocalized Excited States. *Sci Adv* **2017**, *3* (5), e1603282.
- (177) Wang, L.; Ou, Q.; Peng, Q.; Shuai, Z. Theoretical Characterizations of TADF Materials: Roles of ΔG and the Singlet–Triplet Excited States Interconversion. *J Phys Chem A* **2021**, *125* (7), 1468–1475.
- (178) Samanta, P. K.; Kim, D.; Coropceanu, V.; Brédas, J.-L. Up-Conversion Intersystem Crossing Rates in Organic Emitters for Thermally Activated Delayed Fluorescence: Impact of the Nature of Singlet vs Triplet Excited States. *J Am Chem Soc* **2017**, *139* (11), 4042–4051.
- (179) Gonçalves, M. S. T. Fluorescent Labeling of Biomolecules with Organic Probes. *Chem Rev* **2009**, *109* (1), 190–212.
- (180) Kanegae, A.; Takata, Y.; Takashima, I.; Uchinomiya, S.; Kawagoe, R.; Usui, K.; Yamashita, A.; Wongkongkatep, J.; Sugimoto, M.; Ojida, A. A Multicolor and Ratiometric Fluorescent Sensing Platform for Metal Ions Based on Arene–Metal-Ion Contact. *Commun Chem* **2021**, *4* (1), 104.

- (181) Zhang, Q.; Li, J.; Shizu, K.; Huang, S.; Hirata, S.; Miyazaki, H.; Adachi, C. Design of Efficient Thermally Activated Delayed Fluorescence Materials for Pure Blue Organic Light Emitting Diodes. *J Am Chem Soc* **2012**, *134* (36), 14706–14709.
- (182) Qian, Y.; Li, J.; Ji, M.; Li, J.; Ma, D.; Liu, A.; Zhao, Y.; Yang, C. Fluorescent Covalent Organic Frameworks: A Promising Material Platform for Explosive Sensing. *Front Chem* **2022**, *10*.
- (183) Dalapati, S.; Jin, S.; Gao, J.; Xu, Y.; Nagai, A.; Jiang, D. An Azine-Linked Covalent Organic Framework. *J Am Chem Soc* **2013**, *135* (46), 17310–17313.
- (184) Ding, H.; Li, J.; Xie, G.; Lin, G.; Chen, R.; Peng, Z.; Yang, C.; Wang, B.; Sun, J.; Wang, C. An AIEgen-Based 3D Covalent Organic Framework for White Light-Emitting Diodes. *Nat Commun* **2018**, *9* (1), 5234.
- (185) Dalapati, S.; Jin, E.; Addicoat, M.; Heine, T.; Jiang, D. Highly Emissive Covalent Organic Frameworks. *J Am Chem Soc* **2016**, *138* (18), 5797–5800.
- (186) Dong, J.; Li, X.; Peh, S. B.; Yuan, Y. Di; Wang, Y.; Ji, D.; Peng, S.; Liu, G.; Ying, S.; Yuan, D.; Jiang, J.; Ramakrishna, S.; Zhao, D. Restriction of Molecular Rotors in Ultrathin Two-Dimensional Covalent Organic Framework Nanosheets for Sensing Signal Amplification. *Chemistry of Materials* **2019**, *31* (1), 146–160.
- (187) Sturla, J.; Etherington, M. K.; Bismillah, A. N.; Higginbotham, H. F.; Trewby, W.; Aguilar, J. A.; Bromley, E. H. C.; Avestro, A.-J.; Monkman, A. P.; McGonigal, P. R. Excited-State Aromatic Interactions in the Aggregation-Induced Emission of Molecular Rotors. *J Am Chem Soc* **2017**, *139* (49), 17882–17889.
- (188) Mei, J.; Leung, N. L. C.; Kwok, R. T. K.; Lam, J. W. Y.; Tang, B. Z. Aggregation-Induced Emission: Together We Shine, United We Soar! *Chem Rev* **2015**, *115* (21), 11718–11940.
- (189) Wei, S.; Zhang, F.; Zhang, W.; Qiang, P.; Yu, K.; Fu, X.; Wu, D.; Bi, S.; Zhang, F. Semiconducting 2D Triazine-Cored Covalent Organic Frameworks with Unsubstituted Olefin Linkages. *J Am Chem Soc* **2019**, *141* (36), 14272–14279.
- (190) Acharjya, A.; Pachfule, P.; Roeser, J.; Schmitt, F.-J.; Thomas, A. Vinylene-Linked Covalent Organic Frameworks by Base-Catalyzed Aldol Condensation. *Angewandte Chemie International Edition* **2019**, *58* (42), 14865–14870.
- (191) Pimputkar, S.; Speck, J. S.; DenBaars, S. P.; Nakamura, S. Prospects for LED Lighting. *Nat Photonics* **2009**, *3* (4), 180–182.
- (192) Ludwig, J.; An, L.; Pattengale, B.; Kong, Q.; Zhang, X.; Xi, P.; Huang, J. Ultrafast Hole Trapping and Relaxation Dynamics in P-Type CuS Nanodisks. *J Phys Chem Lett* **2015**, *6* (14), 2671–2675.
- (193) Thomas, S.; Li, H.; Zhong, C.; Matsumoto, M.; R. Dichtel, W.; Bredas, J.-L.; Dichtel, W. R.; Bredas, J.-L.; R. Dichtel, W.; Bredas, J.-L. Electronic Structure of Two-Dimensional π -Conjugated Covalent Organic Frameworks. *Chemistry of Materials* **2019**, *31* (9), 3051–3065.
- (194) Guido, C. A.; Cortona, P.; Mennucci, B.; Adamo, C. On the Metric of Charge Transfer Molecular Excitations: A Simple Chemical Descriptor. *J Chem Theory Comput* **2013**, *9* (7), 3118–3126.
- (195) Moore, B.; Sun, H.; Govind, N.; Kowalski, K.; Autschbach, J. Charge-Transfer Versus Charge-Transfer-Like Excitations Revisited. *J Chem Theory Comput* **2015**, *11* (7), 3305–3320.
- (196) Guasch, J.; Grisanti, L.; Souto, M.; Lloveras, V.; Vidal-Gancedo, J.; Ratera, I.; Painelli, A.; Rovira, C.; Veciana, J. Intra- and Intermolecular Charge Transfer in Aggregates of Tetrathiafulvalene-Triphenylmethyl Radical Derivatives in Solution. *J Am Chem Soc* **2013**, *135* (18), 6958–6967.
- (197) Painelli, A.; Terenziani, F. Multielectron Transfer in Clusters of Polar-Polarizable Chromophores. *J Am Chem Soc* **2003**, *125* (19), 5624–5625.

- (198) Zheng, C.; Zhong, C.; Collison, C. J.; Spano, F. C. Non-Kasha Behavior in Quadrupolar Dye Aggregates: The Red-Shifted H-Aggregate. *The Journal of Physical Chemistry C* **2019**, *123* (5), 3203–3215.
- (199) Jenekhe, S. A.; Osaheni, J. A. Excimers and Exciplexes of Conjugated Polymers. *Science* (1979) **1994**, 265 (5173), 765 LP – 768.
- (200) Zarrabi, N.; Sandberg, O. J.; Meredith, P.; Armin, A. Subgap Absorption in Organic Semiconductors. *J Phys Chem Lett* **2023**, *14* (13), 3174–3185.
- (201) An, X.; Wei, C.; Bai, L.; Zhou, J.; Wang, L.; Han, Y.; Sun, L.; Lin, J.; Liu, H.; Li, J.; Xu, M.; Ling, H.; Xie, L.; Huang, W. Photoexcitation Dynamics and Energy Engineering in Supramolecular Doping of Organic Conjugated Molecules. *Light Sci Appl* **2023**, *12* (1), 30.
- (202) Herrmann, D.; Niesar, S.; Scharsich, C.; Köhler, A.; Stutzmann, M.; Riedle, E. Role of Structural Order and Excess Energy on Ultrafast Free Charge Generation in Hybrid Polythiophene/Si Photovoltaics Probed in Real Time by Near-Infrared Broadband Transient Absorption. *J Am Chem Soc* **2011**, *133* (45), 18220–18233.
- (203) Zhang, X.; Geng, K.; Jiang, D.; D. Scholes, G. Exciton Diffusion and Annihilation in an Sp² Carbon-Conjugated Covalent Organic Framework. *J Am Chem Soc* **2022**, *144* (36), 16423–16432.
- (204) Feng, T.; Streater, D.; Sun, B.; Duisenova, K.; Wang, D.; Liu, Y.; Huang, J.; Zhang, J. Tuning Photoexcited Charge Transfer in Imine-Linked Two-Dimensional Covalent Organic Frameworks. *J Phys Chem Lett* **2022**, *13* (6), 1398–1405.
- (205) Kim, T. W.; Jun, S.; Ha, Y.; Yadav, R. K.; Kumar, A.; Yoo, C.-Y.; Oh, I.; Lim, H.-K.; Shin, J. W.; Ryoo, R.; Kim, H.; Kim, J.; Baeg, J.-O.; Ihse, H. Ultrafast Charge Transfer Coupled with Lattice Phonons in Two-Dimensional Covalent Organic Frameworks. *Nat Commun* **2019**, *10* (1), 1873.
- (206) Dienstmaier, J. F.; Gigler, A. M.; Goetz, A. J.; Knochel, P.; Bein, T.; Lyapin, A.; Reichlmaier, S.; Heckl, W. M.; Lackinger, M. Synthesis of Well-Ordered COF Monolayers: Surface Growth of Nanocrystalline Precursors versus Direct On-Surface Polycondensation. *ACS Nano* **2011**, *5* (12), 9737–9745.
- (207) Stokes, A. R.; Wilson, A. J. C. The Diffraction of X Rays by Distorted Crystal Aggregates - I. *Proceedings of the Physical Society* **1944**, *56* (3), 174–181.
- (208) Dodson, R. A.; Wong-Foy, A. G.; Matzger, A. J. The Metal–Organic Framework Collapse Continuum: Insights from Two-Dimensional Powder X-Ray Diffraction. *Chemistry of Materials* **2018**, *30* (18), 6559–6565.
- (209) Roldán, R.; Castellanos-Gomez, A.; Cappelluti, E.; Guinea, F. Strain Engineering in Semiconducting Two-Dimensional Crystals. *Journal of Physics: Condensed Matter* **2015**, *27* (31), 313201.
- (210) Ma, H.; Wei, M.; Jin, F.; Chen, T.; Ma, Y. Two-Dimensional COF with Rather Low Exciton Binding Energies Comparable to 3D Inorganic Semiconductors in the Visible Range for Water Splitting. *The Journal of Physical Chemistry C* **2019**, *123* (40), 24626–24633.
- (211) Burke, D. W.; Sun, C.; Castano, I.; Flanders, N. C.; Evans, A. M.; Vitaku, E.; McLeod, D. C.; Lambeth, R. H.; Chen, L. X.; Gianneschi, N. C.; Dichtel, W. R. Acid Exfoliation of Imine-linked Covalent Organic Frameworks Enables Solution Processing into Crystalline Thin Films. *Angewandte Chemie International Edition* **2019**.
- (212) Liu, W.; Li, X.; Wang, C.; Pan, H.; Liu, W.; Wang, K.; Zeng, Q.; Wang, R.; Jiang, J. A Scalable General Synthetic Approach toward Ultrathin Imine-Linked Two-Dimensional Covalent Organic Framework Nanosheets for Photocatalytic CO₂ Reduction. *J Am Chem Soc* **2019**, *141* (43), 17431–17440.

- (213) Mei, J.; Diao, Y.; Appleton, A. L.; Fang, L.; Bao, Z. Integrated Materials Design of Organic Semiconductors for Field-Effect Transistors. *J Am Chem Soc* **2013**, *135* (18), 6724–6746.
- (214) Patwardhan, S.; Kocherzhenko, A. A.; Grozema, F. C.; Siebbeles, L. D. A. Delocalization and Mobility of Charge Carriers in Covalent Organic Frameworks. *The Journal of Physical Chemistry C* **2011**, *115* (23), 11768–11772.
- (215) Li, H.; Brédas, J.-L. Large Out-of-Plane Deformations of Two-Dimensional Covalent Organic Framework (COF) Sheets. *J Phys Chem Lett* **2018**, *9* (15), 4215–4220.
- (216) Li, Y.; Ullrich, C. A. Time-Dependent Transition Density Matrix. *Chem Phys* **2011**, *391* (1), 157–163.
- (217) Bäppler, S. A.; Plasser, F.; Wormit, M.; Dreuw, A. Exciton Analysis of Many-Body Wave Functions: Bridging the Gap between the Quasiparticle and Molecular Orbital Pictures. *Phys Rev A (Coll Park)* **2014**, *90* (5), 52521.
- (218) Fujimoto, K. J. Transition-Density-Fragment Interaction Combined with Transfer Integral Approach for Excitation-Energy Transfer via Charge-Transfer States. *J Chem Phys* **2012**, *137* (3), 34101.
- (219) Yu, J.; Anderson, R.; Li, X.; Xu, W.; Goswami, S.; Rajasree, S. S.; Maindan, K.; Gómez-Gualdrón, D. A.; Deria, P. Improving Energy Transfer within Metal–Organic Frameworks by Aligning Linker Transition Dipoles along the Framework Axis. *J Am Chem Soc* **2020**, *142* (25), 11192–11202.
- (220) Hestand, N. J.; Spano, F. C. Interference between Coulombic and CT-Mediated Couplings in Molecular Aggregates: H- to J-Aggregate Transformation in Perylene-Based π -Stacks. *J Chem Phys* **2015**, *143* (24), 244707.
- (221) Weingarten, A. S.; Kazantsev, R. V.; Palmer, L. C.; McClendon, M.; Koltonow, A. R.; Samuel, A. P. S.; Kiebal, D. J.; Wasielewski, M. R.; Stupp, S. I. Self-Assembling Hydrogel Scaffolds for Photocatalytic Hydrogen Production. *Nat Chem* **2014**, *6* (11), 964–970.
- (222) Kazantsev, R. V.; Dannenhoffer, A. J.; Weingarten, A. S.; Phelan, B. T.; Harutyunyan, B.; Aytun, T.; Narayanan, A.; Fairfield, D. J.; Boekhoven, J.; Sai, H.; Senesi, A.; O'Dogherty, P. I.; Palmer, L. C.; Bedzyk, M. J.; Wasielewski, M. R.; Stupp, S. I. Crystal-Phase Transitions and Photocatalysis in Supramolecular Scaffolds. *J Am Chem Soc* **2017**, *139* (17), 6120–6127.
- (223) Weingarten, A. S.; Kazantsev, R. V.; Palmer, L. C.; Fairfield, D. J.; Koltonow, A. R.; Stupp, S. I. Supramolecular Packing Controls H₂ Photocatalysis in Chromophore Amphiphile Hydrogels. *J Am Chem Soc* **2015**, *137* (48), 15241–15246.
- (224) Terenziani, F.; Painelli, A. Supramolecular Interactions in Clusters of Polar and Polarizable Molecules. *Phys Rev B* **2003**, *68* (16), 165405.
- (225) Bardi, B.; Dall'Agnese, C.; Moineau-Chane Ching, K. I.; Painelli, A.; Terenziani, F. Spectroscopic Investigation and Theoretical Modeling of Benzothiadiazole-Based Charge-Transfer Chromophores: From Solution to Nanoaggregates. *The Journal of Physical Chemistry C* **2017**, *121* (32), 17466–17478.
- (226) Sanyal, S.; Painelli, A.; Pati, S. K.; Terenziani, F.; Sissa, C. Aggregates of Quadrupolar Dyes for Two-Photon Absorption: The Role of Intermolecular Interactions. *Physical Chemistry Chemical Physics* **2016**, *18* (40), 28198–28208.
- (227) Hestand, N. J.; Zheng, C.; Penmetcha, A. R.; Cona, B.; Cody, J. A.; Spano, F. C.; Collison, C. J. Confirmation of the Origins of Panchromatic Spectra in Squaraine Thin Films Targeted for Organic Photovoltaic Devices. *The Journal of Physical Chemistry C* **2015**, *119* (33), 18964–18974.
- (228) Giri, G.; Verploegen, E.; Mannsfeld, S. C. B.; Atahan-Evrenk, S.; Kim, D. H.; Lee, S. Y.; Becerril, H. A.; Aspuru-Guzik, A.; Toney, M. F.; Bao, Z. Tuning Charge Transport in Solution-Sheared Organic Semiconductors Using Lattice Strain. *Nature* **2011**, *480* (7378), 504–508.

- (229) Nguyen, T.-Q.; Doan, V.; Schwartz, B. J. Conjugated Polymer Aggregates in Solution: Control of Interchain Interactions. *J Chem Phys* **1999**, *110* (8), 4068–4078.
- (230) Hofacker, A.; Neher, D. Dispersive and Steady-State Recombination in Organic Disordered Semiconductors. *Phys Rev B* **2017**, *96* (24), 245204.
- (231) Chen, X.-K.; Coropceanu, V.; Brédas, J.-L. Assessing the Nature of the Charge-Transfer Electronic States in Organic Solar Cells. *Nat Commun* **2018**, *9* (1), 5295.
- (232) Vezie, M. S.; Azzouzi, M.; Telford, A. M.; Hopper, T. R.; Sieval, A. B.; Hummelen, J. C.; Fallon, K.; Bronstein, H.; Kirchartz, T.; Bakulin, A. A.; Clarke, T. M.; Nelson, J. Impact of Marginal Exciton–Charge-Transfer State Offset on Charge Generation and Recombination in Polymer:Fullerene Solar Cells. *ACS Energy Lett* **2019**, *4* (9), 2096–2103.
- (233) Tran, L. D.; Presley, K. F.; Streit, J. K.; Carpena-Núñez, J.; Beagle, L. K.; Grusenmeyer, T. A.; Dalton, M. J.; Vaia, R. A.; Drummy, L. F.; Glavin, N. R.; Baldwin, L. A. Divergent Properties in Structural Isomers of Triphenylamine-Based Covalent Organic Frameworks. *Chemistry of Materials* **2022**, *34* (2), 529–536.
- (234) Yang, J.; Ghosh, S.; Roeser, J.; Acharjya, A.; Penschke, C.; Tsutsui, Y.; Rabeah, J.; Wang, T.; Djoko Tameu, S. Y.; Ye, M. Y.; Grüneberg, J.; Li, S.; Li, C.; Schomäcker, R.; Van De Krol, R.; Seki, S.; Saalfrank, P.; Thomas, A. Constitutional Isomerism of the Linkages in Donor–Acceptor Covalent Organic Frameworks and Its Impact on Photocatalysis. *Nat Commun* **2022**, *13* (1).
- (235) Vardhan, H.; Al-Enizi, A. M.; Nafady, A.; Pan, Y.; Yang, Z.; Gutiérrez, H. R.; Han, X.; Ma, S. Single-Pore versus Dual-Pore Bipyridine-Based Covalent–Organic Frameworks: An Insight into the Heterogeneous Catalytic Activity for Selective C–H Functionalization. *Small* **2021**, *17* (22), 2003970.
- (236) Wang, X.; Fu, Z.; Zheng, L.; Zhao, C.; Wang, X.; Chong, S. Y.; McBride, F.; Raval, R.; Bilton, M.; Liu, L.; Wu, X.; Chen, L.; Sprick, R. S.; Cooper, A. I. Covalent Organic Framework Nanosheets Embedding Single Cobalt Sites for Photocatalytic Reduction of Carbon Dioxide. *Chemistry of Materials* **2020**, *32* (21), 9107–9114.
- (237) Ruan, X.; Yang, Y.; Liu, W.; Ma, X.; Zhang, C.; Meng, Q.; Wang, Z.; Cui, F.; Feng, J.; Cai, F.; Yuan, Y.; Zhu, G. Mechanical Bond Approach to Introducing Self-Adaptive Active Sites in Covalent Organic Frameworks for Zinc-Catalyzed Organophosphorus Degradation. *ACS Cent Sci* **2021**, *7* (10), 1698–1706.
- (238) Leng, W.; Peng, Y.; Zhang, J.; Lu, H.; Feng, X.; Ge, R.; Dong, B.; Wang, B.; Hu, X.; Gao, Y. Sophisticated Design of Covalent Organic Frameworks with Controllable Bimetallic Docking for a Cascade Reaction. *Chemistry – A European Journal* **2016**, *22* (27), 9087–9091.
- (239) Zhang, M.; Chen, J.; Zhang, S.; Zhou, X.; He, L.; Sheridan, M. V.; Yuan, M.; Zhang, M.; Chen, L.; Dai, X.; Ma, F.; Wang, J.; Hu, J.; Wu, G.; Kong, X.; Zhou, R.; Albrecht-Schmitt, T. E.; Chai, Z.; Wang, S. Electron Beam Irradiation as a General Approach for the Rapid Synthesis of Covalent Organic Frameworks under Ambient Conditions. *J Am Chem Soc* **2020**, *142* (20), 9169–9174.
- (240) Popov, D. A.; Luna, J. M.; Orchanian, N. M.; Haiges, R.; Downes, C. A.; Marinescu, S. C. A 2,2'-Bipyridine-Containing Covalent Organic Framework Bearing Rhenium(i) Tricarbonyl Moieties for CO₂ Reduction. *Dalton Transactions* **2018**, *47* (48), 17450–17460.
- (241) Bhadra, M.; Sasmal, H. S.; Basu, A.; Midya, S. P.; Kandambeth, S.; Pachfule, P.; Balaraman, E.; Banerjee, R. Predesigned Metal-Anchored Building Block for In Situ Generation of Pd Nanoparticles in Porous Covalent Organic Framework: Application in Heterogeneous Tandem Catalysis. *ACS Appl Mater Interfaces* **2017**, *9* (15), 13785–13792.
- (242) Jati, A.; Dey, K.; Nurhuda, M.; Addicoat, M. A.; Banerjee, R.; Maji, B. Dual Metalation in a Two-Dimensional Covalent Organic Framework for Photocatalytic C–N Cross-Coupling Reactions. *J Am Chem Soc* **2022**, *144* (17), 7822–7833.

- (243) Han, Y.; Di, J.-Q.; Zhao, A.-D.; Zhang, Z.-H. Synthesis, Characterization and Catalytic Performance of Palladium Supported on Pyridine-Based Covalent Organic Polymer for Suzuki-Miyaura Reaction. *Appl Organomet Chem* **2019**, *33* (10), e5172.
- (244) Wang, R.; Kong, W.; Zhou, T.; Wang, C.; Guo, J. Organobase Modulated Synthesis of High-Quality β -Ketoenamine-Linked Covalent Organic Frameworks. *Chemical Communications* **2021**, *57* (3), 331–334.
- (245) Chen, H.; Gu, Z.-G.; Zhang, J. Chiral-Induced Ultrathin Covalent Organic Frameworks Nanosheets with Tunable Circularly Polarized Luminescence. *J Am Chem Soc* **2022**, *144* (16), 7245–7252.
- (246) Lu, Z.; Yang, H.; Fu, X.; Zhao, Y.; Xiao, L.; Zhang, Z.; Hou, L. Visible Light-Regulated Heterogeneous Catalytic PET-RAFT by High Crystallinity Covalent Organic Framework. *Macromol Rapid Commun* **2021**, *42* (20), 2100384.
- (247) Wang, N.; Liu, J.; Tang, L.; Wei, X.; Wang, C.; Li, X.; Ma, L. Facile Synthesis of Rh Anchored Uniform Spherical COF for One-Pot Tandem Reductive Amination of Aldehydes to Secondary Imines. *ACS Appl Mater Interfaces* **2021**, *13* (21), 24966–24975.
- (248) Nguyen, Q. M.; Abouezzi, J.; Ristroph, L. Early Turbulence and Pulsatile Flows Enhance Diodicity of Tesla's Macrofluidic Valve. *Nat Commun* **2021**, *12* (1), 2884.
- (249) Natraj, A.; Ji, W.; Xin, J.; Castano, I.; W. Burke, D.; M. Evans, A.; J. Strauss, M.; Ateia, M.; S. Hamachi, L.; C. Gianneschi, N.; A. AlOthman, Z.; Sun, J.; Yusuf, K.; R. Dichtel, W. Single-Crystalline Imine-Linked Two-Dimensional Covalent Organic Frameworks Separate Benzene and Cyclohexane Efficiently. *J Am Chem Soc* **2022**, *144* (43), 19813–19824.
- (250) Asbury, J. B.; Wang, Y.; Lian, T. Time-Dependent Vibration Stokes Shift during Solvation: Experiment and Theory. *Bull Chem Soc Jpn* **2002**, *75* (5), 973–983.
- (251) Kurz, P.; Probst, B.; Spingler, B.; Alberto, R. Ligand Variations in [ReX(Diimine)(CO)₃] Complexes: Effects on Photocatalytic CO₂ Reduction. *Eur J Inorg Chem* **2006**, *2006* (15), 2966–2974.
- (252) Benson, E. E.; Sampson, M. D.; Grice, K. A.; Smieja, J. M.; Froehlich, J. D.; Friebe, D.; Keith, J. A.; Carter, E. A.; Nilsson, A.; Kubiak, C. P. The Electronic States of Rhenium Bipyridyl Electrocatalysts for CO₂ Reduction as Revealed by X-Ray Absorption Spectroscopy and Computational Quantum Chemistry. *Angewandte Chemie International Edition* **2013**, *52* (18), 4841–4844.
- (253) Oppelt, K. T.; Sevéry, L.; Utters, M.; Tilley, S. D.; Hamm, P. Flexible to Rigid: IR Spectroscopic Investigation of a Rhenium-Tricarbonyl-Complex at a Buried Interface. *Physical Chemistry Chemical Physics* **2021**, *23* (7), 4311–4316.
- (254) El Nahhas, A.; van der Veen, R. M.; Penfold, T. J.; Pham, V. T.; Lima, F. A.; Abela, R.; Blanco-Rodríguez, A. M.; Zális, S.; Vlček, A.; Tavernelli, I.; Rothlisberger, U.; Milne, C. J.; Chergui, M. X-Ray Absorption Spectroscopy of Ground and Excited Rhenium–Carbonyl–Diimine Complexes: Evidence for a Two-Center Electron Transfer. *J Phys Chem A* **2013**, *117* (2), 361–369.
- (255) Cannizzo, A.; Blanco-Rodríguez, A. M.; El Nahhas, A.; Šebera, J.; Zális, S.; Vlček, A. Jr.; Chergui, M. Femtosecond Fluorescence and Intersystem Crossing in Rhenium(I) Carbonyl–Bipyridine Complexes. *J Am Chem Soc* **2008**, *130* (28), 8967–8974.
- (256) Hone, C. A.; Kappe, C. O. Towards the Standardization of Flow Chemistry Protocols for Organic Reactions. *Chemistry–Methods* **2021**, *1* (11), 454–467.
- (257) Sun, S.-C.; Jiang, H.; Chen, Z.-Y.; Chen, Q.; Ma, M.-Y.; Zhen, L.; Song, B.; Xu, C.-Y. Bifunctional WC-Supported RuO₂ Nanoparticles for Robust Water Splitting in Acidic Media. *Angewandte Chemie International Edition* **2022**, *61* (21), e202202519.

- (258) Blakemore, J. D.; Gray, H. B.; Winkler, J. R.; Müller, A. M. Co₃O₄ Nanoparticle Water-Oxidation Catalysts Made by Pulsed-Laser Ablation in Liquids. *ACS Catal* **2013**, 3 (11), 2497–2500.
- (259) Li, D.; Baydoun, H.; Verani, C. N.; Brock, S. L. Efficient Water Oxidation Using CoMnP Nanoparticles. *J Am Chem Soc* **2016**, 138 (12), 4006–4009.
- (260) Lu, Z.; Yang, C.; He, L.; Hong, J.; Huang, C.; Wu, T.; Wang, X.; Wu, Z.; Liu, X.; Miao, Z.; Zeng, B.; Xu, Y.; Yuan, C.; Dai, L. Asymmetric Hydrophosphonylation of Imines to Construct Highly Stable Covalent Organic Frameworks with Efficient Intrinsic Proton Conductivity. *J Am Chem Soc* **2022**, 144 (22), 9624–9633.
- (261) Feng, X.; Liu, L.; Honsho, Y.; Saeki, A.; Seki, S.; Irle, S.; Dong, Y.; Nagai, A.; Jiang, D. High-Rate Charge-Carrier Transport in Porphyrin Covalent Organic Frameworks: Switching from Hole to Electron to Ambipolar Conduction. *Angewandte Chemie International Edition* **2012**, 51 (11), 2618–2622.
- (262) Fu, S.; Jin, E.; Hanayama, H.; Zheng, W.; Zhang, H.; Di Virgilio, L.; Addicoat, M. A.; Mezger, M.; Narita, A.; Bonn, M.; Müllen, K.; Wang, H. I. Outstanding Charge Mobility by Band Transport in Two-Dimensional Semiconducting Covalent Organic Frameworks. *J Am Chem Soc* **2022**, 144 (16), 7489–7496.
- (263) Ou, Z.; Liang, B.; Liang, Z.; Tan, F.; Dong, X.; Gong, L.; Zhao, P.; Wang, H.; Zou, Y.; Xia, Y.; Chen, X.; Liu, W.; Qi, H.; Kaiser, U.; Zheng, Z. Oriented Growth of Thin Films of Covalent Organic Frameworks with Large Single-Crystalline Domains on the Water Surface. *J Am Chem Soc* **2022**, 144 (7), 3233–3241.
- (264) Yao, L.; Rodríguez-Camargo, A.; Xia, M.; Mücke, D.; Guntermann, R.; Liu, Y.; Grunenberg, L.; Jiménez-Solano, A.; Emmerling, S. T.; Duppel, V.; Sivula, K.; Bein, T.; Qi, H.; Kaiser, U.; Grätzel, M.; Lotsch, B. V. Covalent Organic Framework Nanoplates Enable Solution-Processed Crystalline Nanofilms for Photoelectrochemical Hydrogen Evolution. *J Am Chem Soc* **2022**, 144 (23), 10291–10300.
- (265) Kang, C.; Zhang, Z.; Usadi, A. K.; Calabro, D. C.; Baugh, L. S.; Yu, K.; Wang, Y.; Zhao, D. Aggregated Structures of Two-Dimensional Covalent Organic Frameworks. *J Am Chem Soc* **2022**, 144 (7), 3192–3199.
- (266) Jeon, N. J.; Lee, H. G.; Kim, Y. C.; Seo, J.; Noh, J. H.; Lee, J.; Seok, S. Il. O-Methoxy Substituents in Spiro-OMeTAD for Efficient Inorganic–Organic Hybrid Perovskite Solar Cells. *J Am Chem Soc* **2014**, 136 (22), 7837–7840.
- (267) Koskinen, P.; Mäkinen, V. Density-Functional Tight-Binding for Beginners. *Comput Mater Sci* **2009**, 47 (1), 237–253.
- (268) Hourahine, B.; Aradi, B.; Blum, V.; Bonafé, F.; Buccheri, A.; Camacho, C.; Cevallos, C.; Deshayé, M. Y.; Dumitrică, T.; Dominguez, A.; Ehlert, S.; Elstner, M.; van der Heide, T.; Hermann, J.; Irle, S.; Kranz, J. J.; Köhler, C.; Kowalczyk, T.; Kubař, T.; Lee, I. S.; Lutsker, V.; Maurer, R. J.; Min, S. K.; Mitchell, I.; Negre, C.; Niehaus, T. A.; Niklasson, A. M. N.; Page, A. J.; Pecchia, A.; Penazzi, G.; Persson, M. P.; Řezáč, J.; Sánchez, C. G.; Sternberg, M.; Stöhr, M.; Stuckenberg, F.; Tkatchenko, A.; Yu, V. W. -z.; Frauenheim, T. DFTB+, a Software Package for Efficient Approximate Density Functional Theory Based Atomistic Simulations. *J Chem Phys* **2020**, 152 (12), 124101.
- (269) Elstner, M.; Porezag, D.; Jungnickel, G.; Elsner, J.; Haugk, M.; Frauenheim, Th.; Suhai, S.; Seifert, G. Self-Consistent-Charge Density-Functional Tight-Binding Method for Simulations of Complex Materials Properties. *Phys Rev B* **1998**, 58 (11), 7260–7268.
- (270) Ullrich, C. A. *Time-Dependent Density-Functional Theory: Concepts and Applications*; OUP Oxford, 2011.
- (271) Martin, R. L. Natural Transition Orbitals. *J Chem Phys* **2003**, 118 (11), 4775–4777.

- (272) Brunauer, S.; Emmett, P. H.; Teller, E. Adsorption of Gases in Multimolecular Layers. *J Am Chem Soc* **1938**, *60* (2), 309–319.
- (273) Thommes, M.; Kaneko, K.; Neimark, A. V.; Olivier, J. P.; Rodriguez-Reinoso, F.; Rouquerol, J.; Sing, K. S. W. Physisorption of Gases, with Special Reference to the Evaluation of Surface Area and Pore Size Distribution (IUPAC Technical Report). *Pure and Applied Chemistry* **87** (9–10), 1051–1069.
- (274) Walton, K. S.; Snurr, R. Q. Applicability of the BET Method for Determining Surface Areas of Microporous Metal–Organic Frameworks. *J Am Chem Soc* **2007**, *129* (27), 8552–8556.
- (275) Burdinski, D.; Wieghardt, K.; Steenken, S. Intramolecular Electron Transfer from Mn or Ligand Phenolate to Photochemically Generated Ru(III) in Multinuclear Ru/Mn Complexes. Laser Flash Photolysis and EPR Studies on Photosystem II Models. *J Am Chem Soc* **1999**, *121* (46), 10781–10787.
- (276) Yagi, M.; Kaneko, M. Molecular Catalysts for Water Oxidation. *Chem Rev* **2001**, *101* (1), 21–36.
- (277) Ashford, D. L.; Gish, M. K.; Vannucci, A. K.; Brennaman, M. K.; Templeton, J. L.; Papanikolas, J. M.; Meyer, T. J. Molecular Chromophore–Catalyst Assemblies for Solar Fuel Applications. *Chem Rev* **2015**, *115* (23), 13006–13049.
- (278) Kärkäs, M. D.; Johnston, E. V.; Verho, O.; Åkermark, B. Artificial Photosynthesis: From Nanosecond Electron Transfer to Catalytic Water Oxidation. *Acc Chem Res* **2014**, *47* (1), 100–111.
- (279) Magnuson, A.; Berglund, H.; Korall, P.; Hammarström, L.; Åkermark, B.; Styring, S.; Sun, L. Mimicking Electron Transfer Reactions in Photosystem II: Synthesis and Photochemical Characterization of a Ruthenium(II) Tris(Bipyridyl) Complex with a Covalently Linked Tyrosine. *J Am Chem Soc* **1997**, *119* (44), 10720–10725.
- (280) Heisenberg, W. Zum Paulischen Ausschließungsprinzip. *Ann Phys* **1931**, *402* (7), 888–904.
- (281) Heisenberg, W. Kausalgesetz Und Quantenmechanik. *Erkenntnis* **1931**, *2* (1), 172–182.
- (282) Schottky, W. Halbleitertheorie Der Sperrschicht. *Naturwissenschaften* **1938**, *26* (52), 843.
- (283) Mott, N. F. Note on the Contact between a Metal and an Insulator or Semi-Conductor. *Mathematical Proceedings of the Cambridge Philosophical Society* **1938**, *34* (4), 568–572.
- (284) P., R. The Theory of the Properties of Metals and Alloys. *Nature* **1937**, *139* (3513), 348–349.
- (285) Shaffer, D. W.; Xie, Y.; Concepcion, J. J. O–O Bond Formation in Ruthenium-Catalyzed Water Oxidation: Single-Site Nucleophilic Attack vs. O–O Radical Coupling. *Chem Soc Rev* **2017**, *46* (20), 6170–6193.
- (286) Bozoglian, F.; Romain, S.; Ertem, M. Z.; Todorova, T. K.; Sens, C.; Mola, J.; Rodríguez, M.; Romero, I.; Benet-Buchholz, J.; Fontrodona, X.; Cramer, C. J.; Gagliardi, L.; Llobet, A. The Ru–Hbpp Water Oxidation Catalyst. *J Am Chem Soc* **2009**, *131* (42), 15176–15187.
- (287) Vereshchuk, N.; Matheu, R.; Benet-Buchholz, J.; Pipelier, M.; Lebreton, J.; Dubreuil, D.; Tessier, A.; Gimbert-Suriñach, C.; Ertem, M. Z.; Llobet, A. Second Coordination Sphere Effects in an Evolved Ru Complex Based on Highly Adaptable Ligand Results in Rapid Water Oxidation Catalysis. *J Am Chem Soc* **2020**, *142* (11), 5068–5077.
- (288) Song, N.; Concepcion, J. J.; Binstead, R. A.; Rudd, J. A.; Vannucci, A. K.; Dares, C. J.; Coggins, M. K.; Meyer, T. J. Base-Enhanced Catalytic Water Oxidation by a Carboxylate–Bipyridine Ru(II) Complex. *Proceedings of the National Academy of Sciences* **2015**, *112* (16), 4935–4940.
- (289) Duan, L.; Bozoglian, F.; Mandal, S.; Stewart, B.; Privalov, T.; Llobet, A.; Sun, L. A Molecular Ruthenium Catalyst with Water-Oxidation Activity Comparable to That of Photosystem II. *Nat Chem* **2012**, *4* (5), 418–423.

- (290) Xie, Y.; Shaffer, D. W.; Lewandowska-Andralojc, A.; Szalda, D. J.; Concepcion, J. J. Water Oxidation by Ruthenium Complexes Incorporating Multifunctional Bipyridyl Diphosphonate Ligands. *Angewandte Chemie International Edition* **2016**, 55 (28), 8067–8071.
- (291) Kamdar, J. M.; Marelus, D. C.; Moore, C. E.; Rheingold, A. L.; Smith, D. K.; Grotjahn, D. B. Ruthenium Complexes of 2,2'-Bipyridine-6,6'-Diphosphonate Ligands for Water Oxidation. *ChemCatChem* **2016**, 8 (19), 3045–3049.
- (292) Shaffer, D. W.; Xie, Y.; Szalda, D. J.; Concepcion, J. J. Lability and Basicity of Bipyridine-Carboxylate-Phosphonate Ligand Accelerate Single-Site Water Oxidation by Ruthenium-Based Molecular Catalysts. *J Am Chem Soc* **2017**, 139 (43), 15347–15355.
- (293) Matheu, R.; Ertem, M. Z.; Benet-Buchholz, J.; Coronado, E.; Batista, V. S.; Sala, X.; Llobet, A. Intramolecular Proton Transfer Boosts Water Oxidation Catalyzed by a Ru Complex. *J Am Chem Soc* **2015**, 137 (33), 10786–10795.
- (294) Matheu, R.; Ertem, M. Z.; Gimbert-Suriñach, C.; Sala, X.; Llobet, A. Seven Coordinated Molecular Ruthenium–Water Oxidation Catalysts: A Coordination Chemistry Journey. *Chem Rev* **2019**, 119 (6), 3453–3471.
- (295) Duan, L.; Fischer, A.; Xu, Y.; Sun, L. Isolated Seven-Coordinate Ru(IV) Dimer Complex with [HOHOH]– Bridging Ligand as an Intermediate for Catalytic Water Oxidation. *J Am Chem Soc* **2009**, 131 (30), 10397–10399.
- (296) de Klerk, A.; Furimsky, E.; Spivey, J. J. *Catalysis in the Refining of Fischer-Tropsch Syncrude*; Catalysis Series; The Royal Society of Chemistry, 2010.
- (297) Sudiro, M.; Bertucco, A.; Ruggeri, F.; Fontana, M. Improving Process Performances in Coal Gasification for Power and Synfuel Production. *Energy & Fuels* **2008**, 22 (6), 3894–3901.
- (298) Reese, M.; Marquart, C.; Malmali, M.; Wagner, K.; Buchanan, E.; McCormick, A.; Cussler, E. L. Performance of a Small-Scale Haber Process. *Ind Eng Chem Res* **2016**, 55 (13), 3742–3750.
- (299) Kang, J.; He, S.; Zhou, W.; Shen, Z.; Li, Y.; Chen, M.; Zhang, Q.; Wang, Y. Single-Pass Transformation of Syngas into Ethanol with High Selectivity by Triple Tandem Catalysis. *Nat Commun* **2020**, 11 (1), 827.
- (300) Turner, J.; Sverdrup, G.; Mann, M. K.; Maness, P.-C.; Kroposki, B.; Ghirardi, M.; Evans, R. J.; Blake, D. Renewable Hydrogen Production. *Int J Energy Res* **2008**, 32 (5), 379–407.
- (301) Whipple, D. T.; Kenis, P. J. A. Prospects of CO₂ Utilization via Direct Heterogeneous Electrochemical Reduction. *J Phys Chem Lett* **2010**, 1 (24), 3451–3458.
- (302) Gray, H. B. Powering the Planet with Solar Fuel. *Nat Chem* **2009**, 1 (1), 7.
- (303) Appel, A. M.; Bercaw, J. E.; Bocarsly, A. B.; Dobbek, H.; DuBois, D. L.; Dupuis, M.; Ferry, J. G.; Fujita, E.; Hille, R.; Kenis, P. J. A.; Kerfeld, C. A.; Morris, R. H.; Peden, C. H. F.; Portis, A. R.; Ragsdale, S. W.; Rauchfuss, T. B.; Reek, J. N. H.; Seefeldt, L. C.; Thauer, R. K.; Waldrop, G. L. Frontiers, Opportunities, and Challenges in Biochemical and Chemical Catalysis of CO₂ Fixation. *Chem Rev* **2013**, 113 (8), 6621–6658.
- (304) Lewis, N. S.; Nocera, D. G. Powering the Planet: Chemical Challenges in Solar Energy Utilization. *Proceedings of the National Academy of Sciences* **2006**, 103 (43), 15729 LP – 15735.
- (305) Vermaas, D. A.; Smith, W. A. Synergistic Electrochemical CO₂ Reduction and Water Oxidation with a Bipolar Membrane. *ACS Energy Lett* **2016**, 1 (6), 1143–1148.
- (306) Sato, S.; Arai, T.; Morikawa, T. Toward Solar-Driven Photocatalytic CO₂ Reduction Using Water as an Electron Donor. *Inorg Chem* **2015**, 54 (11), 5105–5113.

- (307) Barlow, J. M.; Yang, J. Y. Thermodynamic Considerations for Optimizing Selective CO₂ Reduction by Molecular Catalysts. *ACS Cent Sci* **2019**, 5 (4), 580–588.
- (308) Nichols, A. W.; Machan, C. W. Secondary-Sphere Effects in Molecular Electrocatalytic CO₂ Reduction. *Front Chem* **2019**, 7.
- (309) Riplinger, C.; Sampson, M. D.; Ritzmann, A. M.; Kubiak, C. P.; Carter, E. A. Mechanistic Contrasts between Manganese and Rhenium Bipyridine Electrocatalysts for the Reduction of Carbon Dioxide. *J Am Chem Soc* **2014**, 136 (46), 16285–16298.
- (310) Fisher, B. J.; Eisenberg, R. Electrocatalytic Reduction of Carbon Dioxide by Using Macrocycles of Nickel and Cobalt. *J Am Chem Soc* **1980**, 102 (24), 7361–7363.
- (311) Beley, Marc.; Collin, J. Paul.; Ruppert, Romain.; Sauvage, J. Pierre. Electrocatalytic Reduction of Carbon Dioxide by Nickel Cyclam²⁺ in Water: Study of the Factors Affecting the Efficiency and the Selectivity of the Process. *J Am Chem Soc* **1986**, 108 (24), 7461–7467.
- (312) Morris, R. H. Estimating the Acidity of Transition Metal Hydride and Dihydrogen Complexes by Adding Ligand Acidity Constants. *J Am Chem Soc* **2014**, 136 (5), 1948–1959.
- (313) Waldie, K. M.; Ostericher, A. L.; Reineke, M. H.; Sasayama, A. F.; Kubiak, C. P. Hydricity of Transition-Metal Hydrides: Thermodynamic Considerations for CO₂ Reduction. *ACS Catal* **2018**, 8 (2), 1313–1324.
- (314) DuBois, D. L.; Berning, D. E. Hydricity of Transition-Metal Hydrides and Its Role in CO₂ Reduction. *Appl Organomet Chem* **2000**, 14 (12), 860–862.
- (315) Morris, A. J.; Meyer, G. J.; Fujita, E. Molecular Approaches to the Photocatalytic Reduction of Carbon Dioxide for Solar Fuels. *Acc Chem Res* **2009**, 42 (12), 1983–1994.
- (316) Matsubara, Y. Standard Electrode Potentials for the Reduction of CO₂ to CO in Acetonitrile–Water Mixtures Determined Using a Generalized Method for Proton-Coupled Electron-Transfer Reactions. *ACS Energy Lett* **2017**, 2 (8), 1886–1891.
- (317) Mayer, J. M. PROTON-COUPLED ELECTRON TRANSFER: A Reaction Chemist's View. *Annu Rev Phys Chem* **2004**, 55 (1), 363–390.
- (318) Chaplin, R. P. S.; Wragg, A. A. Effects of Process Conditions and Electrode Material on Reaction Pathways for Carbon Dioxide Electroreduction with Particular Reference to Formate Formation. *J Appl Electrochem* **2003**, 33 (12), 1107–1123.
- (319) Firet, N. J.; Smith, W. A. Probing the Reaction Mechanism of CO₂ Electroreduction over Ag Films via Operando Infrared Spectroscopy. *ACS Catal* **2017**, 7 (1), 606–612.
- (320) Kumar, B.; Llorente, M.; Froehlich, J.; Dang, T.; Sathrum, A.; Kubiak, C. P. Photochemical and Photoelectrochemical Reduction of CO₂. *Annu Rev Phys Chem* **2012**, 63 (1), 541–569.
- (321) Smith, B. J.; Parent, L. R.; Overholts, A. C.; Beaucage, P. A.; Bisbey, R. P.; Chavez, A. D.; Hwang, N.; Park, C.; Evans, A. M.; Gianneschi, N. C.; Dichtel, W. R. Colloidal Covalent Organic Frameworks. *ACS Cent Sci* **2017**, 3 (1), 58–65.